Electrodeposited Nanoparticles: Properties and Photocatalytic Applications

Eoin E. Sheridan, B.Sc.

A Thesis Presented at Dublin City University for the Degree of Doctor of Philosophy

Supervisors:
Prof. Robert J. Forster
Dr. Tia Keyes
Prof. Richard Crooks

Ph.D. 2009

I hereby certify that this material, which I now submit for assessment on the programme of study leading to the award of Doctor of Philosophy is entirely my own work, that I have exercised reasonable care to ensure that the work is original, and does not to the best of my knowledge breach any law of copyright, and has not been taken from the work of others save and to the extent that such work has been cited and acknowledged within the text of my work.

Signed: _____

ID No.: _____

Date: _____

Acknowledgements

I gratefully acknowledge the support, guidance and advice afforded to me by Prof. Robert Forster over these past years. His input of ideas and enthusiasm has ensured that this thesis has reached completion. I am also grateful to Dr. Tia Keyes, who has been instrumental in the progress of my project. Prof. Richard Crooks also played an important role in my development as a researcher, and I am thankful to him for accepting me into his research group.

I am grateful to those people with whom I worked and who assisted me in the work detailed in this thesis. Johan, Uju, Colm, Lynda, Bincy, Francois and Kwok in particular were generous with their time and opinions.

I would also like to acknowledge all of those people who supported me during the course of my Ph.D. program. My friends who gave me emotional support and helped me in dealing with stress; Bincy, Colm, Lynda, Michele, Susan, Karen, Claudio, Anita, Francois, Cori, Bleu and Fionnuala. My family were similarly vital to me in getting through the last few years, Ciara, Kevin and Alan, and my grandfather Eddie, all of whom suffered my bad moods and in many ways felt the stresses of my work as much as I did. My Parents Stephen and Bernadette in particular brought me into this world, have been an inspiration to me, and continue to support, advise and educate me to this day.

I would like to thank the Irish Research Council for Science, Engineering and Technology for support under the Embark initiative.

Table of Contents

Abstract

Electrodeposited Nanoparticles: Properties and Photocatalytic Applications

The work presented in this thesis reports on fundamental studies into electrodeposition of gold and silver nanoparticulate spheroids on a conducting substrate, Fluorine-doped tin-oxide, and the manipulation of the electrodeposition conditions in order to influence and control the size and surface concentration of spheroids. Methods to control the deposition included chemical modification of the surface with an adsorbed monolayer of 3-aminopropyldimethylmethoxysilane, and manipulation of the potential pulse scheme, especially using a double pulse "nucleation and growth" approach. The optimised method for production of silver and gold nanoparticulate surfaces was utilised to selectively create surfaces that yield strong surface enhanced Raman scattering (SERS) enhancements, as well as metal enhanced fluorescence. These enhancements have been quantified using the probe molecules Trans-1,2-bis(4-pyridyl)ethylene (BPE) and $[Os(bpy)_2Qbpy]^{2+}$ respectively (where bpy is 2,2'-bipyridyl and Qbpy is 2,2':4,4'':4'4''-quarterpyridyl).

Spontaneously formed, densely packed monolayers of $[Os(bpy)_2PIC]^{2+}$ have been formed on fluorine-doped tin-oxide (FTO) electrodes, and films of $[Os(bpy)_2Qby]^{2+}$ have been formed on silver nanoparticulate decorated FTO (where bpy is 2,2'-bipyridyl, PIC is 2-(4-carboxyphenyl)imidazo[4,5-f][1,10]phenanthroline, and Qbpy is 2,2':4,4'':4'4''-quarterpyridyl). The quenching mechanism of the polyoxotungstate anion α-$[S_2W_{18}O_{62}]$ (POW) on the two osmium polypyridyl complexes in solution has been identified by analysis of the Stern-Volmer plots. The quenching of monolayers of these complexes by POW, coupled to the electrochemical regeneration of the ground state osmium complex by potential application at the FDTO electrode, has been used to photo-catalytically reduce methyl viologen.

Finally a wireless gold bipolar electrode in a microchannel, whose potential is floating and managed by exerting potential control over the electrolyte solution rather than individual electrodes, has been used as the basis for an electrochemiluminescent DNA microsensor. The function of the DNA microsensor has been optimised to maximise signal intensity by altering the ECL solution, and by manipulating the pathway by which the ECL reaction proceeds. DNA binding has been detected based on catalysis of the oxygen reduction reaction (ORR) at (DNA linked) platinum nanoparticles. The ORR can be replaced with other reduction reactions to detect other species such as anthraquinones. The possibility of using this device for quantitative sensing of both DNA and other species is discussed.

1 Introduction and Review of Relevant Literature

In recent years, the driving forces in medical research are shifting more and more towards diagnostic progress as the significant benefits of early diagnosis of many life threatening diseases, such as cancer, heart disease and diabetes are recognised. The development of diagnostic tests that can be used to detect biomarkers for diseases such as these at extremely low concentrations would facilitate diagnosis of such diseases at earlier stages. Much of the work in this thesis focuses on finding ways to improve the sensitivity and performance of analytical techniques commonly employed, or that could be employed in diagnostic analysis, for example surface enhanced Raman scattering, fluorescence spectroscopy, electrochemical detection and Electrogenerated chemiluminescence. Nanoparticles of gold and silver have been recognised for their enhancing abilities in some of these techniques owing to their remarkable photophysical and geometric properties [1-3]. Electrodeposition offers a means of fabricating nanoparticle modified surfaces in a quick and facile manner, in which the nanoparticles are electrically contacted, and extremely stable [4]. In this work, methods of electrodepositing nanoparticles in a controlled manner will be explored, and the properties of the new surfaces produced will be investigated with particular emphasis on diagnostic applications, and other interesting areas such as photocatalysis.

1.1 Electrodeposition: Theory and Kinetics

Electrodeposition is a process whereby a potential difference is applied to an electrode at an electrolyte interface resulting in electron transfer between the electrode and an ionic species in the electrolyte and the subsequent deposition of atoms of that species onto the electrode. It is a process that has been studied and employed for over 200 years since it was first utilised in 1805 by Luigi Brugnatelli to form decorative and protective coatings [5]. It has only been in the last 75 years, with the advent of electron microscopy [6], that electrodeposition science has extended into the study of micro and nano-structural properties of electrodeposits [4, 7, 8], and only in the last 40 years has the study of nanoparticles formed by electrodeposition become the

subject of scientific consideration [9, 10]. More recently, electrodeposition has been used for electroforming [11], fabrication of integrated circuits [12] and magnetic recording devices [13], as well as electrochemical microfabrication [14] and nanofabrication [15]. Many of these technologies fall outside the scope of this project, so this literature survey will focus on nanofabrication, and in particular electrochemical deposition of metal nanostructures.

Metals are most frequently (but not exclusively) employed as the depositing species, this is because of the large amount of ionisable metal salts available that, when present in their ionic form in an electrolyte, are easily reduced to their atoms by application of a modest potential difference [5]. The goal of electrodeposition is often to confer a new property on the electrode, such as chemical stability, metallic brightness or nanoscale roughness, these properties can be conferred by many common metals such as copper, silver, gold and alloys of these metals. The choice of metal, and the particular salt of that metal, depends on the objectives of the electrodeposition; there is a great deal of information in the literature regarding the properties of electrodeposits depending on the choice of metal salt [5, 16].

The mechanism by which electrodeposition proceeds can be understood as follows; a cation in solution is reduced at the surface of the electrode due to the application of an applied potential (the electrochemical driving force) and the injection of an electron from the electrode into the cation. The cation forms an adatom upon reduction and migrates over the surface of the electrode to an energetically favourable site where it bonds, see Figure 1.1. Energetically favourable sites include scratches, dislocations, steps, kinks and other defects [17]. Further reduction occurs and the subsequently produced adatoms aggregate with the first to form a nucleus of the electrodeposit. These nuclei “grow” as more adatoms migrate to the nuclei. If the potential is applied for sufficient time, and there is adequate concentration of metal ions in solution the electrode surface exposed to the electrolyte eventually becomes completely covered with the electrodeposit (Figure 1.1c). The focus of this literature survey is on the production of

nanoparticles by electrodeposition of gold and silver ions, this requires the cessation of the electrodeposition process before growing nuclei begin to coalesce to form a coating.

In order for electrodeposition to occur charge transfer must be induced. This is achieved by means of application of electrical potential from a power source (e.g. a potentiostat). The applied potential (*E*) energises the electrons in the Fermi level of the electrode, allowing for flow of electrons from the electrode to a species in solution or vice versa [17]. Electrodeposition of metals requires neutralisation of a positively charged metal ion in solution according to the general equation;

$$M^{z+} + ze^{-} \leftrightarrow M_{Dep} \tag{1.1}$$

A potential negative of the equilibrium potential of the metal species is required to force this reaction to proceed. The least negative potential at which this can occur is called the standard reduction potential *(E^0)*. Normally electrodeposition is carried out at potentials significantly more negative of the reduction potential of the species in question. The overpotential (η) is a measure of the magnitude of potential beyond the reduction potential that has been applied:

$$\eta = E - E^0 \tag{1.2}$$

The overpotential is a measure of the energy put into the electrochemical system to overcome the energy barrier for the reaction (electrodeposition).

The current passed during an electrochemical deposition can be related to the charge (Q) passed according to the equation

$$Q = it \tag{1.3}$$

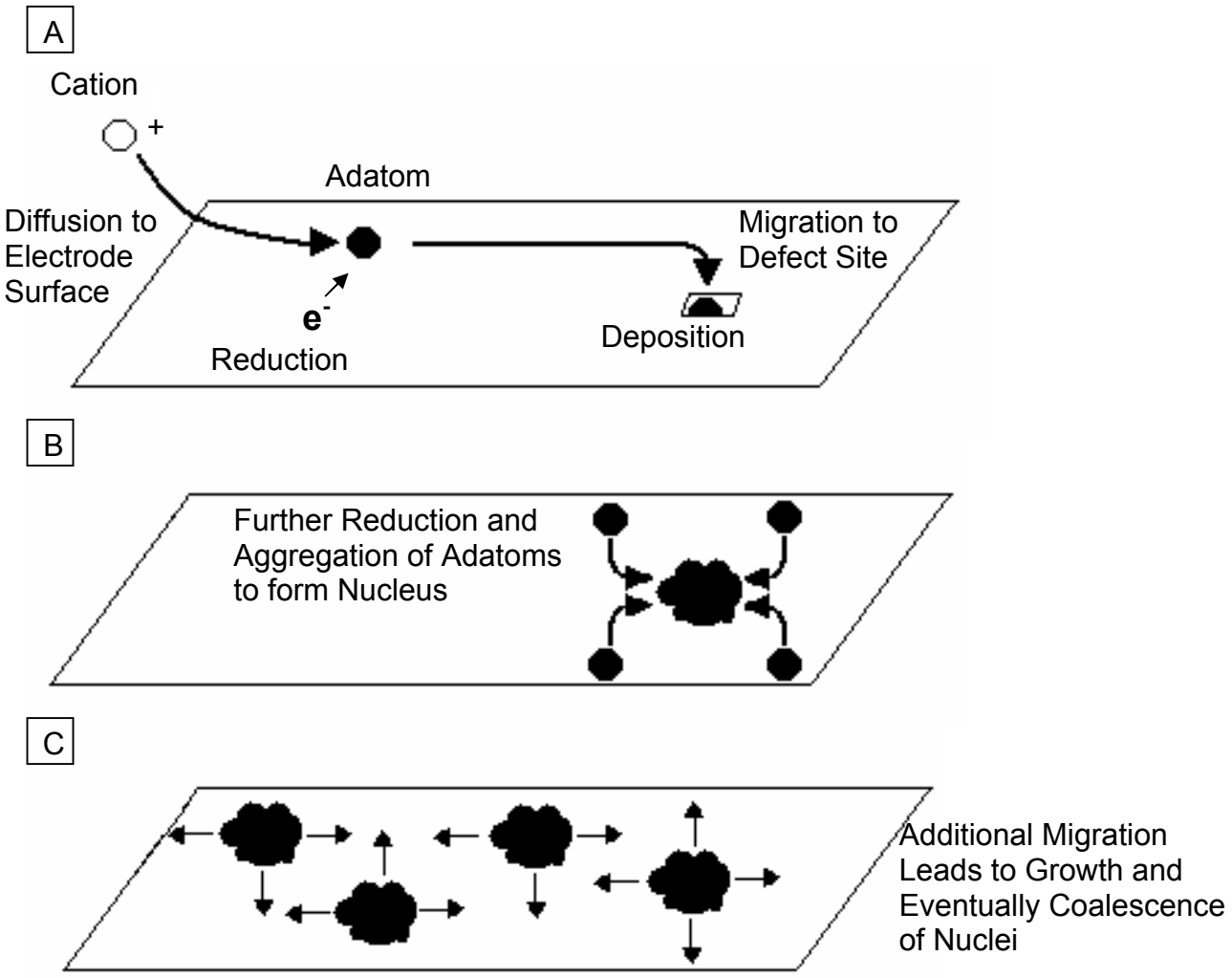

Figure 1.1 Graphical representation of process of electrodeposition.

where i is current and t is time. The charge passed during an electrochemical deposition can be related to the amount of depositing species reacted at the electrode interface according to Faraday's law:

$$Q = nFN \tag{1.4}$$

where N is the number of moles of depositing species reacted, and F Faraday's constant (96,487C) is equal to the charge of one mole of electrons. And from this value (N) the mass, volume and thickness of the deposit can be estimated. This equation assumes 100% coulometric efficiency, which does not occur in practice, therefore the actual amount of species deposited is less than the figure calculated by this equation. Side reactions of other species in the electrolyte at the electrode, reduction of hydrogen and incomplete reduction of multivalent ions result in a reduction of the coulometric efficiency. The coulometric efficiency can be estimated using an electrochemical quartz crystal microbalance, an instrument capable of measuring the mass of metal deposited on an electrode with great accuracy.

Electrodeposition can be performed using several techniques, the most commonly employed methods are galvanostatic electrodeposition and potentiostatic electrodeposition. Galvanostatic electrodeposition involves the flow of a constant current at the working electrode, the potential is controlled in order to keep the current constant. When the deposition is potentiostatically controlled a constant potential is applied to the working electrode and the current is measured as a function of time. Potentiostatic control has been used during this project as it allows for better measurement and control of the kinetics of the electrodeposition process. A typical potentiostatic deposition transient is shown in Figure 1.2. The rate of the reaction at the working electrode can be limited by diffusion or by kinetics. Figure 1.2 is an example where a sufficiently large overpotential was applied and deposition becomes diffusion limited after a few ms. The general shape of the current transient was unaffected by the applied overpotential. In each case the current initially rises as the barrier to nucleation is breached and the

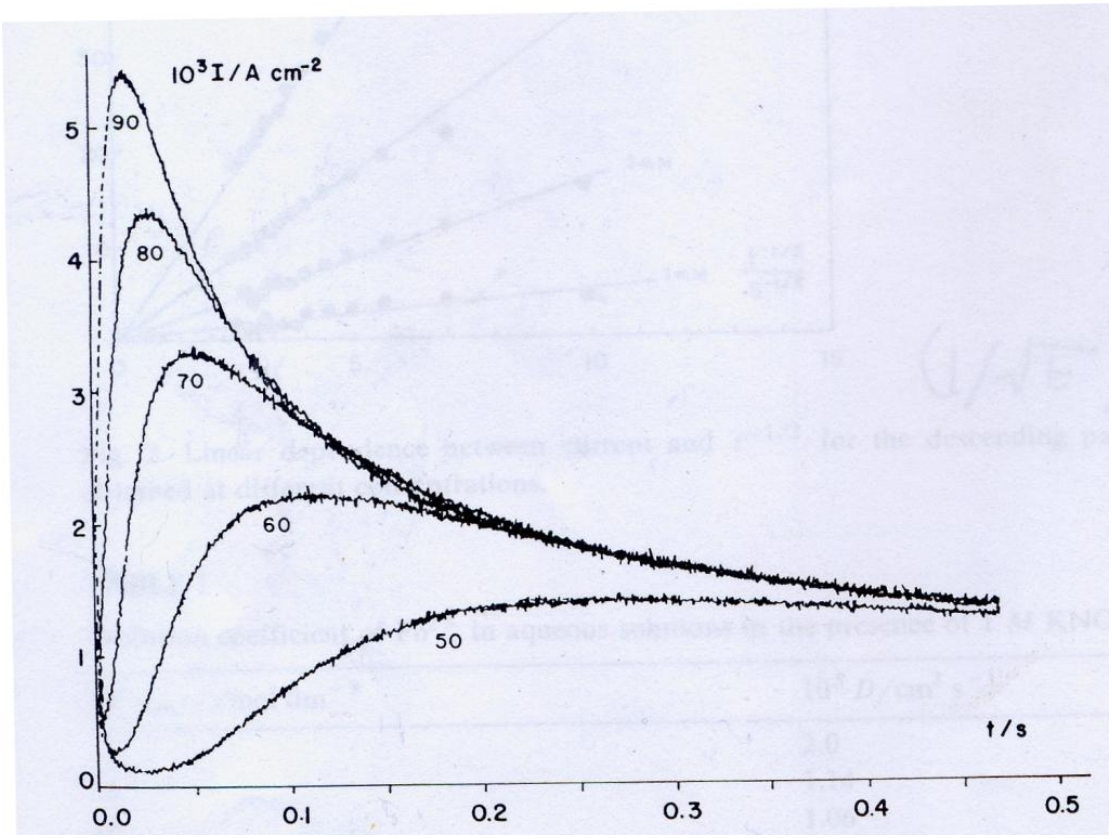

Figure 1.2 Typical current transient obtained for the electrodeposition of a metal (lead) by potentiostatic deposition. Electrodeposition of lead on glassy carbon from 0.01M $Pb(NO_3)_2$ in 1M KNO_3 at the deposition overpotential (mV) indicated. Taken from Scharifker et al. [18].

expanding nuclei provide increasingly bigger surfaces at which further reduction can occur, therefore allowing more current to flow. At this point the reaction is kinetically controlled. It does not take long (in this example between 0.02s and 0.2s) until the concentration of metal ions at the electrode begins to deplete and this results in a switch to diffusion controlled growth of the nuclei. This is seen experimentally as a dropping off of the current density. The magnitude of overpotential effects the height of the current maximum as well as the time at which it occurs. The significance of the shape of the current transient is discussed in the next section.

1.2 Measurement and Manipulation of Electrodeposition Kinetics

1.2.1 Kinetics of Nucleation

The rate of appearance of stable new growth centres follows first order kinetics therefore the number density of centres is given by:

$$N(t) = N_0\{1 - \exp(-At)\} \tag{1.5}$$

where N_o is the number of active sites where nucleation is possible, t is time and A is the first order nucleation rate constant which is a function of several parameters (e.g. potential, concentration and substrate).

When A is large

$$N(t) = N_0 \tag{1.6}$$

This equation describes instantaneous nucleation. Essentially if the rate constant A is very large then all of the available sites are nucleated at t = 0.

And when the value of A is smaller

$$N(t) = N_0 At \tag{1.7}$$

This equation describes the process of progressive nucleation. If A is small only a fraction of available sites will be nucleated at t = 0, and over time more sites become nucleated. The importance of this dependence on the rate becomes clear when it is considered that the rate can be controlled experimentally by the applied electrodeposition overpotential.

1.2.2 Nucleation and Growth of 2D Centres

Following nucleation, growth can proceed by two different mechanisms. The first is 2-dimensional (2D) growth whereby adatoms attach at the edge of existing nuclei to form 2D islands. Nuclei eventually coalesce to form a single layer of electrodeposit on the electrode after which nucleation occurs again over the first deposited layer. This process can be repeated indefinitely. The second possible process is 3-dimensional (3D) growth which involves addition of adatoms with equal probability at any point on the surface, resulting in the growth upwards as well as laterally at similar rates.

The net current density (I) for a 2D (layer by layer) deposition when nucleation is instantaneous is given by;

$$I = \frac{2N_0 \pi n F k^2 h M t}{\rho} \tag{1.8}$$

And when progressive nucleation occurs it is given by;

$$I = \frac{2AN_0 \pi F k^2 h M t^2}{\rho} \tag{1.9}$$

where M = molecular weight, k = rate of incorporation (mol cm^{-2} s^{-1}), n is the number of electrons transferred, F is Faraday's constant, h is the height of the nucleus (a monolayer) and ρ is the density of the deposit. These equations describe the case for independent 2D growth centres. In practice this only occurs for a very short time until the diffusion zones of the growth centres begin to overlap (diffusion zone coupling). To take account of overlapping growth centres the Avrami theorem [19] is used. The effect of this in calculating the current densities is the following:

$$I = \frac{2\pi nFMhN_0k^2t}{\rho} \times \exp\left(\frac{-\pi N_0M^2k^2t^2}{\rho^2}\right) \quad (1.10)$$

For instantaneous nucleation, and

$$I = \frac{\pi nFMhAN_0k^2t^2}{\rho} \times \exp\left(\frac{-\pi AN_0M^2k^2t^3}{3\rho^2}\right) \quad (1.11)$$

for progressive nucleation.

The exponential factor introduced by the Avrami theorem results in a maximum in the current density ($I_{\max}$). Using the co-ordinates of this maximum (I_m, t_m) a reduced variable form of these equations can be generated;

$$\frac{I}{I_m} = \frac{t}{t_m} \times \exp\left[\frac{-(t^2 - t_m^2)}{2t_m^2}\right] \quad (1.12)$$

$$\frac{I}{I_m} = \frac{t^2}{t_m^2} \times \exp\left[\frac{-2(t^3 - t_m^3)}{3t_m^3}\right] \quad (1.13)$$

for instantaneous and progressive nucleation, respectively. These expressions can be used to create a dimensionless plot as shown in Figure 1.3. This plot will be of the same shape as the relevant deposition transient normalised as $I/I_{\max}$ Vs $t/t_{\max}$ for the electrodeposition of a metal via either instantaneous or progressive nucleation, and therefore a positive match can be used as confirmation of the nucleation mode (instantaneous or progressive) and the growth mode (2D or 3D).

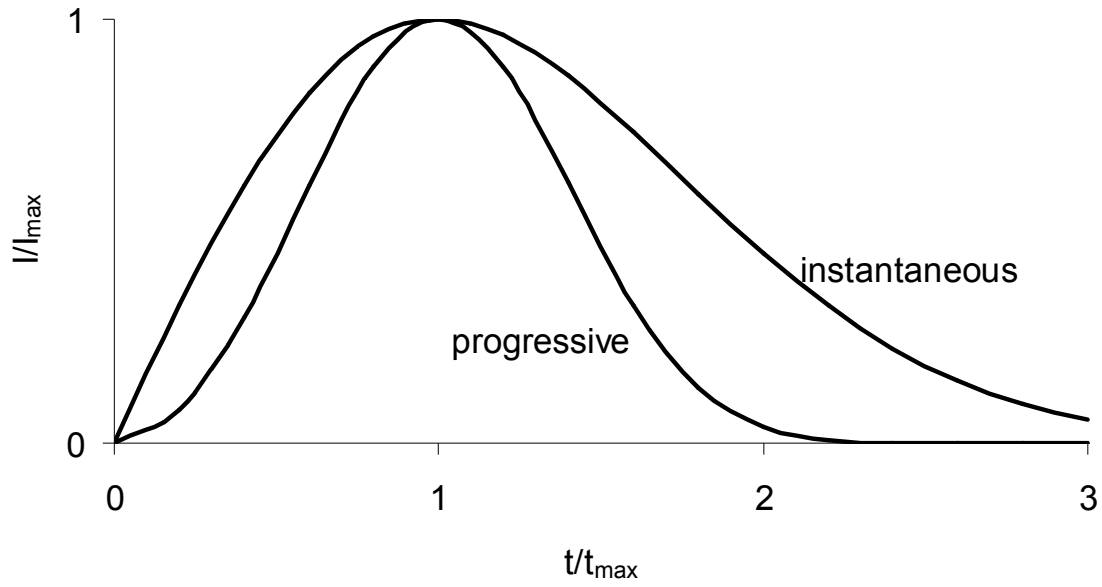

Figure 1.3 Theoretical dimensionless plots for the 2D growth of electrodeposited islands by instantaneous and progressive nucleation.

1.2.3 Nucleation and Growth of 3D Centres

A similar treatment for the 3D growth mechanism has been developed by Scharifker and Hills [20] when growth is diffusion controlled. The equivalent dimensionless equations for diffusion controlled 3D nucleation are;

Instantaneous

$$\left(\frac{I}{I_m}\right)^2 = \frac{1.9542}{t/t_m} \times \left[1 - \exp\left(-1.2564\frac{t}{t_m}\right)\right]^2 \qquad (1.14)$$

Progressive

$$\left(\frac{I}{I_m}\right)^2 = \frac{1.2254}{t/t_m} \times \left[1 - \exp\left(-2.3367\left\{\frac{t}{t_m}\right\}^2\right)\right]^2 \qquad (1.15)$$

Theoretical current transients of these equations are shown in Figure 1.4.

Using experimental data to create similar dimensionless plots it is possible to compare the shape of the curve obtained to those seen in Figures 1.3 and 1.4 to determine whether the nucleation mode is instantaneous or progressive and the growth mechanism 2D or 3D. This method of characterisation of the nucleation and growth mode has been widely used [21-23]. The validity and accuracy of results obtained from these dimensionless plots has been questioned [24-27] and defended [28, 29] in the literature. The result of the dimensionless plot is dependent to a very large extent on a single point in the current transient (I_m, t_m) and it is frequently possible to obtain results that fall between the curves for progressive and instantaneous nucleation and it has been claimed that the result obtained can sometimes be erroneous [26]. Nonetheless the result of the dimensionless plot, if taken as a guide to the mode of nucleation and growth, can be a useful tool for characterisation of electrochemically deposited substrates, and there are currently no alternative methods of analysis of the deposition transient to determine the nucleation and growth modes in the literature.

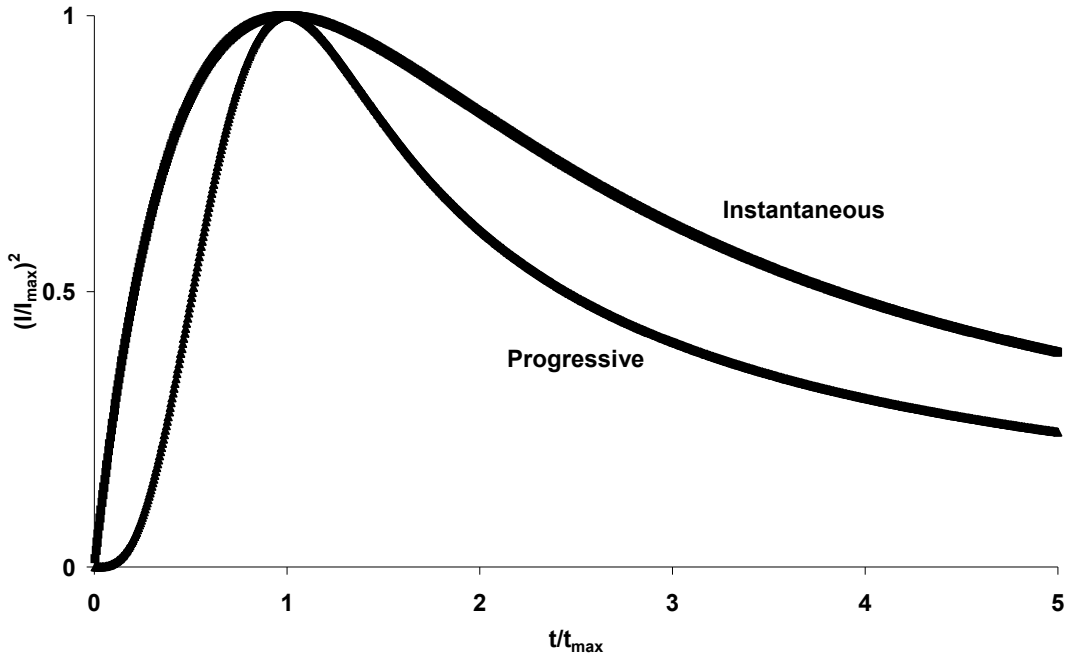

Figure 1.4 Theoretical dimensionless plots for the 3D growth of electrodeposited islands by instantaneous and progressive nucleation.

1.2.4 Control of Nucleation and Growth Modes

It is often desirable to be able to select the nucleation and or growth modes occurring during and electrodeposition experiment. This is of particular relevance to this project as a key objective of the project is to produce high surface area metal island films with monodisperse particle size. In order to achieve size monodispersity instantaneous nucleation is essential, and 3D growth is preferable to produce high surface area hemispherical deposits. Characterisation and manipulation of the nucleation and growth modes is therefore essential if these kinds of substrates are to be produced. Some of the methods that have been used in the literature to control nucleation and growth modes are discussed below.

Hernandez et al. [21] have investigated the manipulation of the nucleation and growth mode of silver electrodeposition on glassy carbon from $AgNO_3$. The variables that they considered were metal salt concentration and deposition potential. Using dimensionless plots (Figures 1.3 and 1.4) to qualitatively analyse the data they were able to describe the effect of these variables on the nucleation and growth modes. When they varied metal salt concentration in the range 10^{-4} M to 0.3 M they recorded 2D growth at low concentrations, and as the concentration was increased there was a switch to 3D growth. It seems that the greater metal ion concentration facilitated the growth of larger 3-dimensional structures. When they varied the deposition potential they found that progressive nucleation occurred at low overpotentials and as the overpotential was increased (more negative potentials) the nucleation mode shifted to instantaneous. This is to be expected as the greater amount of energy provided by a larger overpotential overcomes the energy barrier for nucleation at a greater number of sites. This trend has been observed experimentally by several other groups [30-32].The effect of potential on the nucleation mode is demonstrated in Figure 1.5.

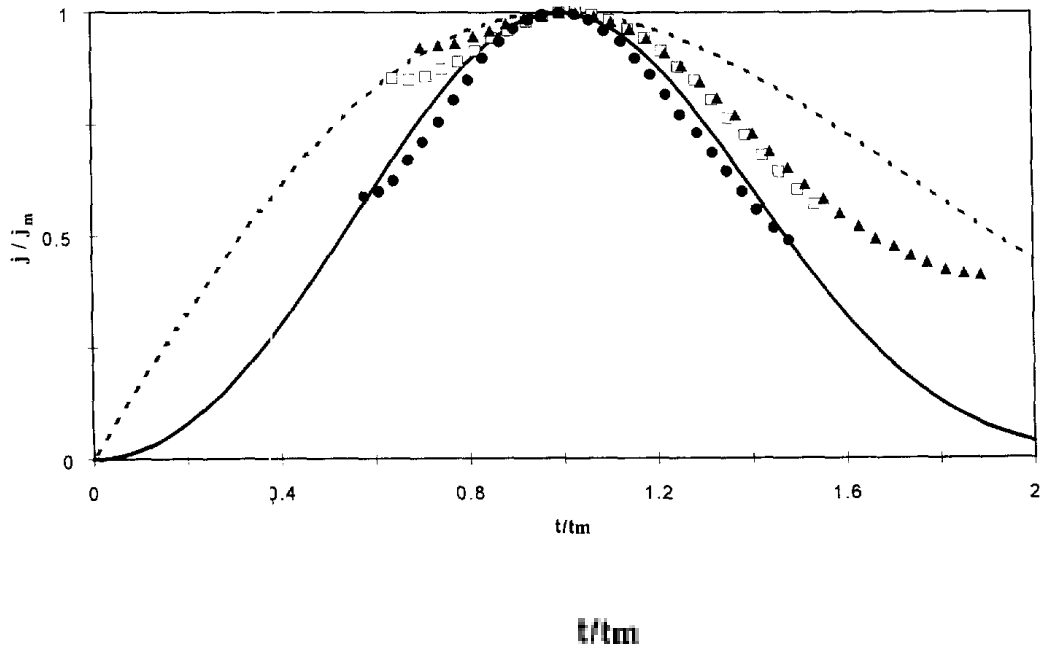

t/tm

Figure 1.5 Dimensionless plot (2D) of the deposition of Ag on glassy carbon from 10^{-4} M $AgNO_3$ at a potential of (●) -100mV, (□) -150mV and (▲) -250mV. Theoretical curves for (———) progressive nucleation, (- - - - -) instantaneous nucleation. Taken from reference [21].

Penner et al. [30, 33] have developed a method of separating the nucleation and growth modes into separate potentiostatic pulses. The method works by applying a high overpotential nucleation pulse for a very short time (typically 5ms), designed to instantaneously seed the surface with nuclei at all available nucleation sites. This is followed by a growth pulse at a much lower overpotential for a longer period of time causing growth of the nuclei. The benefit of this technique is that it allows growth to occur at a low overpotential without nucleating progressively.

The reason why it is important to eliminate progressive nucleation from the deposition process is that new nuclei grow for a shorter period of time than old ones and this can cause significant size polydispersity. Using a large deposition overpotential would eliminate progressive nucleation however it would introduce a new problem that also results in significant size polydispersity namely diffusion zone coupling. Every growing nucleus is surrounded by a depletion layer, this is the volume of electrolyte surrounding the nucleus where the concentration of metal ions is depleted compared to the bulk. If the diffusion zones of two nearby nuclei expand to the extent that they join together (See Figure 1.6), or couple, then the supply of metal ions to these nuclei will be slower compared to the supply of ions to an isolated nucleus under the same conditions. This will result in slower growth of the coupled nuclei compared to the isolated nuclei. The expansion of the diffusion zone around a nucleus is a function of growth rate, the faster the uptake of ions by the nucleus the faster the expansion of the depletion layer. Therefore, a slow growth rate (low overpotential) causes less diffusion zone coupling and this results in greater size monodispersity. Using this two-pulse method Penner's group has produced arrays of high density, size monodisperse metal nanoparticles therefore their work has had a significant influence on the work of this project.

Floate et al. [31] have suggested that exposing the electrolyte solution to ultrasonic waves can influence the nucleation mode. They reported that electrodeposition of cobalt on glassy carbon occurred at a faster rate and tended to be more instantaneous under sonication conditions (20 kHz). The

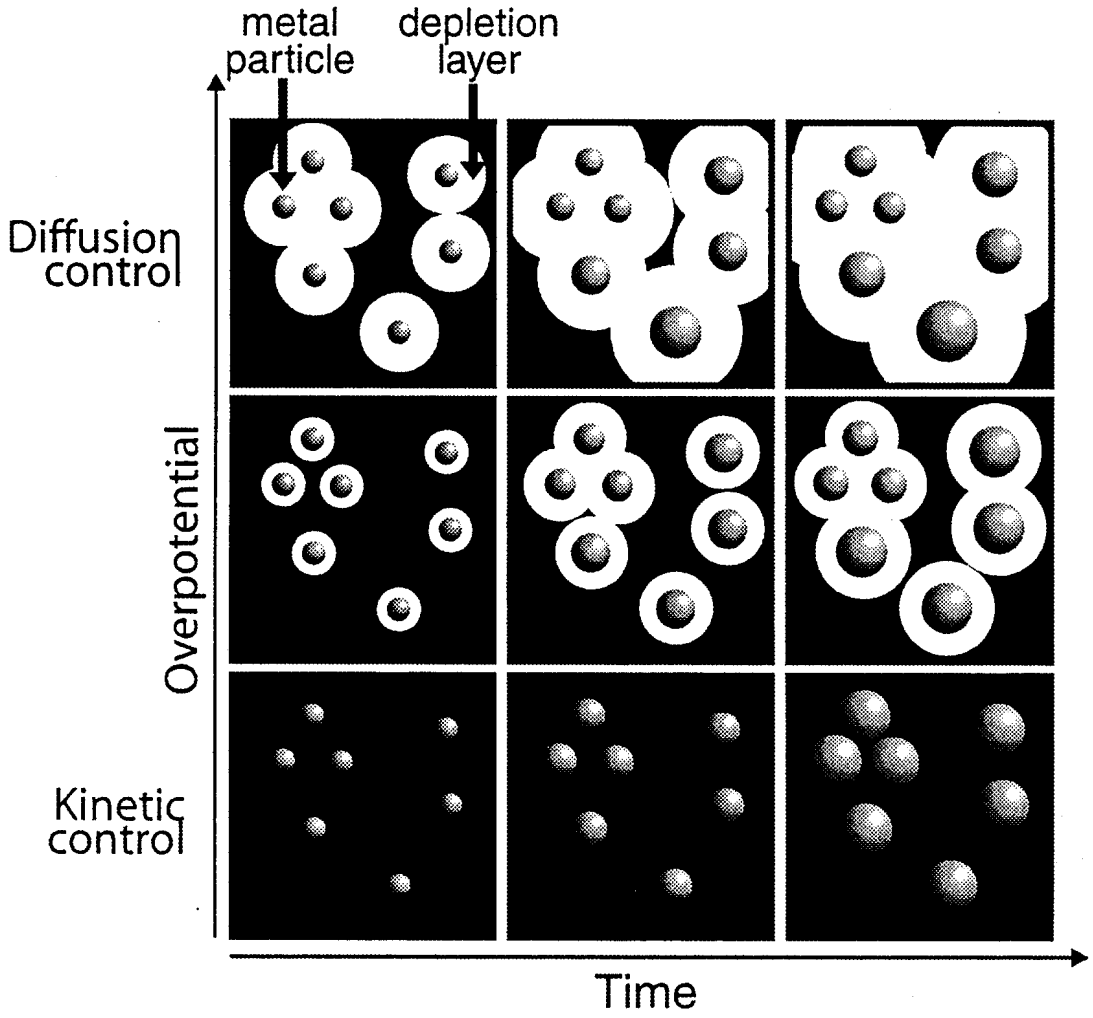

Figure 1.6 Effect of deposition overpotential on extension of depletion layer from the surface of growing metal particles and the inducement of diffusion zone coupling. Taken from Penner et al. [30].

explanation of these results is that the electroactive species become activated by the ultrasonic wave as well as influencing mass transport at the working electrode. There are drawbacks to this method however as the mixing of the electrolyte solution resulting from sonication no doubt affects the accuracy of the kinetic treatments described in the previous section which assume deposition is entirely kinetically controlled therefore an unstirred solution. The results have to be confirmed using another method and in this case the authors used AFM imaging to demonstrate the effect of sonication and these confirmed the finding.

Electrolyte additives can influence electrodeposition through adsorption on the growth centres (nuclei) or adsorption on the working electrode. The effect of adsorbed additives on the kinetics of nucleation and growth can be positive or negative or neutral. Additives can promote certain growth modes and/or hinder other growth modes, and they can alter the morphology and crystallographic orientation of the final deposits. Additives can exert their influence through various mechanisms. The dominant and best understood mechanisms by which additives affect electrodeposition are by changing the concentration of growth sites and/or adions on the surface and shifting the diffusion coefficient and the activation energy for surface diffusion of adions on the surface. These mechanisms are discussed in detail below:

Martín et al. [34] have discussed the effects of the addition of citric acid and chloride ions as additives in the electrodeposition of gold island films, of the type under investigation in this project, from a solution of $AuCl_3$.HCl. As shown in Figure 1.7 the addition of citric acid resulted in smaller, denser gold deposits with less branching and therefore a more rounded 3D shape. The addition of excess chloride ions (as NaCl) had the opposite effect, it caused more branching of the growth centres and resulted in decreased nucleus density and increased mean nucleus size. The mechanism proposed by the authors is that citric acid preferentially adsorbs at gold island edges and results in an increase in the energy barriers for interterrace and corner gold adatom diffusion thereby promoting 3D growth at the expense of 2D lateral growth. This results in smaller, rounder deposits that are capable of

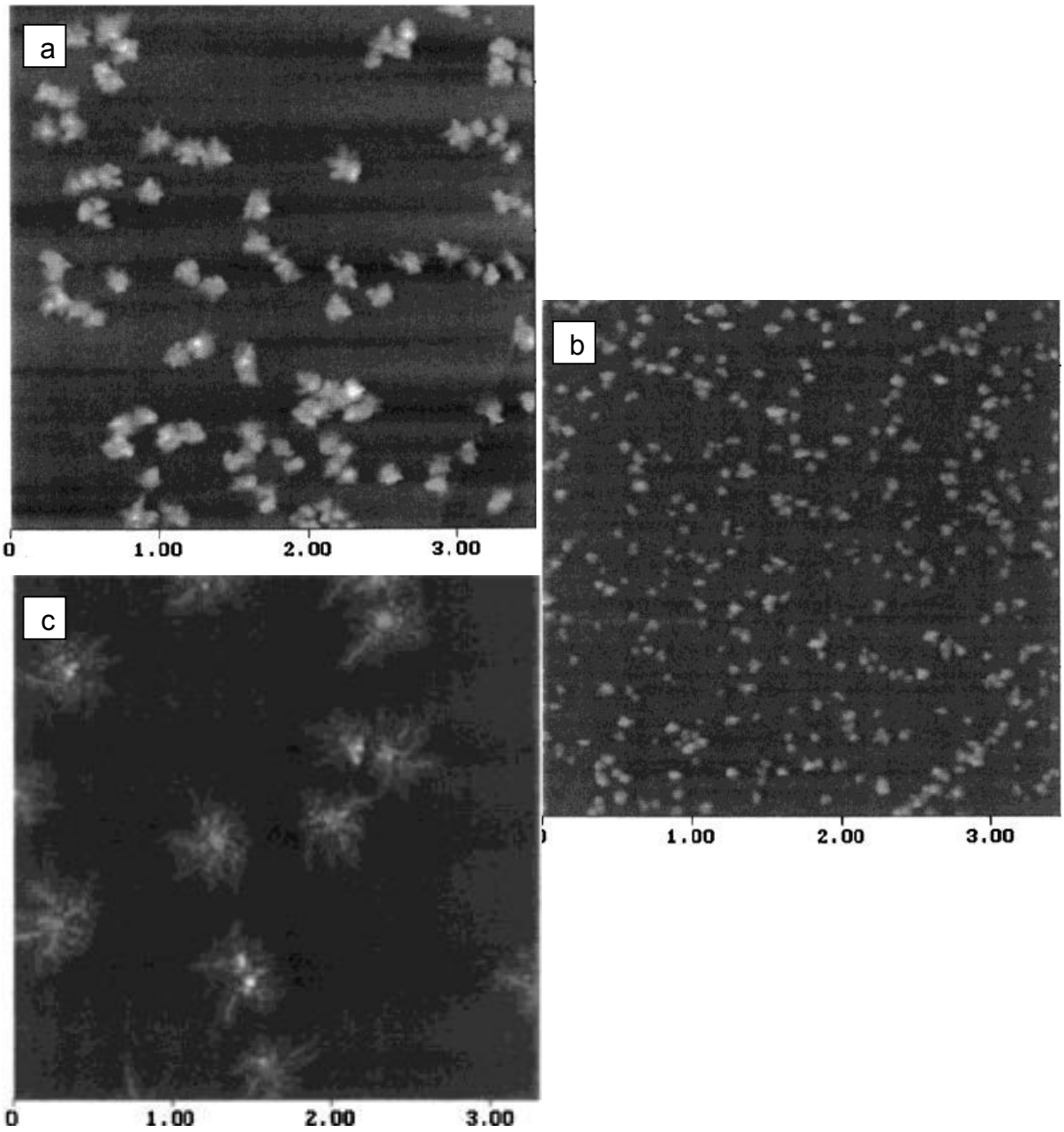

Figure 1.7 STM images of gold nanoparticles electrodeposited under similar conditions on graphite from $AuCl_3$.HCl containing (a) no additive, (b) citric acid, (c) chloride ions. Modified from reference [34].

depositing at a greater density. The mechanism reported for the action of chloride ions is the opposite case. The excess chloride ions result in a decrease in the activation energy barrier for gold adatom surface diffusion by the formation of a gold-chloride complex ion. This promotes lateral growth resulting in larger, less dense deposits forming in dendritic patterns. Similar results for the electrodeposition of silver (from $AgNO_3$) in the presence of citric acid have been reported elsewhere [35].

El-Deab et al. [36] investigated the effects of some additives on the electrodeposition of gold from acidic $NaAuCl_4$ onto various substrates. Iodide (I^-) has a strong specific adsorptivity onto gold, therefore freshly formed nanodeposits of gold are covered with a monolayer of iodide ions rapidly. The negative charge of the iodide ions adsorbed on the gold islands prevents coalescence of neighbouring islands through repulsive forces, resulting in smaller deposit sizes. Cysteine had the opposite effect and resulted in an increase in gold deposit sizes. The authors hypothesized that carboxylic and amino groups on the thiol chain of the cysteine molecule were interacting through hydrogen bonding thereby encouraging coalescence of neighbouring islands. These results are demonstrated in the SEM images shown in Figure 1.8.

Layson and Columbia [37] have studied the mechanism of the action of lead acetate on platinum electrodeposition to yield platinum blacks. Platinum black electrodes consist of a cathode (often platinum metal itself) that has been modified with platinum nanoparticles in the size range 15-30nm such that the optical properties of the platinum nanoparticles are altered and appear black [38]. The authors studied the formation of platinum blacks from chloroplatinate (K_2PtCl_6) on highly oriented pyrolytic graphite (HOPG) electrodes. They suggested that lead ions adsorbed on the HOPG surface acted as electron transfer sites between the electrode surface and the platinum ions in solution resulting in a greater number of nucleation sites. This in turn yields smaller particle sizes and greater deposition density – the most important features of a platinum black electrode.

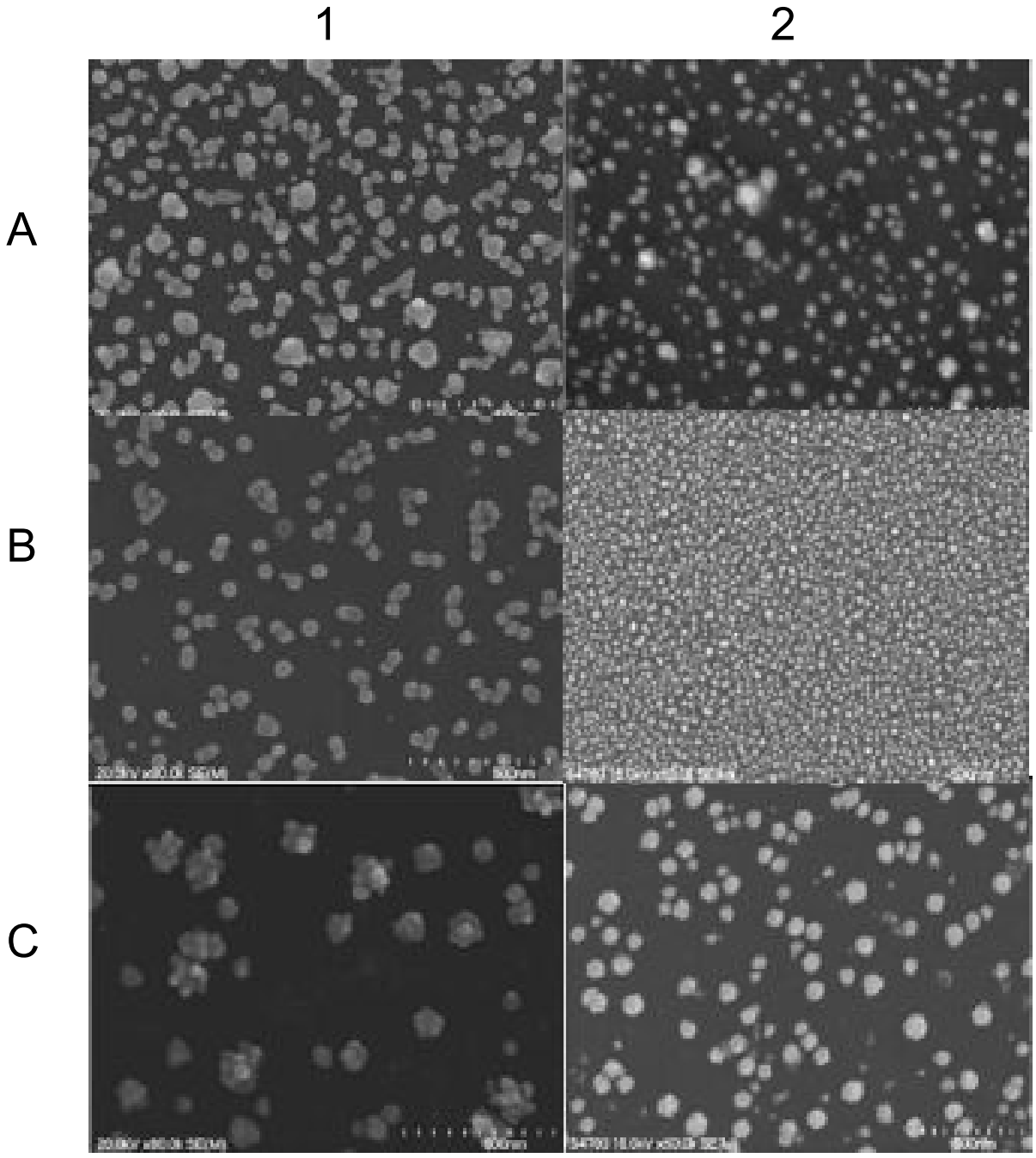

Figure 1.8 SEM images of gold electrodeposited from acidic NaAuCl4 onto (1) Highly Oriented Pyrolytic Graphite (HOPG) and (2) Glassy Carbon in the presence of the following additives: (A) none, (B) Iodide, (C) Cyteine. Taken from Reference [36].

Control of particle density in the manner demonstrated in the above examples is a significant objective of this project therefore the use of some of these additives will be investigated. There are many other examples of electrolyte additives in use concerned primarily with the finish of electroplated metals (e.g. the brightness, hardness and anti-corrosive properties). As these additives do not affect the nanostructural properties of the electrodeposit they fall outside the scope of this literature review.

1.3 Nanoparticles: Properties and Applications

The emerging science of nanotechnology has come to the fore in recent years and is now seen as one of the most important and exciting multidisciplinary technologies [39, 40]. As such a broad-reaching subject it would be impossible to properly discuss all of the facets of this intriguing area of science within this literature review, nanoparticles are however seen as a vital instrument in nanotechnology [41, 42] so their significance to this field is discussed with particular relevance to the topics of this project. There is no strict definition of the term nanoparticle. It is frequently taken to mean particles with diameter less than 100nm; however this distinction is somewhat arbitrary as metal particles with diameters larger than this frequently share properties with their smaller counterparts that are not shared with the bulk metal. For the purpose of this literature review it is more important to define particles by their spectroscopic, optical, electrochemical and catalytic properties therefore the term nanoparticle will be used to define particles in the 0-200nm range as appropriate.

Nanoparticle technology can be divided into two distinct areas, interfacial nanoparticles and nanoparticle solutions or colloids. Colloidal solutions fall outside the scope of this project as they cannot be readily produced by electrodeposition therefore their unique properties are not discussed at length. However, there are some excellent reviews in the literature [43-45]. Interfacial nanoparticles share many of their properties with their colloidal counterparts. There are advantages to using both interfacial and colloidal systems, the main advantages of interfacial systems are that they provide a surface on which a chemical reaction can take place and be monitored. If the surface is electrically conducting it provides electrical contact to the nanoparticles so that they can be utilised in electrochemical investigations and in the case of electrochemically deposited nanoparticles there is potential for the surface to be reusable due to the stability and strong attachment of the metal nanoparticles.

Metal nanoparticles are a subject of great interest due to their many advantages compared to the bulk metal. The properties of nanoparticles that differ from those of the bulk metal are the localised surface plasmon band, surface area related properties and fluorescence. There are a wide range of methods described in the literature for the production of metal nanoparticles of the types described below; the main ones are electrodeposition [46-49], chemical synthesis [50-52], sputter coating [53-55], UV light irradiation [56, 57] and electron beam irradiation [56, 58].

1.3.1 Surface Plasmon Resonance

Surface plasmons are electron density oscillations in the conduction band that occur at a metal/dielectric interface. The most commonly encountered of such interfaces are metal/water and metal/air, the latter of which is the type encountered in this project and therefore is of most importance to this literature review. The surface plasmons propagate evanescently from the metal/dielectric interface like a wave. As with any wave, the amplitude of the surface plasmon wave can be enhanced when a wave of light of resonant wavelength is incident on it. Excitation of the surface plasmon band by electromagnetic radiation is termed surface plasmon resonance (SPR). Stronger surface plasmons are associated with roughened metal surfaces. Surface plasmon active metals include copper, titanium, chromium and the most importantly (due to their stability, versatility of their chemistries and strong surface plasmon absorption in the UV-Vis region) silver and gold.

At the metal/dielectric interface of nanoparticulate metallic materials localized surface plasmon fields are supported. Localized surface plasmons occur only at nanoparticulate interfaces and result primarily due to the quantum size effect, which is that the de Broglie wavelength of the valence electrons is of the same order of the size of the particle itself. This means that from a quantum mechanical point of view the nanoparticles act as quantum dots of zero dimensions [42] and the valence electrons of the atoms within the nanoparticle oscillate collectively, in a much stronger fashion than the oscillation observed at smooth metal/dielectric interfaces. The collective oscillation of electrons is at a frequency characteristic of the metal itself and

the nanoparticle size. When electromagnetic radiation at the appropriate wavelength is incident on such metal nanoparticles, the electromagnetic field of the incoming light increases the amplitude of the plasmon field oscillations.

There are two very important results of this effect. Firstly, noble metal nanoparticles in solution or immobilized on a suitable substrate display an absorption maximum corresponding to the frequency of light resonant with the frequency of oscillation of the surface plasmon electrons of the nanoparticles. This is called the localized surface plasmon absorption. For metals like silver, gold and copper it is found in the UV-Vis region of the spectrum, and is not detected in the absorption spectrum of the corresponding bulk metal. Secondly, molecules adsorbed on the surface of nanoparticles under resonant excitation are subjected to electromagnetic fields of much greater intensity than the intensity of the incident light alone (intensity is proportional to square of electric field amplitude). This results in a substantial increase in the intensity of Raman scatter and (in the case of luminophores) fluorescent intensity. This effect is considered the major contributor towards the enhancement of signal in surface enhanced Raman scattering [59-61] and metal enhanced fluorescence [62-64].

The wavelength of the LSPR absorption and the magnitude of enhancement of the local electromagnetic field are believed to be products of the nanoparticle size and nanoparticle proximity (interparticle spacing), although this has been studied in the literature [42, 65-70] there are so many different systems to consider (e.g. nanoparticles in solution or immobilised, made of copper or silver or gold, consisting of spheres or hemispheres or pyramids excited at different wavelengths) that the exact relationships are not well understood. In cases like this project, where electrodeposited hemispheres of silver and gold are considered, the optimal size and interparticle distance for surface plasmon resonance must be determined to a large extent experimentally. Natan et al. have reported strongest SPR signal from gold nanoparticles in the 30 nm – 60 nm size range when immobilised on a surface [71]. Of more importance to this project is the conditions that

produce the greatest Raman and fluorescence enhancements, these are discussed later.

The surface plasmon absorption can be used for detection in a sensing device. This is because the wavelength and intensity of the surface plasmon absorption is affected by the refractive index of the contacting medium, meaning absorption of analyte molecules to the metal surface results in a shift in the surface plasmon band. The most commonly used example of this is the BIAcore system [72]; antibodies to a target molecule such as a protein are developed and immobilised on a gold surface. UV-Vis reflectance spectrophotometry is used to measure the wavelength and intensity of the surface plasmon band, then when the surface is exposed to a sample containing the target molecule binding occurs and the resulting shift in refractive index is detected as a shift in the wavelength and intensity of the surface plasmon band. The surface plasmon shift is highly sensitive to changes in the surrounding medium. As the shift in refractive index is proportional to the change in mass at the surface the method is quantitative as well as qualitative. The nature of the anti-body to analyte binding makes this technique very selective also.

Figure 1.9 illustrates the change in the surface plasmon absorption upon adsorption of a probe molecule to a gold nanoparticulate surface, reported by Kalyuzhny et al. [73]. Gold nanoparticulate films were evaporated onto optically transparent quartz and mica substrates in this work. There are many more examples of nanoparticle based surface plasmon sensors using gold [74-76] and silver [66, 77, 78] nanoparticles.

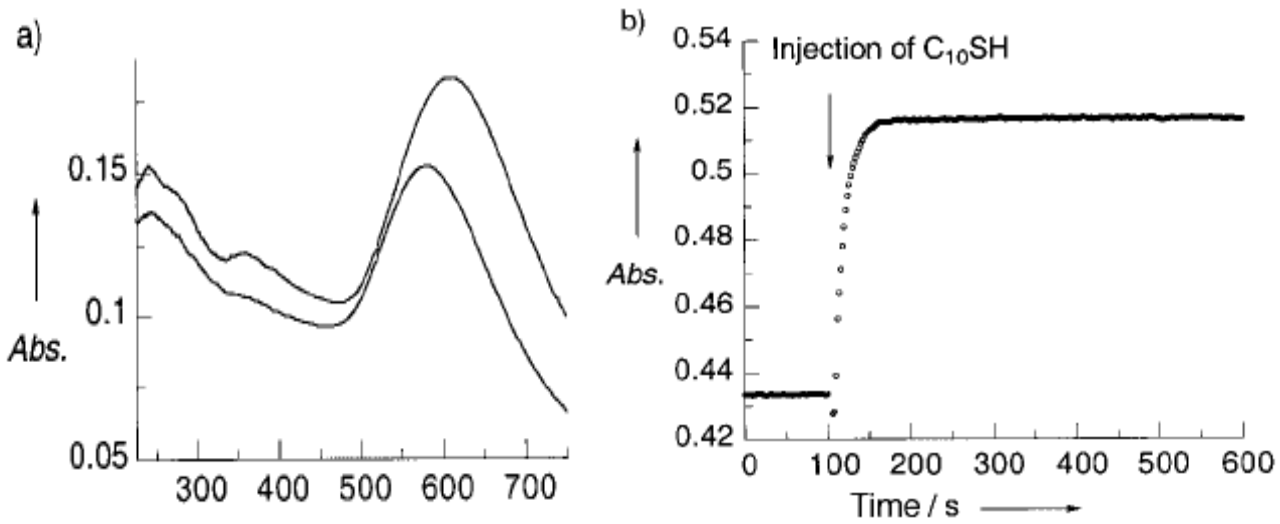

Figure 1.9 (a) Change in absorbance spectrum upon adsorption of probe molecule ($CHCl_3$) to gold island films. (b) Change in absorbance at 720 nm upon injection of probe molecule ($C_{10}SH$) into sample cell, taken from Reference [73].

1.3.2 Surface Area Related Properties

Nanoparticles provide an excellent method of maximising the surface area of a precious metal without using large quantities. This is of particular importance with metals like gold, silver and platinum that are very expensive. Nanoparticles provide a means of achieving very high surface areas. Two important areas that benefit in particular from increased surface areas are electrochemical sensing and catalysis.

1.3.2.1 Electrochemical Sensing

Electrochemical sensing works by electrochemically reducing, or in some cases oxidising a target molecule at an electrode and measuring the response so that the target molecule can be identified and quantified. Electrochemistry is a versatile technology that can be used for the identification of analytes based on their reduction potential. Electrochemistry has the advantage of producing a linear response to concentration therefore it can be utilised for quantitative determination of an analyte.

One of the major barriers to incorporation of electrochemical detection into sensors is the need for large surface area electrodes, often made of expensive noble metals, in order to achieve the desired level of sensitivity. This problem can be mitigated by the use of nanoparticle and nanoparticulate film modified electrodes, where the nanoparticles or nanoparticulate films consist of the expensive noble metal required but have significantly greater surface area to volume ratios compared to a smooth film. This makes possible the production of high surface area electrodes at an acceptable cost, and the porous nature of some of the resulting electrodes means that smaller sample volumes can be analysed, this is particularly important for biological samples when it is not possible or practical to obtain large volumes of sample. In addition in many cases the catalytic properties of noble metal nanoparticles reduces the overpotential of many important electrochemical reactions such as oxidation of NO catalysed by gold nanoparticles [79], ascorbic acid oxidation by gold nanoparticles [80] and hydrogen peroxide oxidation by platinum nanoparticles [81].

In its simplest form an electrochemical sensor reduces/oxidises an analyte at the working electrode (nanoparticulate surface) by application of a potential and measurement of the current response. The magnitude of the current response is proportional to the number of analyte molecules reduced/oxidised, assuming 100% coulometric efficiency and no impurities are being co-reduced. The identity of the analytes can be ascertained by sweeping the potential and recording the potential at which the reduction occurs, in this way the different components of a mixture can be identified based on their reduction potentials. Cyclic voltammetry is the simplest and most commonly used method of achieving this, but other potential sweep methods such as square wave voltammetry and differential pulse voltammetry are highly effective.

An example of such a sensing device has been demonstrated by Goyal et al. [3]. They use an indium tin oxide (ITO) electrode modified with gold nanoparticles as the working electrode (see Figure 1.10a). These surfaces are quite similar to the sort of surfaces produced in this project therefore this paper is significant as it demonstrates another potential use. They use differential pulse voltammetry (DPV) as the detection technique. This involves applying a series of potential pulses of constant amplitude to the sample superimposed on a linearly ramped voltage, the current response is measured just before and after each pulse. The advantage of DVP over cyclic voltammetry is that the effect of charging current is minimised by the presence of the linear ramp, as only the faradaic response is detected the accuracy of the technique is improved. In this paper a calibration curve is plotted of peak current against concentration of the analyte, paracetamol. The method is quite sensitive, the detection limit is 0.18 μM (27 ppb) over the linear range 0.2 μM to 1.5 mM. The use of this technique to detect paracetamol in a number of pharmaceutical samples is demonstrated (see Figure 1.10b). A limitation of this technique is that it works best with simple sample matrices such as these, but to detect analytes in more complex matrices containing multiple impurities requires prior purification of the sample.

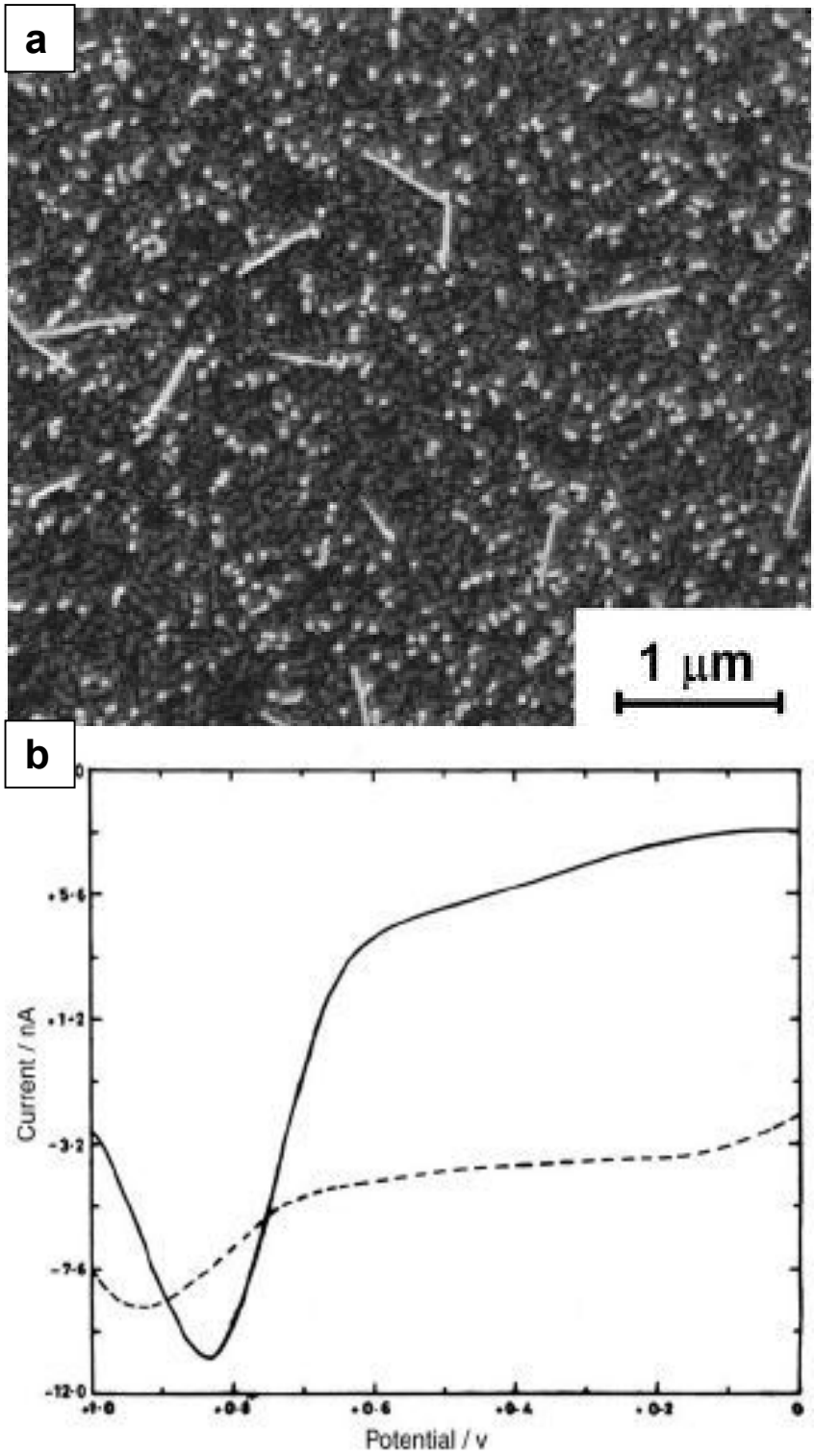

Figure 1.10 (a) Field emission SEM Image of nanogold modified indium tin oxide electrode. (b) A typical differential pulse voltammogram for 1.0 mM paracetamol at pH 7.2 at bare (- - -) and gold nanoparticles modified (—) ITO electrode. Taken from reference [3].

A similar sensor has been proposed by Dai and Compton [82] using gold nanoparticles electrodeposited onto ITO for the detection of arsenic using cyclic voltammetry and linear sweep voltammetry (LSV). They report a limit of detection of 5 ppb using LSV. The authors emphasised that the low cost of the gold nanoparticle modified ITO surfaces made them suitable to be used as a disposable sensor for in field analysis. It could also be possible to do this with nanoparticle modified fluorine-doped tin oxide surfaces as prepared during this project. Electrochemical sensors using similar methods have also been proposed by Wang et al. [83] and Jena et al. [84].

A novel approach has been suggested by Wilson et al. in the form of an electrochemical microarray [85]. In Wilson's microarray a series of 10 platinum disc electrodes (diameter 2 μm – 24 μm), each individually electrically connected to a potentiostat, were used to simultaneously perform 10 CVs with a single sample solution [85]. The advantage of this approach is that each platinum microelectrode could be individually decorated with anti-bodies, or other biological probes to a particular analyte, such that numerous analytes could be determined in a single measurement. However, Figure 1.11 demonstrates that to connect to each of the electrodes the design of the device is quite complicated, and expansion of the number of electrodes to a significant extent would surely not be possible. The authors demonstrated the detection of glucose with this device, and the detection limit for the device was not reported, however the authors claim a linear range to 10 mM, and sensitivity "much lower" than that [85], however, it is unclear if this device can deliver the required sensitivity and linear range to analyse real samples. This device is similar to the DNA microarray discussed in Chapter 6, however the device in Chapter 6 does not require electrical connection to each individual electrode, this gives it a significant advantage over Wilson's device.

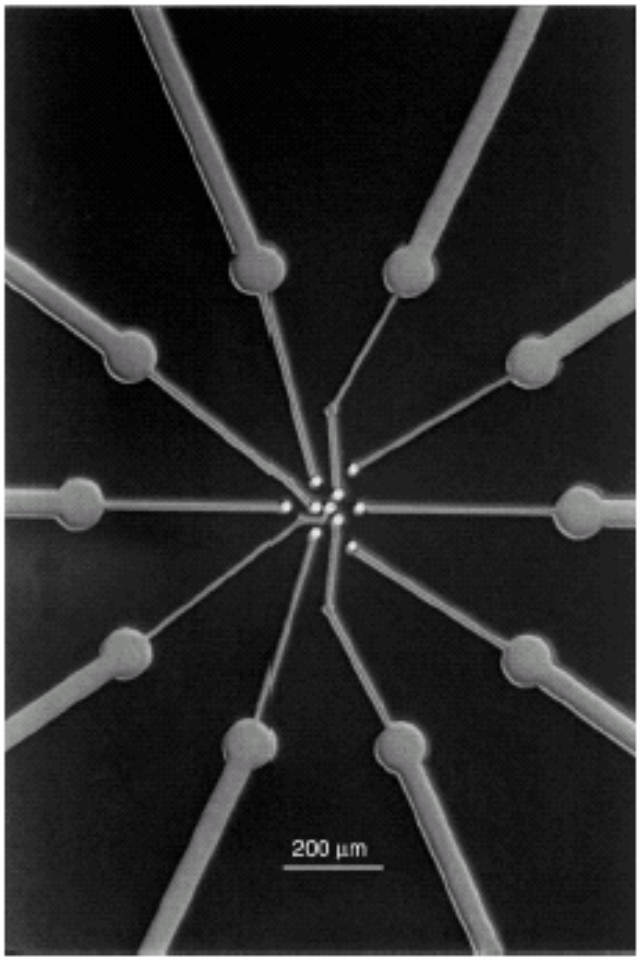

Figure 1.11 Electrochemical microarray of 10, individually addressed, platinum microdiscs (diameter 2 µm – 24 µm). The bright spots are the platinum discs, the duller metal is platinum coated with photoresist. Taken from Wilson et al. [85].

1.3.2.2 Catalysis

In catalysis one of the fundamental concerns is minimising the cost of producing surfaces of precious metal. Catalysts act by providing a site for adsorption for one of more of the reactants therefore the amount of surface area available influences the efficiency of the catalyst. The use of a large block or sheet of the metal required for a catalytic reaction is therefore inefficient and a poor use of resources. Nanoparticles offer an obvious solution to this problem. The metal of interest can either be present as a colloid (made through chemical synthesis) or as a surface bound nanoparticle (made by chemical synthesis and attachment, sputter coating or electrodeposition) depending on the reaction being catalysed and the nature of the product desired. In addition the greater free surface energy of metal nanoparticles compared to that of the bulk metal means that they can catalyse electrochemically driven reactions otherwise not possible [86] e.g. gold nanoparticle catalysed electrochemical oxidation of NO on platinum [79]. Some examples of nanoparticle catalysts are described below:

Ullah et al. [87] have produced platinum nanoparticles (2.5nm diameter) and nanoclusters (40-70nm diameter) by chemical reduction with CTAB (Cetyltrimethylammonium bromide) stabilisation. The resulting nanoparticles and nanoclusters were immobilised electrochemically on a glassy carbon electrode, which was then used as the working electrode for the catalytic electrochemical reduction of oxygen. This involved cyclic voltammetry of oxygen saturated KNO_3. The resultant CVs showing the catalytic reduction of oxygen at the platinum nanoparticle and nanoclusters working electrodes is shown in Figure 1.12. The scientific and industrial importance of the reduction of oxygen is in its possible applications to fuel cells therefore this catalytic reaction of oxygen is enormously important.

Pradhan et al. [88] have demonstrated the use of silver nanoparticles for the industrially important catalytic reduction of nitro aromatic compounds to amino compounds with $NaBH_4$. The silver nanoparticles were in the 7-15nm size range. Reduction of nitro groups to amino groups by $NaBH_4$ is not

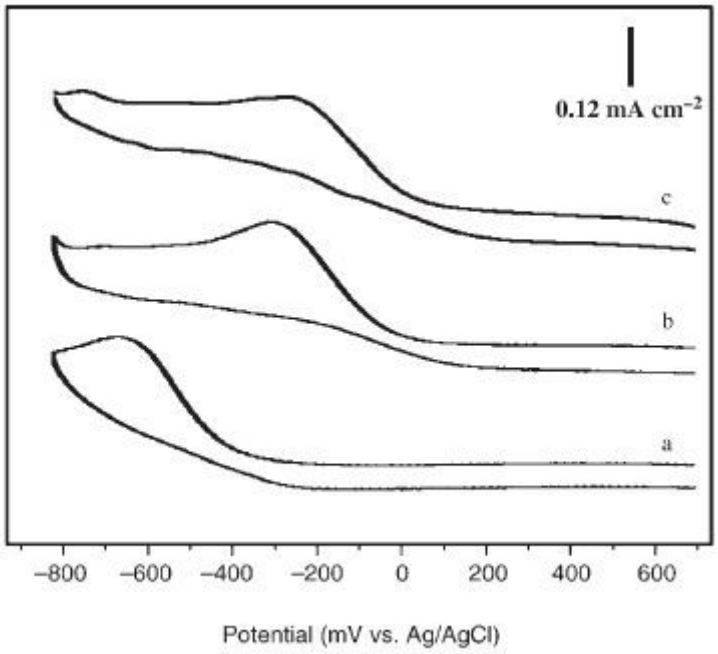

Figure 1.12 CV profiles displaying the reduction of O_2: a) using a GCE modified only with 0.1m $LiClO_4$ electrolyte solution;b) using a GCE modified with Pt nanoparticles in 0.1m $LiClO_4$;c) using a GCE modified with Pt nanoclusters in 0.1m $LiClO_4$. All CV profiles were obtained in O_2-saturated 1M KNO_3 electrolyte solution. Taken from reference [87].

possible under standard conditions without the presence of a catalyst to overcome the energy barrier to the reaction. In the presence of the silver nanoparticles in solution, electron transfer between the reactants is facilitated. This method opens up the possibility for the large scale preparation of amino compounds for industrial purposes.

Schmuki et al. have used silver and gold nanoparticles to enhance the photocatalytic activity of self-organized TiO_2 nanotubular structures [89]. The organic pollutant Acid Orange 7 is photocatalytically decomposed at a TiO_2 electrode surface. The large bandgap of TiO_2 (3.2 eV) means that UV-light irradiation is required to induce electron-hole pairs in the electrode in order for the catalytic reaction to proceed. In this work Schmuki et al. immobilised gold (28 nm) and silver (10 nm) nanoparticles on the TiO_2 surface in order to facilitate electron–hole separation and to promote interfacial electron transfer processes, so that the photocatalytic activity of the TiO_2 electrode was significantly enhanced. The authors report that both metal nanoparticle catalysts significantly enhanced the decomposition of the organic pollutant [89].

Some of the applications of nanoparticles to catalysis discussed above have made use of immobilised gold and silver nanoparticles similar to those produced during this project.

1.3.3 Fluorescence

Fluorescence is a process that involves the absorption of a photon by a molecule resulting in excitation of that molecule followed by emission of a photon at a longer wavelength (lower energy) than the absorbed light (due to loss of energy from internal conversion) as the molecule returns to the ground state (See Jablonski Diagram Figure 1.13). Not all molecules fluoresce, so the technique is limited to use with luminophores and samples that can be labelled with fluorescent probes, which is not practical in every case. Despite these limitations fluorescence is popular due to a large extent to the excellent sensitivity of the technique. While Raman spectroscopy suffers from extremely low cross sections of around 10^{-31} cm^2, typical fluorescence cross sections are approximately 10^{-15} cm^2. The sensitivity of this technique can be further improved in metal enhanced fluorescence, and although enhancements as large as those found in SERS spectroscopy cannot be achieved the technique can still be significantly more sensitive than SERS.

The sensitivity in fluorescence is controlled by the rate of radiative decay of the luminophore; the rate of radiative decay of a luminophore can be significantly altered by placing the luminophore a suitable distance from a metallic surface or particle. Lakowicz [63] has predicted that the presence at a metal surface can result in a 10^6 fold increase in the number of photons detectable from a luminophore, and also relatively high emissions from otherwise non-fluorescent molecules. This effect can be explained by the dipole moment of the luminophore interacting with free electrons in the metal resulting in a change in intensity of the radiation as well as its temporal and spatial distribution [90]. These surface interactions between fluorescent dipole and metal are understood to result from three discrete mechanisms. The first is energy transfer quenching where the luminophore loses its excited state energy to the metal surface through damping of the dipole oscillations by the nearby metal, this is also known as Forster energy transfer and its effect decreases with distance from the surface so it is only found

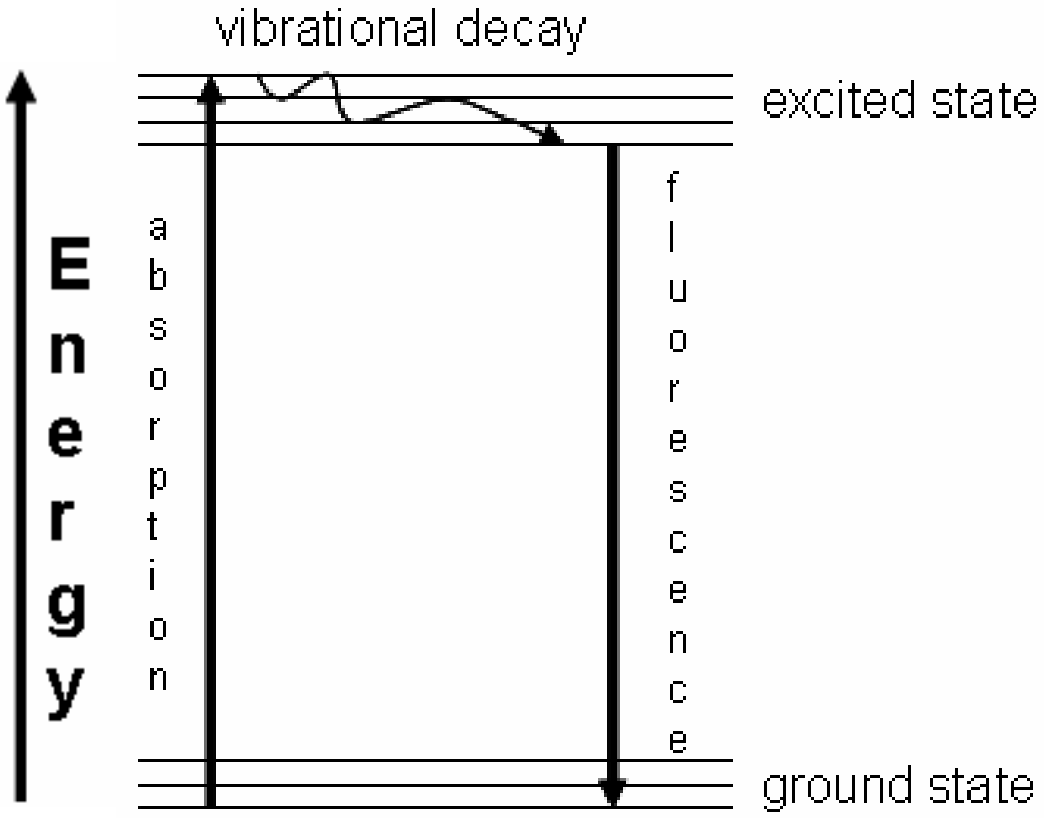

Figure 1.13 Energy level diagram representing the process of fluorescence. An electron is excited from the ground state to an excited state by absorption of a photon. Internal conversion of energy results in the electron moving to a lower energy level. Then the electron returns to the ground state with emission of a photon.

<5nm from the surface. This results in a decrease in fluorescent emission. Another mechanism is amplification of the incident field by the metal due to a concentration of the local excitation intensity by the metal surface plasmon band discussed in Section 1.3.1. Most significant to metal enhanced fluorescence is the third mechanism whereby the nearby roughened metal surface can cause an increase in the intrinsic radiative decay rate of the luminophore.

The radiative decay rate (Γ) can be related to the quantum yield (φ_0) by the following equation:

$$\varphi_0 = \Gamma/(\Gamma + k_{nr}) \quad (1.16)$$

Where k_{nr} is the rate of non-radiative decay, and φ_0 the quantum yield is the fraction of excited luminophores that decay by emission and is proportional to the fluorescent intensity. In addition the fluorescent lifetime of a luminophore (τ_n) is given by;

$$\tau_n = \Gamma^{-1} \quad (1.17)$$

So a luminophore with a high value for radiative decay will have a high quantum yield and a short fluorescent lifetime. Therefore a luminophore which normally has a low quantum yield experiences significant fluorescent enhancement when the radiative decay is increased. On the other hand luminophores with a quantum yield close to unity do not experience significant fluorescent enhancements.

Various studies have been performed into the effect of metal surfaces and colloids on fluorescent intensities and lifetimes. Weitz et al. [91] investigated the $Eu(ETA)_3$ complex on silver island films. In the absence of a metal island surface this complex had a quantum yield of 0.4 and a fluorescent lifetime of 280μs, but when fluorescence spectroscopy was performed on the $Eu(ETA)_3$ complex on a silver island film the quantum yield increased 5-fold to give an

apparent quantum yield of 2.0, and the fluorescent lifetime decreased 100-fold to ~2μs. Similarly Lakowicz et al. [92] investigated the metal enhanced fluorescence of rose Bengal (RB) on silver island films. In this case the fluorescent intensity increased 5 fold from 0.02 to 0.10 while the fluorescent lifetime decreased from 94ps to 6ps.

While it has been recognised that island films provide better fluorescent intensity enhancement compared to their planar counterparts, there has been little investigation into the relationship between metal surface morphology and fluorescence effects. It is known that the metal-luminophore interaction is through-space, and that maximum fluorescence enhancement has been observed at distances between 70-100Å [64]. A mechanism has been proposed suggesting that the increased radiative decay results from suppression of non-radiative decay by metal nanoparticles [93]. The enhancement factors reported in the literature of less than an order of magnitude are relatively small compared to those achieved in SERS investigations. However Lakowicz et al. [63, 64] predict that fluorescent enhancement of several orders of magnitude will eventually be possible.

The principle behind the fluorescence based diagnostics is not dissimilar to that of SERS based diagnostics. In SERS there is an enormous increase in the Raman scattered signal making detection of trace analytes possible by this normally insensitive technique. If the molecule under resonant excitation on a nanoparticulate surface is a luminophore, the enhanced electromagnetic field that it experiences causes an increase in the fluorescent emission intensity of the luminophore. Significantly, the enhanced electromagnetic field causes an increase in the quantum yield of the luminophore. These effects combined could potentially cause an increase in the fluorescent emission of a luminophore of several orders of magnitude. The potential advantages to such a device are that fluorescence experiences a very low background noise level therefore sensitivity is potentially excellent, and the technique is potentially extremely selective.

MacCraith et al. [94] have demonstrated a fluorescence sensor based on silver nanoparticles produced by nanosphere lithography. Silver nanoparticles are deposited into the spaces between polystyrene beads resulting in triangular silver nanoparticles in regular arrays on glass slides. Anti-BSA (Bovine serum albumin) antibodies labelled with the fluorescent dye Cy5 were immobilised on the nanoparticles modified surface via a chemical linker. Such a device could easily be used as a sensor by immobilising the chosen analyte on the nanoparticles surfaces then exposing the surface to antibodies to the surface linked to fluorescent dye molecules. Using this system they estimated the fluorescence signal of the Cy5 was enhanced by a factor of 8. This less than an order of magnitude enhancement is relatively low compared to the enhancement factors achieved from SERS sensors of approximately 10^6. However, metal enhanced fluorescence based sensing is a relatively new technology and it is anticipated that it will be possible to improve the enhancement factor of such devices through optimisation. Such devices would be extremely important tools for biomedical diagnostics, DNA sequencing and genomics.

A similar sensor has been proposed by Ianoul and Bergeron [95], where the sensing substrate consists of untemplated silver nanoparticles immobilised on the surface. The nanoparticles were produced by chemical reduction followed by chemical linkage onto a glass slide. The fluorescent dye used was rhodamine 6G, for this paper the dye was linked directly to the silver nanoparticles, but in a sensor would be linked directly or indirectly to the analyte molecule immobilised on the silver surface. The authors report enhancement factors of up to 30. AFM images of these surfaces are shown in Figure 1.14. The mean particle diameter was typically 70 nm, with particle densities ranging from 1-5 particles per μm^2. These nanoparticles are quite similar to some of the nanoparticles produced in this project in terms of diameter and density therefore the potential applicability of such substrates to fluorescence based sensing is evident.

Lakowicz et al. [96] took a similar surface, i.e. silver nanoparticles immobilised on silanised glass, and by chemical reduction grew the “seed”

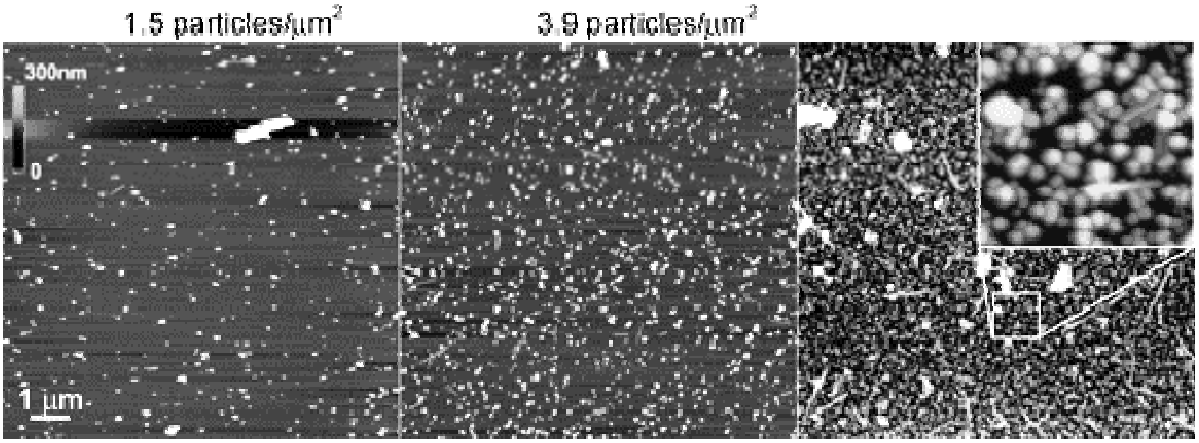

Figure 1.14 AFM images of silver nanoparticulate surfaces used for metal enhanced fluorescence. Taken from reference [95].

nanoparticles into nanorods. They then used these nanorod surfaces to detect the dye molecule indocyanine green (ICG) by metal enhanced fluorescence in the same manner as Ianoul and Bergeron [95]. Figure 1.15 presents the fluorescent emission spectrum of ICG on the bare glass slide and two of the silver nanorod surfaces. The signal is enhanced by a factor of 50 under optimal conditions of high nanorod density. It is significant that the greatest enhancement was recorded from a surface where the density of nanorods was greatest. This could indicate that electromagnetic coupling between adjacent nanorods plays an important role in fluorescence enhancement. This method of nanorod growth could potentially be applied to the nanoparticulate surfaces produced during this project.

Chen et al. have performed single protein molecule detection by metal enhanced fluorescence from a gold nanowire surface [97]. In their device, Chen et al. produced a 30 nm thick gold wire by e-bean evaporation [97]. The device was based on a sandwich assay, whereby a capture aptamer, which specifically binds to the analyte, thrombin, was immobilised on the nanowire surface, and after the sample was exposed to the surface, so that analyte molecules could bind to the capture probe, a detection probe, fluorescently labelled streptavidin, was exposed to the surface, such that any surface bound analyte would be fluorescently labelled. The emission intensity of the luminophore could then be recorded to determine the concentration of thrombin in the sample [97]. In order to prevent signal from non-specifically bound fluorescent labels interfering with the detection process an alternating electrical signal was applied to the gold nanowire such that the signal from surface bound species was modulated, but non-specifically bound luminophores, and other noise, was not modulated, so was easy to distinguish [97]. The authors reported that the fluorescent signal was enhanced 100 fold using this method, and this allowed them to detect single molecules [97].

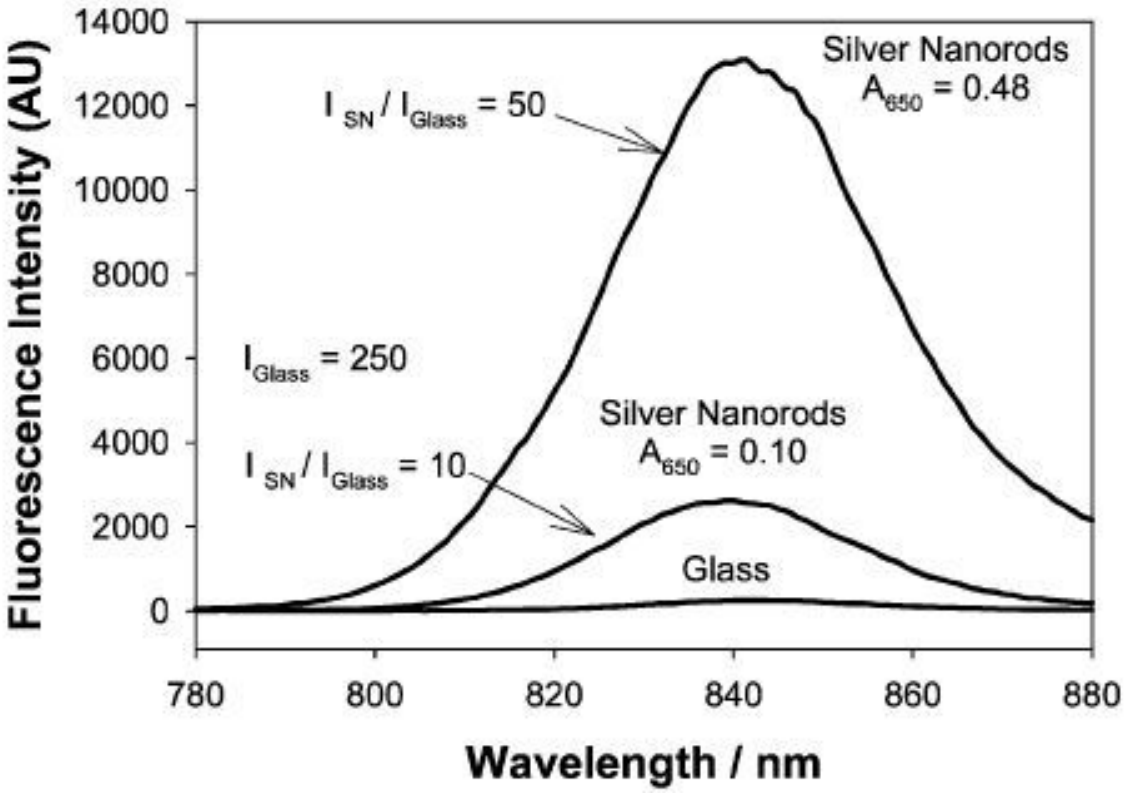

Figure 1.15 Fluorescence emission intensity of ICG-HSA on silver nanorods with low (A650 = 0.10) and high (A650 = 0.48) loading density. Taken from reference [96].

1.3.4 Raman Microscopy

Raman spectroscopy is the measurement of the wavelength and intensity of inelastically scattered light from molecules [98]. A typical Raman spectrometer consists of an excitation source (laser), a system of diffraction gratings to select the wavelength before and after it interacts with the sample, a lens to focus the excitation radiation onto the sample and a detector such as charge coupled device to measure the intensity of the Raman scatter. When a molecule is illuminated with monochromatic light that is not coincident with an electronic transition it is mostly not absorbed, instead it is scattered by the process of Rayleigh scattering. This occurs when an electron is excited to a non-stationary "virtual-state" upon absorption of a photon, and then returns to the ground state with the emission of a photon of the same wavelength. However, a small fraction of the illuminating light (approximately 1 in every 10^6 photons) scatters inelastically [99]. This results when the electron in the virtual excited state returns to a different vibrational state to its original state so that it emits a photon at a different wavelength to the wavelength of the exciting photon. The energy of the scattered photon can be greater (anti-Stokes lines) or less (Stokes lines) than the incident energy depending on the vibrational energy state of the molecule prior to excitation, this is illustrated in Figure 1.16.

In Figure 1.16(a) a ground state electron is promoted to the virtual state but only returns to the V_1 energy state in the ground level, meaning the scattered photon has less energy than the incident radiation. The remaining energy is lost to the molecule through vibrations. This is Stokes Raman scattering and is the more common form of Raman scatter. Figure 1.16(b) demonstrates anti-Stokes Raman scattering; an electron is excited from the V_1 level of the ground state to the virtual state, from here it returns to the ground state with the emission of a photon of higher energy than the incident radiation. Anti-Stokes Raman scattering isn't usually detected as at room temperature there is a low population of electrons in the V_1 energy state.

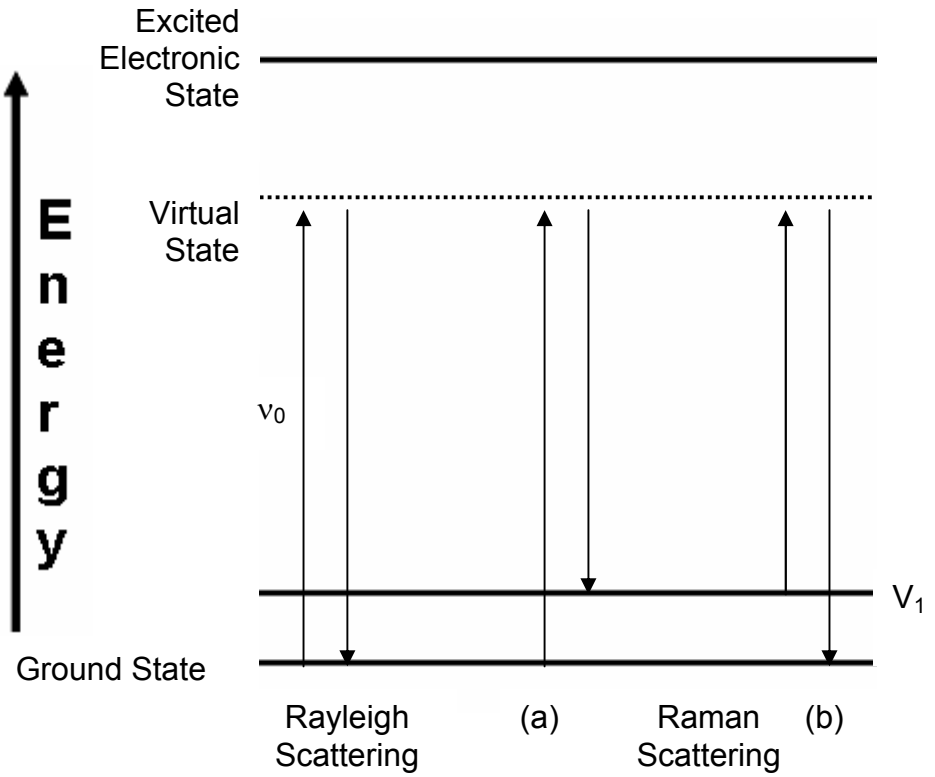

Figure 1.16 Energy Level Diagram representing Rayleigh and Raman Scattering.

The Raman scattered radiation is easy to detect as it is at a different wavelength to that of the incident light. The energy difference (and therefore the difference in λ) is proportional to the vibrational energy of the scattered molecules in the sample, so information about the type of bonds in the sample is obtained. As only ~1 in 10^6 photons undergoes Raman scattering this technique can be considered inherently weak. There are however important complications to the technique that result in strong enhancements of the signal. The first effect is called the resonance Raman effect, and is observed when the excitation frequency is close to the frequency of an electronic transition in the sample molecules. In this case the electrons are promoted to an excited electronic state instead of a virtual state. This promotes downward transitions to the V_1 state [100]. The result is typically a 3 to 4 orders of magnitude increase in the Raman signal for that transition, and sometimes as high as a 6 orders of magnitude increase. As well as providing better sensitivity for detection of the chosen molecule, the resonance Raman effect also provides excellent selectivity, as only molecules with transitions close to resonance with the excitation wavelength experience the enhancement, while other analytes and impurities do not, so the excitation wavelength can be chosen to promote resonance with a particular species.

The second effect is especially important when dealing with interfacial systems such as those encountered during this project. It is called surface enhanced Raman scattering (SERS). An increase in signal by up to 14 orders of magnitude is observed when the sample molecules are adsorbed on a metallic nanoparticle surface [101]. The effect is best seen on rough metal surfaces and on nanoparticles of metals like silver, gold and copper. In Section 1.3.1 the relationship between the surface plasmon band and the SERS effect was described. SERS enhancement is believed to result from two principle mechanisms acting in parallel; the electromagnetic mechanism already described and a chemical mechanism. The chemical mechanism of SERS enhancement is related to the resonance Raman effect, the molecular orbitals of molecules adsorbed on metal surfaces are broadened

by interaction with conduction electrons of the metal. Broadened molecular orbitals facilitates the resonance Raman effect as it broadens the range of frequencies at which resonant enhancement can occur [102]. The chemical enhancement mechanism occurs only at metal surfaces, unlike the electromagnetic enhancement mechanism, roughness is not a significant factor. The chemical mechanism is reported to be responsible for a 2 orders of magnitude increase in the Raman signal [102]. As the electromagnetic enhancement mechanism is caused by surface plasmon waves the adsorbed molecules must be very close to the surface to experience SERS effects, generally $\leq$ 4nm.

Without SERS enhancement, Raman spectroscopy wouldn't be feasible as an analytical technique for sensor and diagnostics technology due to its inherent lack of sensitivity. The enhancement of the Raman signal by 6 or more orders of magnitude by SERS in the presence of metal nanoparticles helps to overcome the insensitivity of the technique and has made it possible for single molecule detection to be achieved [103]. Due to the excellent qualitative information that can be obtained from Raman spectroscopy about the sample it could potentially be an excellent technique for use in sensor and diagnostics technology. Although many of the sensitivity barriers to achieving such a device have been overcome, reproducibility remains a major barrier remaining to producing such a sensor. In order for a commercially viable device to be developed it must be possible to produce SERS substrates with reproducible features such as nanoparticle size, density and with a low particle size range. Moreover the SERS enhancement factor must be reproducible both at different sites on an individual surface and ideally from surface to surface also. Amongst the various SERS based sensors reported in the literature this level of reproducibility is yet to be reported.

Sauer et al. [104] have reported SERS substrates produced by electrodeposition of gold nanoparticles onto a gold electrode, and silver nanoparticles on silver electrodes. They used these surfaces for the detection of probe molecules such as 4-Methylthiophenol (MTP) and trans-

1,2-Bis(4-pyridyl)-ethylene (BPE) with near-IR excitation. They report an enhancement factor of up to 7 orders of magnitude for both surfaces; however they do not demonstrate reproducibility of the enhancement factor. Typical SERS spectra are demonstrated in Figure 1.17. It is possible to re-use these SERS substrates after plasma cleaning.

Nie et al. [65] have performed single nanoparticle SERS on electromagnetically isolated colloidal gold nanoparticles immobilised on polylysine coated glass. They studied the probe molecule crystal violet with 647 nm excitation, an enhancement factor is not reported. Considering that aggregated nanoparticle "hot-spots" have been reported to produce up to 14 orders of magnitude enhancement [103], an understanding of the SERS effect on the individual nanoparticle level is crucial in gaining a proper understanding of SERS, and in order to determine if it is possible to achieve such enhancements in a reproducible manner. A potential advantage of utilising isolated metal nanoparticles is that the Raman enhancement factor is known to vary with the orientation of nanoparticles with respect to one another [105]; isolated nanoparticles would not suffer from this error, and could therefore be used to produce more reproducible results. Isolated noble-metal nanoparticles have the further advantages over arrays such as compactness and precision of placement.

Gaudry et al. [106] have combined SERS and resonance Raman for studies of the interaction between DNA and the various ruthenium complexes. The advantage of using surface enhanced resonance Raman scattering (SERRS) in this case is that the Raman signal is greatly enhanced by the SERS effect, while the fluorescence emission that is inherent to such tris-(bipyridyl) ruthenium complexes is quenched by the resonant Raman effect. SERRS spectra were recorded in silver colloid solution at 488 nm excitation. The experiment is performed by observing a drop in the intensity of the Raman signal of the ruthenium complex upon binding to DNA molecules. Furthermore the authors are able to determine the part of the ruthenium complex that binds with the DNA based on the Raman bands that are

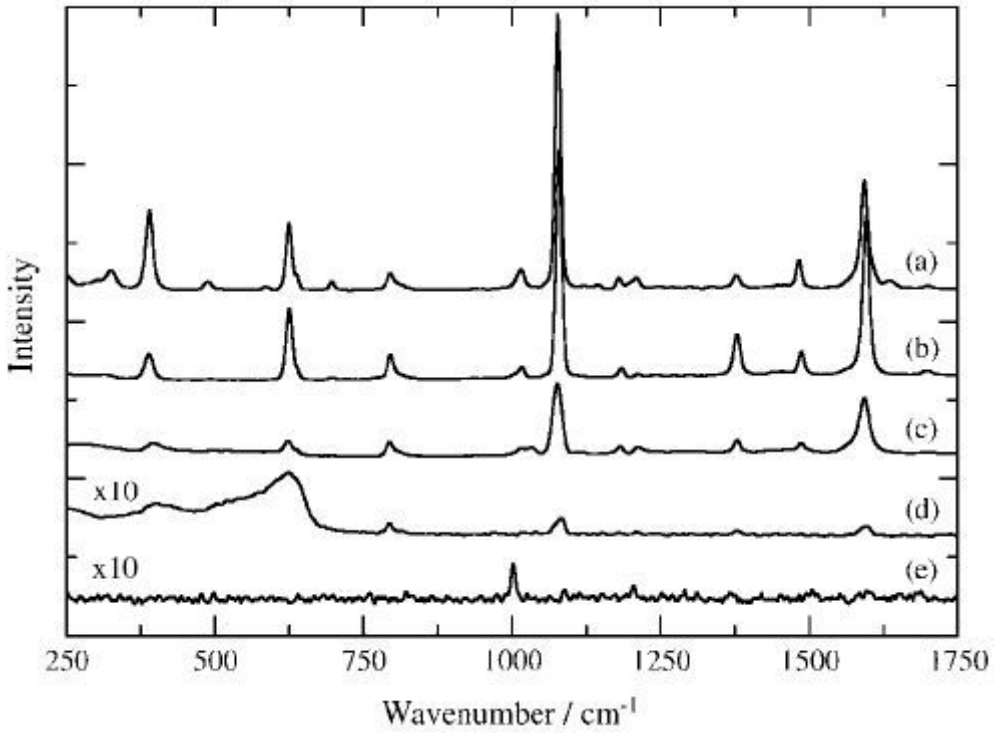

Figure 1.17 SERS spectra recorded of a monolayer of MTP adsorbed on vapor-deposited metal films roughened via electrodeposition: (a) Au; (b) Ag; (c) Cu; (d) Cu surface partially oxidized (Bruker RFS 100, λ_{ex} = 1064 nm, 100 accumulations, resolution 4 cm^{-1}). SERS intensities are normalized to identical experimental conditions by comparison with the Raman spectrum of a 50 μm thick sheet of polystyrene (e). Taken from Reference [104].

reduced in intensity upon binding (See Figure 1.18). This is an excellent example of how the advantages of SERS can be combined with the advantages of resonance Raman for greater sensitivity of detection.

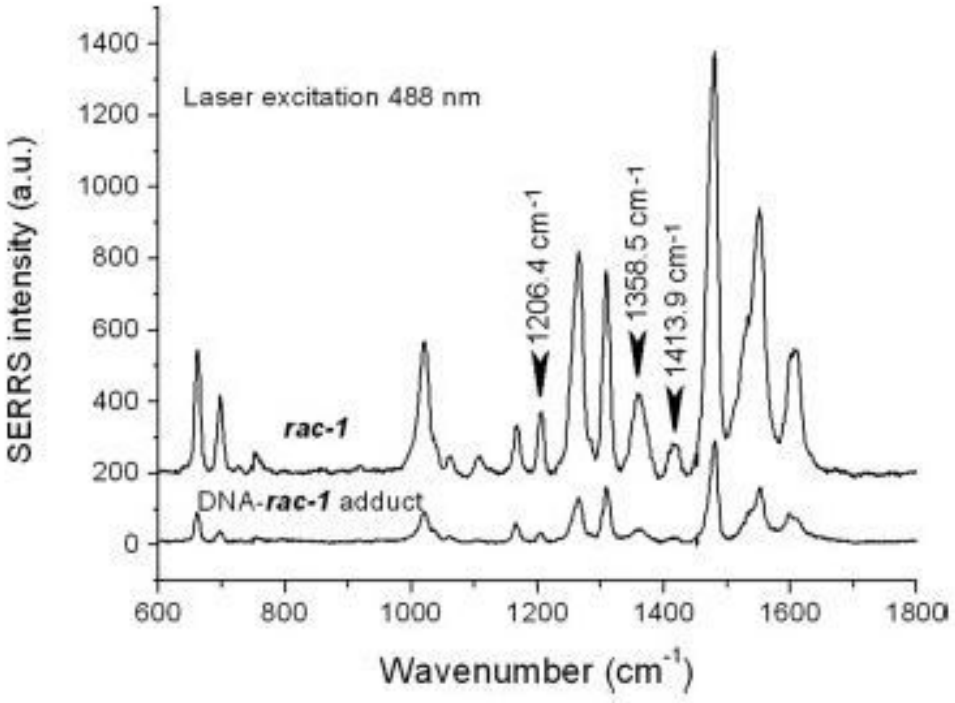

Figure 1.18 SERRS spectra (λ_{ex} = 488 nm) of DNA free (upper trace) and of DNA adduct (lower trace) Ruthenium complex in a silver colloid solution. The specific binding bands bands are signaled. Taken from Reference [106].

1.4 Electrochemical Techniques

1.4.1 The Electrochemical Cell

The fundamental apparatus for all electrochemical techniques is the electrochemical cell. A schematic of a typical three-electrode cell is presented in Figure 1.19. The working electrode is the terminal at which the electrochemical reaction under investigation occurs. The electrochemical reaction is driven by passing a current at the working electrode, for this to occur a second terminal is required to complete the current loop, thus the working and counter electrodes are immersed in the conducting electrolyte to complete the circuit. In order to apply a potential or a current to the working electrode a reference electrode of known potential is also required so that the potential of the working electrode can be measured. The reference electrode is connected to the potentiostat at a point with very high input impedance, this prevents current flowing through the reference electrode so that its potential does not change during the experiment.

1.4.2 Cyclic Voltammetry

Cyclic voltammetry is an electrochemical analytical technique in which current is monitored as a function of electrical potential. In interfacial electrochemistry it is particularly useful as it can provide information about the thermodynamics and kinetics of electron transfer across the electrode electrolyte interface [107]. The process involves applying a triangular waveform to the electrode. Initially a linear negative voltage ramp is applied, which after a time t_1 is reversed to return the potential to its initial value. The application of potential drives the redox reaction generating a current at the electrode in the process. This current is measured and plotted against applied potential to yield a cyclic voltammogram (CV) of the general form shown in Figure 1.20 for a reversible reaction.

Beginning at t_0 as an increasingly negative potential is applied the current increases due to the reduction of analyte at the electrode. Initially the current

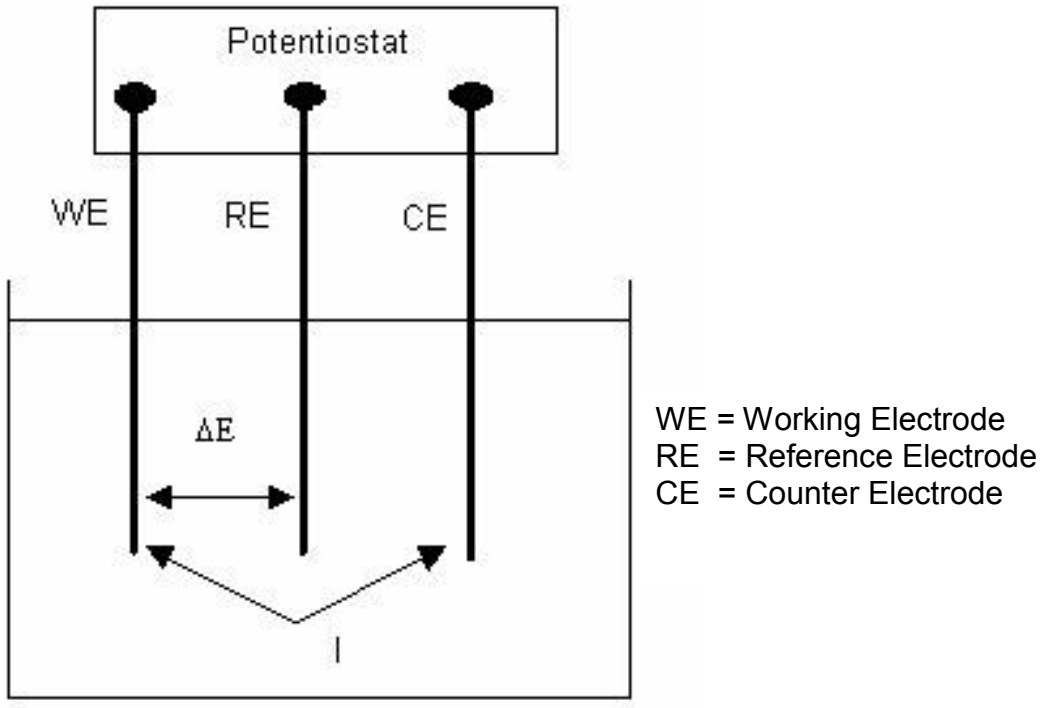

Figure 1.19 Schematic of standard three electrode cell.

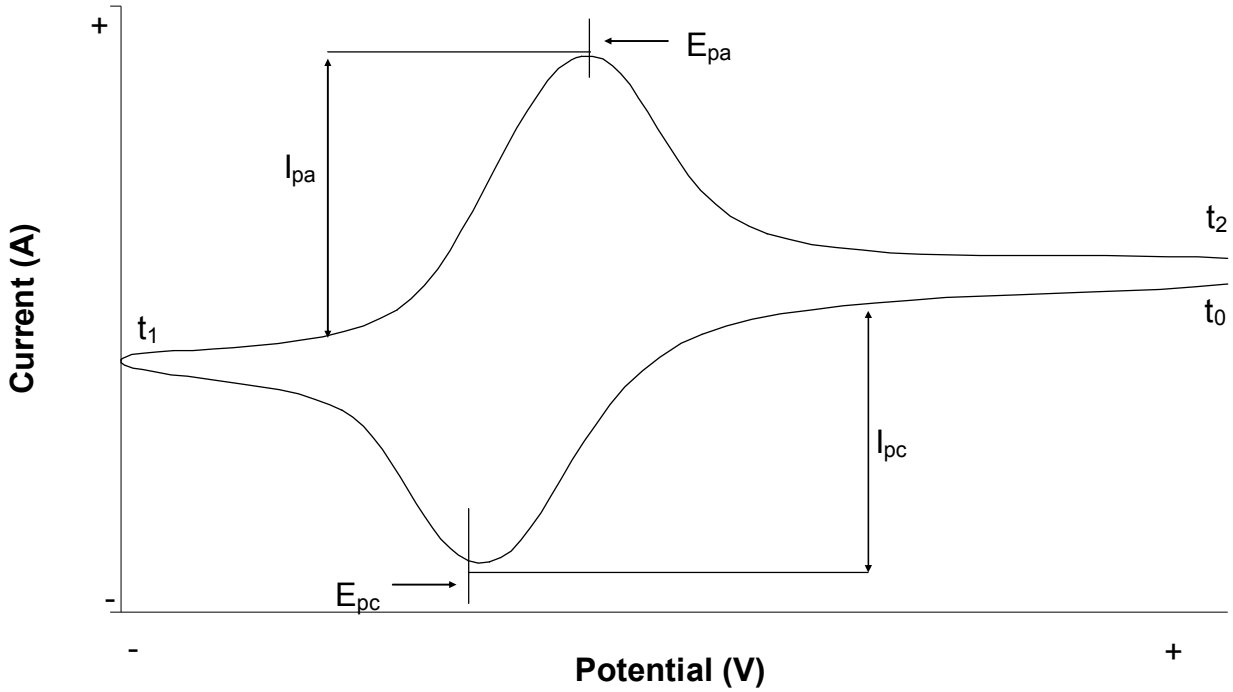

Figure 1.20 General form of Cyclic Voltammogram of a Reversible Redox Couple Under Finite Diffusion Conditions (Using IUPAC conventions for current and potential axes).

continues to grow more negative as the potential becomes more negative, this is due to an increase in the rate of the reaction;

$$Ox + e^- \longleftrightarrow Red \qquad (1.18)$$

Where Ox is the oxidised form of the analyte and Red is the reduced form of the analyte. As the peak current (I_{pc}) is reached the current decreases despite potential being scanned more negatively. This is because the oxidised form of the analyte becomes depleted near the electrode surface due to the increased reaction rate and because mass transport of the oxidised form of the redox couple is not fast enough to maintain the concentration at the same levels as in the bulk solution. This is known as the cathodic wave. At time t_1 the potential is reversed and the reduced analyte near the electrode starts to be oxidised (the reverse of the reaction 1.18) and as an increasingly positive potential is applied an anodic wave is observed which decays after the peak current (I_{pa}) due to depletion of the reduced form of the analyte near the electrode.

One of the most important applications of cyclic voltammetry to this project is to calculate the real surface area of a gold electrode using cyclic voltammetry performed in acid solution. This involves scanning the working electrode between -0.2 V and + 1.45 V (Vrs Ag/AgCl sat KCl) in chloride free 0.5M sulphuric acid electrolyte solution. The positive scan causes formation of a monolayer of gold oxide on the surface of the gold working electrode, the negative scan reduces the oxide layer formed. The CV is of the form shown in Figure 1.21, and because the charge passed is proportional to the number of atoms oxidised/reduced the area under the peak for gold oxide reduction can be used to calculate the real surface area of the working electrode, with each cm^2 of gold oxide surface area requiring 390 µC of charge to be reduced. This method is widely used in the literature [36, 108-111]. In addition to calculating the surface area this procedure also cleans the electrode surface.

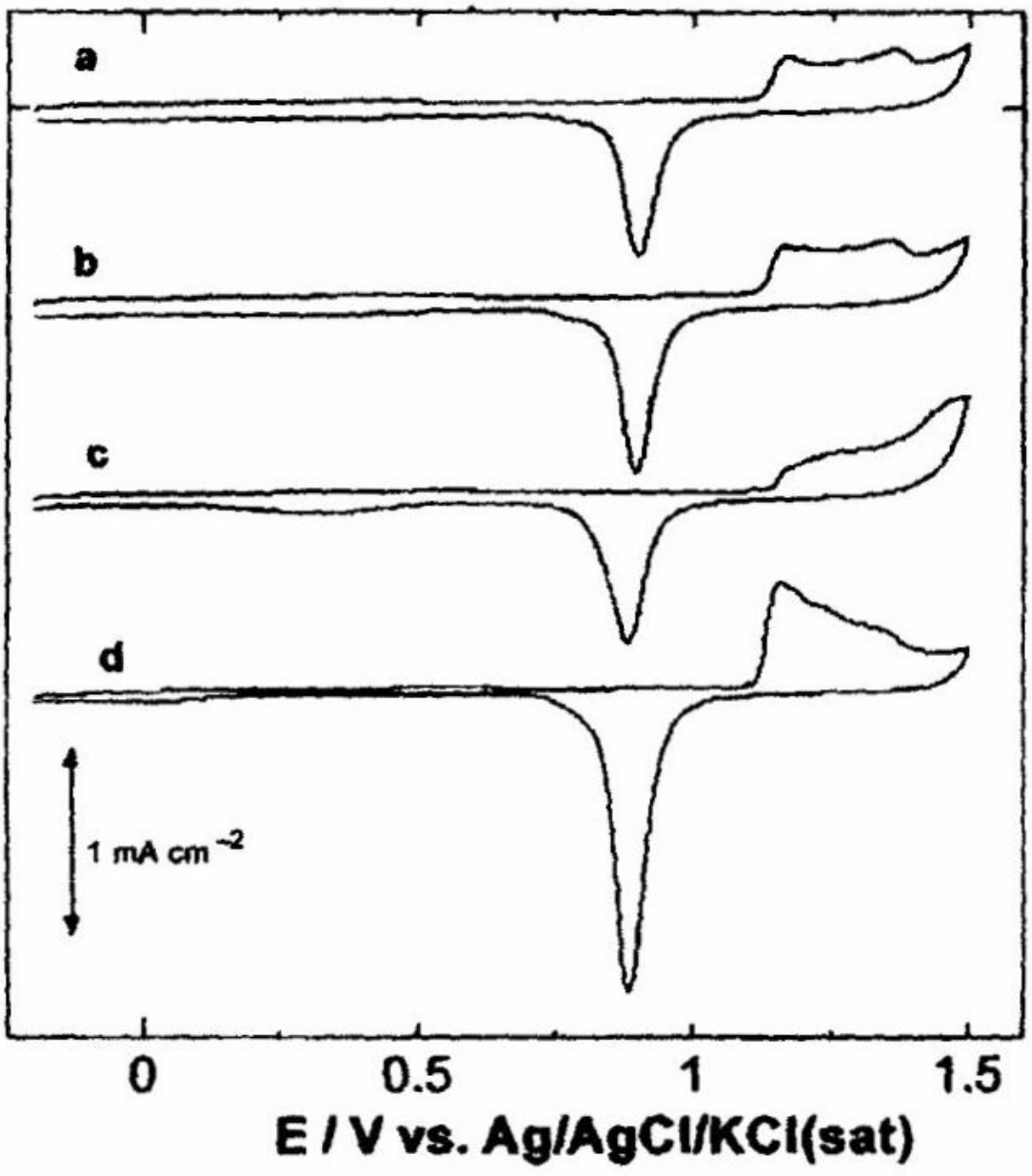

Figure 1.21 CV's of Nano-Au/GC electrodes (a-c) deposited using the following additives; a – none, b – cysteine, c – Iodide. And CV of polycrystalline gold electrode (d). Taken from reference [36].

The peak current (I_p) for the forward scan is described by the Randles-Sevcik equation;

$$i_p = 2.69 \times 10^5 n^{3/2} A(D)^{1/2} C(v)^{1/2} \quad (1.19)$$

where i_p is the peak current (μA), n is the number of electrons transferred, A is the area of the electrode (cm^2), C is the concentration of the electroactive species (mM) and v is the scan rate ($V\ s^{-1}$). D is the diffusion coefficient of the electroactive species ($cm^2\ s^{-1}$).

The equation can be used to analyse the behaviour of a redox couple in solution. A plot of peak current versus square root of scan rate is linear for reversible redox partners. The slope of this plot can be used to determine the diffusion coefficient of the electroactive species [112]. Also by inserting values into this equation it can be used to determine the concentration of electroactive species in solution or the real surface area of a working electrode when D is known.

1.4.3 Chronoamperometry

Chronoamperometry involves the application of a single potential pulse for a period of time while monitoring the current response. The system is held at a potential at which no electrochemical reaction occurs, and then the potential pulse is applied such that the potential is instantly changed to a potential at which an electrochemical reaction will occur at the working electrode resulting in the passage of current. Chronoamperometry is frequently the technique used to carry out electrodepositions as it affords control over the driving force behind the reaction (deposition), and the rate of reaction is easily monitored by observing the current response. The shape of the current transient was described in Section 1.1 (pgs 7-9), analysis of current transients was described in Section 1.2.2 and 1.2.3 (pgs 11-15), the relationship between potential, current and rate of reaction has been described in Section 1.1 (pgs 5-7).

1.4.4 Impedance

In electrochemical impedance spectroscopy a very small magnitude, sinusoidal potential signal is applied to an electrochemical system, as the current response is monitored. The potential imposed is given by $E = E_0 \sin(\omega t)$, where E_0 is the signal amplitude, and ω is the angular frequency. The resulting current has the same frequency as the applied potential but is phase-shifted by the angle φ. The impedance of the system is given by;

$$Z = \frac{\Delta E(\omega)}{\Delta I(\omega)} \tag{1.20}$$

Impedance is made up of real (Z') and imaginary (Z'') parts;

$$Z = Z' + jZ'' \tag{1.21}$$

where $j = \sqrt{-1}$. The real part of the impedance is related to solution resistance, and the imaginary part is related to the double layer capacitance

at the electrode/electrolyte interface. Both of these quantities can be related to the phase angle as follows;

$$Z' = |Z| \cos\varphi \tag{1.22}$$

and

$$Z'' = |Z| \sin\varphi \tag{1.23}$$

A plot of Z' vs. Z'' (the Nyquist plot) gives a line with x-intercept equal to the resistance (R). And a plot of Z'' vs. (1/-ω) yields a straight line whose slope is the double layer capacitance (C_{DL}). The product of R and C_{DL}, the RC constant, is a measure of the time it takes to charge the double layer. 95% of the charging current is discharged after 3 times the RC constant.

1.5 Polyoxometalates; Photocatalytic Properties

Polyoxometalates (POMs) are a series of anionic clusters consisting of a framework of transition metals and oxides. They have the general formula $[M_mO_y]^{x-}$ for isopoly anions and $[Z_zM_mO_y]^{x-}$ for heteropoly anions (the kind encountered in this project). M is usually Mo or W, but can also be V, Nb or Ta. X is the heteroatom, which can be one of many atoms, in this project the heteroatom encountered is S. POMs have been used widely industrially for many years as catalysts in reactions such as hydrocracking, hydrogenation, isomerisation and polymerization. The reason for their excellent catalytic ability is their ability to both accept and release electrons without decomposition [113]. POMs have also found applications in analytical chemistry due to the blue reduction products of many POMs, which make them suitable for the colorimetric determination of various species [113]. More recently POMs have been used in the area of photocatalysis, where their excellent catalytic properties have been found to be further enhanced by photo-excitation, which makes electron transfer to and from the POM species more facile [113-116]. As there is such a broad range of POMs, which have a very large range of applications it is beyond the scope of this literature review to discuss them all. This review focuses on the photocatalytic properties of POMs that are relevant to this project.

Much work involving POM photocatalysis focuses on formation of the excited state of the polyoxometalate anion through absorption of UV-light. The excited state of a redox active species is known to act as both a better oxidant and reductant compared to the ground state [113]. In the case of POMs, which absorb only in the UV-region of the spectrum when in the ground state [115], the excited state POM* is capable of oxidising many organic species, and can be returned to its original redox state either by further electron transfer reactions (e.g. with O_2 or H_2), or by application of a potential at an electrode. An example of this kind of photocatalytic reaction is the photocatalytic production of hydrogen peroxide from propan-2-ol in the presence of decatungstate, $[W_{10}O_{32}]^{4-}$. The reaction mechanism is summarised in Figure 1.22, UV-light excites the decatungstate molecule, and

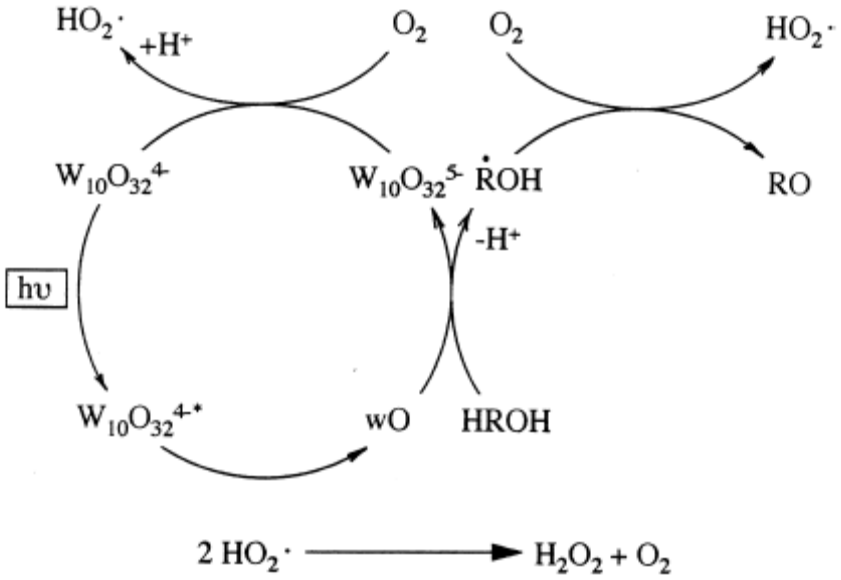

Figure 1.22 Reaction mechanism of photocatalytic production of hydrogen peroxide from propan-2-ol in the presence of decatungstate, taken from reference [117].

it quickly decays to the intermediate species, designated wO. This excited intermediate species donates an electron to propan-2-ol in solution, producing acetone (RO), and leaving the decatungstate cluster in the 5- state. Then $[W_{10}O_{32}]^{5-}$, which is highly reactive, interacts with oxygen to form the $HO_2^{\cdot}$ radical, which is also formed during acetone formation, and the $HO_2^{\cdot}$ radicals combine to form hydrogen peroxide and oxygen. The decatungstate cluster is returned to its original 4- state in the process, so it acts as a catalyst, and is ready to react again [117].

One of the draw-backs of the above system is the requirement for UV excitation in order for the photocatalytic reaction to proceed. It is much more desirable for the reaction to be activated by visible light, such that the reactions can be carried out in sun-light. With this in mind, Keyes et al. have coupled various polyoxometalate clusters to a second metal complex, one with a strong visible absorbance, such that its excited state can be transferred from the metal complex, $[Ru(bpy)_3]^{2+}$ in this case, to the polyoxometalate ($[S_2Mo_{18}O_{62}]^{4-}$) upon absorption of a photon of visible light [114]. In this work it was shown that $[S_2Mo_{18}O_{62}]^{4-}$ effectively quenches the normally intense emission of $[Ru(bpy)_3]^{2+}$ by an associative quenching mechanism [114]. This means that an excited electron is transferred to the polyoxometalate during the quenching process. The same group has utilised this system for the photo-catalytic oxidation of DMF. The principal of the experiment is the same as the reaction demonstrated in Figure 1.22. Instead of a lone polyoxometalate excited by UV-light, a polyoxometalate associated with a strongly absorbing complex ($[Hx_4N]_4[S_2Mo_{18}O_{62}]$) was excited with visible light in order to photo-catalyse the oxidation of DMF [115]. The completion of this reaction was measured as a photo-current, as the polyoxometalate complex was returned to its original state by application of a potential to an electrode in the solution. The current is oxidative as electrons pass from the reduced polyoxometalate to the electrode [115].

1.6 Electrogenerated Chemiluminescence

Electrogenerated Chemiluminescence (ECL) is a technique related to emissive spectroscopic methods such as luminescence and chemiluminescence, but it differs from these methods in that the luminophore excitation process is initiated electrochemically, at an electrode. This can make it a very powerful sensing and diagnostic tool, as the driving force behind the emission reaction, the potential of the working electrode, is easily controlled. As an analytical technique ECL can be extremely useful as it demonstrates linear responses with concentration down to the picomolar level [118, 119], and the technique does not require a light source so scattered light is not an issue. In addition, the technique functions in both an aqueous and non-aqueous environment, and can be linked to many important analytical methods including electrochemical detection [120], flow injection analysis [121], post-column detection in HPLC [122], and capillary electrophoresis [123] and as a label for biological assays and immunoassays [124].

The electronic energy levels involved in ECL are similar to those encountered in fluorescence spectroscopy, except that the energy comes from a chemical reaction rather than a photon. These have been discussed in Section 1.3.3 In brief, excitation raises a ground state electron to the upper vibrational levels of the first excited state. Vibrational relaxation quickly results in the electron reaching the lowest vibrational level of the excited state. Finally, the excited electron returns to the ground state, emitting a photon of light in the process. The difference in ECL is that the excitation process is not brought about as a result of absorption of a photon of light, but is instead induced electrochemically at an electrode. The excited state is achieved by the production of reactive intermediates at the electrode surface, which react to form the excited state luminophore via electron transfer reactions [125]. The ECL excitation can proceed by one of two general mechanisms: Annihilation ECL and Coreactant ECL; the latter of which is encountered in the work in this thesis.

1.6.1 Annihilation ECL

In annihilation ECL, the oxidised and reduced radical forms of a luminophore come into contact with each other and the radicals annihilate each other's radical state, leaving both species at their neutral state, but one of them in the excited state:

$$A - e^- \rightarrow A^{*+}$$
$$A + e^- \rightarrow A^{*-}$$
$$A^{*+} + A^{*-} \rightarrow A^* + A$$
$$A^* \rightarrow A + h\nu$$

Species A above is both oxidised and reduced, by alternate pulsing of the potential of the working electrode between two potential values, to form the cation and anion radicals A^{*+} and A^{*-}, respectively. When these combine an electron is exchanged returning both to their original charge, but leaving one species in an excited state (A*). The excited state molecule then undergoes emissive decay to produce a photon of light. The exact mechanism of the annihilation excited state formation reaction is believed to be more complicated than the simplified form presented above, and a more detailed description of the mechanisms of specific reactions has been the subject of several investigations [125-127]. Examples of luminophores suitable for this kind of annihilation ECL reaction are rubrene, ruthenium(II)tris(2,2'-bipyridine) and diphenylanthracene. They are suitable because they undergo chemically and electrochemically reversible one electron transfer reactions at relatively low potentials [125].

The above reactions are all examples of "energy sufficient" systems, where ΔH^0 of the electron transfer reaction is larger than the energy required to produce the excited singlet state from the ground state [125]. When the ECL proceeds from a species in the excited singlet state such as this it is known as the S-route.

It is possible to replace one of the radical ions in the reaction, such that the luminophore reacts with the radical ion of a second species to produce the excited state, the reaction, and experimental procedure is otherwise the same. An example of this type of annihilation reaction is the ECL reaction of 9,10-diphenylanthracene (DPA) with N,N,N',N'-tetramethyl-p-phenylenediamine (TMPD), in which the DPA* radical is believed to be the ultimate source of the emission [127]. This example happens to be an example where ΔH^0 of the electron transfer reaction (2.03 eV) is significantly lower than the energy required to achieve the singlet excited state of DPA (3.00 eV) [125]. In this case the emitting species is produced through the reaction of triplet state intermediates, i.e. the product of the electron transfer reaction is $^3DPA^*$ (DPA in its excited triplet form, resulting from inter-system crossing), and the singlet excited state is reached by triplet-triplet annihilation of two $^3DPA^*$ species:

$$^3DPA^* + {}^3DPA^* \rightarrow {}^1DPA^* + {}^1DPA$$

This is known as the T-route, it combines the energy of two electron transfer processes to yield sufficient energy to produce the excited single state. This process is known to occur in energy sufficient systems as well as energy insufficient systems [125].

A disadvantage of annihilation ECL is that it requires two separate potential pulses to produce the radical cation and anion in order for the ECL reaction to proceed. This requires that the intermediates be stable enough, and be sufficiently long-lasting so that both are present simultaneously.

1.6.2 Coreactant ECL

In coreactant ECL, a species in the solution is reduced or oxidised by the same potential pulse that oxidises the luminophore, and the intermediate produced reacts with the oxidised form of the luminophore to produce the excited state species. In this way the presence of a coreactant means that only a single potential pulse is required to produce ECL emission. The coreactant typically undergoes bond cleavage in order to enable it to react

with the luminophore [128]. The most important and most frequently studied coreactant ECL system is the $[Ru(bpy)_3]^{2+}$/TPrA (Tripropylamine) system, whose mechanism is discussed in more detail later. Coreactant ECL is very important from an analytical point of view. Annihilation ECL requires a wide potential window in order to generate the ECL reaction intermediates, meaning that only non-aqueous systems can typically be used, and these must be rigorously purified and deoxygenated. Coreactant ECL can be performed in aqueous systems without deoxygenation if desired.

1.6.3 $[Ru(bpy)_3]^{2+}$/TPrA System

The $[Ru(bpy)_3]^{2+}$/TPrA ECL system is one of the most commonly studied ECL systems [125, 129-135]. The reason for its popularity in ECL applications is its extremely strong emissive properties (quantum yield = 0.125), the diverse chemistry of $[Ru(bpy)_3]^{2+}$, and the electrochemical accessibility of the ECL reaction in both aqueous and non-aqueous electrolytes. The $[Ru(bpy)_3]^{2+}$/TPrA ECL system is an example of coreactant ECL. The mechanism of the reaction has been studied in detail, most significantly by Bard and co-workers [136, 137]. By examining the electrochemistry of the reactions, Bard has reported that the $[Ru(bpy)_3]^{2+}$/TPrA system can proceed via two different mechanisms. The first involves direct $[Ru(bpy)_3]^{2+}$ oxidation:

$$[Ru(bpy)_3]^{2+} - e^- \rightarrow [Ru(bpy)_3]^{3+}$$
$$[Ru(bpy)_3]^{3+} + TPrA \rightarrow [Ru(bpy)_3]^{2+} + TPrA^{*+}$$
$$TPrA^{*+} \rightarrow TPrA^{*} + H^+$$
$$TPrA^{*} + [Ru(bpy)_3]^{3+} \rightarrow [Ru(bpy)_3]^{2+*} + TPrA$$
$$[Ru(bpy)_3]^{2+*} \rightarrow [Ru(bpy)_3]^{2+} + h\nu$$

And the second mechanism involves oxidation of the TPrA molecule:

$$TPrA - e^- \rightarrow TPrA^{*+}$$
$$TPrA^{*+} \rightarrow TPrA^{*} + H^+$$
$$TPrA^{*} + [Ru(bpy)_3]^{3+} \rightarrow [Ru(bpy)_3]^{2+*} + TPrA$$
$$[Ru(bpy)_3]^{2+*} \rightarrow [Ru(bpy)_3]^{2+} + h\nu$$

Bard et al. [136, 137] have found that the second mechanism above is a significantly more efficient ECL process than the first and results in up to 100 times greater ECL signal intensity. The reason for the far greater efficiency of the latter mechanism can be explained by the extremely short excited state lifetime of TPrA [138] (0.2 ms [125]). The first mechanism involves a TPrA molecule being oxidised by an oxidised $[Ru(bpy)_3]^{3+}$ molecule, then the $TPrA^*$ radical must interact with a different $[Ru(bpy)_3]^{3+}$ molecule before it loses its excited state through non-radiative processes. The second mechanism involves direct oxidation of the TPrA molecule so that it does not have to diffuse to two different $[Ru(bpy)_3]^{3+}$ molecules making it a much more efficient process.

It is therefore desirable to select the second TPrA oxidation mechanism over the first, less efficient, mechanism beginning with $[Ru(bpy)_3]^{2+}$ oxidation in order to maximise the ECL intensity and therefore device sensitivity. TPrA (E_0 = 0.8 V [137]) is oxidised at a less positive potential than $[Ru(bpy)_3]^{2+}$ (E_0 = 1.1 V) so the second pathway can be encouraged by controlling the potential applied to the device. However, TPrA oxidation is hindered at gold and platinum surfaces due to the formation of oxides (occurring particularly when potentials are applied to aqueous solutions in order to initiate an ECL reaction), and due to the hydrophilic nature of the gold and platinum surfaces. The presence of bromide ions at low concentrations has been reported to dissolve gold oxide, and inhibit its formation at the gold electrode and therefore encourage the second ECL pathway, resulting in up to a 100 fold increase in the ECL signal [137]. Similarly, the additive triton-X, a surfactant, alters the hydrophobicity of the gold surface allowing TPrA to adsorb at the surface, and encouraging the TPrA oxidation pathway. This has been reported to yield up to 10 times enhancement of the ECL intensity [136]. At a less hydrophilic surface, such as indium tin-oxide, TPrA oxidation occurs more readily, and the second pathway occurs without any additives present, producing a much stronger ECL signal than at a gold or platinum surface, in the absence of additives such as bromide or triton-X [136].

1.6.4 Applications of ECL

In this thesis ECL is a very useful technique for the design of an electrochemical micro-sensor (Chapter 6). In this work the detection event is decoupled from the electrochemical reaction under investigation by monitoring the ECL emission occurring at one pole of an electrode that results directly from the electrochemical reaction occurring at the other end. Crooks et al. have demonstrated a electrochemical DNA microarray sensor based on ECL detection [139, 140]. In these devices one or more bipolar electrodes of either gold or indium-tin oxide (ITO) were deposited on a glass support, which was surrounded by a poly(dimethylsiloxane) (PDMS) microchannel as shown in Figure 1.23. The electrode was not connected electrically to any source, and its potential was controlled by controlling the potential of the solution in which it was immersed. The solution potential was controlled by applying a potential difference between the ends of the microchannel. Resistance within the channel results in a potential gradient along the channel. The potential drop in the solution between the two ends of the electrode surface (E_{elec}) can be considered to be equal to the potential drop across the channel (E_{tot}) multiplied by the fraction of the channel occupied by the electrode (L_{elec}/L_{tot}), this is illustrated in Figure 1.23. In a standard device with channel length 12 mm, and electrode length 1 mm, a potential difference of 12 V across the channel would result in a potential difference in the solution across the electrode surface of 1 V. The current passing at the bipolar electrode was not measured directly, but instead indirectly by measuring the ECL signal [139, 140].

As the electrode was not grounded to any electron source, its potential can float, and will sit at an energy level intermediate of the potentials of species in solutions to facilitate electron transfers between them. Figure 1.24 illustrates how the electrochemical reaction can proceed without applying potential directly to the electrode. In a standard electrochemical experiment the energy of the electronic levels in the metal electrode are shifted by changing the electrode potential. When the energy levels of the electrode

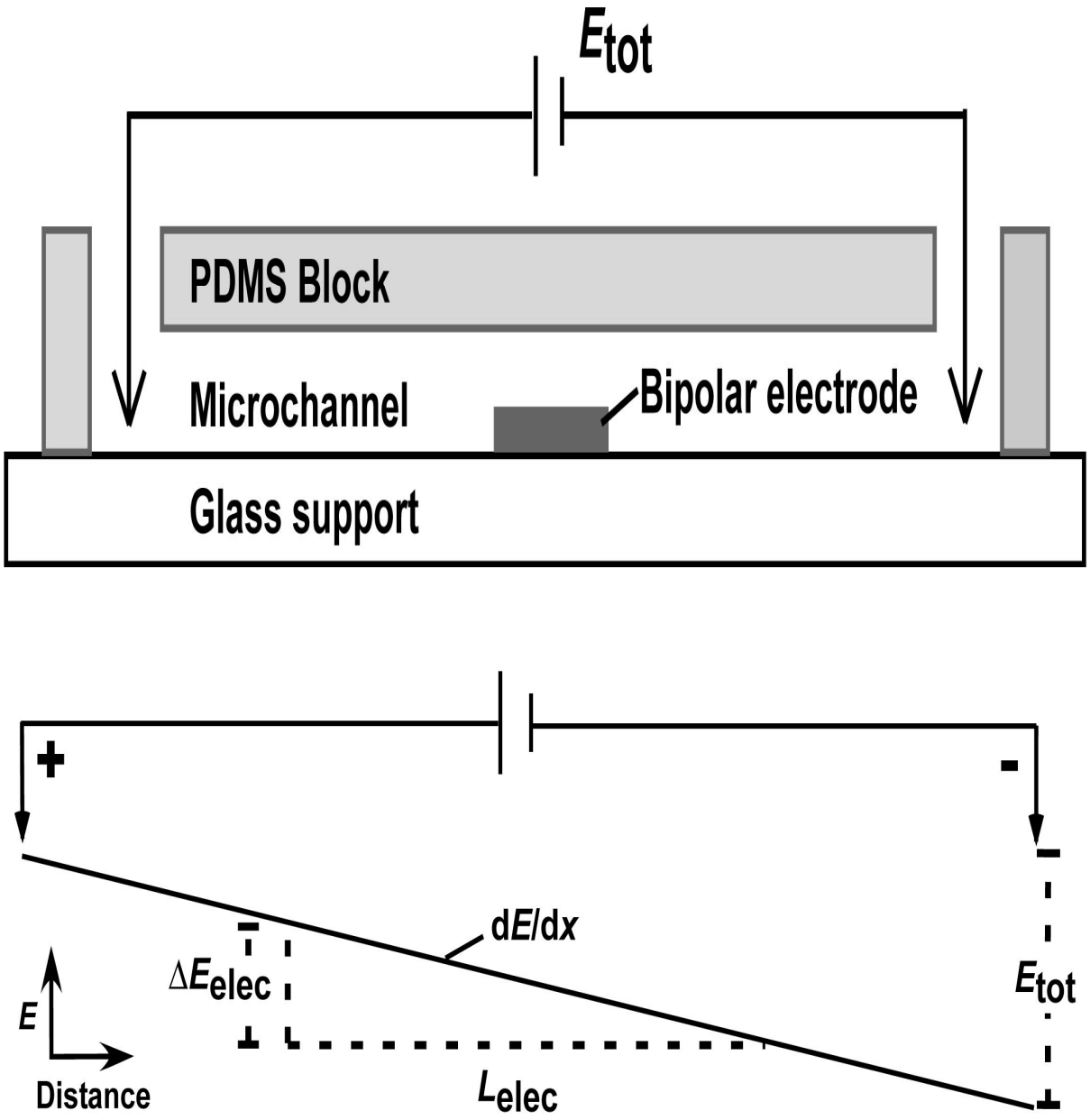

Figure 1.23 Top: Set-up of device used by Crooks et al. Bottom: Potential drop across the microchannel length, taken from Crooks et al. [139].

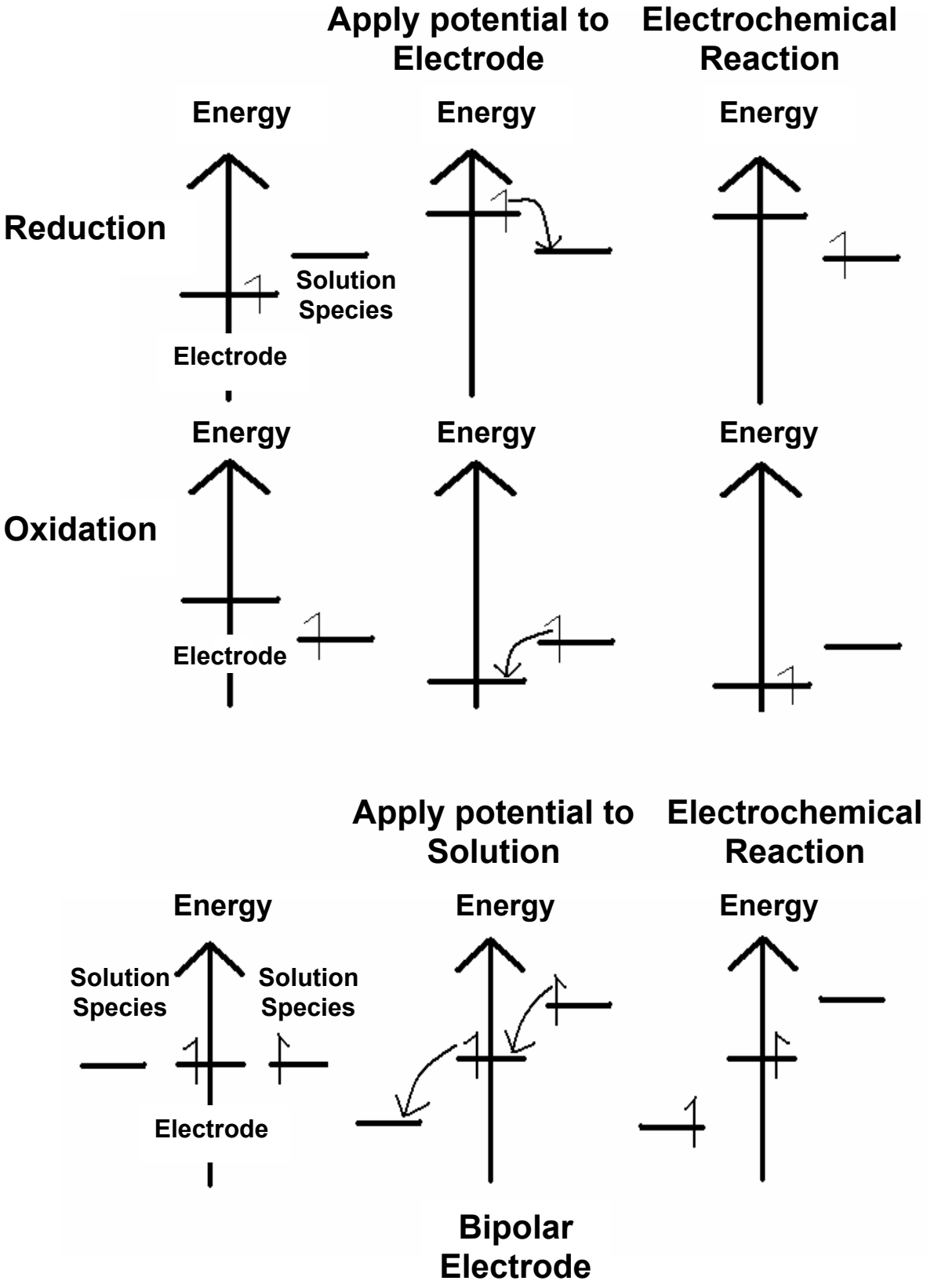

Figure 1.24 Energy level diagrams showing energy levels of electrode and solution species for an oxidation and reduction reaction in a standard electrochemical experiment (top), and at a bipolar electrode when a potential gradient is applied to the solution instead of the electrode

are sufficiently high or low that an electron can be transferred to or from the solution the electrochemical reaction can proceed. When an electrochemical reaction proceeds at a bipolar electrode the solution potential changes along the length of the microchannel such that the potential of the solution is different at each pole of the electrode. The electrode potential is floating and thus can take up a potential intermediate of the reduction and oxidation potentials of two of the solution phase species. If the potential drop across the length of the electrode is sufficiently large, the electrode can facilitate the reduction and oxidation processes simultaneously as shown in Figure 1.23. Significantly, oxidation and reduction are intrinsically coupled and the requirement for charge balance at the electrochemical cell means that the rate of oxidation and reduction are equal. In order for the reactions to occur at the bipolar electrode, the potential drop in solution across the bipolar electrode must equal the difference between the oxidation and reduction potentials of the two electrochemically active species [139, 140].

It is envisaged that the device proposed by Crooks et al. could be used for the sensitive and selective detection of numerous analytes simultaneously at different electrodes within the same channel. The analytes can be identified by the onset potential of ECL emission, which is dependent on the formal potentials of the half reactions involved, or by immobilisation of specific DNA for a particular analyte. The concentration of analyte is proportional to the ECL intensity [139, 140]. This device is the basis for much of the research presented in Chapter 6.

1.7 Conclusions

It is clear from this literature review that nanoparticle science offers an excellent opportunity to enhance the performance of many analytical techniques, but at present this opportunity is not being fully exploited. In areas such as SERS and fluorescence the ability to enhance signal has been recognised, but up to now it has not been achieved in a manner reproducible enough to make the techniques reliable. The use of polyoxometalates as photocatalyts is an area of much promise, that up until now has not been fully explored, and which may also benefit from nanoparticle science also. Finally the electrochemiluminescent microsensor device of crooks et al. [139] is an extremely promising device for multiple analyte determination in a sensitive manner, improving its performance and optimising it for quantitative analysis is a significant challenge.

References

[1] Bell, S. E. J. and Sirimuthu, N. M. S., *Chem. Soc. Rev.*, 2008. **37**(5): 1012-1024.

[2] Zhang, J., Fu, Y., Chowdhury, M. H., and Lakowicz, J. R., *J. Phys. Chem. C*, 2008. **112**(1): 18-26.

[3] Goyal, R. N., Gupta, V. K., Oyama, M., and Bachheti, N., *Electrochem. Commun.*, 2005. **7**(8): 803-807.

[4] Landolt, D., *Journal of the Electrochemical Society*, 2002. **149**: S9-S20.

[5] Schlesinger, M. and Paunovic, M., *Modern Electroplating*. 4 ed. 2000, USA: Wiley.

[6] Haguenau, F., Hawkes, P. W., Hutchison, J. L., Satiat-Jeunemaitre, B., Simon, G. T., and Williams, D. B., *Microscopy and Microanalysis*, 2003. **9**(2): 96-138.

[7] Blum, W., *Journal of the Electrochemical Society*, 1952. **99**(2): C31-C33.

[8] McKinney, B. and Faust, C., *Journal of the Electrochemical Society*, 1977. **124**: 379C-386C.

[9] Dickson, E. W., Jacobs, M. H., and Pashley, D. W., *Philosophical Magazine*, 1965. **11**(111): 575-&.

[10] Hills, G. J., Schiffrin, D. J., and Thompson, J., *Electrochim. Acta*, 1974. **19**(11): 657-670.

[11] Bearss, J., Chan, C., and Meyer, W., *Compound Bore Nozzle for Ink Jet Printhead and Method of Manufacture*, Hewlett-Packard, Editor. 1987: USA.

[12] Honma, H., Oyamada, K., and Koiwa, I., *Electrochemistry*, 2006. **74**(1): 2-11.

[13] Andricacos, P. C. and Robertson, N., *Ibm Journal of Research and Development*, 1998. **42**(5): 671-680.

[14] Datta, M. and Landolt, D., *Electrochim. Acta*, 2000. **45**(15-16): 2535-2558.

[15] Tseng, A. A., Notargiacomo, A., and Chen, T. P., *Journal of Vacuum Science & Technology B*, 2005. **23**(3): 877-894.

[16] Watanabe, T., *Nano-Plating Microstructure Control Theory of Plated Film and Data Base of Plated Film Microstructure*. 2004, UK: Elsevier.

[17] Paunovic, M. and Schlesinger, M., *Fundamentals of Electrochemical Deposition*. 1998, USA: Wiley.

[18] Mostany, J., Mozota, J., and Scharifker, B. R., *J. Electroanal. Chem.*, 1984. **177**(1-2): 25-37.

[19] Avrami, M., *Journal of Chemical Physics*, 1939. **7**: 1103-1112.

[20] Scharifker, B. and Hills, G., *Electrochim. Acta*, 1983. **28**(7): 879-889.

[21] Miranda-Hernandez, M., Palomar-Pardave, M., Batina, N., and Gonzalez, I., *J. Electroanal. Chem.*, 1998. **443**(1): 81-93.

[22] Rynders, R. M. and Alkire, R. C., *Journal of the Electrochemical Society*, 1994. **141**(5): 1166-1173.

[23] Bulhoes, L. O. S. and Mascaro, L. H., *Journal of Solid State Electrochemistry*, 2004. **8**(4): 238-243.

[24] Hyde, M. E. and Compton, R. G., *J. Electroanal. Chem.*, 2003. **549**: 1-12.
[25] Heerman, L. and Tarallo, A., *Electrochem. Commun.*, 2000. **2**(2): 85-89.
[26] Sluytersrehbach, M., Wijenberg, J., Bosco, E., and Sluyters, J. H., *J. Electroanal. Chem.*, 1987. **236**(1-2): 1-20.
[27] Mirkin, M. V. and Nilov, A. P., *J. Electroanal. Chem.*, 1990. **283**(1-2): 35-51.
[28] Scharifker, B. R., Mostany, J., Palomar-Pardave, M., and Gonzalez, I., *Journal of the Electrochemical Society*, 1999. **146**(3): 1005-1012.
[29] Palomar-Pardave, M., Scharifker, B. R., Arce, E. M., and Romero-Romo, M., *Electrochim. Acta*, 2005. **50**(24): 4736-4745.
[30] Liu, H., Favier, F., Ng, K., Zach, M. P., and Penner, R. M., *Electrochim. Acta*, 2001. **47**(5): 671-677.
[31] Floate, S., Hyde, M., and Compton, R. G., *J. Electroanal. Chem.*, 2002. **523**(1-2): 49-63.
[32] PalomarPardave, M., Ramirez, M. T., Gonzalez, I., Serruya, A., and Scharifker, B. R., *Journal of the Electrochemical Society*, 1996. **143**(5): 1551-1558.
[33] Liu, H. and Penner, R. M., *Journal of Physical Chemistry B*, 2000. **104**(39): 9131-9139.
[34] Martin, H., Carro, P., Creus, A. H., Gonzalez, S., Andreasen, G., Salvarezza, R. C., and Arvia, A. J., *Langmuir*, 2000. **16**(6): 2915-2923.
[35] Zarkadas, G. M., Stergiou, A., and Papanastasiou, G., *Electrochim. Acta*, 2005. **50**(25-26): 5022-5031.
[36] El-Deab, M. S., Sotomura, T., and Ohsaka, T., *Journal of the Electrochemical Society*, 2005. **152**(1): C1-C6.
[37] Layson, A. R. and Columbia, M. R., *Microchem J.*, 1997. **56**(1): 103-113.
[38] Feltham, A. M. and Spiro, M., *Chemical Reviews*, 1971. **71**(2): 177-&.
[39] Lane, N., *Journal of Nanoparticle Research*, 2001. **3**(2-3): 95-103.
[40] West, J. L. and Halas, N. J., *Annual Review of Biomedical Engineering*, 2003. **5**: 285-292.
[41] Pedroso, S. and Guillen, I. A., *Combinatorial Chemistry & High Throughput Screening*, 2006. **9**(5): 389-397.
[42] Daniel, M. C. and Astruc, D., *Chemical Reviews*, 2004. **104**(1): 293-346.
[43] Fendler, J. H. and Meldrum, F. C., *Advanced Materials*, 1995. **7**(7): 607-632.
[44] Shipway, A. N., Katz, E., and Willner, I., *Chemphyschem*, 2000. **1**(1): 18-52.
[45] Stuart, M. A. C., *Colloid Polym. Sci.*, 2008. **286**(8-9): 855-864.
[46] Riley, D., *Current Opinion in Colloid and Interface Science*, 2002. **7**: 186-192.
[47] El-Deab, M. S. and Ohsaka, T., *Electrochem. Commun.*, 2002. **4**(4): 288-292.
[48] Bandyopadhyay, S. and Chakravorty, D., *Journal of Materials Research*, 1997. **12**(10): 2719-2724.
[49] Gloaguen, F., Leger, J. M., Lamy, C., Marmann, A., Stimming, U., and Vogel, R., *Electrochim. Acta*, 1999. **44**(11): 1805-1816.

[50] Dokoutchaev, A., James, J. T., Koene, S. C., Pathak, S., Prakash, G. K. S., and Thompson, M. E., *Chem. Mat.*, 1999. **11**(9): 2389-2399.
[51] Brust, M., Walker, M., Bethell, D., Schiffrin, D. J., and Whyman, R., *Journal of the Chemical Society-Chemical Communications*, 1994(7): 801-802.
[52] Jana, N. R., Gearheart, L., and Murphy, C. J., *Chemical Communications*, 2001(7): 617-618.
[53] Hirasawa, M., Shirakawa, H., Hamamura, H., Egashira, Y., and Komiyama, H., *Journal of Applied Physics*, 1997. **82**(3): 1404-1407.
[54] Birtcher, R. C., Donnelly, S. E., and Schlutig, S., *Physical Review Letters*, 2000. **85**(23): 4968-4971.
[55] Kaatz, F. H., Chow, G. M., and Edelstein, A. S., *Journal of Materials Research*, 1993. **8**(5): 995-1000.
[56] Fukushima, M., Yanagi, H., Hayashi, S., Suganuma, N., and Taniguchi, Y., *Thin Solid Films*, 2003. **438**: 39-43.
[57] Bertino, M. F., Gadipalli, R. R., Martin, L. A., Story, J. G., Heckman, B., Guha, S., and Leventis, N., *Journal of Sol-Gel Science and Technology*, 2006. **39**(3): 299-306.
[58] Gu, X. N., Ye, M., Wu, X. L., Wei, L., Hu, Y., Hou, X. G., Liu, X. G., and Liu, A. D., *Nuclear Instruments & Methods in Physics Research Section B-Beam Interactions with Materials and Atoms*, 2006. **247**(2): 279-284.
[59] Campion, A. and Kambhampati, P., *Chem. Soc. Rev.*, 1998. **27**(4): 241-250.
[60] Moskovits, M., *Reviews of Modern Physics*, 1985. **57**(3): 783-826.
[61] Otto, A., *J. Raman Spectrosc.*, 1991. **22**(12): 743-752.
[62] Barnes, W. L., *Journal of Modern Optics*, 1998. **45**(4): 661-699.
[63] Lakowicz, J. R., *Analytical Biochemistry*, 2001. **298**(1): 1-24.
[64] Lakowicz, J. R., Geddes, C. D., Gryczynski, I., Malicka, J., Gryczynski, Z., Aslan, K., Lukomska, J., Matveeva, E., Zhang, J. A., Badugu, R., and Huang, J., *J. Fluoresc.*, 2004. **14**(4): 425-441.
[65] Krug, J. T., Wang, G. D., Emory, S. R., and Nie, S. M., *Journal of the American Chemical Society*, 1999. **121**(39): 9208-9214.
[66] McFarland, A. D. and Van Duyne, R. P., *Nano Letters*, 2003. **3**(8): 1057-1062.
[67] Jiang, J., Bosnick, K., Maillard, M., and Brus, L., *Journal of Physical Chemistry B*, 2003. **107**(37): 9964-9972.
[68] Wang, H., Levin, C. S., and Halas, N. J., *Journal of the American Chemical Society*, 2005. **127**(43): 14992-14993.
[69] Emery, S. R., Haskins, W. E., and Nie, S. M., *Journal of the American Chemical Society*, 1998. **120**(31): 8009-8010.
[70] Zhao, L. L., Kelly, K. L., and Schatz, G. C., *Journal of Physical Chemistry B*, 2003. **107**(30): 7343-7350.
[71] Lyon, L. A., Pena, D. J., and Natan, M. J., *Journal of Physical Chemistry B*, 1999. **103**(28): 5826-5831.
[72] Hashimoto, S., *Principles of Biacore*. Real Time Analysis of Biomolecular Interactions, ed. K. Nagata and H. Handa. 2000, Tokyo: Springer-Verlag.
[73] Kalyuzhny, G., Vaskevich, A., Schneeweiss, M. A., and Rubinstein, I., *Chemistry-a European Journal*, 2002. **8**(17): 3850-3857.

[74] Okamoto, T. and Yamaguchi, I., *Journal of Physical Chemistry B*, 2003. **107**(38): 10321-10324.
[75] Puckett, S. D., Heuser, J. A., Keith, J. D., Spendel, W. U., and Pacey, G. E., *Talanta*, 2005. **66**(5): 1242-1246.
[76] Kurniawan, F., Tsakova, V., and Mirsky, V. M., *Electroanalysis*, 2006. **18**(19-20): 1937-1942.
[77] Numata, T., Otani, Y., and Umeda, N., *Japanese Journal of Applied Physics Part 2-Letters & Express Letters*, 2006. **45**(29-32): L810-L813.
[78] Haes, A. J., Zou, S. L., Zhao, J., Schatz, G. C., and Van Duyne, R. P., *Journal of the American Chemical Society*, 2006. **128**(33): 10905-10914.
[79] Zhu, M., Liu, M., Shi, G. Y., Xu, F., Ye, X. Y., Chen, J. S., Jin, L. T., and Jin, J. Y., *Analytica Chimica Acta*, 2002. **455**(2): 199-206.
[80] Raj, C. R., Okajima, T., and Ohsaka, T., *J. Electroanal. Chem.*, 2003. **543**(2): 127-133.
[81] You, T. Y., Niwa, O., Tomita, M., and Hirono, S., *Analytical Chemistry*, 2003. **75**(9): 2080-2085.
[82] Dai, X. A. and Compton, R. G., *Analytical Sciences*, 2006. **22**(4): 567-570.
[83] Wang, L., Bai, J. Y., Huang, P. F., Wang, H. J., Zhang, L. Y., and Zhao, Y. Q., *Electrochem. Commun.*, 2006. **8**(6): 1035-1040.
[84] Jena, B. K. and Raj, C. R., *Chemistry-a European Journal*, 2006. **12**(10): 2702-2708.
[85] Yu, P. G. and Wilson, G. S., *Faraday Discuss.*, 2000: 305-317.
[86] Luo, X. L., Morrin, A., Killard, A. J., and Smyth, M. R., *Electroanalysis*, 2006. **18**(4): 319-326.
[87] Ullah, M. H., Chung, W. S., Kim, I., and Ha, C. S., *Small*, 2006. **2**(7): 870-873.
[88] Pradhan, N., Pal, A., and Pal, T., *Colloids and Surfaces a-Physicochemical and Engineering Aspects*, 2002. **196**(2-3): 247-257.
[89] Paramasivalm, I., Macak, J. M., and Schmuki, P., *Electrochem. Commun.*, 2008. **10**(1): 71-75.
[90] Lakowicz, J. R., *Principles of Fluorescence Spectroscopy*. 2 ed. 1999, New York: Plumen Publishers.
[91] Weitz, D. A., Garoff, S., Hanson, C. D., Gramila, T. J., and Gersten, J. I., *Optics Letters*, 1982. **7**(2): 89-91.
[92] Lakowicz, J. R., Shen, Y. B., D'Auria, S., Malicka, J., Fang, J. Y., Gryczynski, Z., and Gryczynski, I., *Analytical Biochemistry*, 2002. **301**(2): 261-277.
[93] Sarathy, K. V., Narayan, K. S., Kim, J., and White, J. O., *Chemical Physics Letters*, 2000. **318**(6): 543-548.
[94] Stranik, O., McEvoy, H. M., McDonagh, C., and MacCraith, B. D., *Sensors and Actuators B-Chemical*, 2005. **107**(1): 148-153.
[95] Ianoul, A. and Bergeron, A., *Langmuir*, 2006. **22**(24): 10217-10222.
[96] Aslan, K., Leonenko, Z., Lakowicz, J. R., and Geddes, C. D., *Journal of Physical Chemistry B*, 2005. **109**(8): 3157-3162.
[97] Huang, S. X. and Chen, Y., *Nano Letters*, 2008. **8**(9): 2829-2833.
[98] Aroca, R., *Surface Enhanced Vibrational Spectroscopy*. 2006, Hoboken, NJ: Wiley.

[99] Gardiner, D. and Graves, P., *Practical Raman Spectroscopy*. 1989, New York: Springer-Verlag.
[100] Smith, E. and Dent, G., *Modern Raman Spectroscopy a Practical Approach*. 2005, Sussex: Wiley.
[101] Kneipp, K., Kneipp, H., Manoharan, R., Hanlon, E. B., Itzkan, I., Dasari, R. R., and Feld, M. S., *Applied Spectroscopy*, 1998. **52**(12): 1493-1497.
[102] Campion, A., Ivanecky, J. E., Child, C. M., and Foster, M., *Journal of the American Chemical Society*, 1995. **117**(47): 11807-11808.
[103] Kneipp, K., Wang, Y., Kneipp, H., Perelman, L. T., Itzkan, I., Dasari, R., and Feld, M. S., *Physical Review Letters*, 1997. **78**(9): 1667-1670.
[104] Sauer, G., Brehm, G., and Schneider, S., *J. Raman Spectrosc.*, 2004. **35**(7): 568-576.
[105] Moskovits, M., Tay, L. L., Yang, J., and Haslett, T., *Sers and the Single Molecule*, in *Optical Properties of Nanostructured Random Media*. 2002, Springer-Verlag Berlin: Berlin. p. 215-226.
[106] Gaudry, E., Aubard, J., Amouri, H., Levi, G., and Cordier, C., *Biopolymers*, 2006. **82**(4): 399-404.
[107] Forster, R., Keyes, T., and Vos, J., *Interfacial Supramolecular Assemblies*. 2003, Wiltshire: Wiley.
[108] Trasatti, S. and Petrii, O. A., *Pure and Applied Chemistry*, 1991. **63**(5): 711-734.
[109] Angersteinkozlowska, H., Conway, B. E., Hamelin, A., and Stoicoviciu, L., *Electrochim. Acta*, 1986. **31**(8): 1051-1061.
[110] Dall'Antonia, L. H., Tremiliosi-Filho, G., and Jerkiewicz, G., *J. Electroanal. Chem.*, 2001. **502**(1-2): 72-81.
[111] Zhong, J., Qi, Z. M., Dai, H., Fan, C. H., Li, G. X., and Matsuda, N., *Analytical Sciences*, 2003. **19**(5): 653-657.
[112] Kaifer, A. and Kaifer, M., *Supramolecular Electrochemistry*. 1999, Germany: Wiley-VCH.
[113] Papaconstantinou, E., *Chem. Soc. Rev.*, 1989. **18**(1): 1-31.
[114] Keyes, T. E., Gicquel, E., Guerin, L., Forster, R. J., Hultgren, V., Bond, A. M., and Wedd, A. G., *Inorganic Chemistry*, 2003. **42**(24): 7897-7905.
[115] Fay, N., Hultgren, V. M., Wedd, A. G., Keyes, T. E., Forster, R. J., Leane, D., and Bond, A. M., *Dalton Transactions*, 2006(35): 4218-4227.
[116] Fay, N., Bond, A. M., Baffert, C., Boas, J. F., Pilbrow, J. R., Long, D. L., and Cronin, L., *Inorganic Chemistry*, 2007. **46**(9): 3502-3510.
[117] Tanielian, C., *Coord. Chem. Rev.*, 1998. **180**: 1165-1181.
[118] Cruser, S. A. and Bard, A. J., *Analytical Letters*, 1967. **1**(1): 11 - 17.
[119] Ege, D., Becker, W. G., and Bard, A. J., *Analytical Chemistry*, 1984. **56**(13): 2413-2417.
[120] Fahnrich, K. A., Pravda, M., and Guilbault, G. G., *Talanta*, 2001. **54**(4): 531-559.
[121] Lin, M. S., Wang, J. S., and Lai, C. H., *Electrochim. Acta*, 2008. **53**(26): 7775-7780.
[122] Noffsinger, J. B. and Danielson, N. D., *Analytical Chemistry*, 1987. **59**(6): 865-868.
[123] Han, B., Du, Y., and Wang, E., *Microchem J.*, 2008. **89**(2): 137-141.

[124] Blackburn, G. F., Shah, H. P., Kenten, J. H., Leland, J., Kamin, R. A., Link, J., Peterman, J., Powell, M. J., Shah, A., Talley, D. B., Tyagi, S. K., Wilkins, E., Wu, T. G., and Massey, R. J., *Clinical Chemistry*, 1991. **37**(9): 1534-1539.
[125] Richter, M. M., *Chemical Reviews*, 2004. **104**(6): 3003-3036.
[126] Bard, A. and Faulkner, L., *Electrochemical Methods: Fundamentals and Applications*. 2 ed. 2001, USA: Wiley.
[127] Faulkner, L. and Bard, A. J., *Electroanalytical Chemistry*. Vol. 10. 1977, New York: Dekker.
[128] Rubinstein, I. and Bard, A. J., *Journal of the American Chemical Society*, 1981. **103**(3): 512-516.
[129] Takahashi, F. and Jin, J., *Electroanalysis*, 2008. **20**(14): 1581-1586.
[130] Yin, X. B., Sha, B. B., Zhang, X. H., He, X. W., and Xie, H., *Electroanalysis*, 2008. **20**(10): 1085-1091.
[131] Wei, H., Liu, J., Zhou, L., Li, J., Jiang, X., Kang, J., Yang, X., Dong, S., and Wang, E., *Chemistry-a European Journal*, 2008. **14**(12): 3687-3693.
[132] Hun, X. and Zhang, Z. J., *Electroanalysis*, 2008. **20**(8): 874-880.
[133] Burkhead, M. S., Wang, H. Y., Fallet, M., and Gross, E. M., *Analytica Chimica Acta*, 2008. **613**(2): 152-162.
[134] Zanarini, S., *J. Phys. Chem. C*, 2008. **112**(8): 2949-2957.
[135] Bard, A. J., *Electrogenerated Chemiluminescence*. 2004, New York: Marcel Dekker.
[136] Zu, Y. B. and Bard, A. J., *Analytical Chemistry*, 2001. **73**(16): 3960-3964.
[137] Zu, Y. B. and Bard, A. J., *Analytical Chemistry*, 2000. **72**(14): 3223-3232.
[138] Kanoufi, F., Zu, Y. B., and Bard, A. J., *Journal of Physical Chemistry B*, 2001. **105**(1): 210-216.
[139] Chow, K. F., Mavre, F., and Crooks, R. M., *Journal of the American Chemical Society*, 2008. **130**(24): 7544-+.
[140] Zhan, W., Alvarez, J., and Crooks, R. M., *Journal of the American Chemical Society*, 2002. **124**(44): 13265-13270.

2 Experimental

2.1 Preparation of Gold and Silver Modified FDTO Surfaces by Electrodeposition

2.1.1 Electrochemistry

All electrochemical experiments were carried out in a three-electrode cell at room temperature (22 $\pm$ 3^{o} C) using a CH instruments model 660 electrochemical workstation. The cell consisted of a working electrode, a platinum mesh counter electrode (surface area 15.9cm^2) and a Ag/AgCl (sat KCl) reference electrode. All potentials are quoted Vs. Ag/AgCl (sat KCl) unless otherwise stated. When the electrolyte was $AgNO_3$ in nitric acid, the reference electrode was connected to the cell via a nitric acid salt bridge. When ultra-pure (chloride free) sulfuric acid was the electrolyte a sulphuric acid salt bridge was used. Fluorine doped tin oxide (FDTO) coated glass (Hartford Glass Inc.) was used as the working electrode (resistance 8Ω/cm^2, geometric surface area 0.25cm^2). All electrolyte solutions were made up using Milli-Q water and were purged with argon gas prior to use and were made fresh each day.

2.1.2 Gold nanoparticle electrodeposition

Gold electrodeposition experiments were carried out with potassium chloride (Aldrich) (0.1M) as the supporting electrolyte. Hydrogen tetrachloroaurate(III) trihydrate (Aldrich) (0.001M) was the gold salt used. Various deposition regimes were investigated. The single pulse method involved application of a single potential pulse of intermediate overpotential until the desired charge had been passed. The two pulse method was carried out in two stages; a short, large, overpotential nucleation pulse lasting up to 100 ms was followed by a longer, smaller overpotential growth pulse, lasting up to 100s. Electrodeposition was carried out on bare FDTO and aminopropyldimethylmethoxysilane (ADMMS) modified FDTO.

2.1.3 Silver nanoparticle electrodeposition

Silver electrodeposition experiments were carried out with nitric acid (Riedel de Haen) (0.1M) as the supporting electrolyte. Citric acid (Sigma Aldrich) (0.015M) was added to the silver electrolyte to improve nanoparticle uniformity. Silver nitrate (Sigma Aldrich) (0.001M) was the silver salt used. The two pulse regime was also applied to silver electrodeposition onto bare FDTO.

2.1.4 Calculation of RC time constant

In order to accurately analyse current transients for electrodeposition, the time required to charge the electric double layer must be calculated. This is given by the product of the resistance (R) and capacitance (C), the RC time constant. Before this time has elapsed the current passing results from a mixture of faradaic and non-faradaic processes. Since analysis of the current transients requires that only faradaic processes occur it is important that the RC time constant is quantified, and if necessary experimental parameters altered to minimise the RC constant. R and C can be measured by impedance, where R is the y-intercept value for a plot of –Z''(imag) vrs Z'(real) and C is given by 1/slope of a plot of –Z''(imag) vrs 1/angular frequency. Electrochemical impedance spectroscopy (EIS) was carried out using a CH instruments model 660a electrochemical workstation at a potential of 0.35V over the frequency range 10 KHz to 1 Hz. The potential of 0.35 V was chosen as it lay at the median of the range of gold electrodeposition potentials for which current transient analysis was performed (0.2V – 0.5V). Various supporting electrolyte solutions and concentrations were investigated (in the absence of the electroactive metal salt) to determine the optimum supporting electrolyte composition.

2.1.5 Preparation of FDTO electrodes

FDTO was chosen as the working electrode for these investigations due to its low cost (€0.07 per slide), optical transparency at visible wavelengths, high conductivity (8 $\Omega\,cm^{-2}$), and its large electrochemical potential window. FDTO electrodes were prepared by rinsing in water and then in acetone prior to heating at 400^{o} C in air for 10 minutes to remove any adsorbed

species. Teflon insulating tape was wrapped around the slide leaving a surface area of 0.25cm^2 of the FDTO surface. Slides were stored FDTO side up in petri dishes to minimise their exposure to the environment. When they were ready to be used as working electrodes the uncovered FDTO surface was immersed in the electrolyte.

2.1.6 FDTO surface area determination

For the determination of the geometric surface area of the FDTO glass electrodes a transparent ruler and an overhead projector were used. The ruler was focused onto a sheet of A4 sized paper on the wall using the projector. The area of the A4 sheet was measured using the projected scale of the ruler and this was noted. Then without shifting the focus of the projector a FDTO electrode was placed on the projector, and at the same position on the wall the projection of the active area of the FDTO electrode was traced onto a fresh sheet of A4 paper. Finally this shape was cut out and weighed, and its weight compared to the mean weight of a full sheet of A4 paper. The relative weight of the cut-out compared to the A4 sheet was estimated to be equal to the relative area of that electrode compared to the projected area of the A4 sheet.

2.1.7 Chemical Modification of FDTO

FDTO electrodes were modified with a 3-aminopropyldimethylmethoxysilane (ADMMS) (Fluorochem) monolayer by immersing the FDTO slides in a 0.001M ADMMS solution in toluene (Aldrich) for 48 hours. When removed from the solution, the FDTO was rinsed with pure toluene to remove any physically adsorbed material and then dried in a stream of high purity argon.

2.1.8 SEM Characterisation of Metal Deposits

Scanning electron microscopy (SEM) was carried out using the Hitachi S-3000N scanning electron microscope. SEM image analysis was carried out using Image J version 1.37d image analysis software, to calculate mean particle size, particle density and interparticle spacing for an individual surface the data from SEM images taken at six random sites on each surface was combined.

2.2 Photonic Properties of Surfaces Decorated with Metal Nanoparticles

2.2.1 Spectroscopic Analysis

UV-Vis spectrophotometry was carried out with the Perkin Elmer Lambda 900 UV-Vis Spectrophotometer. FDTO samples were immersed in acetonitrile (Sigma Aldrich) for UV-Vis analysis, complexes were dissolved in acetonitrile, and scanned between 350 nm and 800 nm. Bare, clean FDTO in acetonitrile (FDTO samples) or acetonitrile alone (solutions) were used to blank the instrument. Raman spectroscopy was carried out on the HORIBA Jobin-Yvon Labram HR 2000 confocal Raman microscope using 632 nm and 785 nm excitation from a solid-state laser. An argon ion laser (Coherent) was used to excite at 458 nm, 488 nm and 514 nm. The lasers were focused with a 10x objective in each case; the laser spot diameter was calculated as the laser wavelength (λ/nm) x 3.874 x 10^{-3} (2f# x λ). The probe molecule selected for Raman spectrometry was BPE. Fluorescence Spectrometry was carried out using a Varian Cary Eclipse fluorescence spectrophotometer (solution phase samples). Solutions were made up in degassed acetonitrile, and acetonitrile was used as a blank. A HORIBA Jobin-Yvon Labram HR 2000 confocal microscope was used for emission spectroscopy for surface immobilised species (on FDTO). The probe molecule for fluorescence measurements was $[Os(bpy)_2Qbpy]^{2+}$.

2.2.2 Irradiation of Nanoparticles

Nanoparticle irradiation studies were carried out using a broadband Oriel Instruments xenon arc lamp with 450 watt power output. Silver nanoparticle covered FDTO samples were masked on one side, and irradiated on the other side. Samples were irradiated for 5 hours and were subsequently examined using scanning electron microscopy to investigate the effect of the irradiation process on the silver nanoparticles.

2.2.3 Gold Nanoparticle Real Surface Area Determination

The real surface area of the gold nanoparticle modified surfaces was determined by cyclic voltammetry performed in acid solution. In a 0.5 M ultra

pure sulphuric acid electrolyte the potential was cycled between -0.25 V and 1.45 V. This caused formation of a gold oxide monolayer, followed by reduction of this gold oxide monolayer. The charge passed during the reduction of the gold oxide monolayer is proportional to the real surface area of the gold nanoparticulate surface, with each cm^2 of gold surface consuming 390 µC [1].

2.2.4 Silver Nanoparticle Real Surface Area Determination

The electrochemical method for estimation of the real surface area of gold does not work for silver due to difficulties in forming a silver oxide monolayer [2]. Therefore in order to assess the real surface area of silver nanoparticle electrodes the surface area had to be estimated based on the SEM images captured of the surface. Using the mean diameter, nanoparticle density and the geometric surface area of the FDTO slide it was possible to estimate the surface area of a single nanoparticle, and then all the nanoparticles by assuming that each nanoparticle was a perfect hemisphere. To test the accuracy of this method the real surface area of a gold nanoparticle sample whose area was known based on cyclic voltammetry results was estimated based on analysis of the SEM images of the surface.

2.2.5 Chemical Modification of FDTO

To modify FDTO electrodes with a Trans-1,2-bis(4-pyridyl)ethylene (BPE) (Aldrich) monolayer or an $[Os(bpy)_2Qbpy]^{2+}$ (synthesised by Yann Pellegrin) monolayer the nanoparticle covered electrodes were immersed in a 0.001M solution of BPE in methanol (Sigma-Aldrich) or $[Os(bpy)_2Qbpy]^{2+}$ in methanol respectively for 48 hours. When removed from the solution the FDTO slide was rinsed with pure solvent to remove any unbound or physisorbed BPE or $[Os(bpy)_2Qbpy]^{2+}$ to ensure only a chemisorbed monolayer was present. The slide was then dried in a stream of high purity argon. BPE and $[Os(bpy)_2Qbpy]^{2+}$ were used to modify nanoparticle modified slides after electrodeposition for spectroscopic examination.

2.3 Photo-Catalysis of Methyl Viologen Reduction by Polyoxo-Metallate Associated with Osmium Complex

2.3.1 Materials

$[Os(bpy)_2PIC(H_2)]$ and $[Os(bpy)_2Qby(ClO_4)_2]$ was received from Yann Pellegrin.

α-$[S_2W_{18}O_{62}]$ was synthesised according to the published method [3] by Jie Zhu.

2.3.2 Electrochemistry

All electrochemical experiments were carried out in a three-electrode cell at room temperature using a CH instruments model 660 electrochemical workstation. The cell consisted of a working electrode, a platinum wire counter electrode and a reference electrode. For aqueous experiments the reference electrode was a Ag/AgCl (sat KCl) reference, for non-aqueous experiments the reference was a silver wire electrode, calibrated using ferrocene (Fc/Fc^+). Fluorine doped tin oxide (FTO) coated glass (Hartford Glass Inc.) was used as the working electrode (resistance $8\,\Omega/cm^2$, geometric surface area $0.25cm^2$). When the photocurrent experiment was carried out the cell was designed to expose a circular area on the FTO of diameter 3.8 mm. This gave a real surface area of 0.1134 cm^2. All solutions were purged with argon gas prior to use and were made fresh each day.

2.3.3 Monolayer Formation

FTO electrodes were modified with spontaneously formed monolayers of $Os(bpy)_2PIC$ and $Os(bpy)_2Qby$ by immersing the electrode in a 1 mM methanolic solution of the complex for 48 hours. When removed from the solution, the FTO was rinsed with pure methanol to remove any physically adsorbed material and then dried in a stream of high purity argon.

2.3.4 Optical Spectroscopy

Fluorescent emission spectra were recorded using a Varian Cary Eclipse fluorescence spectrophotometer with 450 nm excitation and collection slit open at 10 mm. Low temperature (77K) emission spectroscopy was carried

out by immersing cuvette containing a solution of the sample [10 μM in butyronitrile: propionitrile (55:45)] in liquid nitrogen for 5 mins. The sample was then excited at 355 nm using a Spectron Q-switched Nd-YAG laser. Emission was detected in a right angled configuration to the laser using an Oriel model IS520 gated intensified CCD coupled to an Oriel model MS125 spectrograph. Luminescent lifetimes were undertaken on a PICoquant Timeharp, time correlated single photon counting spectrometer using 450 nm excitation. All solutions were purged with argon gas prior to measurement. Raman spectroscopy was carried out on the HORIBA Jobin-Yvon Labram HR 2000 confocal Raman microscope using an argon ion laser (Coherent) to excite at 514 nm. The lasers were focused with a 10x objective in each case.

2.3.5 Photo-Catalysis Experiments

The photo-catalysis experiment was performed using a specially produced single compartment electrochemical cell of height 10 mm. The working electrode (FDTO) was sealed to the base of the cell which contained an opening of diameter 3.8 mm. The counter (Pt wire) and reference (Ag wire) electrodes were placed in the top of the cell such that they did not obstruct the path between the working electrode and the laser, which was incident on the working electrode from above. The excitation source was a Continuum Minilite pulsed laser and was emitting at 355 nm. During the experiment the working electrode was held at 0.1 V, a potential sufficiently negative enough to reduce Os^{3+} to Os^{2+} without reducing any of the other species in the electrolyte. After the current was allowed some time to settle the laser pulse was switched on, and after 30-50 seconds the laser was switched off again and the current was allowed to stabilise again before the experiment was stopped. The electrolyte contained 200 μM methyl viologen, 1mM $LiClO_4$ and 100 μM POW.

2.4 Wireless Electrogenerated Chemiluminescence Microsensor for DNA Detection

2.4.1 Materials

Gold-coated chromium-glass slides (EMF, Ithaca, NY) were used to fabricate the bipolar electrodes. The poly(dimethylsiloxane) (PDMS) microfluidic channel was prepared from Sylgard 184 (Dow Corning, Midland, MI). 6-Mercapto-1-hexanol, Ru(bpy)3Cl2 •6H2O (bpy = 2,2'-bipyridine) , and tri-n-propylamine were obtained from Sigma-Aldrich. Platinum nanoparticles were synthesised by Francois Mavré according to a published method [4], and had mean diameter of 3.9 $\pm$ 0.8 nm.

DNA oligonucleotides sequences were purchased from Integrated DNA Technologies (Coralville, IA) and used without further purification. The sequences and modifications are as follows:
capture probe, (5'-CAC GAC GTT GTA AAA CGA CGG CCA G-(CH2)6 SH-3');
target, (5'-CTG GCC GTC GTT TTA CAA CGT CGT G-(CH2)6 SH-3').

2.4.2 Device Fabrication

Standard lithographic methods were used to prepare the gold electrodes on glass slides and to fabricate the microfluidic device. Briefly, a layer of positive photoresist (~10 μm thick, AZ P4620) was spin coated onto the gold slides and then they were exposed to UV light though a positive photomask with the electrode microstructure design on it. The microstructures were transferred to the gold slides after developing the photoresist in the developer solution and etching of the gold and chromium adhesion layers. The gold layer was dissolved in an aqueous solution containing 5% iodine and 10% potassium iodide for 2 min. After that, the chromium adhesion layer was etched by an aqueous solution containing 9% ammonium cerium(IV) nitrate and 6% perchloric acid for one minute. The electrodes were cleaned in acetone and then piranha solution prior to forming the microfluidic device.

The poly(dimethylsiloxane) (PDMS) microfluidic channel was prepared from Sylgard 184 (Dow Corning, Midland, MI) by soft lithography. The dimensions of the channel were 1.2 cm long, 1.75 mm wide, and 28 μm high. A hole puncher with 1.0 mm diameter was used to form the reservoirs at the two ends of the microchannel for the flowing of solution and application of an external electric field. The gold microfabricated slides and the PDMS microchannels were air-plasma treated before they were bound together with the electrodes located at the center of the channel. In the bipolar electrode experiments, the electric field was applied using a power supply via two gold driving electrodes at the ends of the microchannel.

2.4.3 Electrochemiluminescence Measurements

A microscope (Nikon AZ100, Nikon Co., Tokyo, Japan) equipped with a CCD camera (Cascade, Photometrics Ltd., Tucson, AZ) was used to obtain the optical and luminescence micrographs. Micrographs were proceed using V++ Precision Digital Imaging software (Digital Optics, Auckland, New Zealand). The experiment proceeded by applying a potential difference between the wells of the ECL device using a Lambda Model LLS 9120 power supply. Upon application of the potential to the device the ECL emission was recorded using the CCD camera. The measurements were taken in a dark room.

2.4.4 Surface modification of bipolar electrodes

The bipolar electrodes were fabricated by using a standard photolithographic method. Prior to electrode modification, the microfabricated gold slide was cleaned in a piranha solution for 10 min. The surface of each gold, bipolar electrode was modified with single-strand DNA (ssDNA) capture probes by placing 15 μL of the thiol-functionalized DNA solution (2.5 μM in TE buffer containing 10.0 mM Tris, 1.00 mM EDTA, and 0.10 M NaCl, pH 7.4) on the electrode surfaces. The solution remained in contact with the electrode for 2 h in a sealed humidity chamber at 20-25^{o} C. The same DNA modification procedure was carried out on a macroscopic disk gold electrode, and the surface coverage of the DNA probe was found to be 2.1 x 10^{-12} mol cm^{-2} by a previously reported procedure [5]. Next, the electrodes were rinsed with a

TE buffer solution to remove excess DNA solution. A 6-mercaptohexanol solution (1 μM in 1 vol% ethanol in water) was then brought into contact with the electrode surfaces for 1 h to back-fill vacancies within the S6 DNA submonolayer. TE buffer rinsing was used to remove excess thiol solution, and then the electrodes were ready for experiments. Target DNA labelled with Pt NPs was prepared by mixing a 25:1 molar ratio of DNA:Pt-NPs for 30 min. This solution was placed onto the probe-modified bipolar electrodes for 2 h in a sealed humidity chamber at 20-25^{o} C. Finally, TE buffer was used to remove excess target DNA.

2.4.5 Electrochemistry

All electrochemical experiments were carried out in a three-electrode cell at room temperature (22 $\pm$ 3^{o} C) using a CH instruments model 650C electrochemical workstation. The cell consisted of a working electrode, a platinum mesh counter electrode and a Ag/AgCl (sat KCl) reference electrode. All potentials are quoted Vs. Ag/AgCl (sat KCl) unless otherwise stated. The working electrode was a gold disk electrode (d = 2 mm). All electrolyte solutions were made up using Milli-Q water and were purged with nitrogen gas prior to use and were made fresh each day.

References

[1] Trasatti, S. and Petrii, O. A., *Pure and Applied Chemistry*, 1991. **63**(5): 711-734.

[2] Motheo, A. J., Machado, S. A. S., Van Kampen, M. H., and Santos Jr., J. R., *Journal of the Brazilian Chemical Society*, 1993. **4**(3): 122-127.

[3] Fay, N., Bond, A. M., Baffert, C., Boas, J. F., Pilbrow, J. R., Long, D. L., and Cronin, L., *Inorganic Chemistry*, 2007. **46**(9): 3502-3510.

[4] Yang, J., Lee, J. Y., and Too, H. P., *Analytica Chimica Acta*, 2006. **571**(2): 206-210.

[5] Steel, A. B., Herne, T. M., and Tarlov, M. J., *Analytical Chemistry*, 1998. **70**(22): 4670-4677.

3 Preparation of Gold and Silver Modified FDTO Surfaces by Electrodeposition

3.1 Introduction

Noble metal nanoparticle surfaces are an area of intense research interest, owing to their interesting properties, such as high surface area, and a strong surface plasmon absorbance [1-8]. Many of these properties make nanoparticle surfaces excellent platforms for sensing and diagnostic devices based on methods such as surface enhanced Raman [9], metal enhanced fluorescence [10] and electrochemical detection [11] as well as other applications such as catalysis [12]. The properties of these surfaces depend on the nanoparticle size and relative positioning. In order to produce optimised surfaces it must be possible to produce nanoparticles in a controlled manner, such that the size and surface coverage of particles can be accurately controlled. There are several methods available for nanoparticle formation on a surface including; chemical synthesis and immobilisation [13-15], sputter coating [16-18] and irradiation based methods [19, 20]. The method chosen for these investigations was electrodeposition. The advantages of electrodeposition over the other techniques are that it is an extremely simple and quick method, and produces extremely stable, strongly attached nanoparticles, and there is less tendency for the formation of clusters that is often seen in some of the other methods [21].

The nature of the surfaces desired in this work is represented in Scheme 1. It consists of noble metal nanoparticles formed in a single layer on the conducting surface such that the diameter and interparticle spacing of the nanoparticles is controlled. In this way the properties of the nanoparticle surfac can be tuned for a particular application. For example the nanoparticle diameter has been shown to be extremely influential on the degree of enhancement observed in SERS spectroscopy [22, 23]. Thus, by controlling the nanoparticle diameter it is possible to produce a surface

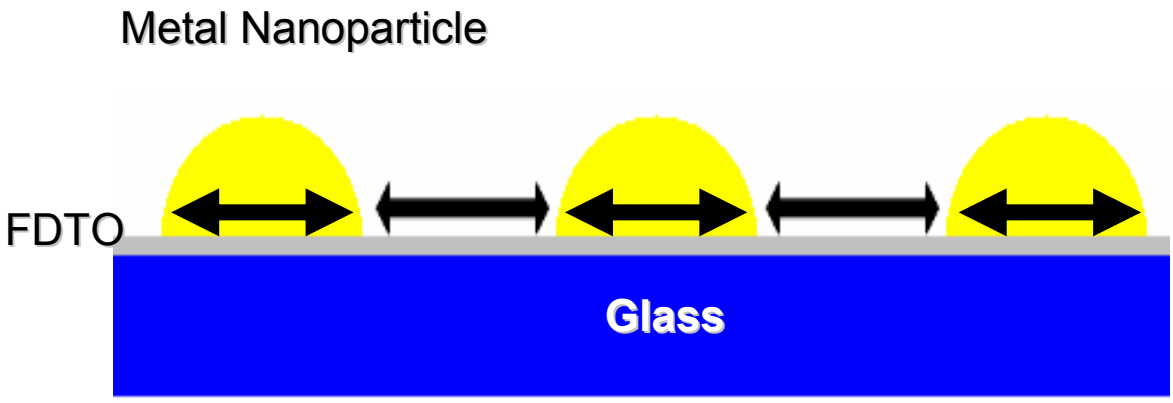

Scheme 1: Desired surface properties; metal nanoparticles of controlled diameter and controlled interparticle spacing electrodeposited on an inexpensive conducting surface.

suited for SERS based sensing. The key properties are the nanoparticle size, nanoparticle size distribution and number density of nanoparticles on the surface (i.e. interparticle spacing). Other properties of the surface that would be desirable are low cost, and ease of preparation. For these reasons the conducting substrate fluorine-doped tin-oxide (FDTO) was chosen as the substrate. It is extremely inexpensive (€0.07 per electrode), and dozens of electrodes can be prepared, ready for electrodeposition in an hour.

In this work, methods for controlling the above properties of nanoparticle surfaces, produced by electrodeposition, are presented. Many of these properties can be controlled by careful choice of electrochemical potential, and duration of the deposition potential. Limiting the particle size distribution is a particular challenge, as diffusion zone coupling (see literature review) often leads to a significant broadening of the size distribution of nanoparticles. In the literature review it was explained how electrodeposition proceeds via a nucleation and growth mechanism. Producing size monodisperse nanoparticles by electrodeposition requires that the electrodeposition proceed via instantaneous nucleation, so that all nanoparticles are growing for the same amount of time, from the beginning of the experiment. In addition the rate of growth must be limited so that coupling of diffusion zones is kept to a minimum. Methods used to control the nucleation mode and growth rate in this work include chemical modification of the electrode surface, and control of the deposition potential waveform. The nucleation mode of the surfaces produced is characterised by scanning electron microscopy, and by analysing the current transients using the dimensionless plots described in the literature review.

The surfaces produced in this chapter will be used in later chapters, where their applications shall be explored. The ability to control the properties of the surfaces will be very important in this later work.

3.2 Determination of Charging Current

The charging current is the current passed due to non-faradaic processes that occur upon application of an electrochemical potential to an electrode/electrolyte interface, such as during an electrochemical deposition. Much information about the nature of the electrochemical reaction can be obtained from the current transient recorded during the electrochemical experiment. However, analysis of the current transients resulting from an electrodeposition is only possible after the charging current has been passed, as the current observed during this time is as a result of faradaic and non-faradaic processes and it is not possible to distinguish the faradaic processes. The charging current can be quantified in terms of the RC time constant. This is the product of the resistance (R) and the capacitance (C) of the system, and yields a time which indicates the temporal characteristics of the charging current. Electrochemical impedance spectroscopy was used to determine the RC-time constant in the presence of two electrolytes under consideration for use as the supporting electrolyte in the electrodeposition experiments, KCl and H_2SO_4. Resistance (R) is obtained from the x-intercept value for a plot of –Z''(imag) versus Z'(real) and capacitance (C) is given by 1/slope of a plot of –Z''(imag) versus 1/angular frequency. Some typical impedance plots of Z" vs 1/angular frequency are presented in Figure 3.1 for the different supporting electrolytes and at different concentrations. An example plot of –Z''(imag) vrs Z'(real) is presented in Figure 3.2. The values determined for R, C and RC are summarised in Table 3.1.

The duration of the charging current was quite short for both supporting electrolytes at all concentrations. The greatest RC constant determined was < 2 ms, and there was a general trend towards a shorter charging current at greater supporting electrolyte ionic strength. As the ionic strength increased the resistance was expected to decrease, and the capacitance (ability to store charge) is expected to increase, this is what was observed. KCl produced a shorter duration charging current than K_2SO_4 so it was chosen as the supporting electrolyte for gold electrodeposition. The greatest RC

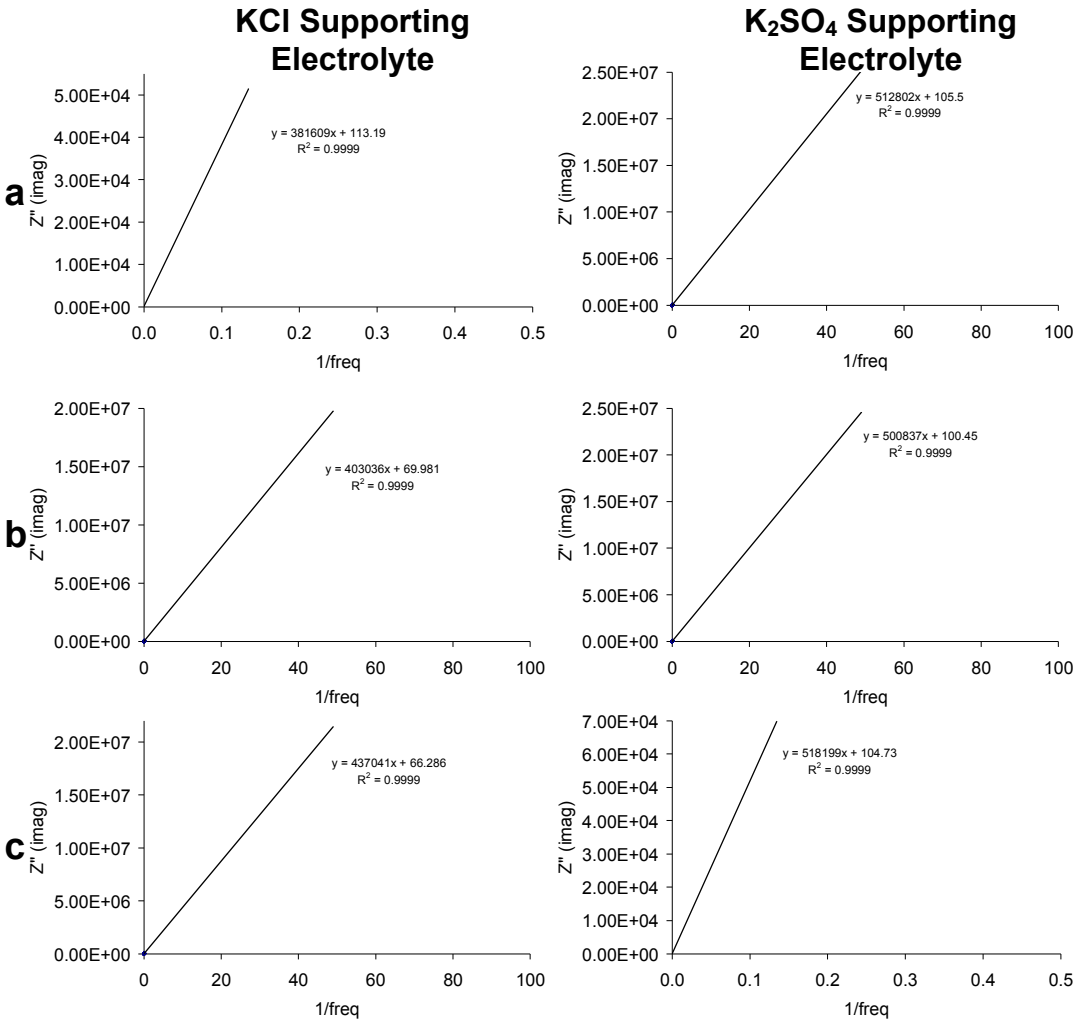

Figure 3.1 Plots of Z'' (imag) vs 1/angular frequency for the determination of interfacial capacitance at a 0.25cm^2 surface area FDTO electrode in the indicated supporting electrolyte with an ionic strength of (a) 0.03, (b) 0.3, (c) 0.75. Impedance was measured at -0.35 V over the frequency range 10 KHz to 1 Hz.

Table 3.1 Effect of supporting electrolyte concentration on RC constant, the area normalised capacitance was estimated based on the geometric surface area rather than the real surface area

Electrolyte	**Ionic Strength**	**R (ohm)**	**C (x 10^{-6} F)**	**C/A (F cm^{-2})**	**RC (ms)**
0.03M KCl	0.03	212 ± 9	3.81 ± 0.2	1.42 x 10^{-5}	0.8087
0.3M KCl	0.3	41 ± 2	3.91 ± 1.2	1.46 x 10^{-5}	0.1607
0.75M KCl	0.75	35 ± 1	3.14 ± 0.3	1.17 x 10^{-5}	0.1106
0.01M K_2SO_4	0.03	287 ± 13	6.51 ± 0.4	2.60 x 10^{-5}	1.8704
0.1M K_2SO_4	0.3	50 ± 4	9.29 ± 0.3	3.71 x 10^{-5}	0.4660
0.25M K_2SO_4	0.75	47 ± 4	4.53 ± 0.4	1.81 x 10^{-5}	0.2133

constant recorded for KCl was 0.8 ms, if τ = 0.8 ms and 95% of the double layer charging current is discharged at t = 3 τ [24] then the charging current is effectively discharged after ~ 2.5 ms. This is not significant on the scale of a typical gold electrodeposition experiment which typically lasted at least 10 s. Therefore, it is acceptable to use KCl supporting electrolyte at any concentration within the range investigated in this experiment. A typical gold salt concentration used was 0.001 M, it is normal to choose a supporting electrolyte concentration 100 times greater than the electroactive species, so a concentration of 0.1 M KCl was chosen as the standard supporting electrolyte.

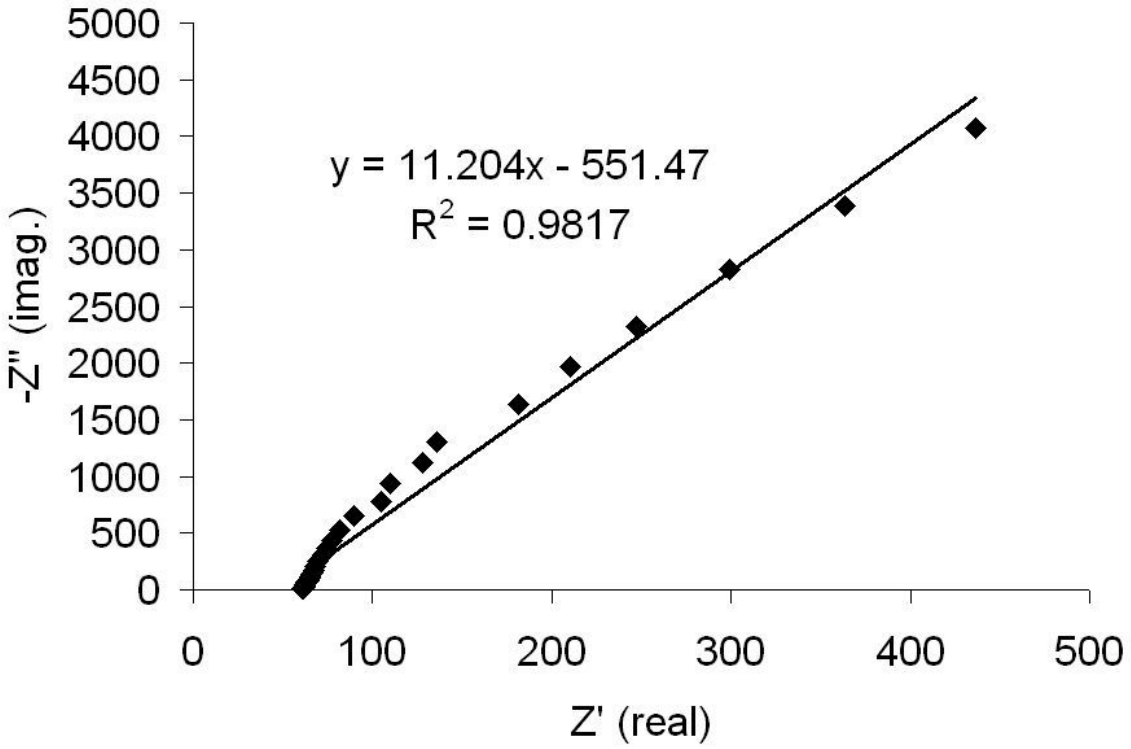

Figure 3.2 Typical plot of –Z'' (imag) against Z' (real) used to calculate resistance (from the x intercept). Recorded from a 0.25 cm^2 FDTO electrode in 0.3 M KCl.

3.3 Cyclic Voltammetry

3.3.1 Characterisation of Nucleation of Gold on FDTO

In order to characterise the nucleation process and to obtain information about the reduction potential of the gold salt, and therefore the potentials at which the metal can be electrodeposited, cyclic voltammetry was carried out using the proposed electrodeposition electrolyte. Based on journal articles where gold nanoparticles similar in size and morphology to those of interest in this project have been produced, the gold salt chosen for these investigations was hydrogen tetrachloroaurate trihydrate ($HAuCl_4.3H_2O$) and a gold salt concentration of 1 mM was chosen [25-27].

Figure 3.3 illustrates cyclic voltammograms for a 1 mM tetrachloroaurate plating solution at an FDTO electrode. The first scan contains a characteristic "nucleation loop" which arises from the greater overpotential required for nucleation onto FDTO compared to deposition of gold onto gold [28]. In the first negative going scan the peak potential is approximately -200 mV while in subsequent scans the peak potential is approximately 350mV. The significant reduction in the overpotential for deposition following the first scan indicates that the stripping process is incomplete, that gold nuclei remain on the FDTO surface and that subsequent growth occurs predominantly at the remaining gold sites rather than onto the bare FDTO surface. This confirms the widely reported theory that electrodeposition proceeds by nucleation and then growth of these nuclei [29-38]. The reduction potential for $HAuCl_4$ is given as 0.8 V [21], there are a couple of reasons why the peak current in Figure 3.3 deviates from this. Firstly the energy of the surface has an effect on the peak current as evidenced by the greater overpotential required for nucleation than for growth. Secondly the IR drop, which is a product of the current and resistance, can result in a significant negative shift in the reduction peak in cyclic voltammetry, this occurs especially in systems like this with a working macro-electrode. The IR drop is 16.4 $\pm$ 1.4 mV at a 0.25 cm^2 FDTO electrode under the conditions used in Figure 3.3.

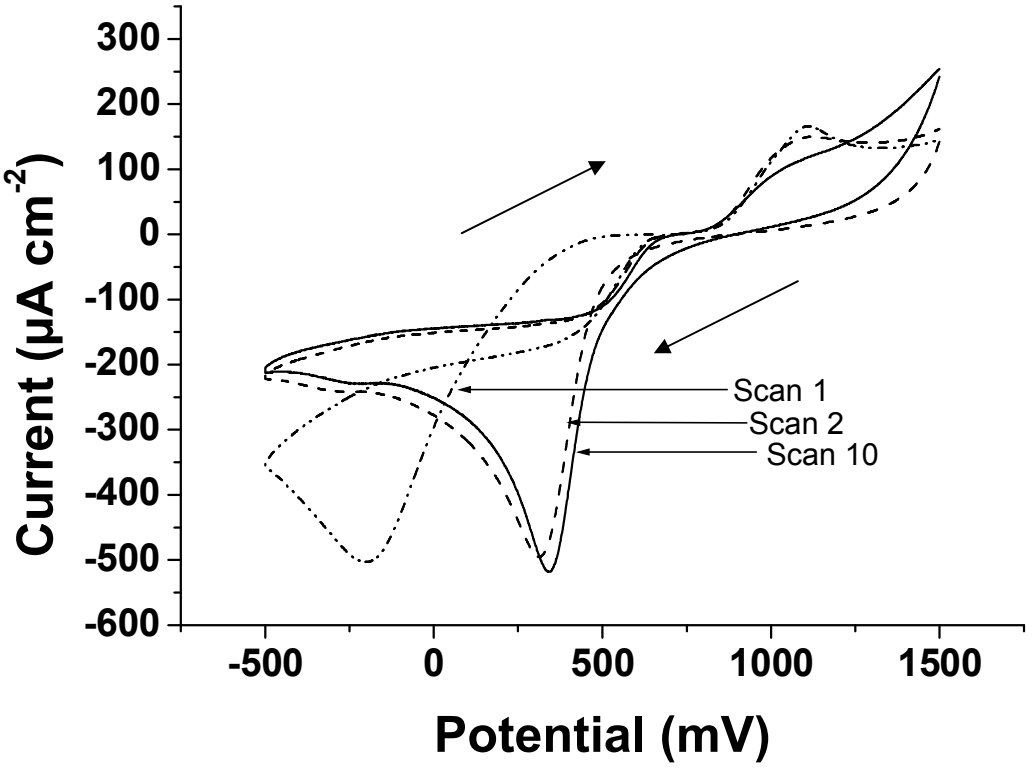

Figure 3.3 Cyclic Voltammograms at 100mV s^{-1} for the deposition and stripping of gold from 0.001M $HAuCl_4$ in 0.1M KCl on 0.25cm^2 FDTO.

3.3.2 Characterisation of Nucleation of Gold on Chemically Modified FDTO

Depositing a spontaneously adsorbed monolayer will affect the rate of heterogeneous electron transfer to the $AuCl_4^-$ ion in solution and may alter its interfacial concentration. Figure 3.4 illustrates the effect of modifying the FDTO electrode with a 3-aminopropyldimethylmethoxysilane (ADMMS) monolayer on the electrodeposition process. The cyclic voltammograms exhibit a similar overall response to that seen at the bare electrode and the characteristic nucleation loop is again present. Significantly, the peak potential for the first scan shifts in a positive potential direction by approximately 380 mV to 200 mV at the modified electrode. This shift indicates that nucleation on the ADMMS surface is thermodynamically more facile than on the bare FDTO surface. This behaviour most likely reflects a reduction in the activation energy of surface diffusion of adions (E_{adi}) at the modified surface [39]. As expected, for subsequent scans, gold on gold deposition proceeds and the presence of the ADMMS monolayer has relatively little effect on the energetics of deposition after nucleation has occurred followed by incomplete stripping.

3.3.3 Characterisation of Nucleation of Silver on FDTO

CVs of silver electrodeposition and stripping from the silver nitrate electrolyte are presented in Figure 3.5. It is evident that there was no “nucleation loop” in the first or subsequent scans, thus indicating that the stripping process was much more complete compared to the gold CVs. This is further supported by the absence of a large shift between the peak potential from the first and subsequent scans. The evidence indicates that most of the silver deposited in the first negative sweep was oxidatively removed from the surface. An explanation for the greater efficiency of silver nanoparticle stripping compared to gold nanoparticle stripping is that gold nanoparticle stripping occurs at a potential of about 1000 mV for this system, and this coincides with the potential for gold oxide formation. This competing process prevents complete stripping. The potential of silver nanoparticle stripping (~ 550 mV) occurs at a significantly less positive potential than that of silver

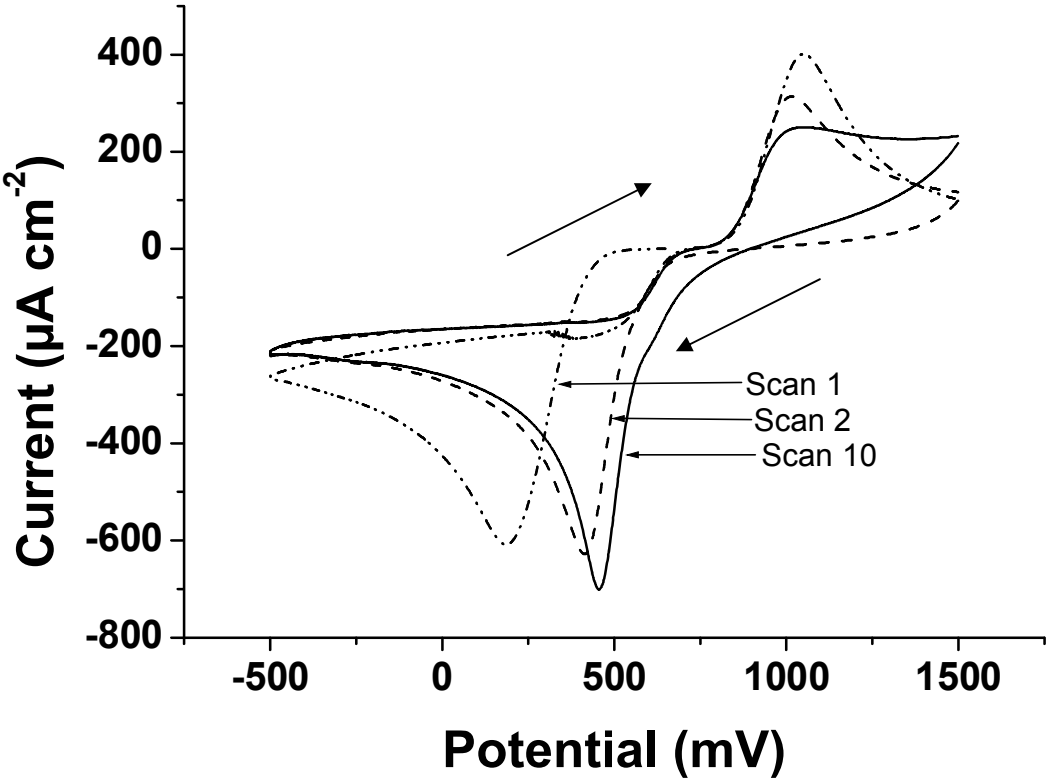

Figure 3.4 Cyclic Voltammograms at 100mV s^{-1} for the deposition and stripping of gold from 0.001M $HAuCl_4$ in 0.1M KCl on ADMMS modified 0.25cm^2 FDTO.

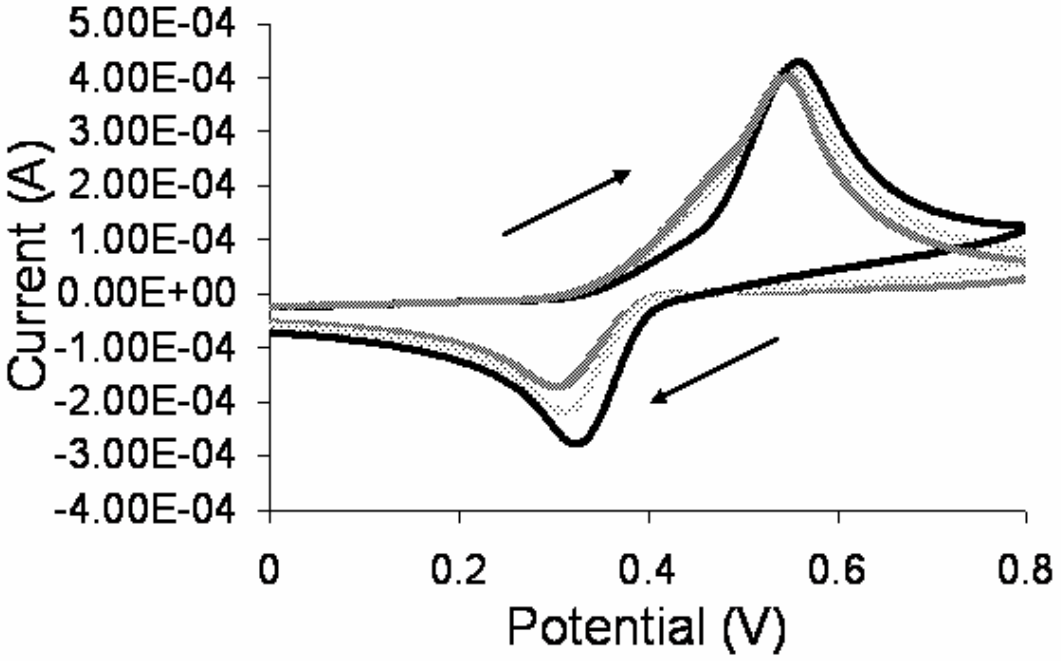

Figure 3.5 Cyclic Voltammograms at 100mV s^{-1} for the deposition and stripping of silver from 0.001M $AgNO_3$ in 0.1M HNO_3 and 0.015 M citric acid on 0.25cm^2 FDTO. Scan 1 (dark grey), Scan 2 (light grey) and Scan 10 (black).

oxide formation (~ 1100 mV). The supporting electrolyte chosen for silver nanoparticle electrodeposition was H_2SO_4. This was in accordance with the literature for silver electrodeposition [40, 41], and because H_2SO_4 yielded a sufficiently low RC constant. KCl could not be used as the supporting electrolyte due to the formation of AgCl in solution.

3.4 Gold Nanoparticles on Bare FDTO by Single Pulse Electrodeposition

Various studies of the potentiostatic electrodeposition of metals have shown that increasing the overpotential, e.g. in chronoamperometry, results in a shift from progressive 3D diffusion limited nucleation and growth to instantaneous 3D diffusion limited nucleation and growth [29, 35, 42, 43]. When a fixed potential was applied to the working electrode, at a sufficient overpotential in a suitable metal electrolyte, electrodeposition proceeded according to the deposition curves presented in Figure 3.6. In this case the curves are for electrodeposition of gold (from $HAuCl_4$) onto FDTO. As the potential is first applied current begins to flow as nucleation occurs. The current increased initially corresponding to the nuclei increasing in size and offering more sites for attachment of adatoms. However, as more time passes the concentration of metal ions at the electrode surface begins to drop below that of the concentration in the bulk solution. Diffusion of ions to the electrode becomes the rate limiting process and this corresponds to a drop in current. The maximum current (I_{max}) occurs at the time t_{max}, the time t_{max} depends on the overpotential as a greater overpotential results in a faster reaction rate and therefore the current maximum is reached faster. This is demonstrated in Figure 3.6 when more negative potential was applied (greater overpotential) the maximum current was reached in a shorter time and was accordingly of greater magnitude.

A significant objective of this project is to produce nanoparticulate surfaces of controlled particles size, density and size distribution. To control these properties by electrodeposition the nucleation and growth kinetics must be managed. The ability to control the nucleation and growth dynamics through the applied potential was investigated for the electrodeposition of gold nanoparticles from $HAuCl_4$ onto FDTO by comparing the dimensionless $[(I/I_{max})^2$ vs. $t/t_{max}]$ form of the current transients with the theoretical curves for 3D progressive and instantaneous nucleation coupled to diffusion controlled growth developed by Scharifker and Hills [30]. Figure 3.7 illustrates

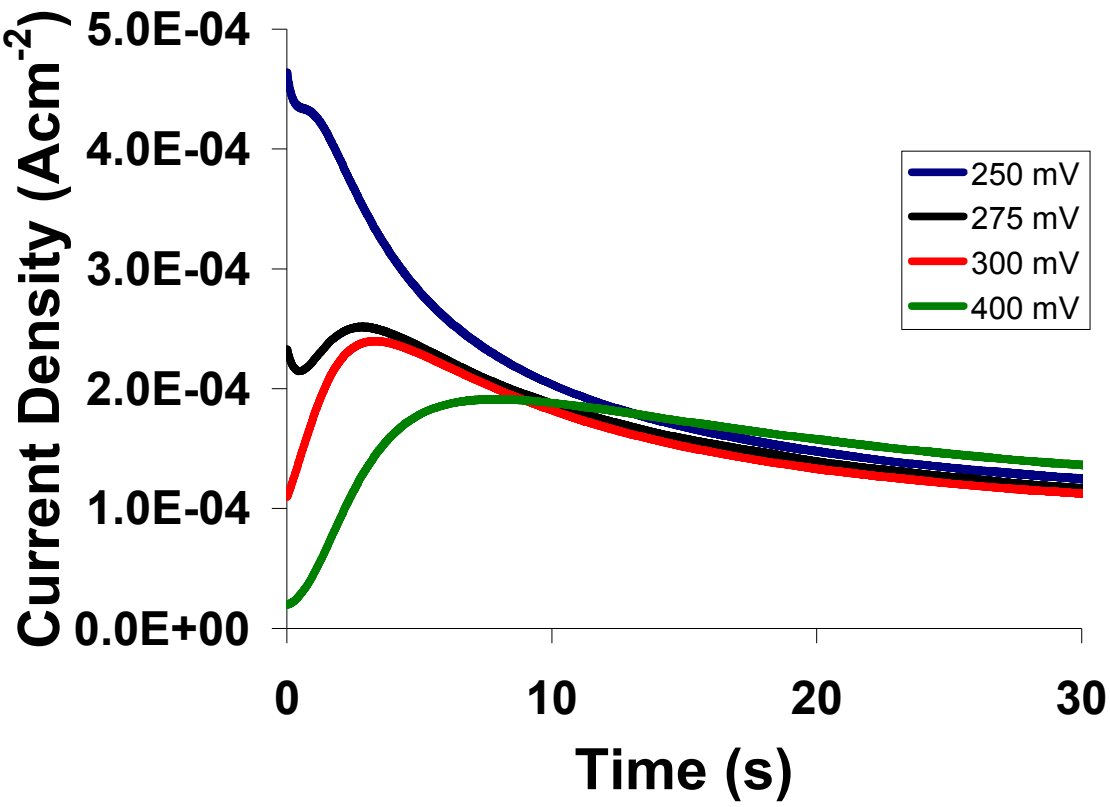

Figure 3.6 Potentiostatic transients for electrodeposition of gold from 0.001 M $HAuCl_4$ in 0.1M KCl on FDTO using a single deposition pulse at the indicated potential.

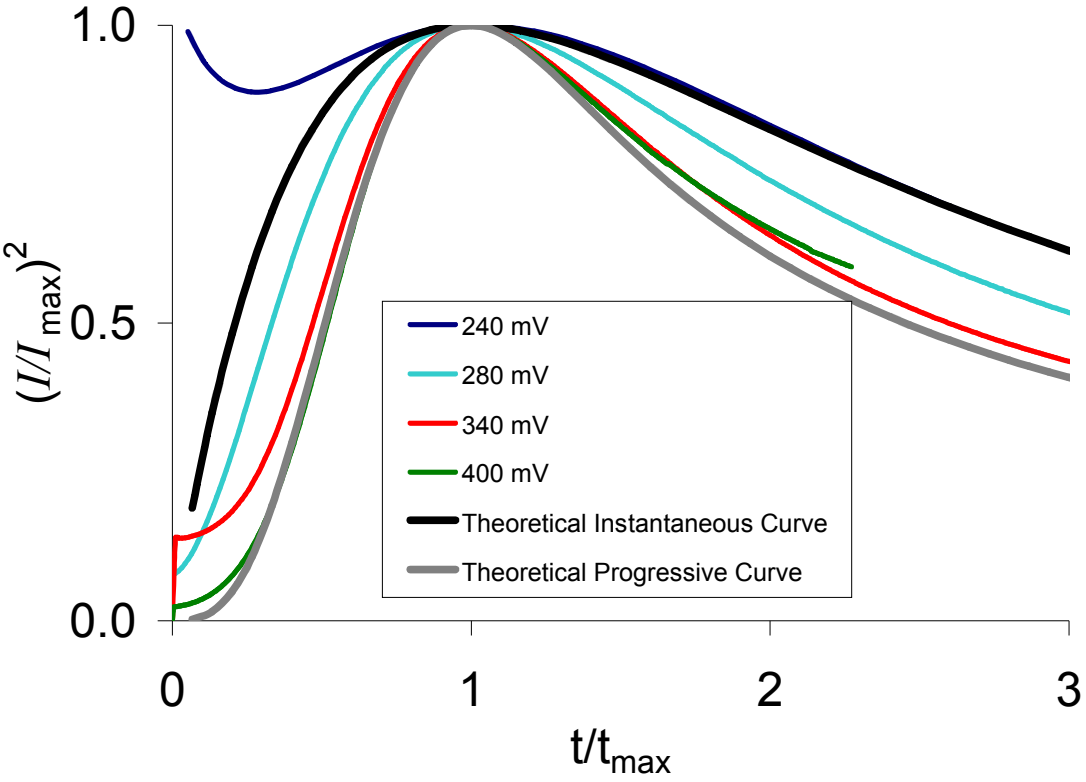

Figure 3.7 Dimensionless current transients for the potentiostatic deposition of gold nanoparticles from 0.001M $HAuCl_4$ in 0.1M KCl at the indicated potentials.

dimensionless I-t plots for electrodeposition from a 0.001 M $HAuCl_4$ solution onto bare FDTO as well as the theoretical curves for instantaneous and progressive nucleation. This figure shows that the nucleation mode shifted from progressive nucleation at relatively more positive applied potentials, 400 and 340 mV, to instantaneous nucleation at approximately 240 mV. These conclusions regarding the nucleation mode are supported by the SEM images in Figure 3.8. When a potential of 300 mV and 400 mV was applied the dimensionless plot indicated that progressive nucleation had occurred. The SEM images of surfaces produced by applying these potentials showed nanoparticles with a large degree of variation in nanoparticle diameter. This is consistent with progressive nucleation. When the applied potential was 240 mV the dimensionless plot indicated that instantaneous nucleation had occurred. Under these conditions the nanoparticles in the SEM images appeared much more uniform in diameter. This is consistent with nanoparticles that have nucleated instantaneously, and have therefore all been growing for the same timescale.

There was a large initial current evident in the transient at 240 mV, this current takes a shape typical of charging current, the duration of this charging current was approximately 1 s, significantly longer than the duration of the charging current estimated in Section 3.2 of up to 2.5 ms. The source of this unexpectedly large charging current was unclear, however even this relatively large charging current did not affect interpretation of the dimensionless current transient in Figure 3.7.

The observation that nucleation mode could be controlled is significant because instantaneous nucleation is important in order to maximise particle size monodispersity. However, it is also desirable to grow the particles at a small overpotential in order to control diffusion zone coupling. Therefore, finding a balance between a large nucleation overpotential and a small overpotential for particle growth is key.

The different nucleation and growth modes significantly affected the size and density of gold nanoparticles. This is demonstrated by Figure 3.8 where

SEM images of 3 samples are presented that were deposited under similar conditions at different potentials. In these SEM images the gold nanoparticles are seen as white dots on the dark FDTO surface. At more negative potentials (greater overpotential) the density of nanoparticles was much greater and as a result of a similar quantity of gold depositing at a much greater number of nuclei the nanoparticles are significantly smaller. The density of growth centres is related to the nucleation mode, instantaneous nucleation resulted in a very high density of nanoparticles, and progressive nucleation resulted in lower densities at more positive potentials. However, the surfaces produced in this way still had relatively low nanoparticle densities and even the most dense surfaces had densities of under 1 particle per μm^2. Some of the potential sensing applications of these surfaces include surface enhanced Raman, fluorescence and electrochemical sensors. In order to improve sensitivity from such a surface it will be important that the nanoparticle density is greater than that seen in Figure 3.8. This is necessary to increase the metal surface area, for maximum analyte loading. In addition, to facilitate electromagnetic interaction of the surface plasmon fields surrounding the nanoparticles, the interparticle separation is required to be less than or equal to the twice the mean nanoparticle size [44]. Therefore, it was necessary to investigate methods of increasing the nanoparticle density.

The effect of performing the electrodeposition at even more negative potentials was investigated as a method of increasing the nucleation density. In theory, having identified the potential at which instantaneous nucleation occurs, applying a more negative potential should not result in a greater nucleation density as all of the possible nucleation sites should be populated at any potential at which instantaneous nucleation occurs. Application of a single pulse of potentials between -200 mV and -500 mV did however result in an increase in nanoparticle density. This result highlights a significant flaw in the use of dimensionless plots to characterise the nucleation mode. The validity of the dimensionless plot has been questioned in the literature [36, 37, 45, 46] and these results demonstrate experimentally that when

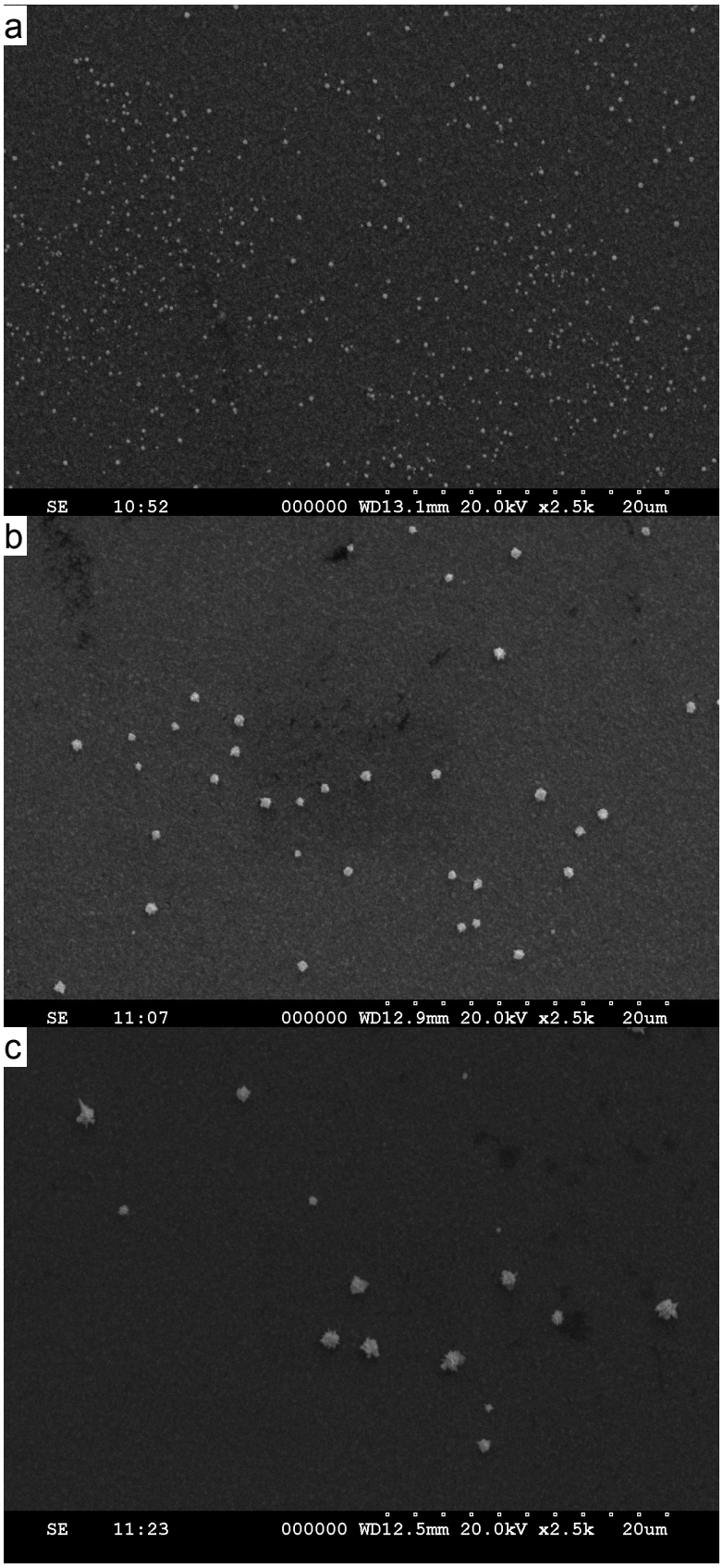

Figure 3.8 SEM Images of gold nanoparticles electrodeposited on FDTO from 0.001M $HAuCl_4$ in 0.1M KCl by a single pulse, until a charge of 4.3 $mCcm^{-2}$ had been passed, at (a) 240 mV, (b) 300 mV, (c) 400 mV.

instantaneous nucleation is indicated by the dimensionless plot that the maximum density of nanoparticles has not necessarily been achieved.

The results of increasing the overpotential (i.e. applying a more negative potential) are presented in the SEM images in Figure 3.9. With greater overpotentials there was a trend towards greater nanoparticle densities. In Figure 3.9 the same charge (4.3 mC cm^{-2}) was passed during each deposition, which explains why the nanoparticle size became smaller at greater overpotentials. Effectively the same number of gold atoms were divided between a greater number of nucleation sites. It is also significant that in Figure 3.9c the size distribution of nanoparticles is very large (RSD = 69%). This result indicates that at potentials negative of -200 mV diffusion zone coupling becomes highly significant for this system. By extending the potential to even more negative values the problems of uncontrolled particle size and size distribution made it impractical to use such a method for the production of suitable sensing platforms. Therefore, a method for increasing particle density, while maintaining control over nanoparticle size and size distribution was required.

In Figure 3.9c the FDTO layer is evident as a light grey coating under the white nanoparticles. The FDTO is most evident in this image due to contrast effects, and not because there was any alteration to the FDTO surface resulting from the deposition process. Also in Figure 3.9c there are some darker patches on the FDTO surface which resulted from charging in those areas following focusing at those points at higher magnification for a period of time. Charging is a term used to describe the build up of charge on a surface during SEM imaging and occurs particularly in poorly conducting surfaces, and when high magnification is used. The dark patches in Figure 3.9c do not indicate that there was any damage to the FDTO surface before imaging, this conclusion is supported by the presence of nanoparticles within the charged areas, indicating that the FDTO layer was intact during the electrodeposition process.

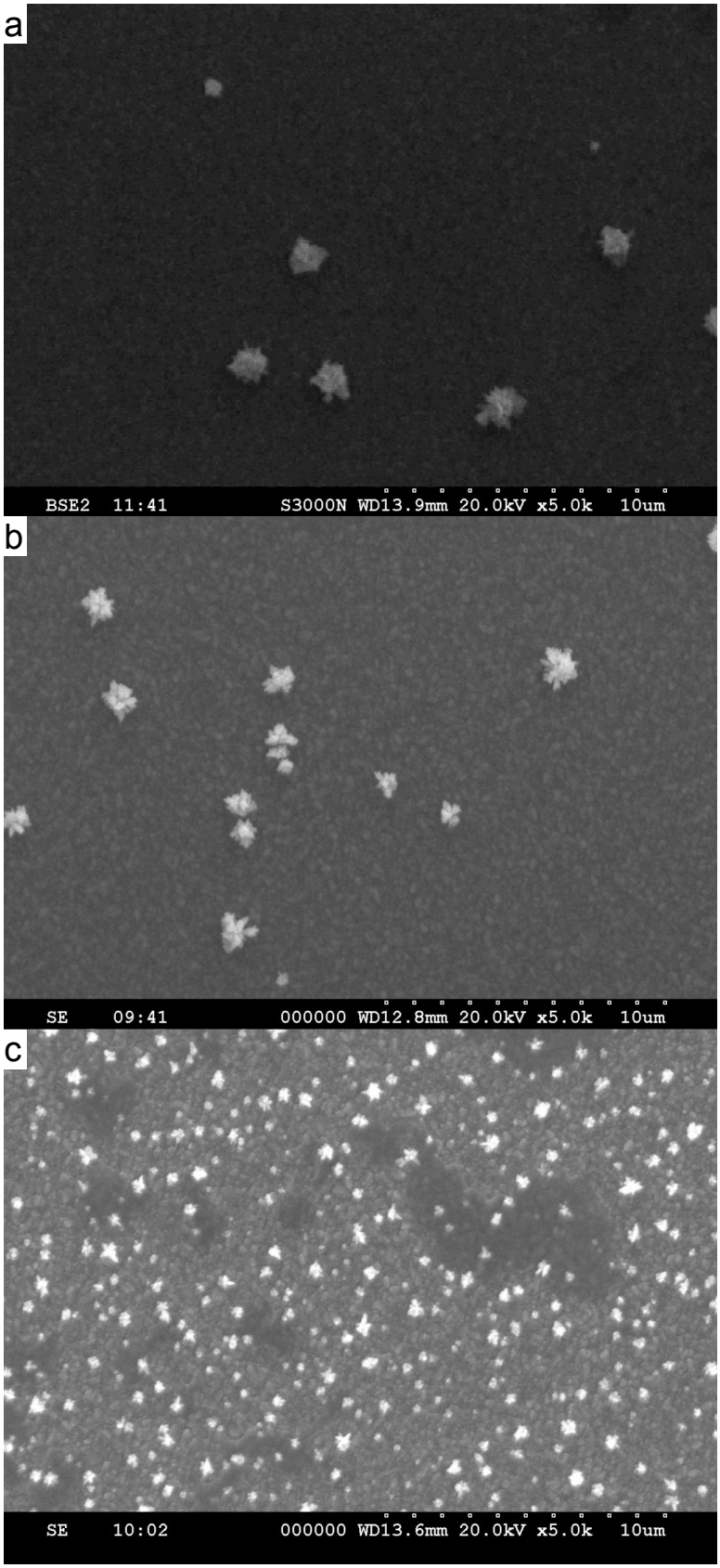

Figure 3.9 SEM Images of gold nanoparticles electrodeposited on FDTO from 0.001M $HAuCl_4$ in 0.1M KCl by a single pulse, until a charge of 4.3 $mCcm^{-2}$ had been passed, at (a) 400 mV, (b) -50 mV, (c) -300 mV.

3.5 Control of Nucleation and Growth by Chemical Modification of the Electrode

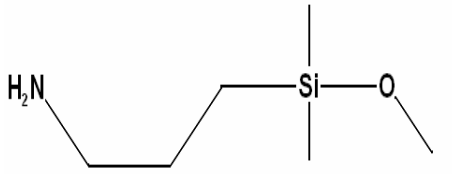

The single pulse electrodeposition method was successful at producing arrays of nanoparticles with controlled size, and with limited control over nucleation density. However, for the kind of applications envisaged under this project a greater deal of control over the density and size distribution of nanoparticles was required. In addition to greater control over the nanoparticle density, the ability to increase the density significantly, such that the nanoparticles in the array interact electromagnetically, is desirable. One method considered to improve the particle density without prompting diffusion zone coupling was to modify the FDTO surface with a self-assembled monolayer (SAM). A monolayer of a simple amine terminated group, 3-aminopropyldimethylmethoxysilane (ADMMS, Scheme 1), may provide a more uniform surface on which electrodeposition can occur. Moreover, it alters the surface energy and kinetics of deposition at the surface making instantaneous nucleation possible at lower overpotentials thereby reducing diffusion zone coupling.

Figure 3.10 shows the effect on the dimensionless plot of modifying the FDTO surface with an ADMMS monolayer. In the presence of this monolayer the dimensionless plot indicated that the nucleation and growth mode shifted from progressive nucleation to instantaneous nucleation at a potential of 390 mV. There are two possible explanations for the shift from progressive to instantaneous nucleation in the presence of the ADMMS monolayer. It is possible that the ADMMS monolayer, as a surface, has a higher energy than FDTO and therefore required less energy to initiate nucleation than the FDTO surface, it has been shown before that nucleation is more facile on higher energy surfaces [47]. This hypothesis is supported by Figure 3.4 (section 3.3.2) which indicates that in the first CV the peak

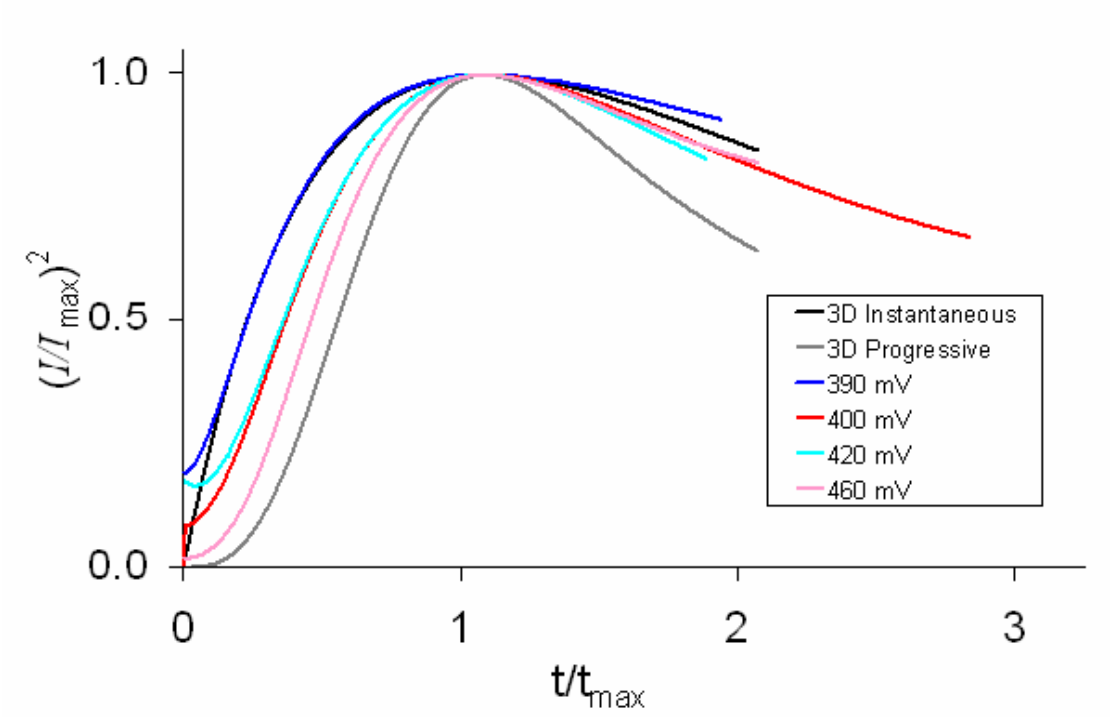

Figure 3.10 Dimensionless plots for deposition from 0.001M $HAuCl_4$ in 0.1M KCl on ADMMS modified FDTO at the indicated deposition potential.

current occurred at a more positive potential for nucleation of gold onto ADMMS than gold onto FDTO (Figure 3.3).

The second possible cause of the shift from progressive to instantaneous nucleation is a change in the concentration of gold ions at the ADMMS surface compared to at the unmodified surface. The ADMMS molecule used for modification of the FDTO surface is bound to the surface via the methoxy-silane group, forming a Si-O-Sn bond, leaving the amine head-group exposed. As the gold salt used is an acid, the solution has a low pH (~pH 3). This low pH causes the amine group to become protonated, as ADMMS has a Pk_a of approximately 9 [48], and electrostatic association of the negatively charged $AuCl_4^-$ ions at the electrode surface may occur resulting in the interfacial gold concentration being higher than that found in the bulk solution. If this is the case the increased concentration of $AuCl_4^-$ ions at the surface could be responsible for the shift from progressive towards instantaneous nucleation at a single potential, as was seen in Figure 3.10 when the potential was changed. To investigate this possibility, a single pulse experiment on bare FDTO was performed with different gold salt concentrations. The concentration range from 0.001 to 0.02 M $HAuCl_4$ was investigated (concentrations greater than 0.02 M did not result in diffusion controlled growth and could not therefore be analysed by dimensionless transients).

Figure 3.11 shows the dimensionless form of the deposition transients for the gold salt concentration dependent experiments. These transients indicate that at higher bulk salt concentrations the response shifts from progressive to instantaneous nucleation thereby confirming the possibility that preconcentration of $AuCl_4^-$ ions at the monolayer modified electrode could switch the nucleation mode. The estimated density of ADMMS molecules on the FDTO surface based on calculations using the simulation software Gaussian is approximately 3.4×10^{14} molecules per cm^2. This figure is similar to the values estimated for similar molecules on various surfaces [49, 50]. If a significant fraction of these sites were associated with an $AuCl_4^-$ ion it would result in up to a 20 fold increase in the concentration of $AuCl_4^-$ ions at the FDTO surface compared to the bulk which the results of Figure 3.11

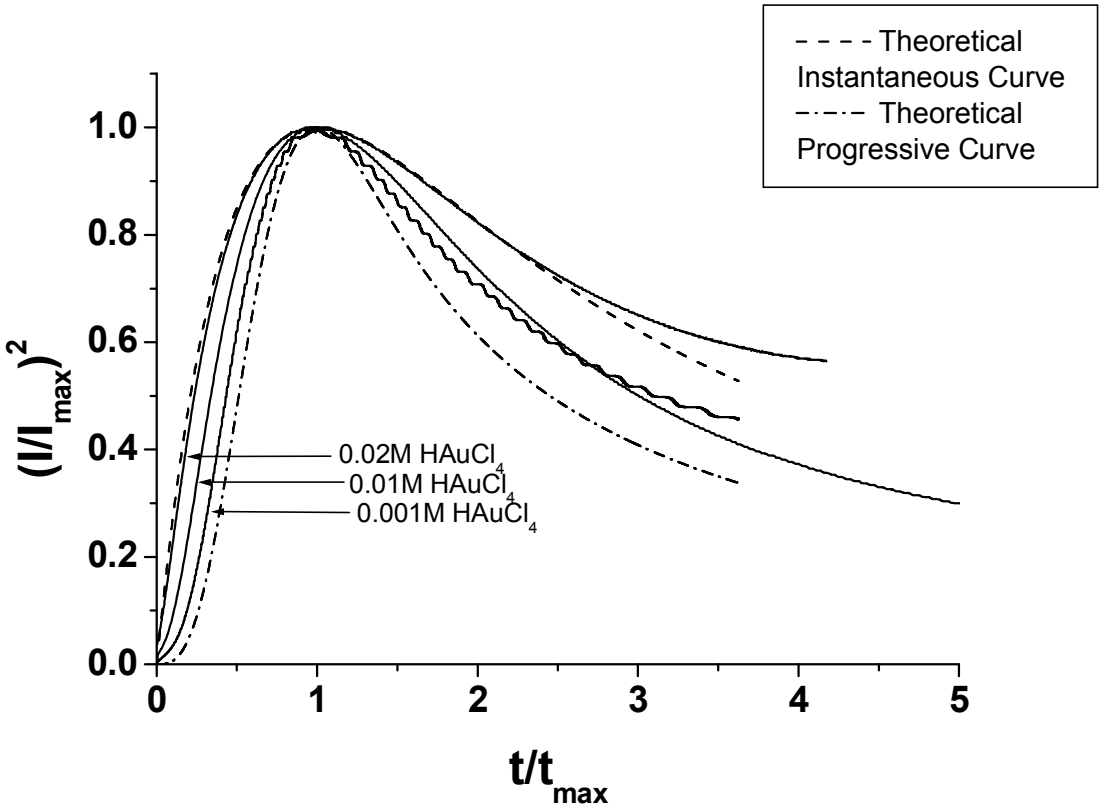

Figure 3.11 Dimensionless current transients of varying bulk gold salt concentrations in the electrolyte for the deposition of gold onto FDTO by chronoamperometry at a potential of 400mV.

confirm is sufficient to induce instantaneous nucleation. It is likely that the two mechanisms outlined above working in combination were responsible for the shift from progressive to instantaneous nucleation at the applied potential of 400 mV in the presence of the ADMMS monolayer.

The ability to control the nucleation mode by use of a monolayer is of itself of scientific interest to the kinetics of nucleation and growth in gold electrodeposition. However in the context of this project it is important that the use of an ADMMS monolayer can help achieve better control over the nucleation density and particle size distribution of the electrodeposition. The dimensionless plots indicate that instantaneous nucleation has occurred at a potential of 390 mV. However, analysis of the SEM images in Figure 3.12 indicates that the nucleation density is very low. The nucleation density at 390 mV was not significantly greater than at 420 mV so the particle size was unsurprisingly also similar. At 460 mV the density was lower and the particle size greater, which was not unexpected for such a low overpotential. Overall the nucleation density was significantly lower than the maximum seen using similar conditions on an unmodified FDTO surface. This indicates that either the ADMMS modified FDTO surface does not provide as many sites for nucleation such as steps, defects and dislocations, due perhaps to the smoother nature of the surface, or the dimensionless plots are not reliable for the determination of the nucleation mode under these conditions. Based on the apparent unreliability of the dimensionless plots it was decided for future investigations to characterise the nucleation mode based on analysis of SEM images alone.

The magnitude of the current passed during the electrodeposition of gold nanoparticles onto the ADMMS modified surface was larger than at the unmodified surface, for example, when a pulse of 300 mV was applied the peak current was approximately 400 μA at the modified surface compared to approximately 200 μA at the unmodified surface. This suggests that a greater amount of gold was deposited onto the ADMMS surface than the bare FDTO. It was possible that as well as the large nanoparticles evident in Figure 3.12 that there was also a blanket of much smaller nanoparticles, of

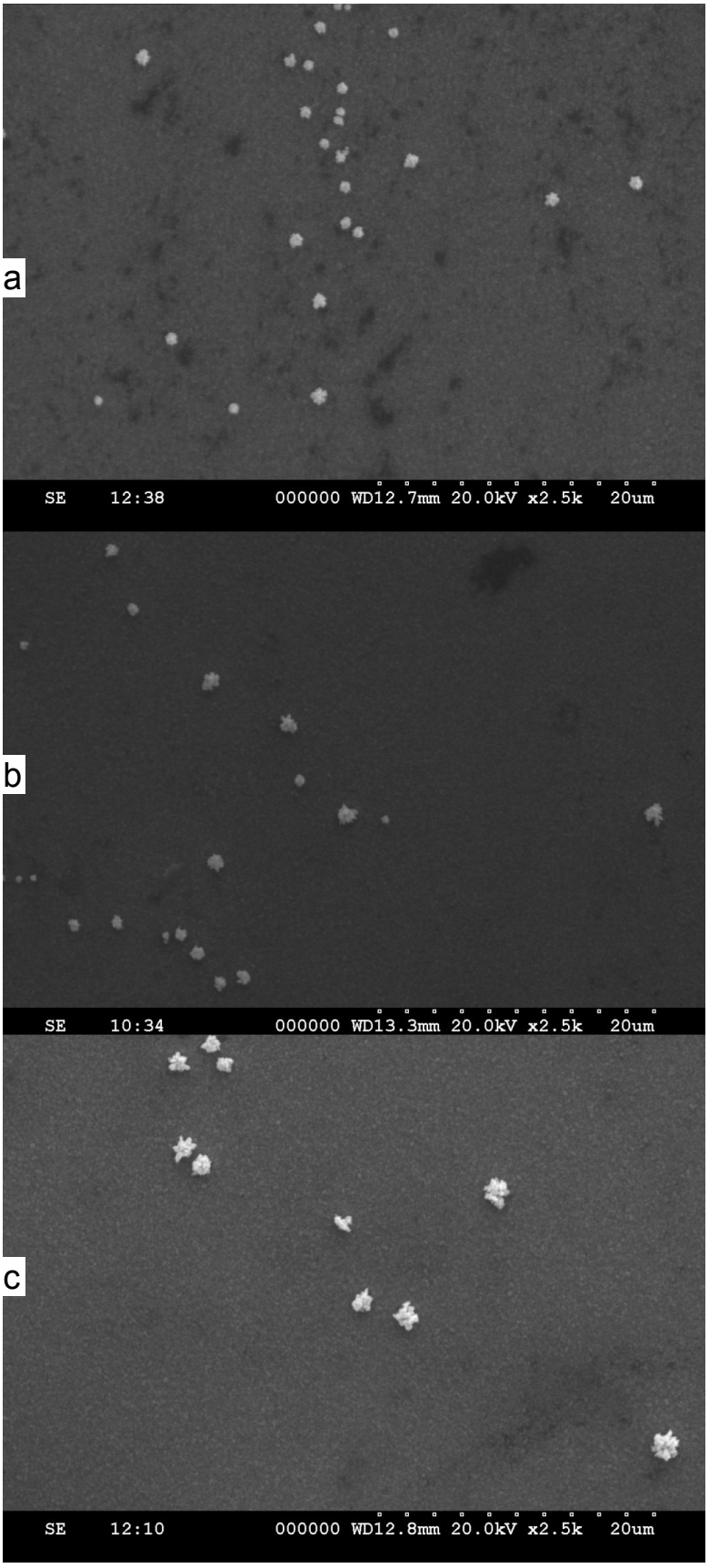

Figure 3.12 SEM Images of gold nanoparticles electrodeposited on ADMMS modified FDTO from 0.001M $HAuCl_4$ in 0.1M KCl by a single pulse, until a charge of 4.3 $mCcm^{-2}$ had been passed, at (a) 390 mV, (b) 420 mV, (c) 460 mV.

the order of 10 – 20 nm in diameter that were too small to be resolved by the scanning electron microscope. Such a bimodal distribution of nanoparticles has been reported previously [51]. A bimodal distribution of nanoparticles would explain the enhanced kinetic response of the ADMMS modified surface compared to the FDTO surface, however if it is the case that the surface is also populated with high surface density gold nanoparticles in the 10 – 20 nm size range then these nanoparticles would be too small for the purposes under investigation in this project.

The inability to produce suitable nanoparticle surfaces of high densities means that ADMMS modified FDTO is not a suitable platform for the electrodeposition of gold nanoparticles for the sensor applications of this project.

3.6 Control of Nucleation and Growth by use of Double-Pulse Method

In order to achieve instantaneous nucleation without having a large driving force for growth, it is necessary to separate the nucleation and growth steps. For example, a nucleation pulse with a sufficiently large overpotential to achieve instantaneous nucleation is first applied to effectively seed the surface with nuclei. Then, the potential can be changed so that growth proceeds at the desired rate. This double-pulse method, as a method of controlling particle size distribution, was first proposed by Penner's group [31, 32, 52]. Using this method the nucleation densities achieved at high overpotentials in Section 3.4 may be repeated whilst minimising diffusion zone coupling and achieving better control over the nanoparticle size.

The two pulse method is compared to the single pulse method in Figure 3.13. In this example gold nanoparticles are deposited by (a) a single 400 mV pulse and (b) a nucleation pulse of -1200 mV for 100 ms followed by a growth pulse of 600 mV. The experimental conditions are otherwise kept constant; the total charge passed was 4.3 mC cm^{-2} from an electrolyte of 1 mM $HAuCl_4$ and 0.1 M KCl. From visual inspection of the SEM images it is clear that the two pulse method results in smaller nanoparticles at a much greater density compared to the single pulse method. Software analysis of the images indicates that the density of nanoparticles in image b is over 450 times greater than image a. The size distribution of the nanoparticles is similar, 27% and 29% for a and b, respectively. The significantly lower density of nanoparticles in image a meant that diffusion zones were also further apart and diffusion zone coupling would have been expected to be less significant. The fact that the particle size distribution has not increased appreciably at the higher density seen in image b is therefore significant. Compared to the size distribution of 69% of a sample grown with a single pulse of -300 mV under the same conditions (Figure 3.9) there is clear evidence that the two pulse method has been successful at reducing

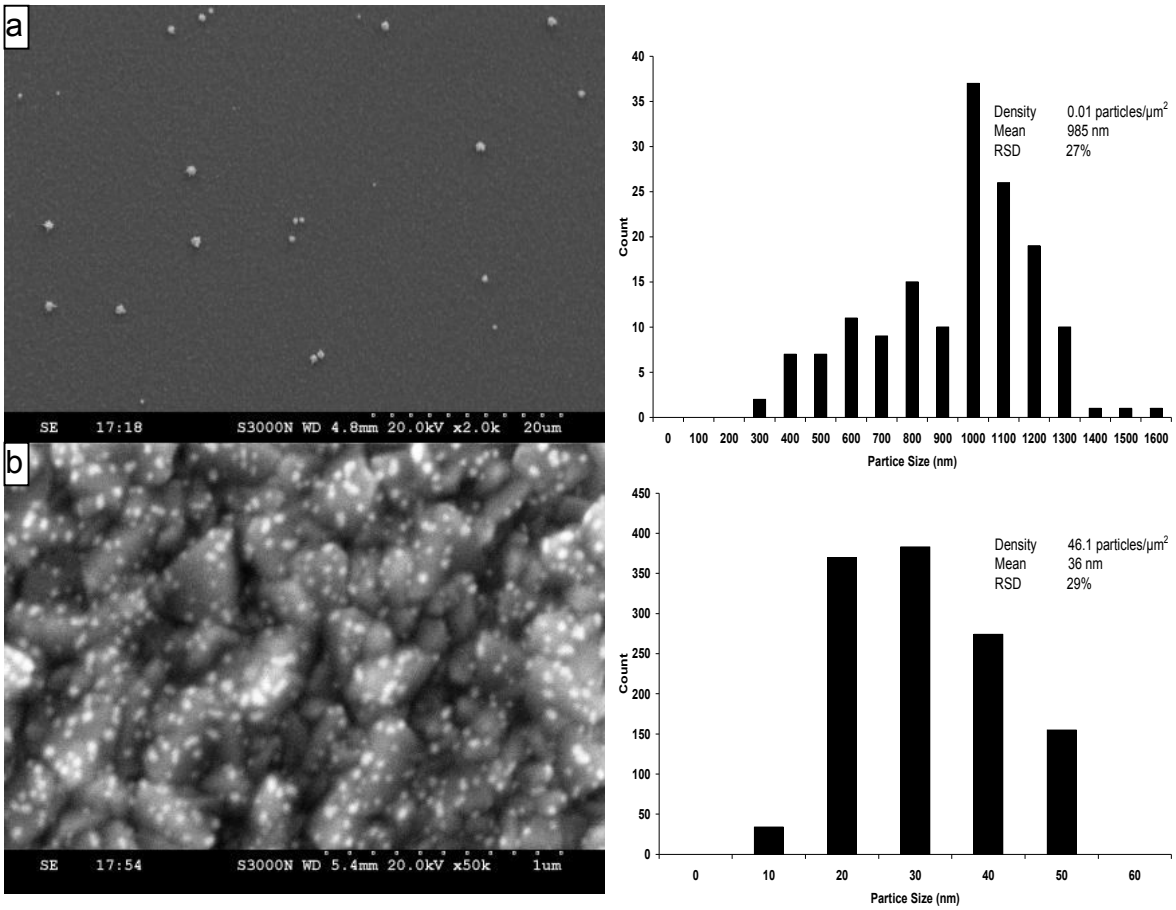

Figure 3.13 SEM images and particle diameter distribution histograms for gold nanoparticles electrodeposited from 0.001 M $HAuCl_4$ in 0.1M KCl until a charge of 4.3 mC cm^{-2} had been passed at (a) 400mV (mag = 2k) and (b) -1200mV for 10 ms then 600 mV (mag = 50k).

diffusion zone coupling while at the same time significantly increasing the particle density. On a smoother surface such as a single crystal gold surface or highly oriented pyrolytic graphite (HOPG) a lower size distribution would be expected in the nanoparticle size. This effect has been demonstrated by Penner et al. [31].

To optimise the two-pulse method for the production of high density, low size, monodisperse nanoparticles conditions such as the length and potential of the nucleation pulse and the potential and charge passed of the growth pulse were varied. Figure 3.14 illustrates typical SEM images of the nanoparticle arrays produced. These SEM images show the relatively rough underlying FDTO surface with the gold nanoparticles appearing as small bright spots. The most significant results of these experiments are presented in Table 3.2. It was found that the greatest nucleation densities were achieved at nucleation potentials (E_{nu}) negative of -1000 mV with the nucleation density lower at potentials negative of -1600 mV presumably due to gas evolution. The length of the nucleation pulse (t_{nu}) also affected the nucleation density with greater densities at longer nucleation times up to 100 ms. The growth potential (E_{gr}) affected the size and monodispersity of the resultant particles with best results being obtained at 600mV. Unsurprisingly, the greater the charge passed (Q_{gr}) the greater the resultant mean particle diameter. Figure 3.14 illustrates the general principle that nucleation density increased as nucleation overpotential was increased, and the nanoparticle size increased as the growth overpotential was increased (and with it the total charge passed).

Figure 3.15 illustrates some of the principles mentioned above; the greatest nanoparticle densities were produced by using the most negative nucleation pulses, and the charge passed had a direct relationship with the mean nanoparticle size.

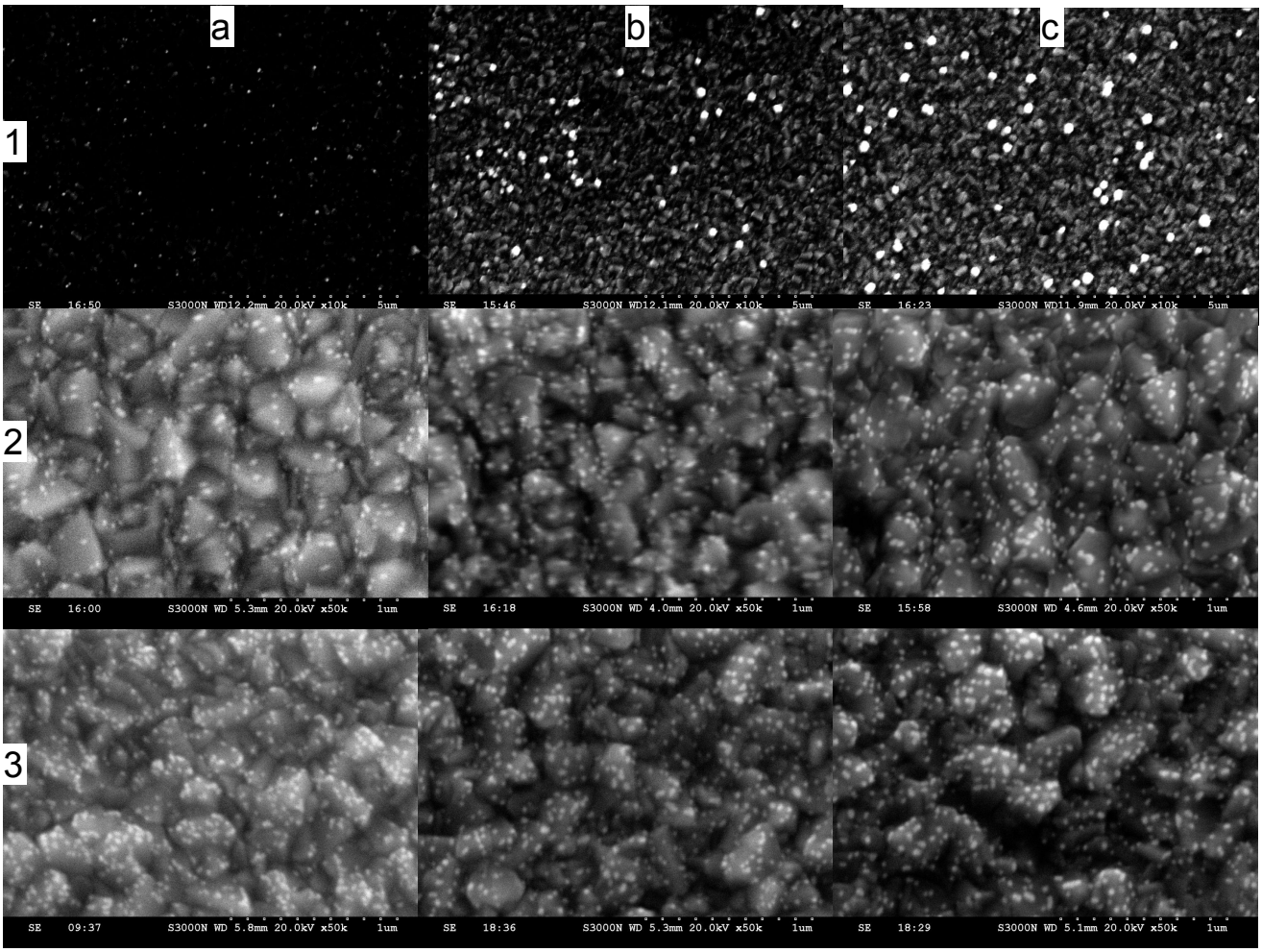

Figure 3.14 SEM images of gold nanoparticles electrodeposited from 0.001 M $HAuCl_4$ in 0.1M KCl using a 100 ms nucleation pulse of (1) -400 mV, (2) -800 mV, (3) -1200 mV, and a 30 s growth pulse of (a) 700 mV, (b) 600 mV, (c) 400 mV.

Table 3.2 Effect of Nucleation and Growth Potentials and Times on the Mean Diameter and Density of Gold Nanoparticles Electrodeposited on Fluorine-Doped Tin Oxide.

E_{nu} (mV)	t_{nu} (ms)	E_{gr} (mV)	Q_{gr} (10^{-3} C cm^{-2})	Mean Diameter (nm)[a]	Coverage (particles μm^{-2})[a]	RSD (%)[a]
-	-	400	4.3	985	0.01	27
-700	100	400	8.6	66	42.7	40
-1200	10	600	4.3	36	46.1	29
-1400	10	600	4.3	43	41.8	32
-1600	10	600	4.3	36	45.8	30
-1800	10	600	4.3	43	35.1	34
-2000	10	600	4.3	45	25.7	33
-1200	100	600	4.3	39	50.9	33
-1200	5	600	4.3	39	30.7	34
-1200	10	600	2.2	32	35.5	25
-1200	10	400	4.3	39	62.5	32

[a] Calculated by analysis of six SEM images captured at random locations on the FDTO surface.

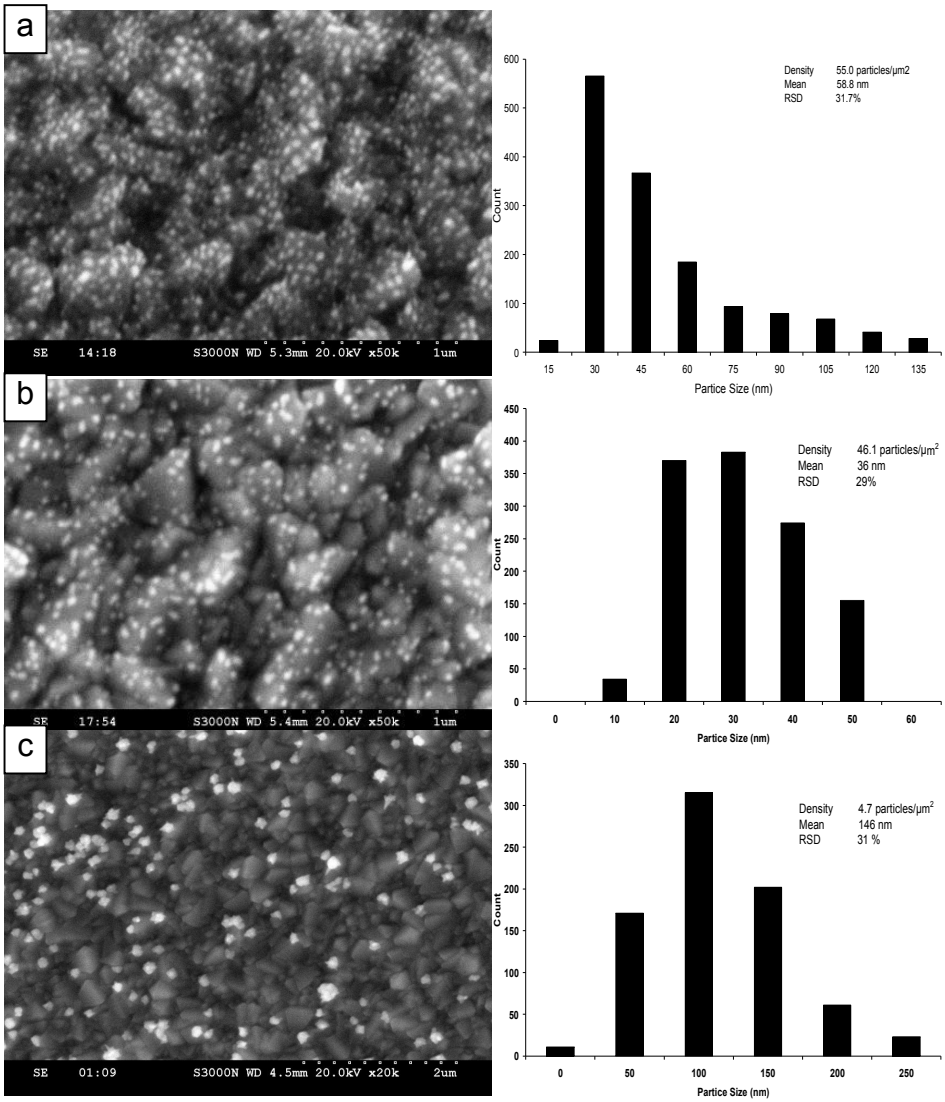

Figure 3.15 SEM images and particle size distribution histograms for gold nanoparticles electrodeposited onto FDTO from 0.001M $HAuCl_4$ and 0.1M KCl using a two pulse method. Nucleation pulse was for a duration of 100ms at a potential of (a) -2.000V (b) -1.200 V (c) -0.450 V. The growth pulse was 0.400 V until a charge of (a) 8.0 mC cm^{-2} (b) 6.0 mC cm^{-2} (c) 10.0 mC cm^{-2} had been passed.

The optimised method for the production of very high density gold nanoparticles on FDTO with controlled size distribution and controllable nanoparticle size was selected as a two pulse electrodeposition from 0.001 M $HAuCl_4$ + 0.1M KCl, with a nucleation pulse of -1200mV for 100 ms, and a growth pulse of 600 mV until a charge appropriate to the size of nanoparticle desired had been passed. Moreover, by selecting the nucleation potential and the charge passed at the working electrode it was possible to control the nanoparticle density and nanoparticle size, so using this method it is possible to tune the characteristics of the nanoparticulate surface to suit the needs of the application as desired.

3.7 Production of Electrodeposited Silver Nanoparticulate Surfaces

The electrodeposition method for the production of gold nanoparticles can be applied to other metal salts for the production of nanoparticles of other metals such as silver, copper and nickel. Minor changes to the method are required to compensate for different reduction potentials of the metal salt in question, and changes to the electrolyte bath are also required to ensure the supporting electrolyte does not interfere with the deposition process. Silver nanoparticles have been employed for many of the same applications as gold nanoparticles of interest to this project. In fact silver nanoparticles are reported to yield stronger enhancements, particularly for SERS, than gold nanoparticles under similar conditions [53, 54] therefore the method for electrodeposition of gold nanoparticles on FDTO was applied to silver nanoparticles to investigate the degree of control that could be achieved over the size, density and size monodispersity of silver nanoparticles. The same two pulse method was applied to the electrodeposition of silver nanoparticles from 0.001 M $AgNO_3$, 0.1 M HNO_3 and 0.015 M citric acid (citric acid is reported to promote greater silver nanoparticle density and deposit homogeneity [55]) and the experimental variables were optimized in the same way as they were for gold electrodeposition.

As with gold electrodeposition it was found that for silver electrodeposition by the two pulse method a potential significantly negative of the reduction potential of the silver salt (0.6 V) was required for dense nucleation. Various potentials were investigated for the nucleation potential; the greatest nucleation density was achieved with a nucleation pulse of -1.600 V for a duration of 20 ms. The growth pulse was again required to be much closer to the reduction potential of the salt. The greatest control over particle size and particle size distribution was achieved with a growth pulse of 300 mV.

As described for the gold nanoparticles, the mean diameter depends on the amount of charge passed during the growth pulse. Despite optimizing the

conditions for silver nanoparticle electrodeposition it was not possible to produce silver nanoparticle surfaces of the same density and monodispersity as achieved for gold. The maximum density of silver nanoparticles on FDTO obtained was 6 particles per μm^2 (minimum density = 0.5 particles per μm^2). The distribution of nanoparticle size was RSD = ~40% (See Figure 3.16). In order for nanoparticles to electromagnetically interact, such that they affect the photonic properties of one another (e.g. SERS enhancement factor) the interparticle separation is reported to be required to be at most twice the mean particle diameter [44]. Therefore, for a system like this with such low particle densities, the nanoparticles cannot be considered to be electromagnetically interacting so enhancements observed in the spectroscopic behaviour can be considered to be coming from electromagnetically isolated nanoparticles rather than coupled nanoparticles. This opens up the possibility to demonstrate single nanoparticle SERS enhancements.

It was not possible to produce electromagnetically interacting nanoparticulate arrays using this method, only isolated silver nanoparticle surfaces. The gold electrodeposition method was capable of producing dense, electromagnetically interacting nanoparticle arrays as well as isolated gold nanoparticle surfaces. It was possible to control the density and size of the silver nanoparticles within the limits of maximum and minimum density outlined above in the same manner as could be achieved with the gold nanoparticle surfaces. A typical series of electrodeposited nanoparticles are presented in Figure 3.17, demonstrating increasing particle density with increasing nucleation overpotential, and increasing particle size with increasing charge passed.

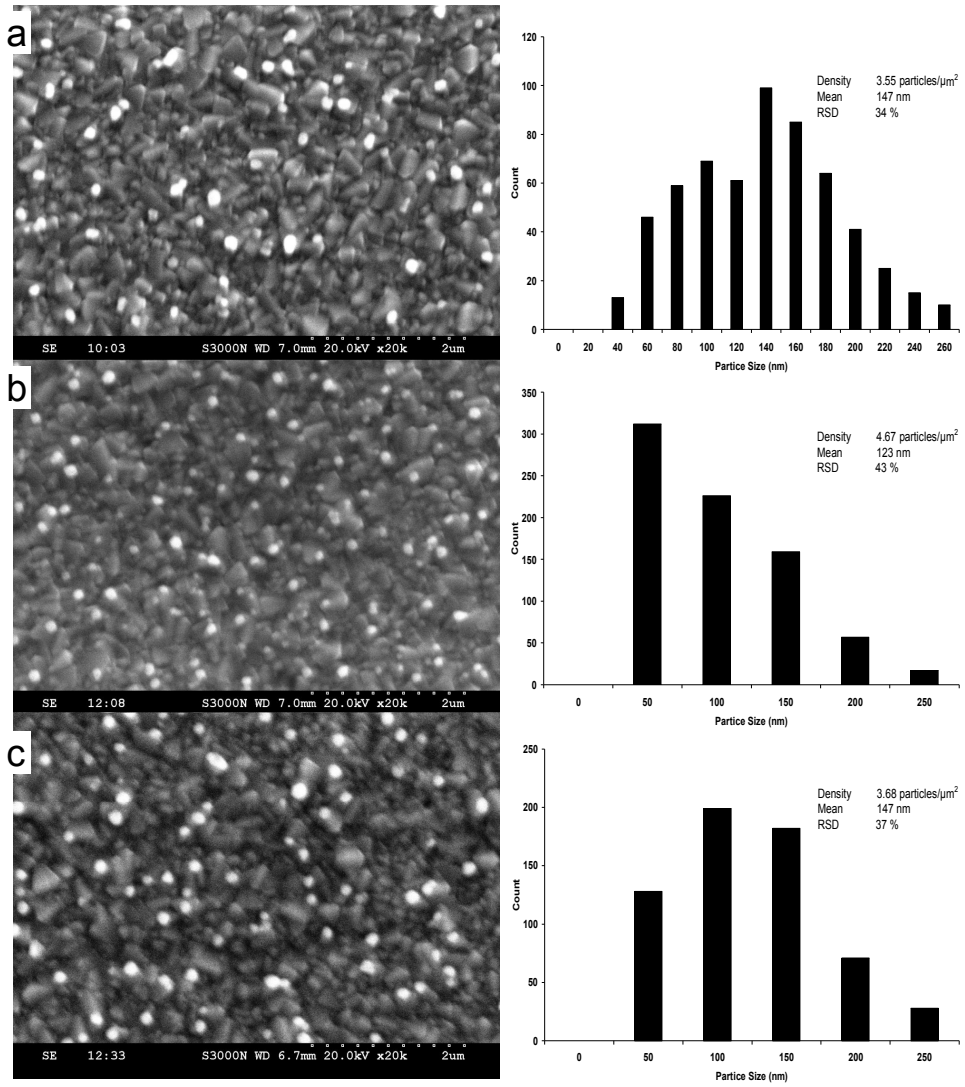

Figure 3.16 SEM images and particle size distribution histograms for silver nanoparticles electrodeposited onto FDTO from 0.001M $AgNO_3$, 0.015M citric acid and 0.1M HNO_3 using two pulse method. A 20 ms nucleation pulse was applied of potential (a) -1000 mV, (b) -1600 mV, (c) -1800 mV. The growth pulse was 300 mV until a charge of 4.3 mC cm^{-2} had been passed.

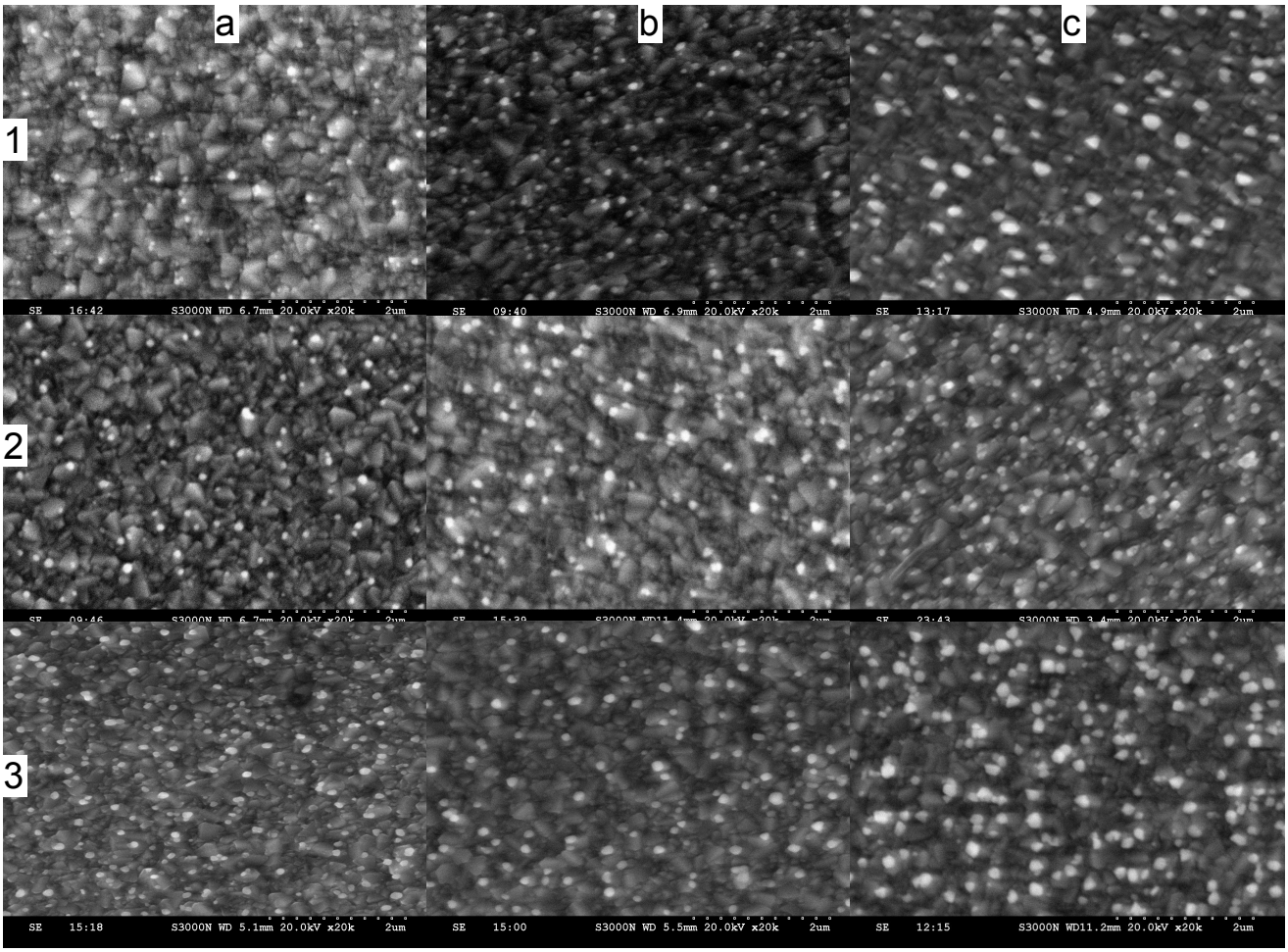

Figure 3.17 SEM images of silver nanoparticles electrodeposited from 0.001 M $AgNO_3$ in 0.1M KCl using a 20 ms nucleation pulse of (1) -1000 mV, (2) -1200 mV, (3) -1600 mV, and a 30 s growth pulse of (a) 600 mV, (b) 400 mV, (c) 300 mV.

3.8 Conclusions

The electrodeposition of precious metal nanoparticles, of gold, onto an electrically conducting, optically transparent fluorine-doped tin-oxide coated glass was investigated. The influence of changing experimental conditions such as electrolyte composition and applied potential were examined to determine the influence of these parameters on electrodeposition kinetics, and the properties of the resulting nanoparticles. It was found that by increasing the gold salt concentration, and by applying a more negative potential to the working electrode, the kinetics of electrodeposition could be influenced. Analysis of the kinetics of the deposition by use of dimensionless plots indicated that instantaneous nucleation could be achieved by controlling these parameters. However, SEM image analysis indicated that when the dimensionless plots indicated that instantaneous nucleation had occurred the maximum density of nanoparticles on the surface had not in fact been achieved, and the density of nanoparticles could be further increased at even more negative potentials.

Two methods to control the nucleation and growth modes of electrodeposition of gold nanoparticles on FDTO were investigated. Chemically modifying the FDTO electrode with a silane terminated alkane-thiol (ADMMS) influenced the current transient of the electrodepositions such that analysis of the kinetics of the deposition by use of dimensionless plots indicated that instantaneous nucleation could be achieved with application of a less negative potential, compared to electrodeposition onto unmodified FDTO. Achieving instantaneous nucleation without applying such a large overpotential would be advantageous as it would facilitate growth of nanoparticles at a slower rate, resulting in a reduction in diffusion zone coupling and therefore increasing particle size monodispersity. However, SEM image analysis indicated that even though the dimensionless plots indicated that instantaneous nucleation had occurred, the density of gold nanoparticles on the chemically modified surface was significantly less than the densities seen when a larger overpotential was applied to the unmodified FDTO surface.

Use of a double-pulse electrodeposition scheme, such that nucleation of nanoparticles on unmodified FDTO was achieved at a very high density, by a very short time-scale potential pulse of high overpotential, and growth then proceeded by a much longer duration, lower overpotential pulse was also investigated. Using this method it was possible to significantly increase the density of nanoparticles on the surface, compared to the other investigated methods. In addition, despite the increase in nanoparticle density on the surface, the particle size polydispersity did not change to a significant extent. This indicates that the double-pulse technique was successful in limiting the affects of diffusion zone coupling. The size and interparticle spacing of the nanoparticles could be controlled within certain limits by controlling the potential and duration of the nucleation and/or growth pulse. This technique was successfully used to electrodeposit silver nanoparticles on FDTO in the same way. Electromagnetically interacting gold nanoparticles of controlled size, as well as electromagnetically isolated gold and silver nanoparticles of controlled size could be produced using this method.

References

[1] Kamat, P. V., *Journal of Physical Chemistry B*, 2002. **106**(32): 7729-7744.

[2] Li, M., Schnablegger, H., and Mann, S., *Nature*, 1999. **402**(6760): 393-395.

[3] Katz, E. and Willner, I., *Angewandte Chemie-International Edition*, 2004. **43**(45): 6042-6108.

[4] Rosi, N. L. and Mirkin, C. A., *Chemical Reviews*, 2005. **105**(4): 1547-1562.

[5] Babu, P. K., Chung, J. H., Oldfield, E., and Wieckowski, A., *Electrochim. Acta*, 2008. **53**(23): 6672-6679.

[6] Selvaraju, T., Das, J., Jo, K., Kwon, K., Huh, C. H., Kim, T. K., and Yang, H., *Langmuir*, 2008. **24**(17): 9883-9888.

[7] Link, S. and El-Sayed, M. A., *Journal of Physical Chemistry B*, 1999. **103**(40): 8410-8426.

[8] Kelly, K. L., Coronado, E., Zhao, L. L., and Schatz, G. C., *Journal of Physical Chemistry B*, 2003. **107**(3): 668-677.

[9] Moskovits, M., *J. Raman Spectrosc.*, 2005. **36**(6-7): 485-496.

[10] Link, S. and El-Sayed, M. A., *Int. Rev. Phys. Chem.*, 2000. **19**(3): 409-453.

[11] Drummond, T. G., Hill, M. G., and Barton, J. K., *Nat. Biotechnol.*, 2003. **21**(10): 1192-1199.

[12] Bell, A. T., *Science*, 2003. **299**(5613): 1688-1691.

[13] Dokoutchaev, A., James, J. T., Koene, S. C., Pathak, S., Prakash, G. K. S., and Thompson, M. E., *Chem. Mat.*, 1999. **11**(9): 2389-2399.

[14] Brust, M., Walker, M., Bethell, D., Schiffrin, D. J., and Whyman, R., *Journal of the Chemical Society-Chemical Communications*, 1994(7): 801-802.

[15] Jana, N. R., Gearheart, L., and Murphy, C. J., *Chemical Communications*, 2001(7): 617-618.

[16] Hirasawa, M., Shirakawa, H., Hamamura, H., Egashira, Y., and Komiyama, H., *Journal of Applied Physics*, 1997. **82**(3): 1404-1407.

[17] Birtcher, R. C., Donnelly, S. E., and Schlutig, S., *Physical Review Letters*, 2000. **85**(23): 4968-4971.

[18] Kaatz, F. H., Chow, G. M., and Edelstein, A. S., *Journal of Materials Research*, 1993. **8**(5): 995-1000.

[19] Fukushima, M., Yanagi, H., Hayashi, S., Suganuma, N., and Taniguchi, Y., *Thin Solid Films*, 2003. **438**: 39-43.

[20] Bertino, M. F., Gadipalli, R. R., Martin, L. A., Story, J. G., Heckman, B., Guha, S., and Leventis, N., *Journal of Sol-Gel Science and Technology*, 2006. **39**(3): 299-306.

[21] Schlesinger, M. and Paunovic, M., *Modern Electroplating*. 4 ed. 2000, USA: Wiley.

[22] Xu, H. X., Aizpurua, J., Kall, M., and Apell, P., *Phys. Rev. E*, 2000. **62**(3): 4318-4324.

[23] Maxwell, D. J., Emory, S. R., and Nie, S. M., *Chem. Mat.*, 2001. **13**(3): 1082-1088.

[24] Bard, A. and Faulkner, L., *Electrochemical Methods: Fundamentals and Applications*. 2 ed. 2001, USA: Wiley.
[25] El-Deab, M. S., Sotomura, T., and Ohsaka, T., *Journal of the Electrochemical Society*, 2005. **152**(1): C1-C6.
[26] El-Deab, M. S., Sotomura, T., and Ohsaka, T., *Electrochim. Acta*, 2006. **52**(4): 1792-1798.
[27] Plieth, W., Dietz, H., Anders, A., Sandmann, G., Meixner, A., Weber, M., and Kneppe, H., *Surf. Sci.*, 2005. **597**(1-3): 119-126.
[28] Kaifer, A. and Kaifer, M., *Supramolecular Electrochemistry*. 1999, Germany: Wiley-VCH.
[29] Mostany, J., Mozota, J., and Scharifker, B. R., *J. Electroanal. Chem.*, 1984. **177**(1-2): 25-37.
[30] Scharifker, B. and Hills, G., *Electrochim. Acta*, 1983. **28**(7): 879-889.
[31] Liu, H., Favier, F., Ng, K., Zach, M. P., and Penner, R. M., *Electrochim. Acta*, 2001. **47**(5): 671-677.
[32] Liu, H. and Penner, R. M., *Journal of Physical Chemistry B*, 2000. **104**(39): 9131-9139.
[33] Palomar-Pardave, M., Scharifker, B. R., Arce, E. M., and Romero-Romo, M., *Electrochim. Acta*, 2005. **50**(24): 4736-4745.
[34] Bulhoes, L. O. S. and Mascaro, L. H., *Journal of Solid State Electrochemistry*, 2004. **8**(4): 238-243.
[35] Sadale, S. B. and Patil, P. S., *Solid State Ion.*, 2004. **167**(3-4): 273-283.
[36] Hyde, M. E. and Compton, R. G., *J. Electroanal. Chem.*, 2003. **549**: 1-12.
[37] Heerman, L. and Tarallo, A., *Electrochem. Commun.*, 2000. **2**(2): 85-89.
[38] Dickson, E. W., Jacobs, M. H., and Pashley, D. W., *Philosophical Magazine*, 1965. **11**(111): 575-&.
[39] Paunovic, M. and Schlesinger, M., *Fundamentals of Electrochemical Deposition*. 1998, USA: Wiley.
[40] Kim, S. S., Na, S. I., Jo, J., Kim, D. Y., and Nah, Y. C., *Applied Physics Letters*, 2008. **93**(7).
[41] Esplandiu, M. J., Schneeweiss, M. A., and Kolb, D. M., *Physical Chemistry Chemical Physics*, 1999. **1**(20): 4847-4854.
[42] Brylev, O., Roue, L., and Belanger, D., *J. Electroanal. Chem.*, 2005. **581**(1): 22-30.
[43] Depestel, L. M. and Strubbe, K., *J. Electroanal. Chem.*, 2004. **572**(1): 195-201.
[44] Zhu, Z. H., Zhu, T., and Liu, Z. F., *Nanotechnology*, 2004. **15**(3): 357-364.
[45] Sluytersrehbach, M., Wijenberg, J., Bosco, E., and Sluyters, J. H., *J. Electroanal. Chem.*, 1987. **236**(1-2): 1-20.
[46] Mirkin, M. V. and Nilov, A. P., *J. Electroanal. Chem.*, 1990. **283**(1-2): 35-51.
[47] Harrison, J. A. and Thirsk, H. R., *The Fundamentals of Metal Deposition*. Vol. 5. 1971, New York: Marcel Dekker.
[48] Swedberg, S. A. L. A., CA), *Capillary Tube with Reduced Protein Interactions and Controllable Electroosmotic Flow*. 1990, Hewlett-Packard Company (Palo Alto, CA): United States.

[49] Love, J. C., Estroff, L. A., Kriebel, J. K., Nuzzo, R. G., and Whitesides, G. M., *Chemical Reviews*, 2005. **105**(4): 1103-1169.
[50] Wasserman, S. R., Tao, Y. T., and Whitesides, G. M., *Langmuir*, 1989. **5**(4): 1074-1087.
[51] Bhattacharya, S., Das, A. K., Banerjee, A., and Chakravorty, D., *Journal of Physical Chemistry B*, 2006. **110**(22): 10757-10761.
[52] Penner, R. M., *Journal of Physical Chemistry B*, 2002. **106**(13): 3339-3353.
[53] Baker, G. A. and Moore, D. S., *Analytical and Bioanalytical Chemistry*, 2005. **382**(8): 1751-1770.
[54] Clark, R. and Hester, R., *Spectroscopy of Surfaces*. Advances in Spectroscopy. 1988, West Sussex: Wiley.
[55] Zarkadas, G. M., Stergiou, A., and Papanastasiou, G., *Electrochim. Acta*, 2005. **50**(25-26): 5022-5031.

4 Photonic Properties of Surfaces Decorated with Metal Nanoparticles

4.1 Introduction

In chapter 3 a series of nanoparticle surfaces were prepared, on which, the size, size distribution and interparticle spacing could be controlled through careful selection of the electrodeposition potential conditions. These surfaces had the additional advantages of being inexpensive, facile and quick to produce, and were prepared on an optically transparent substrate. The purpose of that study was to enable the production of surfaces covered with gold or silver nanoparticles whose properties could be tuned in order to maximise their efficiency and efficacy as platforms for sensing and diagnostic applications such as surface plasmon resonance spectroscopy, surface enhanced Raman spectroscopy and surface enhanced fluorescence spectroscopy. In this chapter some of these surfaces will be utilised as platforms for these applications, and their effectiveness at producing an enhanced signal will be investigated, and compared to similar results from nanoparticle surfaces and suspensions reported in other work in the literature.

Size effects in metal nanoparticles in the 10-200 nm size range result in many useful effects. Most significant among these effects are a strong surface plasmon absorbance [1-4], increased surface area [5-8] and an enhanced electromagnetic field [9-13] which contributes to SERS [2, 13-17] and SEF [3, 9, 18, 19] enhancements. Mainstream commercialisation of devices based on these useful properties of nanoparticles and nanoparticle surfaces has been significantly hindered by a failure to produce nanoparticles that are robust, tuneable and yield high sensitivity and reproducible results. Much of the inability to successfully produce nanoparticle surfaces is linked to the difficulties in controlling the nanoscale features of the surfaces. In the previous chapter it was demonstrated that robust, tuneable nanoparticle surfaces can be produced by the

electrodeposition in a relatively reproducible manner. The issues of sensitivity and reproducibility of signal are considered for some of these surfaces as platforms for some of the sensing and diagnostic applications mentioned above. The ability to selectively tune the properties of the nanoparticle surfaces will allow the surfaces to be optimised for each application. It will also be possible, in some cases, to control the electromagnetic environment in which the nanoparticles lie, by controlling the interparticle spacing.

4.2 Electromagnetic Interaction between Nanoparticles

The degree of electronic interaction between nanoparticles plays an important role in the photonic properties of the nanoparticle array. As electromagnetic coupling of nanoparticles is a through space interaction the interparticle spacing plays a major role in the extent of the interaction. It has been reported that electromagnetic isolation of nanoparticle occurs when the interparticle distance is approximately twice the mean particle diameter or greater [20]. In order to distinguish between surfaces, prepared by electrodeposition, on which the nanoparticles do and do not interact, an estimate of the mean interparticle separation was made. An example of this calculation is shown below:

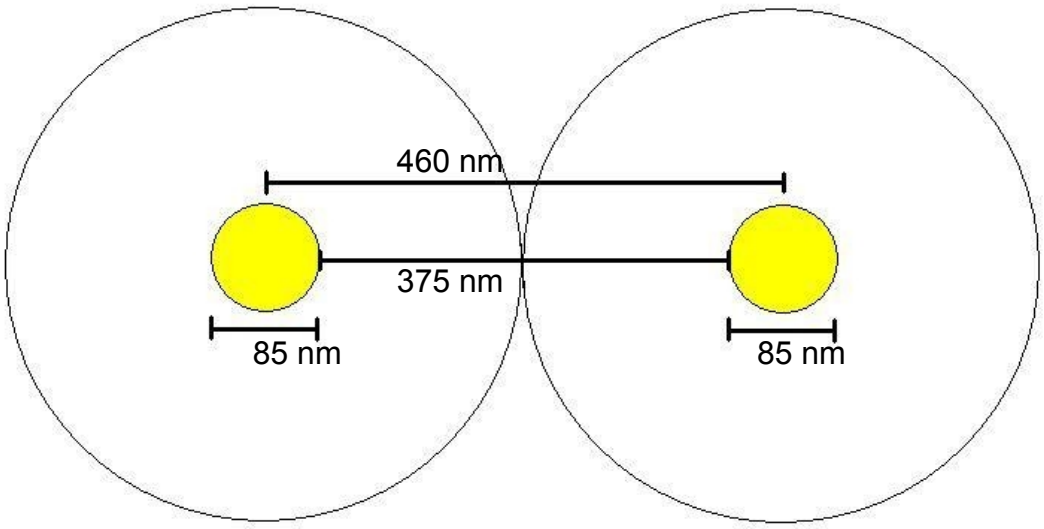

Scheme 1: Caption of typical nanoparticle dimensions demonstrating how interparticle spacing was calculated.

Example calculation; Interparticle Separation of Silver Nanoparticles
Sample r46, mean diameter (D) = 85.0 nm, particle coverage = 6.0 particles μm^{-2}. Distance between nanoparticle centres (x) = 2r
Where r is the radius of a circle around each nanoparticle representing its fraction of the total area on the surface.

In this example the area on the surface (A) surrounding each nanoparticle is:

A	=	1 μm^2/6.0 particles
A	=	0.1666 μm^2 per particle
A	=	πr^2
0.1666 $\mu m^2/\pi$	=	r^2
r^2	=	0.0531 μm^2
r	=	0.2303 µm
x	=	0.4607 µm

Interparticle separation (d) is the distance between the nanoparticle centres minus twice the mean radius of the nanoparticles (2r = D);

d	=	x – D
d	=	460.7 nm – 85.0 nm
d	=	375.7 nm

In this example, the interparticle separation d is greater than twice the mean nanoparticle diameter (D) (d/D = 4.4). Therefore, this sample consists of electromagnetically isolated silver nanoparticles. Interparticle separation estimations for a series of gold and silver nanoparticle arrays of varying size are presented in Table 4.1, again, the nanoparticles are considered to be electromagnetically isolated when $d/D \geq 2$. The silver samples presented in Table 4.1 are isolated by a significant margin. Even at the greatest nanoparticle coverage (6 nanoparticles per μm^2) the diameter of nanoparticles would have to be greater than 150 nm in order to produce electromagnetically interacting nanoparticles. As discussed in the literature survey at such large nanoparticle sizes significant SERS enhancements and other photonic effects would not be expected [21-23].

In contrast, using the method outlined in chapter 3, it was possible to produce surfaces containing electromagnetically interacting (t18, h8, t7), and non-interacting (t16, t17) gold nanoparticles.

Table 4.1 Estimated mean interparticle separation of electrodeposited gold and silver nanoparticle surfaces.

Sample	Metal	Mean Diameter D (nm)	Coverage (particles μm^{-2})	Interparticle Seperation d (nm)	d/D
t18	Gold	109 ± 38	56	42	0.4
h8	Gold	61 ± 26	84	62	1.0
t7	Gold	71 ± 18	30	135	1.9
t16	Gold	44 ± 20	57	105	2.4
t17	Gold	55 ± 25	35	136	2.5
r46	Silver	85 ± 33	6	376	4.4
r50	Silver	112 ± 44	3	539	4.8

4.3 Effect of Irradiation of Silver Nanoparticles

It has been reported irradiation of colloidal silver nanoparticles can convert spheroids to nanoprisms [24]. This effect has been observed following irradiation of a colloidal suspension with a relatively weak intensity (40 w) fluorescent light bulb, and occurs over a period of up to 70 hours [24]. Applications of functionalised nanoparticle surfaces for photocatalysis or photocurrent generation typically involved broadband irradiation of the nanoparticles with a greater intensity light source (typically 100 w) for a shorter period of time (typically < 10 minutes). Therefore, the possibility exists that during the irradiation process the morphology of silver nanoparticles electrodeposited onto FDTO could be changed. This effect must be investigated before conclusions can be drawn about the effect of nanoparticle size and density on the SERS enhancement factor. To investigate if these samples were susceptible to morphological change during irradiation, a typical silver nanoparticle surface was masked so that half of the surface was exposed and half was protected, then the surface was irradiated with polychromatic light from a 450 w xenon-arc lamp for 5 hours. After irradiation, the size and density of nanoparticles on each half of the surface were compared by scanning electron microscopy.

The results of this experiment are presented in Figure 4.1. Figure 4.1a demonstrates the surface without irradiation. Figure 4.1b demonstrates the surface after irradiation from the Xenon arc lamp. Within experimental error there is no difference between the size and density of nanoparticles, this is demonstrated in the low magnification (10,000x) SEM images and is verified by the size distribution histograms and accompanying data. Furthermore, the morphology and shape of the nanoparticles was not changed by the irradiation process, this is seen most clearly in the high magnification (50,000x) SEM images. Therefore, this control experiment confirms that the silver nanoparticle surfaces are stable towards irradiation at higher intensities and for longer periods than used in these investigations. Additionally, this experiment indicates that the immobilised silver nanospheres cannot be

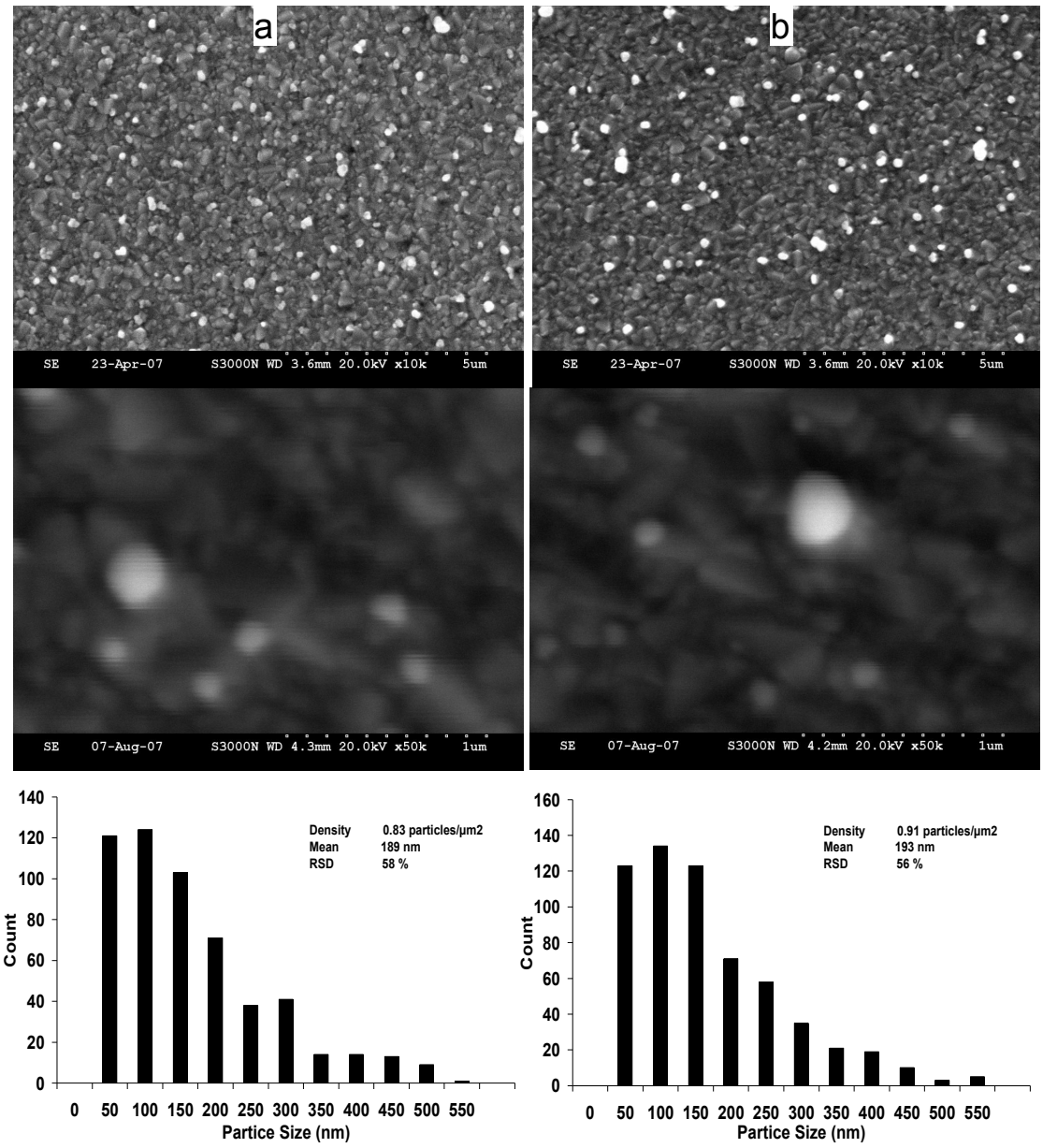

Figure 4.1 SEM images and size distribution histograms of (a) masked side of surface and (b) side of surface irradiated with 450 W Xenon arc lamp for 5 hours.

converted to prisms by irradiation. This behaviour may arise because they are immobilised on the surface when electrodeposited. It is likely that the freedom of movement and interaction of nanoparticles in solution is essential for the coalescence of nanoparticles into larger prism aggregates as found in solution.

4.4 UV-Vis characterization of nanoparticles

Section 1.3.1 described that many of the features of a surface suitable for producing SERS enhancements are also present in surfaces that display strong surface plasmon absorptions (e.g. nanoscale roughness). Nanoscale roughness, a feature of nanoparticle surfaces such as these, results in enhancement of the electromagnetic field experienced by molecules adsorbed on the nanoparticle surfaces. This enhancement results from electron density oscillations within the nanoparticles, which are resonant with light in the UV-visible region, and are consequently enhanced when irradiated with light of resonant wavelength. This results in a stronger electromagnetic field at the nanoparticle surface, and this enhanced field is responsible for the SERS enhancement. Furthermore, these resonant electron density oscillations that enhance the electromagnetic field at the nanoparticle surface are also responsible for the surface plasmon absorption. Thus, surfaces that produce strong SERS enhancements typically display a surface plasmon absorption [25-29]. The gold and silver nanoparticle surfaces produced were characterized by UV-Vis spectrophotometry in order to record their surface plasmon absorption.

A broad surface plasmon absorption band is expected at 520-550 nm for gold nanoparticles in the size range 80-160 nm according to Mie theory [30]. Such a broad band is present in both Figure 4.2 and 4.3 confirming the presence of a localised surface plasmon absorption. These figures represent the absorption spectra of electromagnetically interacting and electromagnetically isolated gold nanoparticles, respectively. In Figure 4.2 there were two absorption bands evident, at around 540 nm and 700 nm. The band at 540 nm is characteristic of the surface plasmon absorption of electromagnetically uncoupled gold nanoparticles [1, 31, 32]. The band at 700 nm is characteristic of electromagnetically interacting nanoparticles [1, 11]. Therefore, it is evident that in this sample, where the nanoparticle surface coverage is high there is a significant proportion of both interacting and non-interacting (isolated) nanoparticles. This was unsurprising given the extremely rough nature of FDTO, it is likely that a significant amount of

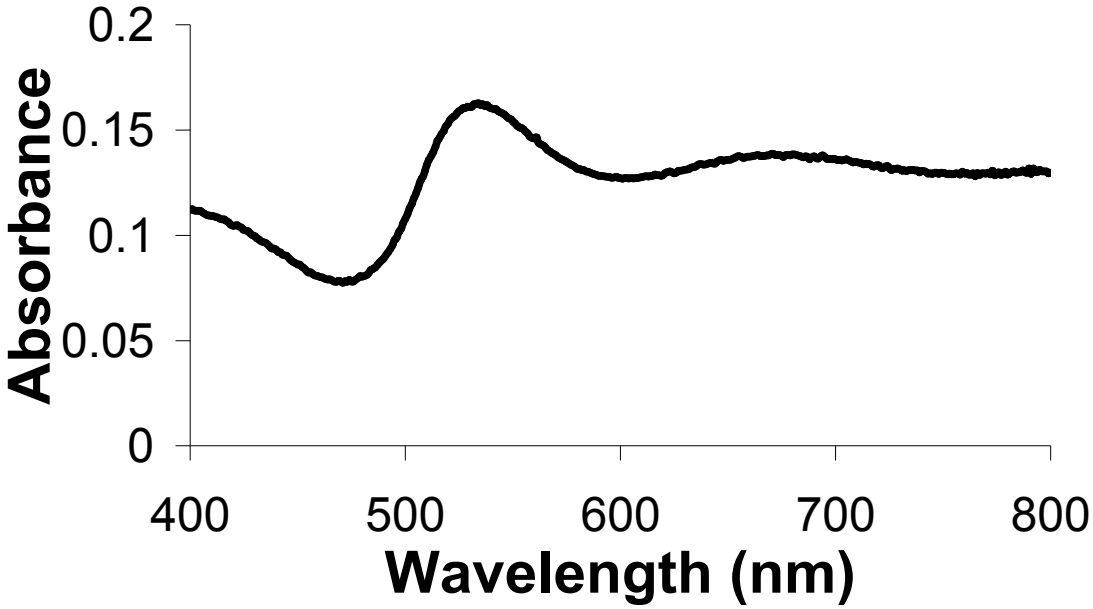

Figure 4.2 UV-Vis spectra demonstrating the surface plasmon band of a high surface coverage gold nanoparticle surface (d/D = 1.0) with mean particle size of 61 ± 26 nm.

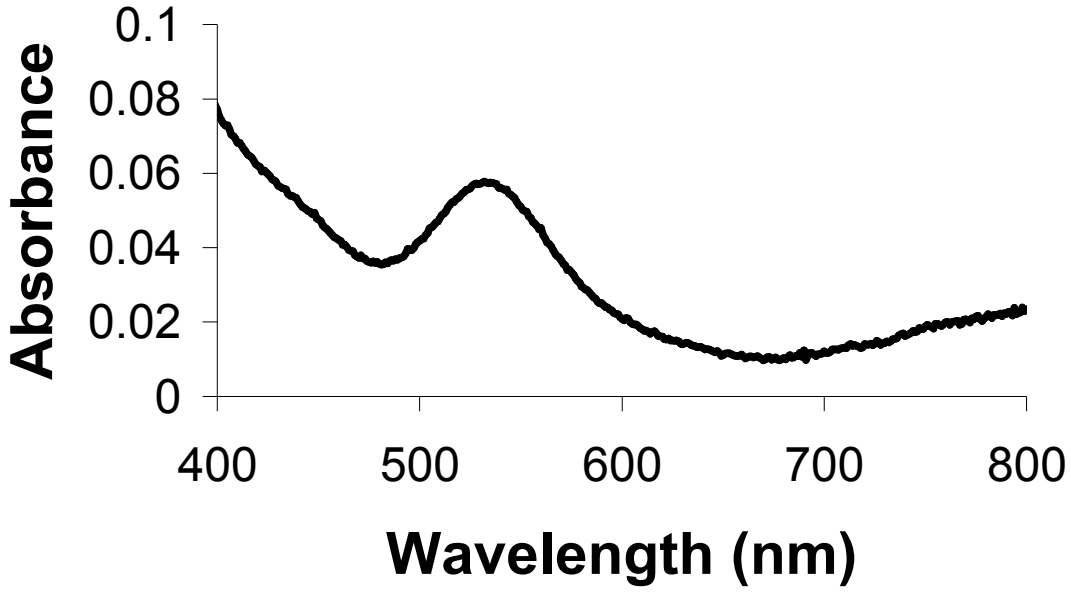

Figure 4.3 UV-Vis spectra demonstrating the surface plasmon band of isolated gold nanoparticle surface (d/D =2.5) with mean particle size of 55 ± nm.

nanoparticles that were in close proximity to other nanoparticles in two dimensions were in fact separated by a greater distance due to changes in height of the surface. The surface typically had height changes of the order of 200 – 300 nm. Figure 4.3 contains only the band at 540 nm resulting from isolated nanoparticles, this observation confirms that on this surface there is relatively little nanoparticle coupling.

For silver nanoparticles the surface plasmon absorption is usually expected at around 400 nm when they are interacting electromagnetically [33, 34]. Where the silver nanoparticles are essentially electromagnetically isolated, the surface plasmon absorption band is reported to occur as a broad peak between 400 nm and 700 nm [35], its exact location depends on the nanoparticle size. Jensen et al. presented theoretical calculations of the position of the surface plasmon absorption based on Mie theory [30], the discrete dipole approximation [36], and the modified long wavelength approximation [23]. Using these models, Jensen predicted that electromagnetically isolated silver nanoparticles in solution in the size range 80 nm - 100 nm would have a surface plasmon absorption between 500 nm and 600 nm depending on the nanoparticle size. The exact position predicted also depends somewhat in the model [35]. The silver nanoparticles analysed in Figure 4.4 have a mean diameter of 85 nm and, consistent with the results of Jensen et al. [35], exhibit an absorption maximum at approximately 540 nm.

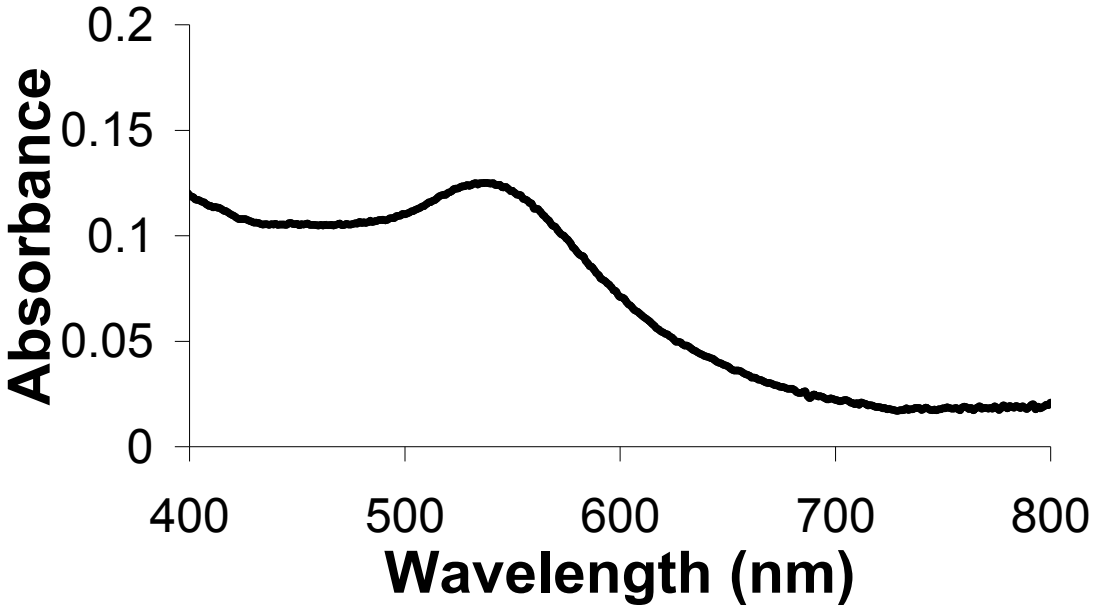

Figure 4.4 UV-Vis spectra demonstrating the surface plasmon band of isolated silver nanoparticle surface (d/D = 4.4) with mean particle size of 85 ± 33 nm.

4.5 Real Surface Area Determination of Gold and Silver Nanoparticle Surfaces

In order to calculate the enhancement factor in SERS the surface coverage of analyte molecules must be determined. In order to determine this accurately, the real surface area of the metal nanoparticle decorated surfaces was determined. The method for determining the real surface area of gold electrodes has long been established [37]. The electrode is immersed in 0.5 M H_2SO_4 and scanned using cyclic voltammetry between -0.25 V and 1.45 V. The shape of the resultant acid voltammogram is illustrated in Figure 4.5. At approximately 1.2 V there is an oxidative peak, corresponding to the formation of a gold oxide monolayer. The reverse sweep contained a reductive peak at 0.9 V that corresponds to reduction of the gold oxide monolayer. The charge passed during the reduction of the gold oxide monolayer can be used to calculate the real surface area. This is a widely utilised technique for determining the roughness factor of gold disk electrodes [5, 38], when the charge per unit area is 390 μC cm^{-2} [37]. Figure 4.5 shows that the shape of the gold oxide formation peak changes during repeated scanning. This is a result of the cleaning effect of cyclic voltammetry performed in acid solution. In the 20^{th} scan in Figure 4.5 there were three distinct peaks evident, these separate peaks are caused by the different crystallographic facets of the clean gold surface [38]. The peaks become resolved when impurities on the surface are removed by the oxidation/reduction cycle.

Table 4.2 shows data for the real surface areas of gold electrodes, and the size and density of the nanoparticles on these surfaces. Unsurprisingly, the real surface area was linked to the surface coverage of nanoparticles, with the greatest real surface area being found on samples with the greatest nanoparticle coverage, as seen by SEM. The real surface area of the samples that were made up of low surface coverage, large nanoparticles is very low; typically < 0.05 cm^2 gold surface area on an FDTO surface of 0.25 cm^2. Such a surface would be unsuitable for use in catalysis or as part of an

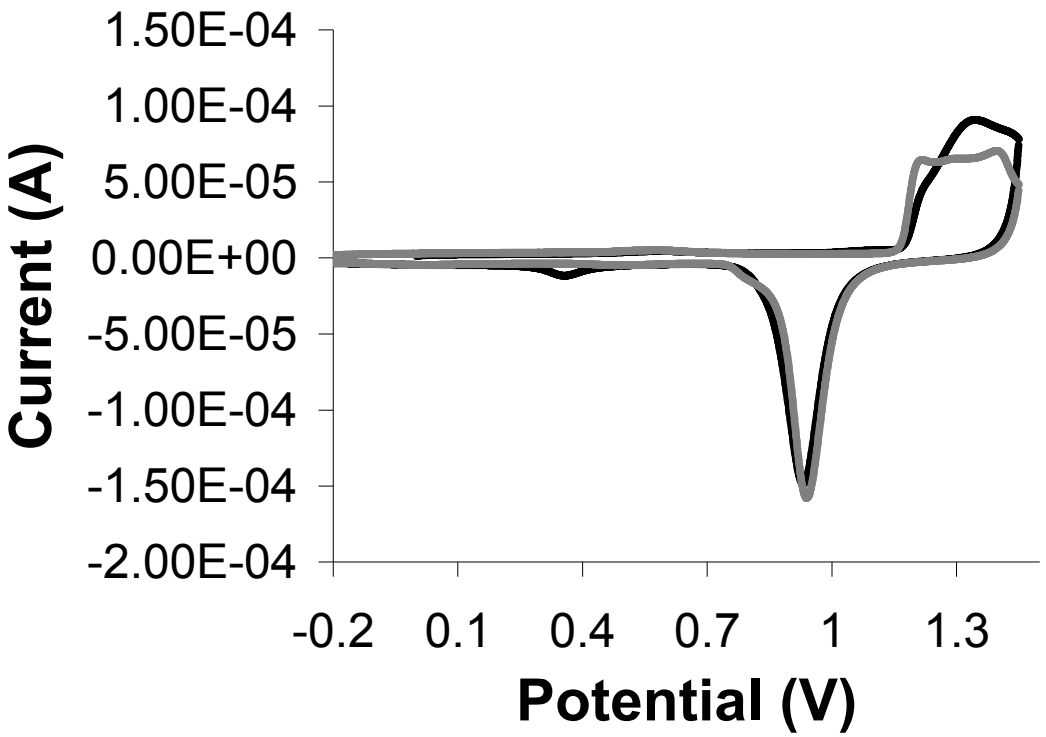

Figure 4.5 First and Last scan of cyclic voltammetry performed in acid solution of gold nanoparticles on FDTO. The CV was carried out in 0.5 M sulphuric acid between -0.25 V and 1.45 V at a scan rate of 0.2 Vs^{-1}. Scan 1 (black), Scan 20 (grey).

Table 4.2 Summary of real surface areas determined by cyclic voltammetry and SEM image analysis for gold nanoparticles electrodeposited on FDTO.

FDTO	Mean Diameter (nm)	Particle Coverage (Particles μm^{-2})	Charge Q (C)	Real Surface Area (cm^2)[I]
n13	122	1.1	3.55×10^{-6}	0.0091
f80	267	2.3	1.95×10^{-5}	0.0499
f79	229	2.5	1.73×10^{-5}	0.0444
n14	105	5.4	7.71×10^{-6}	0.0198
t4	77	32.1	1.07×10^{-4}	0.2731
t8	74	38.5	1.26×10^{-4}	0.3228

[I] Calculated as the charge passed during the reduction of the gold oxide monolayer divided by 3.90×10^{-4} C cm^{-2}.

electrochemical sensor, as such applications require a large metal surface area. Samples t4 and t8 in Table 4.2 have a real surface area greater than the area of the underlying FDTO electrode, but not by a significant amount. To make a surface suitable for use in catalysis or electrochemical sensing, the sample would have to consist of smaller, denser nanoparticles or a porous multilayer gold film. Such surfaces have been produced here but their properties in an analytical context have not been investigated.

Cyclic voltammetry cannot be used to determine the real surface area of a silver electrode. When the potential is scanned in a positive direction at a silver electrode two products form, AgOH and Ag_2O. Since the reduction peaks of these products overlap it is not possible to distinguish them; therefore silver oxide formation and reduction is not a viable method for the determination of the real surface area of silver nanoparticle surfaces. When describing the SERS enhancement factor a number of approximations and assumptions must be made. These include the assumption of a close packed monolayer of the analyte on the surface, and an approximation of the excitation laser spot size based on an assumption of correct focusing of the beam (described in Section 4.6). With such sources of error intrinsic to any estimation of SERS enhancement the value of the SERS enhancement, can only be considered an estimation, providing a relative value for comparison between surfaces.

The SEM images provide a useful method to approximate the real surface area of the surfaces decorated with silver nanoparticles. Every nanoparticle was assumed to be a perfect hemisphere with surface area:

$$A = 2\pi r^2 \qquad (4.1)$$

To estimate the accuracy of this assumption, the same approximation was used to estimate the real surface area of some of the gold nanoparticle surfaces presented in Table 4.2, whose real surface area was known. The results of this analysis are presented in Table 4.3. The relative error in the estimation for the samples with nanoparticle coverage < 6 particles per μm^2

was acceptable within the context of the limitations of estimating SERS enhancement (<30 %). Only surfaces with nanoparticle coverage < 6 particles per μm^2 were considered in Table 4.3. This is because the method of estimating surface area based on SEM image analysis was only performed on silver nanoparticle samples with surface coverage < 6 particles per μm^2.

Typical estimations of real surface areas of silver nanoparticle samples are presented in Table 4.4. Results are typically <0.02 cm^2 silver surface area per sample (with FDTO surface area ~0.25 cm^2). Such a low surface area indicates that it will not be possible to produce surfaces suitable for electrochemical sensing or catalysis using silver nanoparticles based on this method of electrodeposition. It was not possible to increase the nanoparticle density greater than 6 particles per μm^2 without forming aggregates of nanoparticles. The low surface coverage of nanoparticles does not however eliminate the possibility of using these silver nanoparticle surfaces for SERS based sensing.

Table 4.3 Real surface areas determined by cyclic voltammetry, and estimated by SEM image analysis for gold nanoparticles electrodeposited on FDTO.

FDTO	Mean Diameter (nm)	Particle Coverage (Particles μm^{-2})	Real Surface Area (cm^2)	Estimated Real Surface Area (cm^2)	Error (%)
n13	122.2	1.1	0.0091	0.0073	-20
f80	266.7	2.3	0.0499	0.0637	+28
f79	229.3	2.5	0.0444	0.0538	+21
n14	105.4	5.4	0.0198	0.0215	+8
t12	95.0	4.6	0.0134	0.0155	+16
t23	72.3	4.2	.0108	0.0082	-24

Table 4.4 Real surface areas estimated by SEM image analysis for silver nanoparticles electrodeposited on FDTO.

FDTO	Mean Diameter (nm)	Particle Density (Particles μm^{-2})	Estimated Real Surface Area (cm^2)
r47	94.8	3.2	0.0121
t15	103.4	3.8	0.0162
f49	97.8	3.9	0.0140
r46	85.0	6.0	0.0188
L18	105.7	3.8	0.0179

[I] Calculated as the charge passed during the reduction of the gold oxide monolayer divided by 3.90×10^{-4} Ccm^{-2}.
[II] Calculated as $2\pi r^2$ x total number of particles on the surface. Where r is the mean nanoparticle radius and total number of particles is estimated as the density of nanoparticles (particles cm^{-2}) x FDTO surface area.

4.6 SERS Spectroscopy

Having demonstrated the strong surface plasmon absorption present from both silver and gold nanoparticle surfaces fabricated in a controlled manner by electrodeposition it was clear that these surfaces could potentially yield strong SERS enhancements. Using a monolayer of the probe molecule BPE (see scheme 2), Raman spectra of the gold and silver nanoparticle surfaces were recorded at five different excitation wavelengths; 458 nm, 488 nm, 514 nm, 632 nm and 785 nm. To determine the efficiency of these surfaces as SERS substrates the SERS enhancement factor was estimated. The BPE molecule displays a high intensity doublet at approximately 1600 cm^{-1} and 1650 cm^{-1} (see Figure 4.7) corresponding to pyridine ring breathing modes [39]. The integrated intensity of these two peaks was used to estimate the enhancement factor.

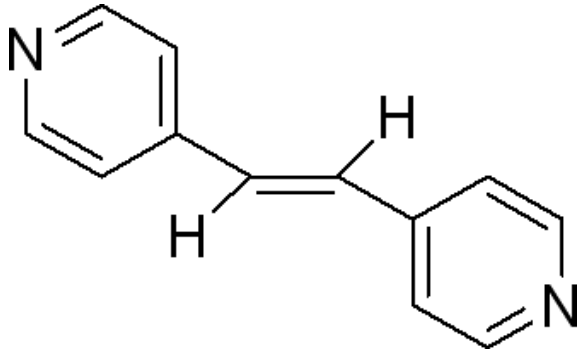

In Section 4.5 the method of estimating the real surface area of nanoparticles on each sample was described. To estimate the SERS enhancement factor the total counts recorded for a particular surface was normalised to the total counts per BPE molecule excited and compared to the counts from a BPE solution also normalised to the total counts per molecule excited. An example of the calculation of SERS enhancement factor is given below:

Example Calculation; SERS enhancement factor

Isolated silver nanoparticle sample, mean diameter 95 nm, Nanoparticle coverage (ρ_{NP}) = 3.2 particles per μm^2. λ_{ex} = 632 nm. f# of Raman microscope lens (10x) = 1.94. Depth of field (DoF) at 632 nm = 13.189 µm. BPE packing density on surface (Γ_{BPE}) = 2.0 x 10^6 molecules μm^{-2} [40]. Avogadro's number = 6.022 x 10^{23}

On Surface

Mean integrated intensity of two peaks at 1600 cm^{-1} and 1650 cm^{-1} from surface (I)

= 1.585 x 10^5

Laser spot diameter (D_{Las}) = 2f# x λ_{ex}

= 2 x 1.94 x 0.632 μm

= 2.45 μm

Laser spot area (A) = πr^2

= π x $(2.45/2)^2$

= 4.71 μm^2

No. of particles per laser spot size (N_p) = A x ρ_{NP}

= 4.71 x 3.2

= 15.07 particles

Silver surface area per laser spot (A_{surf}) = N_p x 2 x πr^2

= 15.07 x 2 π x $(0.095\mu m/2)^2$

= 0.2136 μm^2

Molecules of BPE excited (N_{surf}) = A_{surf} x Γ_{BPE}

= 0.2136 μm^2 x 2 x 10^6

= 4.27 x 10^5 molecules

Normalised Integrated intensity (I_{Norm}) = I/N_{surf}

= 1.585 x 10^5/4.27 x 10^5

= 0.3709

<u>In Solution</u>

Mean integrated intensity of two peaks at 1600 cm^{-1} and 1650 cm^{-1} from 0.005 M BPE standard solution (J)

= 4.192 x 10^4

Excitation volume of laser (V_{Las}) = $2x1/3\pi DoF\left[\frac{(\frac{\sqrt{2}D_{Las}}{2})^2+(\frac{\sqrt{2}D_{Las}}{2}\times\frac{D_{Las}}{2})+(\frac{D_{Las}}{2})^2}{2}\right]$

= 9.134 x 10^{-14} L

Molecules BPE excited (N_{sol}) = V_{Las} x 0.005 M x N_A

= 9.134 x 10^{-14} x 0.005 x N_A

= 2.85 x 10^8 molecules

Normalised Integrated intensity (J_{Norm}) = J/N_{sol}

= 4.192 x 10^4/2.85 x 10^8

= 1.471 x 10^{-4}

Enhancement Factor (EF) = I_{Norm}/J_{Norm}

= 0.3709/1.471 x 10^{-4}

= 2.521 x 10^3

The greatest SERS enhancements are reported to occur when the excitation wavelength is near resonance with the localised surface plasmon absorption as this is the wavelength that stimulates the surface plasmon therefore producing the electromagnetic enhancement [41]. The UV-Vis spectra of the nanoparticle covered surfaces (Figures 4.2-4.4) demonstrated that the surface plasmon absorption is located as a broad band between 500 nm and 600 nm for dense gold nanoparticles, isolated gold nanoparticles and isolated silver nanoparticles. Therefore, of the excitation wavelengths available, 488 nm, 514 nm and 632 nm are resonant or close to resonant with the surface plasmon absorption and would be expected to yield the best SERS enhancements.

A typical spectrum is presented in Figure 4.6. To confirm that the Raman signal could be attributed only to BPE molecules adsorbed on silver, and therefore there was no signal resulting from BPE molecules absorbed on the FDTO surface, the experiment was repeated with bare FDTO which had been immersed in BPE solution; this resulted in a blank spectrum containing no bands characteristic of BPE. Raman spectra were recorded from 6 randomly spaced positions on each surface so that an average enhancement factor (EF) could be determined for the surface. This also afforded the opportunity to determine the reproducibility of the enhancement factor from different sites on the same surface. In order to estimate the enhancement factor, the solution phase Raman spectrum of the probe molecule was recorded. This afforded the opportunity to measure the Raman signal from BPE away from the surface, and therefore unenhanced. The Raman spectrum of a 5 mM solution of BPE is presented in Figure 4.7. The signal intensity was significantly lower than on the surface, and the number of molecules excited in solution was significantly greater than on the surface (see enhancement factor calculation).

The most significant enhancement factors are summarized in Tables 4.5 and 4.6.

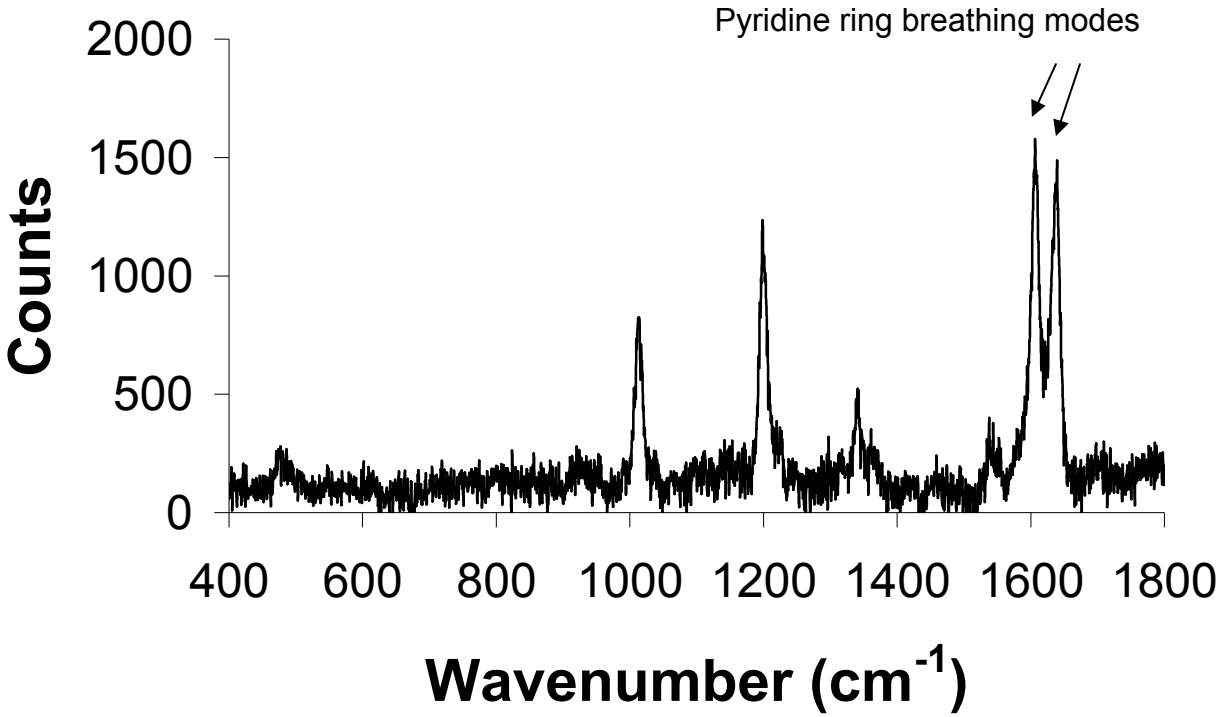

Figure 4.6 Raman spectrum recorded of BPE on FDTO surface electrodeposited with isolated silver nanoparticles of mean diameter 95 nm, excitation wavelength was 632 nm. Integration time was 5 x 20s. Mean enhancement factor = 3575.

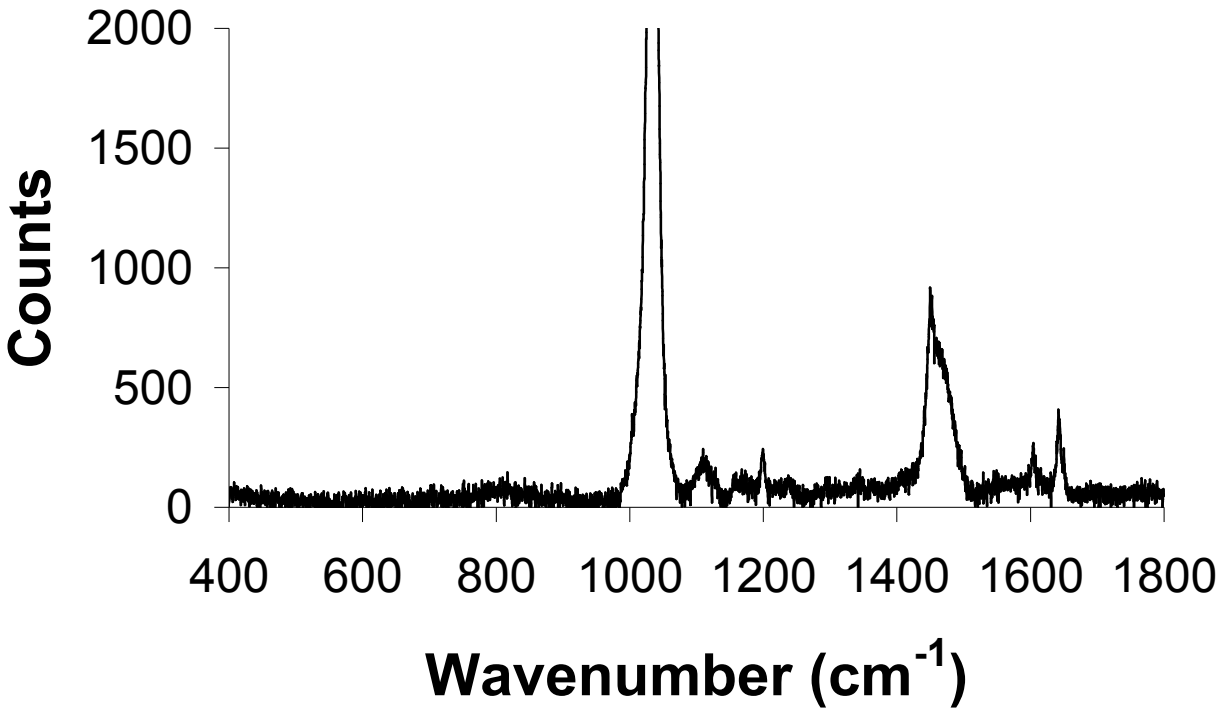

Figure 4.7 Raman spectrum recorded of 5 mM BPE in methanol, excitation wavelength was 632 nm. Integration time was 5 x 20s.

Table 4.5 Summary of enhancement factors estimated from isolated silver nanoparticle surfaces.

Nanoparticle Metal	Mean Diameter(nm)	λ_{ex} (nm)	EF_{mean}	St. Dev.	RSD (%)	EF_{best}
Silver	94.8	458	66	13	20	105
		488	196	37	19	214
		514	411	47	11	581
		632	2521	317	13	3575
Silver	97.8	488	671	49	7	844
		514	2935	144	5	4022
Silver	110.7	458	34	18	53	66
		488	152	43	28	214
		514	118	44	37	192
		632	1071	280	26	1673
Silver	119.4	632	873	89	10	936

Of the five excitation wavelengths investigated, the greatest enhancement factor was recorded at 632 nm for the isolated silver nanoparticle surfaces. It is perhaps significant that this excitation wavelength is not coincident with $\lambda_{max,\ abs}$ of the surface, but is close to resonance. Similarly, it has been reported elsewhere that the greatest SERS enhancements can be achieved when the excitation wavelength is close to resonance [42]. The enhancement factor at 632 nm was as large as 3 orders of magnitude for silver nanoparticle surfaces (best EF = 3575). It was not possible to obtain enhancement factors at 785 nm as a broad peak was present in the spectrum from 1200 cm^{-1} to 1800cm^{-1} which masked the doublet at 1600 cm^{-1} and 1650 cm^{-1} at this excitation wavelength. This broad peak was also observed on a bare FDTO slide therefore the band was believed to result from background processes associated with either the glass or the FDTO. The enhancement factors at 488 nm and 514 nm were smaller (2 orders of magnitude for isolated silver nanoparticles) in most cases. However, one sample had a maximum enhancement factor of 4022 at 514 nm excitation. 60 days later its enhancement factor had decreased by over 75% at all wavelengths, possibly due to adsorption of impurities onto the silver surface.

The greatest enhancement factors recorded from isolated silver nanoparticle samples were recorded from samples with mean particle diameters in the range 90-100 nm. It was found that when the nanoparticles had mean diameter <90 nm the SERS spectrum was very weak. Similarly it can be seen that when the silver nanoparticle size was increased above 100 nm the strength of the SERS enhancement decreased. Silver nanoparticle samples of mean sizes between 50 nm and 200 nm were analysed and those not presented in Table 4.5 either did not yield a defined spectrum, or had an insignificant estimated enhancement factor. These results agree with the literature data available for isolated silver nanoparticles in solution which also reported greatest enhancements from particles of size range 80-100 nm [22, 43].

Table 4.6 Summary of enhancement factors estimated from gold nanoparticle surfaces.

Nanoparticle Metal	Mean Diameter(nm)	λ_{ex} (nm)	EF_{mean}	St. Dev.	RSD (%)	EF_{best}
Gold (uncoupled)	130	632	427	98	23	556
Gold (Coupled)	58	632	654	1236	189	3175
		785	296	36	12	346
Gold (Coupled)	71	632	393	312	80	1016
		785	362	182	50	693
Gold (Coupled)	101	632	101	28	27	138
		785	261	175	67	529

Although it was not possible to produce electromagnetically interacting (high surface coverage) silver nanoparticle surfaces, it was possible to electrodeposit gold nanoparticle surfaces of sufficiently high surface coverage that they were electromagnetically coupled. Some of the results recorded from these dense gold nanoparticle surfaces are presented in Table 4.6. The greatest enhancement factors were recorded from samples with mean particle diameter between 50 nm and 100 nm. The excitation wavelengths that produced the greatest enhancements were 632 nm and 785 nm. This is somewhat unexpected as the surface plasmon absorption of the gold nanoparticles was at approximately 500-550 nm, and 785 nm excitation is quite far from resonance. It was possible to record up to 3 orders of magnitude enhancement from some locations on the surface. However, it was not possible to reproduce such large enhancements from other sites on the surface. It is likely that these locations, where the greatest enhancements were recorded, consisted of areas on the surface where the number density of nanoparticles was greatest such that favourable configurations of nanoparticles occurred, for example the close interaction of three or more nanoparticles in close proximity. It was not possible to produce dense gold nanoparticles of size greater than 100 nm as at this size range coalescence of nanoparticles occurred and the SERS enhancement factor was significantly reduced. A typical SERS spectrum recorded from a high surface coverage gold nanoparticle modified FDTO is presented in Figure 4.8.

Of 10 isolated gold nanoparticle surfaces analysed with mean nanoparticle diameters in the range 50 nm to 250 nm, only one sample produced a sufficiently strong Raman response to calculate the SERS enhancement factor. This sample, with mean diameter 130 nm had a 2 orders of magnitude enhancement at 632 nm excitation and did not have a defined spectrum at the other wavelengths. At 785 nm excitation the broad peak associated with the FDTO surface masked the peaks at 1600 cm^{-1}. This peak was not evident on high surface coverage gold samples due to the greater gold loading blocking excitation of the underlying substrate. A Raman spectrum recorded from this sample is presented in Figure 4.9, the

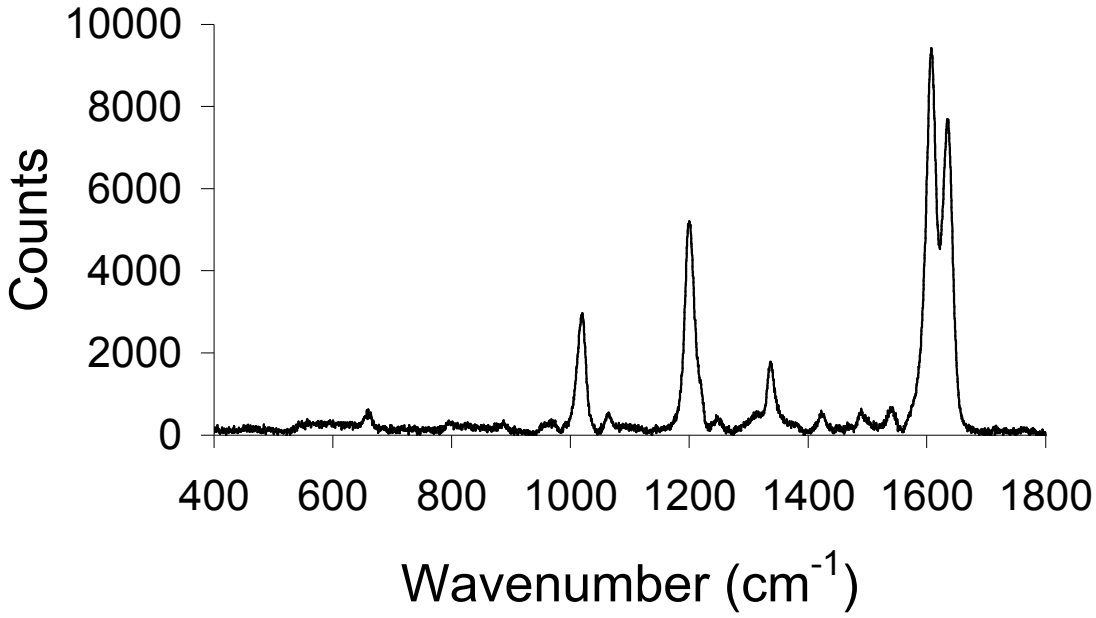

Figure 4.8 Raman spectrum recorded of BPE on FDTO surface electrodeposited with dense gold nanoparticles of mean diameter 71 nm, excitation wavelength was 632 nm. Integration time was 5 x 20s. Enhancement factor = 1016.

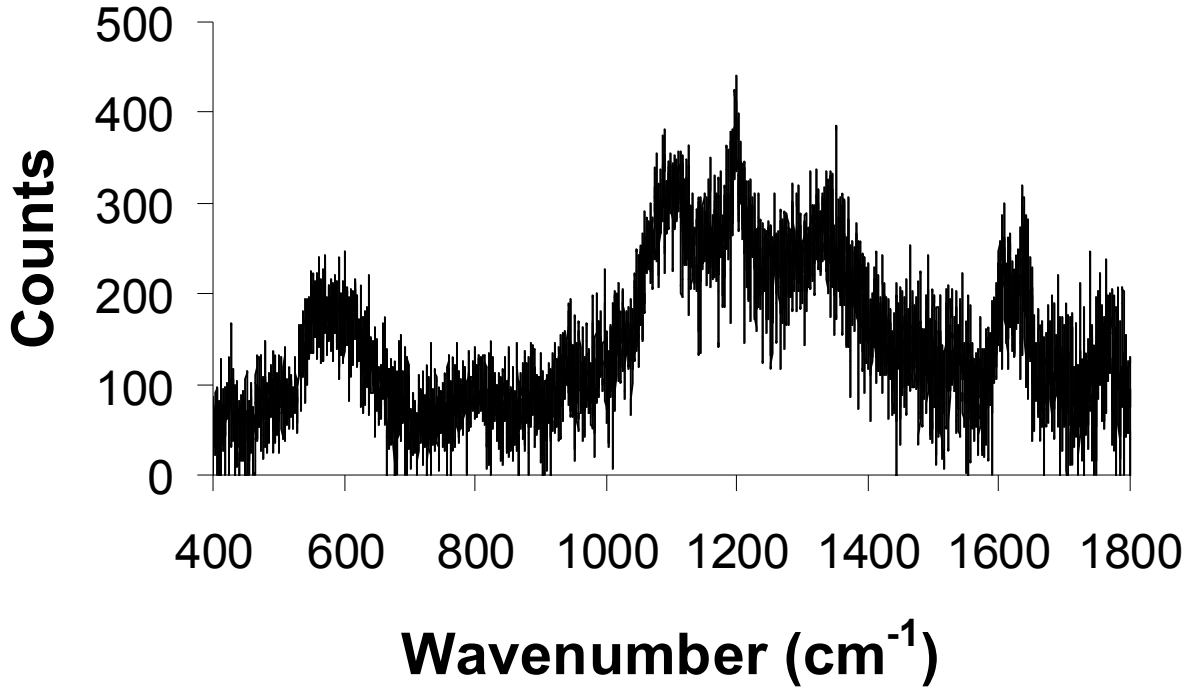

Figure 4.9 Raman spectrum recorded of BPE on FDTO surface electrodeposited with isolated gold nanoparticles of mean diameter 130 nm, excitation wavelength was 632 nm. Integration time was 5 x 20s. Enhancement factor = 556.

signal to noise ratio of this sample was significantly poorer than the spectra recorded from isolated silver nanoparticle surfaces (for example the spectrum in Figure 4.6) and for high surface coverage gold nanoparticle samples. It has been reported that isolated colloidal gold nanoparticles of mean diameter 60-70 nm yield the best SERS enhancements [43], this does not agree with the results reported here. However, this could be due to differences in shape between colloidal spheres and electrodeposited hemispheres, or it could result from interactions between the FDTO surface and the electrodeposited gold nanoparticles. The isolated gold nanoparticle surface was capable of producing approximately the same enhancement factors as the dense gold nanoparticle surfaces. In addition, the isolated gold nanoparticle surface had a lower standard deviation of enhancement factor and consumed less gold in production. Therefore, there are advantages to utilising the electromagnetically uncoupled surface when using gold nanoparticles for SERS enhancements. However, the electromagnetically isolated gold nanoparticle surface was less efficient at enhancing the SERS signal than its silver analogue. Also, the nanoparticle diameter had to be more precisely controlled in order to record a SERS signal from an electromagnetically uncoupled gold nanoparticle surface; this was probably related to the weaker SERS signal recorded from gold nanoparticles than from silver nanoparticles in general.

The enhancement factor recorded from electromagnetically uncoupled silver nanoparticles (10^3) and electromagnetically uncoupled gold nanoparticles (10^2) is similar to results obtained for SERS from isolated colloidal gold nanoparticles of 10^3 [16]. The enhancement factor reported for electromagnetically interacting gold nanoparticles (10^2) is significantly weaker than reported in the literature for similar dense arrays of gold nanoparticles, where enhancements of up to 10^7 were reported on other substrates [44]. The reason for the poor performance in this respect could be related to the inability to narrow the size distribution of nanoparticles, and the absence of nanoparticle “hot-spots”, typically occurring at a point where two or more nanoparticles touch or come in very close contact. Such hot-spots occur frequently in colloidal assemblies, and significantly boost the

average enhancement factor, but do no readily occur by electrodeposition where the nanoparticles are immobile. However, despite providing impressive enhancements, such hot-spots make reproducibility very poor, as the magnitude of the enhancement from any one hot-spot is the product of a number of factors, most notably the 3D spatial position of several solution phase nanoparticles, which are uncontrollable and random. As such, from a quantitative sensing point of view hot-spots are undesirable.

The relative standard deviation of enhancement factor for both silver and gold nanoparticle samples is quite large, typically 20-30%. This represents a significant obstacle to incorporation of such a surface into a SERS based sensing device. The largest source of this imprecision is likely to be the size distribution of the nanoparticles, which for silver nanoparticles was approximately 40% for most samples. The rough nature of the chosen substrate, FDTO, encouraged diffusion zone coupling and afforded an imperfect surface for electrodeposition, making it difficult to narrow the size distribution below 40%. While colloidal suspensions are capable of yielding much lower RSDs in the enhancement factor, as low as 3 % [45], SERS enhancement from surfaces are more difficult to perform reproducibly, with reproducibility across a single surface typically greater than 30 % [46]. With this in mind the reproducibility of the enhancement factor of 20-30% is acceptable. The variation of the enhancement factor is demonstrated in Figure 4.10 which shows six spectra recorded from one surface. There is a significant difference in the integrated intensity of the two peaks used for calculation of enhancement factor. The range of enhancement factors demonstrated in this figure is 1948 – 3575. This represents a 13% relative standard deviation. However, the variation in enhancement factor is not so large that a reproducible quantitative measurement cannot be recorded particularly if coupled with the use of an internal standard and averaging of multiple measurements from each surface.

The relative standard deviation in mean particle size, and enhancement factor was greater for high surface coverage gold nanoparticles (typically50%) than for isolated gold nanoparticles (typically 30%). This is

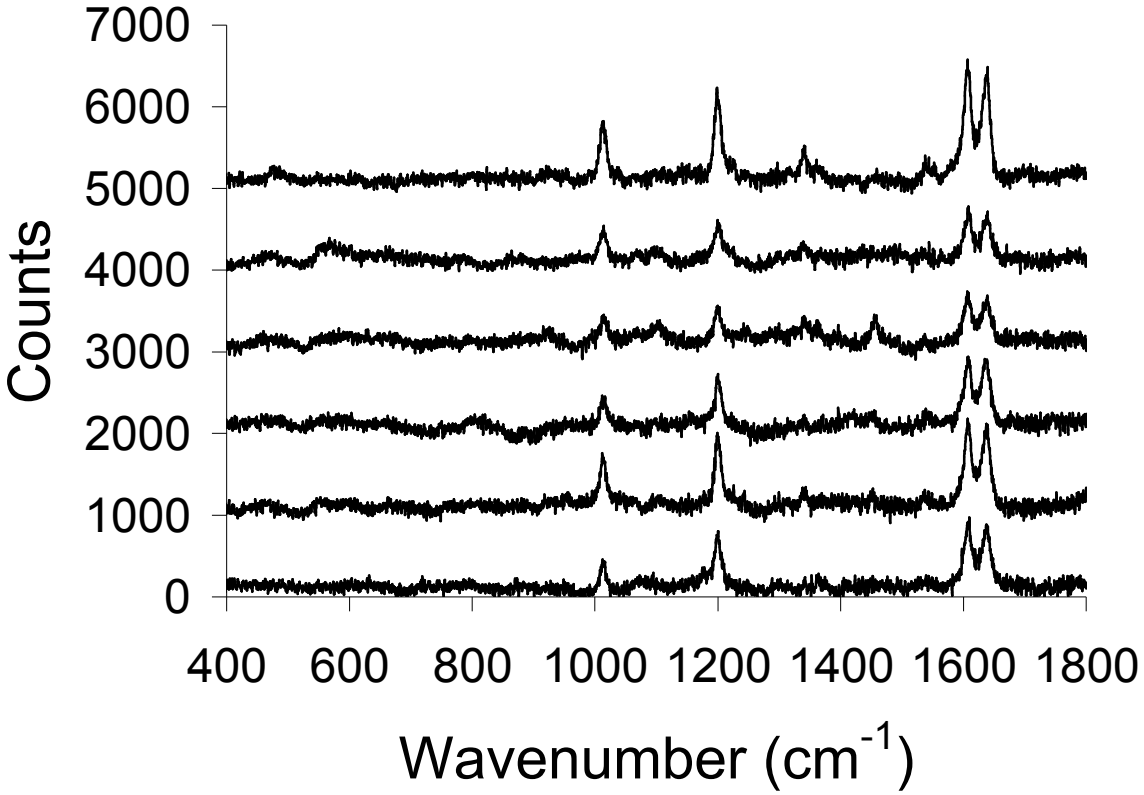

Figure 4.10 Raman spectra recorded at six random locations of BPE on FDTO surface decorated with electromagnetically uncoupled silver nanoparticles of mean diameter 95 nm, (d/D = 4.8), excitation wavelength was 632 nm. Integration time was 5 x 20s. Mean enhancement factor = 2521. Enhancement factor RSD = 13%.

most likely a result of greater degree of diffusion zone coupling occurring when the nanoparticles were growing at a greater density. The increased diffusion zone coupling resulted in a greater size distribution of the nanoparticles, and this resulted in a greater range of enhancement factors from the SERS substrate. Producing stable and reproducible SERS enhancements is currently recognised as one of the greatest challenges in the field of quantitative SERS spectroscopy [14]. To conclude, the main advantages of these surfaces are that they provide an adequate SERS signal enhancement so that qualitative and quantitative analysis will be possible. They can be produced at a low cost, and in a short time such that they can be used for disposable "one-shot" measurements. The reproducibility of the enhancement factor, at 20-30% compares favourably with other similar surfaces and media designed for the same purpose. Finally, having the SERS enhancement media immobilised on a surface provides a significant advantage over using colloidal suspensions as it allows more flexibility in the sampling.

4.7 Fluorescence Properties

An analytical method closely linked to SERS spectroscopy is surface enhanced fluorescence (SEF, also referred to as metal enhanced fluorescence, MEF). The reason behind the similarities between the techniques is that both methods result in a large increase in the analytical signal at roughened metal surfaces. The mechanism of SEF enhancement is discussed in the literature review (Section 1.3.3). As with SERS, the greatest SEF enhancements are frequently found from nanoparticles of gold and, in particular with SEF, of silver. The nanoparticle size range reported to yield the strongest SEF enhancements are silver nanoparticles of diameter 50 nm [3, 18] when the nanoparticles are in solution. When the nanoparticles are surface bound, various nanoparticle sizes have been reported in the literature; 5 nm [47], 80 nm [48], 100-500 nm [19]. The optimum conditions for SEF enhancement, as well as the maximum SEF enhancement factor depend not only on the environment in which the fluorophore is located, but also the nature of the fluorophore itself, with significantly different enhancement factors frequently being reported for different dyes in otherwise identical systems [9, 18]. With the ability to control the size and surface coverage of silver nanoparticles demonstrated in Chapter 3, these surfaces were attractive candidates for SEF investigations.

A monolayer of the fluorescent probe molecule $[Os(bpy)_2Qbpy]^{2+}$ where bpy is 2,2'-bipyridyl and Qbpy is 2,2':4,4'':4'4''-quarterpyridyl (Scheme 3) was formed on the surface of the silver nanoparticles by immersion in a 1 mM methanolic solution. The presence of non-coordinated pyridine moities makes the complex surface active which facilitates investigation of the emission intensity from the silver nanoparticle surface. Typical emission spectra of the osmium complex in solution and immobilised on the isolated silver nanoparticle surface at 632 nm excitation are presented in Figure 4.11 (1 x 20 s exposure). In solution, the fluorescence maximum was located at approximately 780 nm.

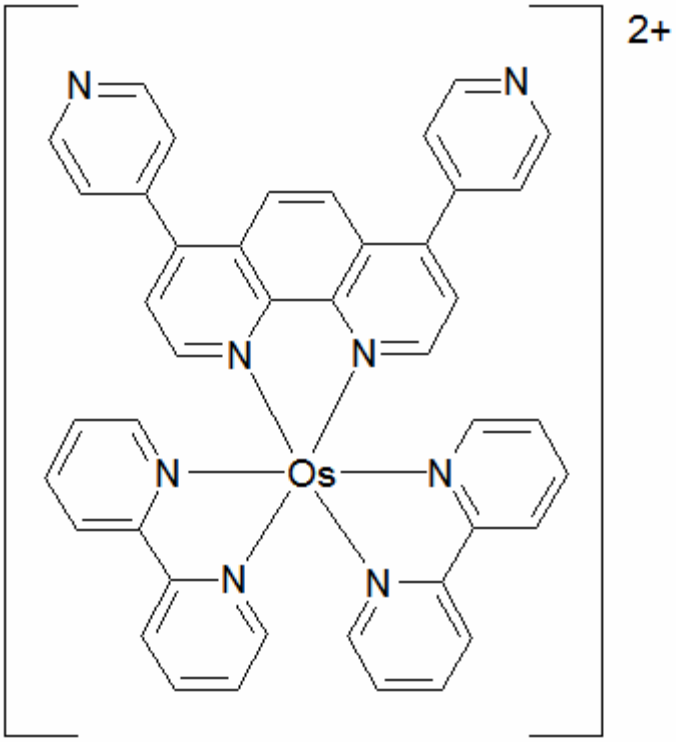

$[Os(bpy)_2Qby]^{2+}$

Upon immobilisation of the osmium complex on the silver nanoparticle surface the peak shifted to higher energy by approximately 40 nm. This shift to higher energy most likely arises from a lower dielectric constant and less efficient solvation of the polar excited state in the monolayer. The magnitude of intensity of the fluorescent signal from the $[Os(bpy)_2Qbpy]^{2+}$ monolayer (on the silver nanoparticles immobilised on the FDTO surface) is quite large, typically 10,000 to 15,000 counts. This is an impressive signal considering that it comes from as few as 2×10^5 $[Os(bpy)_2Qbpy]^{2+}$ molecules (see calculation below Figure 4.11). The signal to noise ratio is extremely large for such a small number of molecules within the excitation spot. The emission spectrum recorded from a solution of $[Os(bpy)_2Qbpy]^{2+}$ was of similar magnitude to the signal recorded from the silver nanoparticle surface, however, this solution contained a significantly greater amount of $[Os(bpy)_2Qbpy]^{2+}$ molecules than were present on the surface, as outlined in the calculation below Figure 4.11.

The enhancement factor for SEF can be calculated in the same manner as with SERS. As with SERS the enhancement factor is estimated based on the area under the emission peak divided by the number of molecules that were within the excited area/volume at the time of the experiment. The Normalised intensity of the emission from the surface is compared to the normalised intensity from a solution of the same complex. The calculation was the same as that used to calculate SERS enhancement factor. In Figure 4.11 the intensity of the emission signal from the $Os(bpy)_2Qbpy]^{2+}$ complex in solution was slightly greater than that from the complex on the surface. However the number of molecules excited in solution was significantly greater than the number immobilised on the surface. The enhancement factor estimated for the spectrum shown is 105. As expected the enhancement is significantly lower than those recorded using SERS spectroscopy. Similar work on silver island films, and on silver nanoparticles in solution by Lakowicz et al. has produced maximum enhancement factors of around 40-50 [3, 18, 48], and Chen et al. have reported enhancement of 100 fold of protein fluorescence from gold nanowires [49]. However, it is

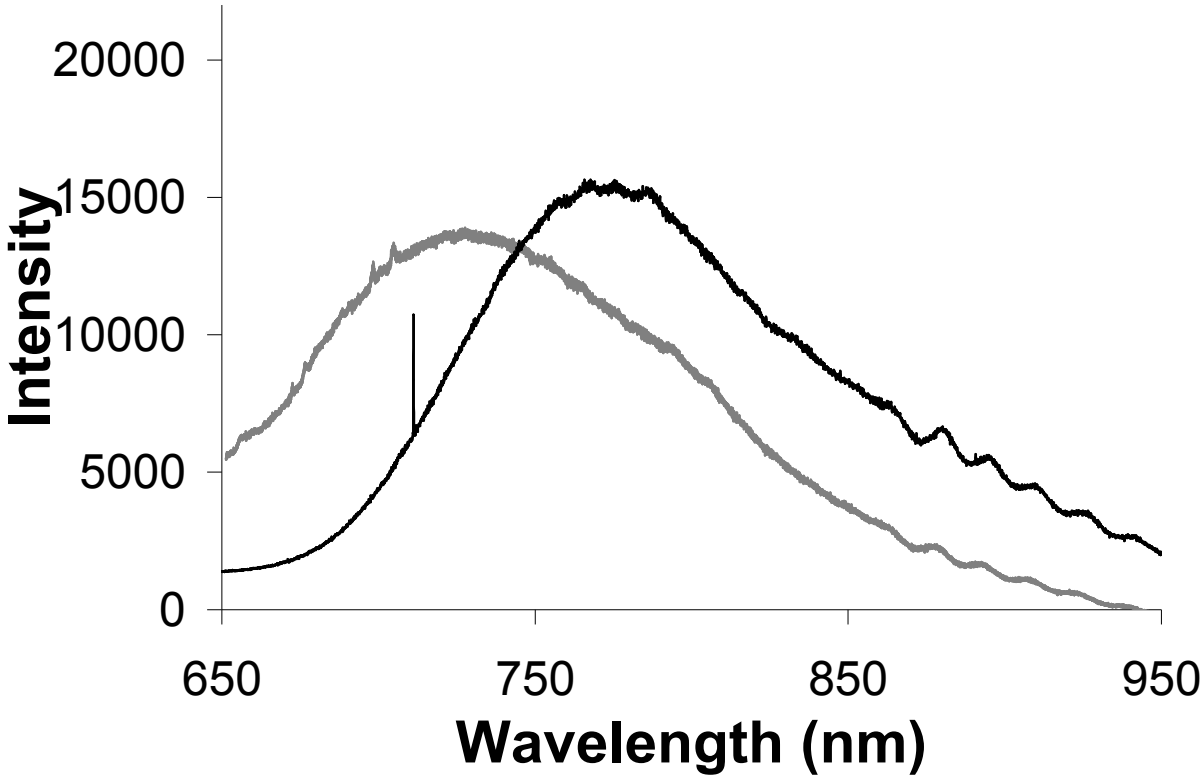

Figure 4.11 Emission spectra of $[Os(bpy)_2Qbpy]^{2+}$: (—) Immobilised on isolated silver nanoparticles of mean diameter 106 nm electrodeposited on FDTO, (—) in 5 mM solution. λ_{ex} = 632 nm, 1 x 20 s acquisition. EF = 105

Estimation of MEF enhancement factor:

Isolated silver nanoparticle sample, mean diameter 106 nm, Nanoparticle coverage (ρ_{NP}) = 3.2 particles per μm^2. λ_{ex} = 632 nm. f# of Raman microscope lens (10x) = 1.94. Depth of field (DoF) at 632 nm = 13.189 µm. Avogadro's number = 6.022×10^{23}

On Surface

Integrated intensity of $[Os(bpy)_2Qbpy]^{2+}$ emission peak	=	2.07×10^9
Laser spot diameter (D_{Las})	=	$2f\# \times \lambda_{ex}$
	=	$2 \times 1.94 \times 0.632$ µm
	=	2.45 µm
Laser spot area (A)	=	πr^2
	=	$\pi \times (2.45/2)^2$
	=	4.71 μm^2
No. of particles per laser spot size (N_p)	=	$A \times \rho_{NP}$
	=	4.71 x 3.8
	=	17.90 particles
Silver surface area per laser spot (A_{surf})	=	$N_p \times 2 \times \pi r^2$
	=	$17.90 \times 2 \pi \times (0.106\mu m/2)^2$
	=	0.3159 μm^2

Molecules of $[Os(bpy)_2Qbpy]^{2+}$ excited (N_{surf}) = $A_{surf} \times \Gamma_{Os}$

= $0.3159\ \mu m^2 \times 6.3 \times 10^5$ molecules/ μm^2

= 2.05×10^5 molecules

Normalised Integrated intensity (I_{Norm}) = I/N_{surf}

= $2.07 \times 10^9 / 2.05 \times 10^5$

= 1.01×10^4

In Solution

Integrated intensity of $[Os(bpy)_2Qbpy]^{2+}$ emission peak from 0.005 M $[Os(bpy)_2Qbpy]^{2+}$ standard solution (J)

= 2.75×10^9

This solution spectrum was recorded with the 10% filter, therefore the corrected intensity (J) is given by

= $2.75 \times 10^9 \times 10$

= 2.75×10^{10}

Excitation volume of laser (V_{Las}) = $2x1/3\ \pi DoF\ [\frac{(\frac{\sqrt{2}D_{Las}}{2})^2 + (\frac{\sqrt{2}D_{Las}}{2} \times \frac{D_{Las}}{2}) + (\frac{D_{Las}}{2})^2}{2}]$

= 9.134×10^{-14} L

Molecules $[Os(bpy)_2Qbpy]^{2+}$ excited (N_{sol}) = $V_{Las} \times 0.005\ M \times N_A$

= $9.134 \times 10^{-14} \times 0.005 \times N_A$

= 2.85×10^8 molecules

Normalised Integrated intensity (J_{Norm}) = J/N_{sol}

= $2.75 \times 10^{10} / 2.85 \times 10^8$

= 96.49

Enhancement Factor (EF) = I_{Norm}/J_{Norm}

= $1.01 \times 10^4 / 96.49$

= 105

difficult to compare enhancement factors directly as the degree of enhancement is influenced strongly by the analyte. These results compare favourably to the literature. The reproducibility of the enhancement factor was also quite impressive, the relative standard deviation in the enhancement factor of the spectra shown in Figure 4.11 was approximately 3%. The relative standard deviation was based on the emission intensity recorded at several points on an individual surface.

To ensure that the $[Os(bpy)_2Qbpy]^{2+}$ complex only adsorbed onto the surface of the silver nanoparticles, and not onto the underlying FDTO also the absorption spectra of FDTO slides with and without silver nanoparticles were recorded following immersion in methanolic osmium solution for 48 hours. The resulting spectra are presented in Figure 4.12. When the FDTO slide was decorated with silver nanoparticles before immersion in the osmium solution (black line) the characteristic osmium absorption spectrum was evident. The osmium complex metal-to ligand charge transfer bands (MLCT) in the visible region (450-480nm) were present. However, in the absence of nanoparticles (grey line) there was no evidence of the presence of $[Os(bpy)_2Qbpy]^{2+}$ on the surface in the spectrum. Therefore, the osmium complex adsorbs only on the silver nanoparticle surface and there is no evidence for non-specific binding to the FDTO surface.

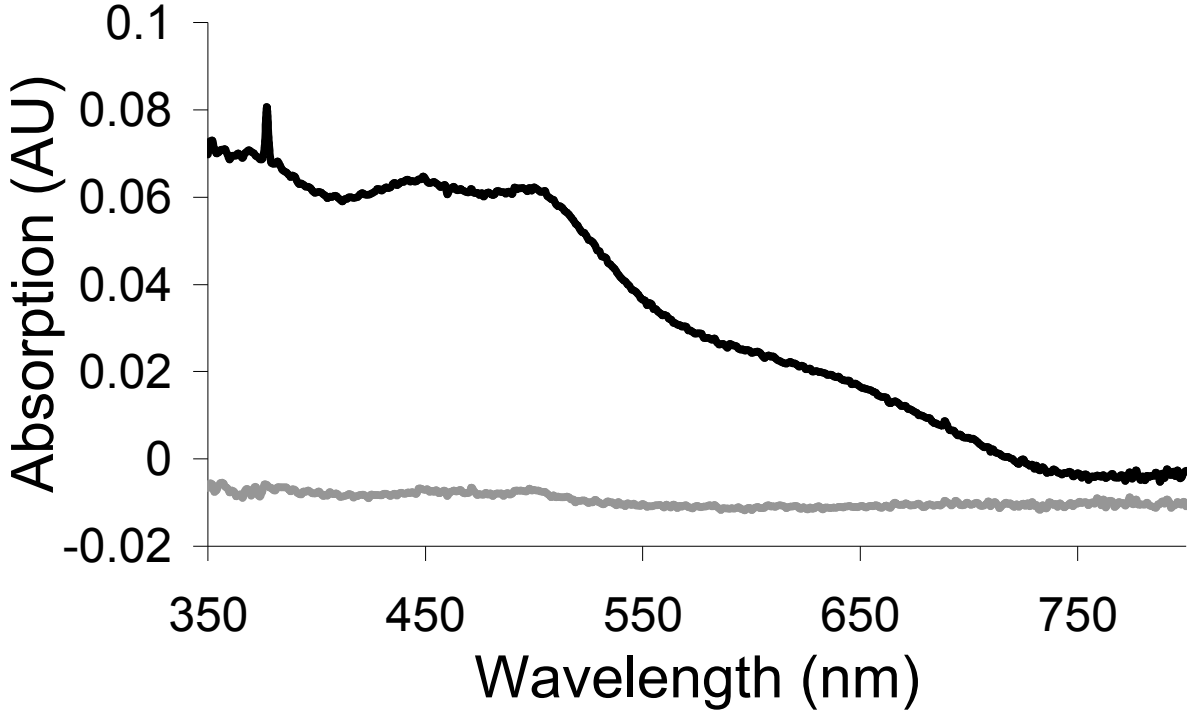

Figure 4.12 UV-Vis absorption spectrum of FDTO following 48 hour immersion in 1mM $[Os(bpy)_2Qbpy]^{2+}$ solution, with silver nanoparticles on the surface (—), without silver nanoparticles on the surface (—).

4.8 Conclusion

Silver and gold nanoparticles have been electrodeposited on fluorine-doped tin oxide in a controlled manner. The size and interparticle spacing of the nanoparticles could be controlled within certain limits by controlling the kinetics of nucleation and growth through a two pulse deposition scheme. Using this method it was possible to produce surfaces covered with isolated gold or silver nanoparticles of controlled size, or electromagnetically interacting gold nanoparticles. The application of these surfaces to SERS has been demonstrated, producing up to a 3 orders of magnitude enhancement factor with silver nanoparticles under optimal conditions, and 2 orders of magnitude with gold nanoparticles. A potential problem with this approach is the large relative standard deviation of the enhancement factor at different locations on the surface, typically 20-30%. Much of the imprecision could be due to the size distribution of nanoparticles which was typically around 40% for the isolated silver nanoparticles. Future work may concentrate on performing these experiments on a smoother surface than FDTO that may enable the narrowing of this size distribution. Nonetheless the standard deviation of the enhancement factor is comparable to similar results in the literature. These surfaces therefore provide a relatively reproducible, strong enhancement of the SERS signal and could be used as part of a diagnostic device.

The fluorescence signal was also significantly enhanced on the silver nanoparticle surfaces, by a factor of greater than 100. Although direct comparison to similar systems was not possible, as fluorescence enhancement factor is dependent on the fluorophore used, this result is impressive compared to similar literature studies, and the fluorescence signal was much more reproducible than the SERS signal. A strong, reproducible fluorescence signal is yielded from these surfaces, making them an ideal platform for fluorescence based diagnostics.

References

[1] Agrawal, V. V., Varghese, N., Kulkami, G. U., and Rao, C. N. R., *Langmuir*, 2008. **24**(6): 2494-2500.

[2] Banholzer, M. J., Millstone, J. E., Qin, L. D., and Mirkin, C. A., *Chem. Soc. Rev.*, 2008. **37**(5): 885-897.

[3] Zhang, J., Fu, Y., Chowdhury, M. H., and Lakowicz, J. R., *J. Phys. Chem. C*, 2008. **112**(1): 18-26.

[4] Haes, A. J., Zou, S. L., Zhao, J., Schatz, G. C., and Van Duyne, R. P., *Journal of the American Chemical Society*, 2006. **128**(33): 10905-10914.

[5] Jia, F. L., Yu, C. F., Ai, Z. H., and Zhang, L. Z., *Chem. Mat.*, 2007. **19**(15): 3648-3653.

[6] Daniel, M. C. and Astruc, D., *Chemical Reviews*, 2004. **104**(1): 293-346.

[7] El-Deab, M. S. and Ohsaka, T., *Electrochem. Commun.*, 2002. **4**(4): 288-292.

[8] Pradhan, N., Pal, A., and Pal, T., *Colloids and Surfaces a-Physicochemical and Engineering Aspects*, 2002. **196**(2-3): 247-257.

[9] Fort, E. and Gresillon, S., *J. Phys. D-Appl. Phys.*, 2008. **41**(1).

[10] Kim, S. S., Na, S. I., Jo, J., Kim, D. Y., and Nah, Y. C., *Applied Physics Letters*, 2008. **93**(7).

[11] Gunnarsson, L., Rindzevicius, T., Prikulis, J., Kasemo, B., Kall, M., Zou, S. L., and Schatz, G. C., *Journal of Physical Chemistry B*, 2005. **109**(3): 1079-1087.

[12] Jiang, J., Bosnick, K., Maillard, M., and Brus, L., *Journal of Physical Chemistry B*, 2003. **107**(37): 9964-9972.

[13] Moskovits, M., Tay, L. L., Yang, J., and Haslett, T., *Sers and the Single Molecule*, in *Optical Properties of Nanostructured Random Media*. 2002, Springer-Verlag Berlin: Berlin. p. 215-226.

[14] Bell, S. E. J. and Sirimuthu, N. M. S., *Chem. Soc. Rev.*, 2008. **37**(5): 1012-1024.

[15] Sheridan, E., Inya-Agha, O., Keyes, T., and Forster, R., *Electrodeposited Noble Metal Sers: Control of Single Nanoparticle Size and Control of Array Interparticle Spacing - Art. No. 64500u*, in *Plasmonics in Biology and Medicine Iv*, T. VoDinh and J.R. Lakowicz, Editors. 2007. p. U4500-U4500.

[16] Kneipp, K., Kneipp, H., Manoharan, R., Hanlon, E. B., Itzkan, I., Dasari, R. R., and Feld, M. S., *Applied Spectroscopy*, 1998. **52**(12): 1493-1497.

[17] Kneipp, K., Wang, Y., Kneipp, H., Perelman, L. T., Itzkan, I., Dasari, R., and Feld, M. S., *Physical Review Letters*, 1997. **78**(9): 1667-1670.

[18] Fu, Y., Zhang, J., and Lakowicz, J. R., *J. Fluoresc.*, 2007. **17**(6): 811-816.

[19] Fu, Y. and Lakowicz, J. R., *Journal of Physical Chemistry B*, 2006. **110**(45): 22557-22562.

[20] Zhu, Z. H., Zhu, T., and Liu, Z. F., *Nanotechnology*, 2004. **15**(3): 357-364.

[21] Emery, S. R., Haskins, W. E., and Nie, S. M., *Journal of the American Chemical Society*, 1998. **120**(31): 8009-8010.
[22] Nie, S. M. and Emery, S. R., *Science*, 1997. **275**(5303): 1102-1106.
[23] Zeman, E. J. and Schatz, G. C., *Journal of Physical Chemistry*, 1987. **91**(3): 634-643.
[24] Jin, R. C., Cao, Y. W., Mirkin, C. A., Kelly, K. L., Schatz, G. C., and Zheng, J. G., *Science*, 2001. **294**(5548): 1901-1903.
[25] Grabar, K. C., Freeman, R. G., Hommer, M. B., and Natan, M. J., *Analytical Chemistry*, 1995. **67**(4): 735-743.
[26] Michaels, A. M., Nirmal, M., and Brus, L. E., *Journal of the American Chemical Society*, 1999. **121**(43): 9932-9939.
[27] Chenal, C., Birke, R. L., and Lombardi, J. R., *Chemphyschem*, 2008. **9**(11): 1617-1623.
[28] Yu, Q. M., Guan, P., Qin, D., Golden, G., and Wallace, P. M., *Nano Letters*, 2008. **8**(7): 1923-1928.
[29] Fang, Y., Seong, N. H., and Dlott, D. D., *Science*, 2008. **321**(5887): 388-392.
[30] Mie, G., *Annalen der Physik*, 1908. **25**: 377-445.
[31] Creighton, J. A. and Eadon, D. G., *J. Chem. Soc.-Faraday Trans.*, 1991. **87**(24): 3881-3891.
[32] Granqvist, C. G. and Hunderi, O., *Phys. Rev. B*, 1977. **16**(8): 3513-3534.
[33] Mulvaney, P., *Langmuir*, 1996. **12**(3): 788-800.
[34] Link, S. and Ei-Sayed, M. A., *Annu. Rev. Phys. Chem.*, 2003. **54**: 331-366.
[35] Jensen, T., Kelly, L., Lazarides, A., and Schatz, G. C., *Journal of Cluster Science*, 1999. **10**(2): 295-317.
[36] Purcell, E. M. and Pennypac.Cr, *Astrophys. J.*, 1973. **186**(2): 705-714.
[37] Trasatti, S. and Petrii, O. A., *Pure and Applied Chemistry*, 1991. **63**(5): 711-734.
[38] El-Deab, M. S., Sotomura, T., and Ohsaka, T., *Journal of the Electrochemical Society*, 2005. **152**(1): C1-C6.
[39] Mayo, D., Miller, F., and Hannah, R., *Course Notes on the Interpretation of Inreared and Raman Spectra*. 2004, Hoboken: Wiley.
[40] Felidj, N., Truong, S. L., Aubard, J., Levi, G., Krenn, J. R., Hohenau, A., Leitner, A., and Aussenegg, F. R., *Journal of Chemical Physics*, 2004. **120**(15): 7141-7146.
[41] Vlckova, B., Gu, X. J., and Moskovits, M., *Journal of Physical Chemistry B*, 1997. **101**(9): 1588-1593.
[42] Kruszewski, S., *Crystal Research and Technology*, 2006. **41**(6): 562-569.
[43] Krug, J. T., Wang, G. D., Emory, S. R., and Nie, S. M., *Journal of the American Chemical Society*, 1999. **121**(39): 9208-9214.
[44] Sauer, G., Brehm, G., and Schneider, S., *Journal of Raman Spectroscopy*, 2004. **35**(7): 568-576.
[45] Bell, S. E. J. and Spence, S. J., *Analyst*, 2001. **126**(1): 1-3.
[46] Faulds, K., Smith, W. E., Graham, D., and Lacey, R. J., *Analyst*, 2002. **127**(2): 282-286.
[47] Zhang, J. and Lakowicz, J. R., *Journal of Physical Chemistry B*, 2006. **110**(5): 2387-2392.

[48] Sabanayagam, C. R. and Lakowicz, J. R., *Nucleic Acids Res.*, 2007. **35**(2).
[49] Huang, S. X. and Chen, Y., *Nano Letters*, 2008. **8**(9): 2829-2833.

5 Photo-Catalysis of Methyl Viologen Reduction by Polyoxometalate Associated with Osmium Complex

5.1 Introduction

Photocatalysis is an extremely important industrial process. It allows for reactions to proceed in the presence of light that would otherwise require other sources of energy in order to proceed. For example, the photocatalytic conversion of CO_2 by TiO_2 reduces emissions of the greenhouse gas, carbon dioxide, using less energy than conventional methods of CO_2 reduction, and can produce useful products such as methane or methanol [1]. An ideal catalytic reduction process would proceed as outlined in Scheme 1. In this Scheme a reduced species, immobilised on an electrode surface is irradiated, and becomes excited. The excited electron undergoes electron transfer to a second species adjacent to the electrode, either in solution or associated with the excited species, resulting in the second species being reduced, and the surface confined species being oxidised. Finally application of a potential can result in the surface confined species being reduced to its original electronic state so that it is ready to react again. The energy for the reduction reaction comes from the irradiation source, with the energy required to return the surface confined species to its original state being significantly less than required to reduce the second species.

An ideal candidate to perform the role of the surface confined species in Scheme 1 would be a strongly adsorbing, organometallic complex such as a transition metal polypyridyl complex. These absorb strongly in the visible region, readily form monolayers on suitable surfaces, and due to their metal-ligand structure possess excellent electron donor and acceptor abilities. An example molecule that could fill the role of reduced species is methyl viologen (MV^{2+}). However, many transition metal polypyridyl complexes are positively charged and the ability to control the electrostatic interaction of the photosensitizer and reaction substrate is important. For example, the

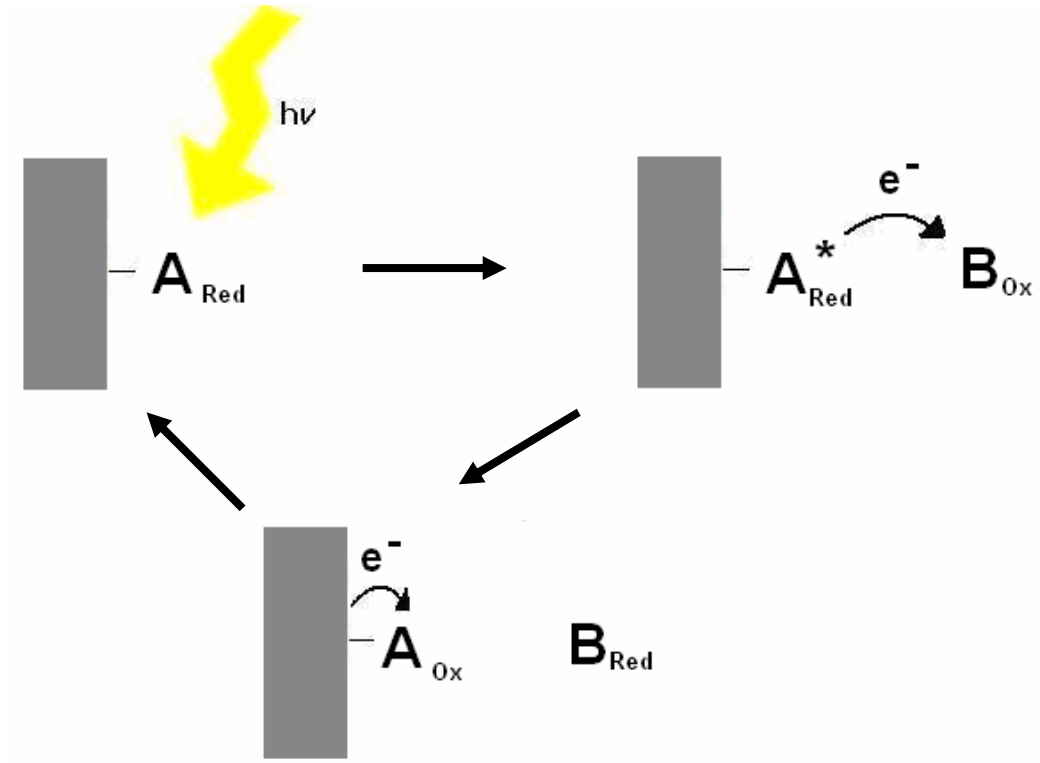

Scheme 1 Ideal photocatalytic reaction

positive charge on a transition metal polypyridyl complexes, and methyl viologen could lead to significant repulsion and a slow cross-reaction rate. Therefore, the ability to control the charge of the surface immobilised species is important. This can be achieved by binding a second component to the immobilised metal complex, which may also further optimise the thermodynamics of the system. For example, polyoxometalates carry anionic charge, and possess excellent electron donor and acceptor abilities. Polyoxometalate anions are known to readily quench the excited state of transition metal polypyridyl complexes via electron transfer, and when in the excited state themselves, are excellent electron donors [2].

Polyoxometalate anions such as the Dawson anion α-$[S_2W_{18}O_{62}]^{4-}$ (POW, Scheme 2) have become an important subject of investigation owing to their interesting redox properties, their catalytic properties and their diverse photochemistry [2-8]. One of the more interesting properties of polyoxometalates is their ability to catalyse many industrially important reactions, for example the photocatalytic degradation of 2,4-dichlorophenol (DCP) in aqueous media [9], the photocatalytic oxidation of cycloalkanes [10] and the photooxidative degradation of N-methylpyrrolidinone [11]. When photonically excited these complexes become powerful electron donors and acceptors [2]. However, a drawback to this technology is that polyoxometalates absorb only very weakly in the visible range, meaning excitation is normally only achieved under UV-light irradiation. For this reason, coupling of the polyoxometalate with a “sensitizer”, that can absorb light in the visible region and transfer the excited state to the polyoxometalate has become a topic of interest [2]. This could allow visible light excitation, rather than UV-light excitation, to be the driving force for important photo-catalytic reactions.

Interactions between polyoxometalate complexes and polypyridyl transition metal complexes such as $[Ru(bpy)_3]^{2+}$ have been of particular interest as the transition metal complex, with its strong absorbance in the visible region of the electromagnetic spectrum, can facilitate α-$[S_2W_{18}O_{62}]^{4-}$ (POW) and α

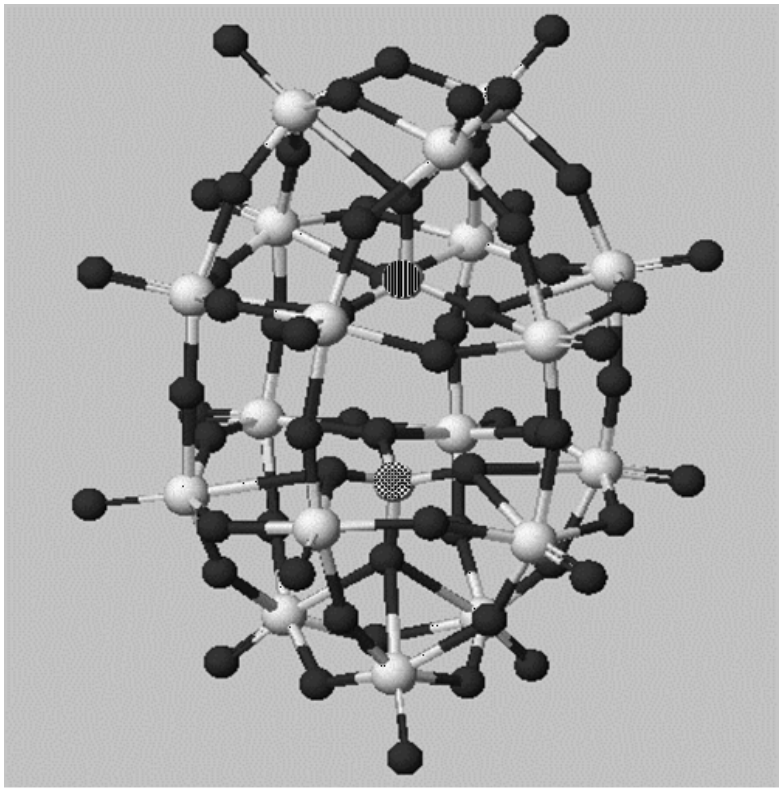

Scheme 2 Structure of α-$[S_2W_{18}O_{62}]^{4-}$

Elements: black = oxygen, white = tungsten, b&w = sulphur.

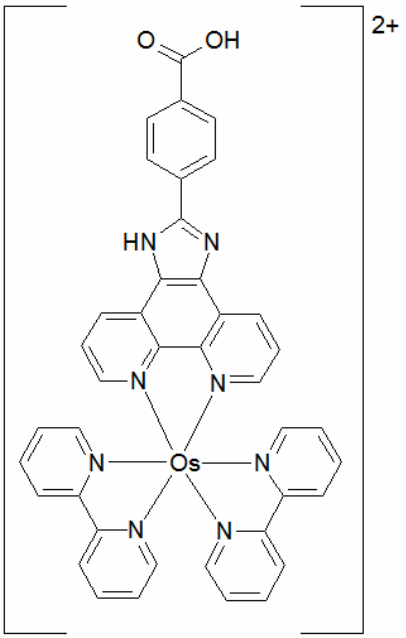

$[Os(bpy)_2PIC(H_2)]$

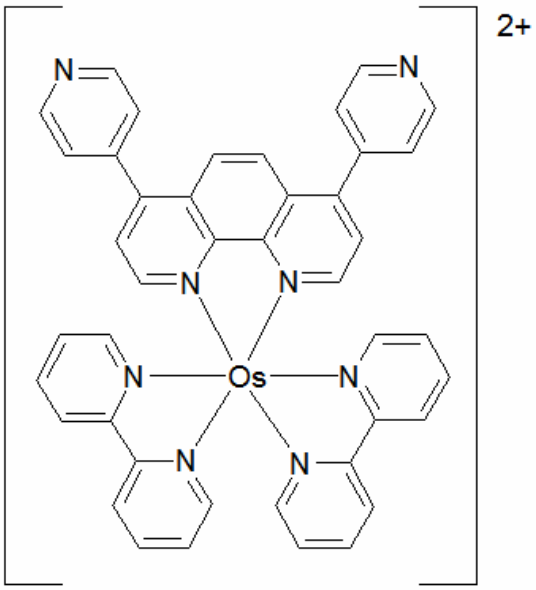

$[Os(bpy)_2Qby(ClO_4)_2]$

Scheme 3 Structure of $[Os(bpy)_2PIC]^{2+}$ and $[Os(bpy)_2Qby]^{2+}$

-$[S_2Mo_{18}O_{62}]^{4-}$ (POM) excitation with visible light. For example, it was demonstrated that α-$[S_2W_{18}O_{62}]^{4-}$ efficiently quenches the emission of $[Ru(bpy)_3]^{2+}$ through formation of a 1:1 and 1:2 (α-$[S_2W_{18}O_{62}]$:Ru) complex, via a static quenching mechanism in acetonitrile [3, 5]. Evidence for static association was derived from the presence of a novel, luminescent, inter-ion charge transfer transition, which was identified by resonance Raman spectroscopy as a $[Ru(bpy)_3]^{2+}$ to α-$[S_2Mo_{18}O_{62}]^{4-}$ charge transfer [3].

Keyes et al. have studied the influence of photo-excitation on the redox properties of some polyoxometalates [2]. α-$[S_2W_{18}O_{62}]^{4-}$ and α-$[S_2Mo_{18}O_{62}]^{4-}$ (POM) were excited with UV-irradiation (355 nm) in the presence of dimethylformamide (DMF), under these conditions the polyoxometalates were photo-reduced, with the concurrent oxidation of DMF, confirmed by spectro-electrochemistry [2]. The quantum yield for DMF oxidation was 2.0 x 10^{-2}, demonstrating the remarkable oxidative power of the excited state polyoxomolybdate [2]. However when the excitation source was in the visible region (420 nm) the process was significantly less efficient, with a quantum yield two orders of magnitude smaller (2 x 10^{-4}) [2]. This was a result of the poor absorption of visible light by polyoxometalates. However, when $[Ru(bpy)_3]^{2+}$ was added to the system the quantum yield for DMF oxidation increased from 2 x 10^{-4} to 8.1 x 10^{-3} under 420 nm excitation. This significant improvement in the photo-oxidation product is ascribed to the formation of a 1:1 and 1:2 α-$[S_2M_{18}O_{62}]$:Ru complex, displaying an optical transition allowing the complex to be excited by visible light [2]. Bond et al. have reported a similar photo-oxidation process, in this case the photo-oxidation of benzyl alcohol, ethanol, and menthol by α-$[S_2W_{18}O_{62}]^{4-}$ and α-$[S_2Mo_{18}O_{62}]^{4-}$, and the subsequent regeneration of the polyoxometalate by application of a potential, making it a photocatalytic process [12].

The excited state quenching ability of α-$[S_2W_{18}O_{62}]^{4-}$ could make it possible to use α-$[S_2W_{18}O_{62}]^{4-}$ as an electron acceptor to a polypyridyl complex, and to manage the electron transfer step by exciting the polypyridyl species. The resultant reduced α-$[S_2W_{18}O_{62}]^{5-}$ complex could then act as a strong reductant, and reduce available species in solution. Furthermore, the

polypyridyl complex can be returned to its original electronic state by application of a modest potential thus making this a photocatalytic reaction. The polypyridyl complexes investigated here were osmium polypyridyl complexes rather than ruthenium complexes. Osmium polypyridyl complexes display similar spectroscopic properties to ruthenium polypyridyl complexes, but their interactions with polyoxometalates have not been investigated to the same extent, particularly with reference to association of polyoxometalates with the polypyridyl complex.

In this chapter, the photocatalytic reduction of methyl viologen, on an optically transparent, conducting substrate with a large electrochemical window – fluorine-doped tin-oxide (FDTO), is reported. The polypyridyl complexes used to facilitate the catalytic reaction were $[Os(bpy)_2PIC(H_2)]$, where bpy is 2,2′-bipyridyl and PIC is 2-(4-carboxyphenyl)imidazo[4,5-f][1,10]phenanthroline, and $[Os(bpy)_2Qby(ClO_4)_2]$ (see Scheme 3), where Qbpy is 2,2':4,4'':4'4''-quarterpyridyl. These complexes were chosen because they display a strong absorbance and emission in the visible region (400-500 nm) so that they have the capacity to reduce α-$[S_2W_{18}O_{62}]^{4-}$ having been photo-excited by visible light. In addition the absorbance band of the osmium complexes overlaps with the surface plasmon band of silver nanoparticles (400-600 nm, see chapter 4), meaning resonant enhancement of the photocatalytic process might be possible. Also, the lower reduction potentials of Os^{3+} compared to MV^{2+} and α-$[S_2W_{18}O_{62}]^{4-}$ opens up the possibility to regenerate the catalyst at lower applied potentials

The desired photocatalytic reaction is outlined in Scheme 4. In step 1 an osmium complex is immobilised on the FDTO surface (or a silver nanoparticle decorated FDTO surface in the case of $[Os(bpy)_2Qby]^{2+}$). In step 2 the osmium complex is excited by a laser pulse (355 nm). In step 3 the excited electron is accepted by an α-$[S_2W_{18}O_{62}]^{4-}$ (POW^{4-}) molecule in solution, either by a collisional mechanism or by associative quenching. This results in a change in the charge of the osmium complex to 3+, and the electron acceptor becomes α-$[S_2W_{18}O_{62}]^{5-}$. The reduced α-$[S_2W_{18}O_{62}]^{5-}$ molecule can act as a powerful reductant, e.g. to reduce methyl viologen,

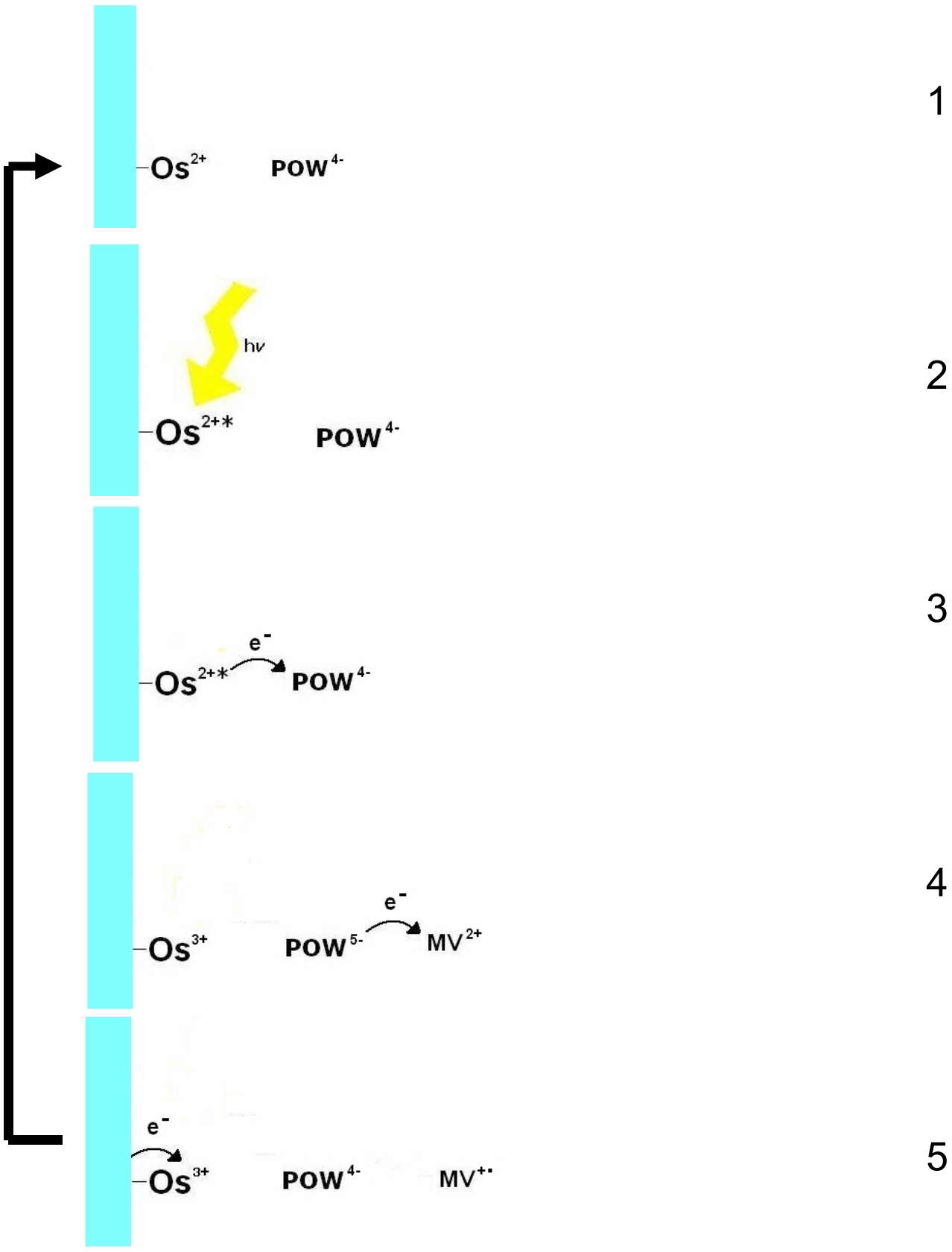

Scheme 4 Reaction scheme of methyl viologen photocatalytic reduction

this is seen in step 4. Finally, in step 5 If the FDTO electrode is held at a potential negative enough to reduce Os^{3+} to Os^{2+} the osmium complex is returned to its original state, and is ready to return to step 1, and therefore begin another catalytic cycle. Overall the osmium complex and α-$[S_2W_{18}O_{62}]$ molecule are returned to their original states, and the catalytic reaction can continue to proceed as long at the osmium complex is excited by the laser pulse, and there are un-reduced methyl viologen molecules in solution.

The potential of the electrode needs to be chosen such that it is sufficiently negative to reduce ground-state Os^{3+} to Os^{2+}, but not negative enough to directly reduce α-$[S_2W_{18}O_{62}]^{4-}$ or methyl viologen. The net outcome of the experiment is the reduction of methyl viologen at a potential at which it would normally not undergo reduction. There are several potential parasitic reactions, which could occur at various points during the photocatalytic reaction. During step 2 (Scheme 4) it is possible that the potential applied at the electrode is sufficient to oxidise or reduce Os^{2+}*, as this species is both a stronger oxidant and reductant than the ground state species. However, in order for this electron transfer to complete it must proceed faster than other potential pathways for the excited electron. The rate constant (k) for the back electron transfer (to the electrode) can be estimated at approximately 10^7 s^{-1} [13]. In the absence of α-$[S_2W_{18}O_{62}]^{4-}$ the back electron injection reaction is improbable as the excited state of Os^{2+}* lasts for approximately 50 ns, which does not allow sufficient time for oxidation/reduction of the excited state Os^{2+}* to occur. The rate constant for electron transfer from Os^{2+}* to α-$[S_2W_{18}O_{62}]^{4-}$ (step 3) is approximately 10^8 s^{-1}, meaning this reaction proceeds at a significantly faster rate than oxidation/reduction of Os^{2+}*, so in the presence of α-$[S_2W_{18}O_{62}]^{4-}$ the back electron injection would not be expected to occur either.

Another possibility is that, during step 3, the excited electron transfers directly from the osmium complex to methyl viologen. Moreover, it is likely that electrostatic effects influence the rate of this electron transfer since both osmium complex and methyl viologen ion are positively charged, resulting in

repulsive forces. Control experiments will be performed in order to confirm that these parasitic electron transfer reactions do not proceed. In step 4, it could be possible for electron transfer to occur from α-$[S_2W_{18}O_{62}]^{5-}$ to Os^{3+}. Transient absorption measurements have shown that regeneration of the Os^{3+} α-$[S_2W_{18}O_{62}]^{5-}$ pair (Step 4) to Os^{2+} α-$[S_2W_{18}O_{62}]^{4-}$ (Step 1) occurs in approximately 20 ns [14], meaning that in order for MV^{2+} reduction to proceed the rate of electron transfer from α-$[S_2W_{18}O_{62}]^{5-}$ to MV^{2+} must be faster than this.

A special electrochemical cell was designed in order to perform these experiments. The cell needed to allow electrolyte, a counter and reference electrode to be placed in contact with the FDTO working electrode, but at the same time the FDTO electrode needed to be facing upwards and have unobstructed access so that the laser could be incident on the surface. The cell was constructed from Teflon, and is represented schematically in Scheme 5. The FDTO electrode was secured to the base with Teflon tape, ensuring a tight seal was made so that electrolyte did not leak from the cell. This set-up facilitated exciting the surface with a laser excitation source whilst simultaneously applying a potential to the FDTO working electrode and measuring the current passing due to osmium reduction in the ground state.

In the first system $[Os(bpy)_2PIC(H_2)]$ was immobilised on bare (unmodified) FDTO. In the second system $[Os(bpy)_2Qby(ClO_4)_2]$ was immobilised on silver nanoparticles which have been formed on an FDTO surface by electrodeposition using the method described in Chapter 3. The potential advantage of using a silver nanoparticle modified surface is both the opportunity to control and increase the real surface area for the photocatalytic reaction, and the possibility to plasmonically enhance the osmium excitation and thus the rate of the photo-catalytic reaction, as the wavelengths of $[Os(bpy)_2Qbpy]^{2+}$ absorption (400-500 nm) and of electrodeposited silver nanoparticles surface plasmon band (400-600 nm) are coincident.

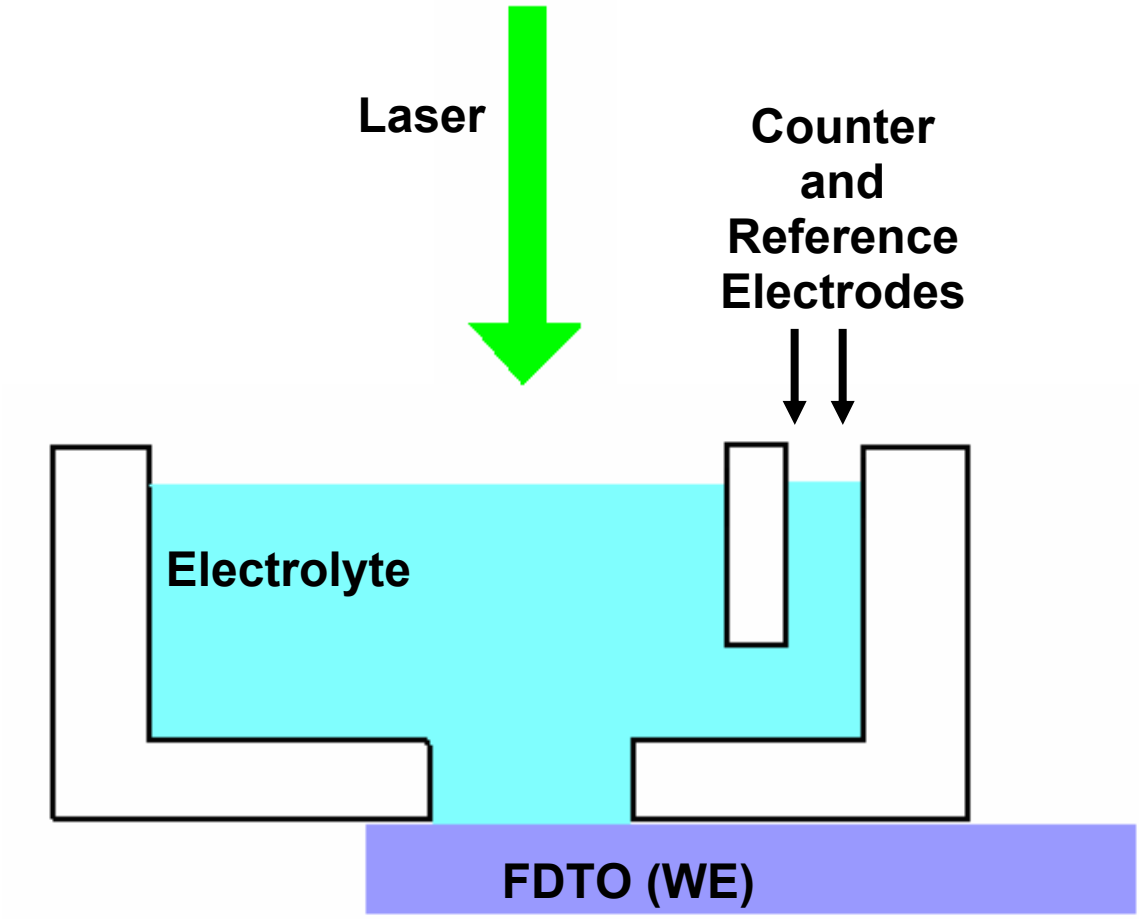

Scheme 5 Representation of cell used for photocatalytic experiments

Methyl viologen is used here as a model sacrificial electron acceptor. It is often used as an electron acceptor in photovoltaic cells [15, 16]. It forms a stable cation radical $MV^{+\cdot}$, and has been used as an electron relay in solar conversion systems [17]. The methyl viologen radical is very important industrially, for example $MV^{+\cdot}$ readily reduces oxygen to produce hydrogen peroxide, an extremely efficient and clean fuel [18]. Therefore, the potential applications of this work lie in solar energy conversion and in fuel-cell technology. This is most likely the fate of the methyl viologen radical in this reaction. The current experimental set-up does not allow for degassing of the electrolyte solution, so $MV^{+\cdot}$ most likely reacts with molecular oxygen in the electrolyte to produce hydrogen peroxide in an extremely rapid reaction.

Here the preparation, electrochemical and photophysical characterisation of spontaneously formed films of $[Os(bpy)_2PIC]^{2+}$ and $[Os(bpy)_2Qbpy]^{2+}$ is reported. The mechanism by which osmium emission is quenched by α-$[S_2W_{18}O_{62}]^{4-}$ is investigated, and the application of this set-up to photo-catalytically reduce methyl viologen is demonstrated.

5.2 Electrochemical Properties

In order to ascertain if excited state electron transfer from $[Os(bpy)_2PIC]^{2+}$ and $[Os(bpy)_2Qbpy]^{2+}$ to α-$[S_2W_{18}O_{62}]^{4-}$ is thermodynamically feasible, the electrochemistry of the polypyridyl complexes was characterised. Figure 5.1 shows solution phase cyclic voltammograms for $[Os(bpy)_2PIC]^{2+}$ and $[Os(bpy)_2Qbpy]^{2+}$ at an FDTO electrode. For both complexes, over this potential window, there is a one electron redox process evident, corresponding to the Os^{2+}/Os^{3+} couple. From these CVs we can estimate the formal potential of the complexes to be approximately 0.7 V for $[Os(bpy)_2PIC]^{2+}$ and approximately 0.8 V for $[Os(bpy)_2Qbpy]^{2+}$. Similar osmium complexes have been reported to have formal potentials in this range [19].

A fully reversible electron transfer process is signified by a peak to peak separation (ΔE_p) of 57 mV under conditions of semi-infinite linear diffusion control [20]. This is somewhat exceeded by both electron transfer processes which exhibit ΔE_p values of 97 mV ($[Os(bpy)_2PIC]^{2+}$) and 108 mV ($[Os(bpy)_2Qbpy]^{2+}$). However, the IR drop, uncompensated resistance, was estimated at approximately 30 mV for this system, owing to the large surface area of the working electrode and the relatively high resistance of acetonitrile. This accounts for the deviation from ideal peak separation. A plot of $\ln i_p$ versus $\ln v$ is linear over the range $0.1 \leq v \geq 1$ V s^{-1} (figure 5.1, inset) indicating the process is diffusion limited.

Figure 5.2 shows scan rate dependant cyclic voltammograms of an $[Os(bpy)_2PIC]^{2+}$ monolayer formed on an FDTO electrode by immersion of the electrode in a 1 mM methanolic solution of the complex for 48 hours. The peak current increases linearly with scan rate, rather than the $v^{1/2}$ dependence expected for a species in solution, indicating the species remains surface confined. The surface coverage, estimated based on the charge passed during the complex reduction, was 1.1 ± 0.2 x 10^{-10} mol cm^{-2}, this indicates the presence of a densely packed monolayer on the surface. It

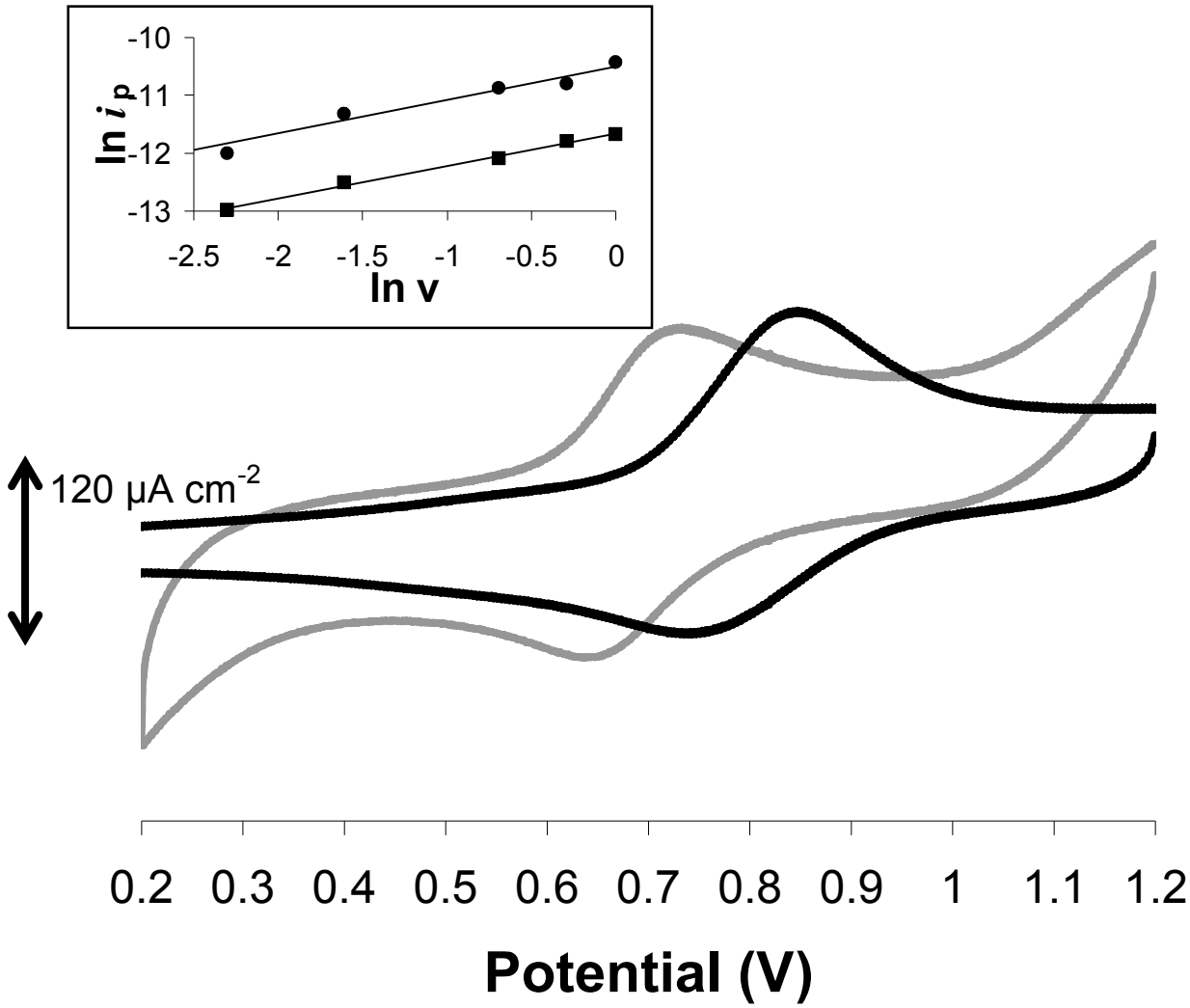

Figure 5.1 Solution phase CVs of $[Os(bpy)_2PIC]^{2+}$ (grey line) and $[Os(bpy)_2Qbpy]^{2+}$ (black line) in 0.1 M $LiClO_4$ in acetonitrile at 0.2 v s^{-1}. Anodic (oxidative) currents are positive. In both cases the solution phase concentration was 1 mM. The working electrode was FDTO of geometric surface area 0.25 cm^2 ($[Os(bpy)_2PIC]^{2+}$) or 0.1 cm^2 ($[Os(bpy)_2Qbpy]^{2+}$). Inset plot of ln ip vs ln v for $[Os(bpy)_2PIC]^{2+}$ (boxes) and $[Os(bpy)_2Qbpy]^{2+}$ (circles).

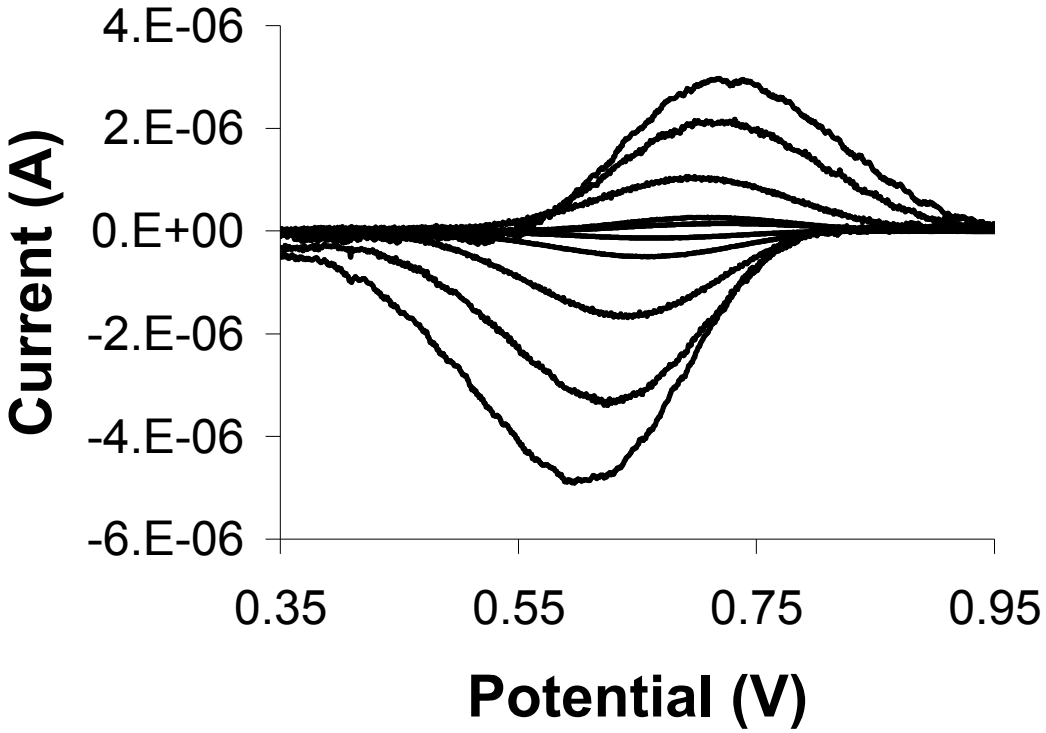

Figure 5.2 Cyclic voltammograms of dense $[Os(bpy)_2PIC]^{2+}$ monolayer spontaneously adsorbed onto FDTO surface (geometric surface area = 0.25 cm^2) in 0.1 M $LiClO_4$. Scan rates (top to bottom) were 1.0, 0.5, 0.1, 0.05 and 0.01 V s^{-1}. Anodic (oxidative) currents are positive. Cvs were baseline corrected using a CHI software orthogonal least square algorithm.

should be noted that although for a complex of approximate diameter 1 nm the footprint area might be expected to facilitate as much as 2.1 x 10^{-10} mol cm^{-2}, the actual occupied area is larger than the footprint area of the molecules due to the presence of a solvation shell, and counter-ions surrounding each molecule. Consequently, the actual area on the surface of each $[Os(bpy)_2PIC]^{2+}$ molecule is significantly larger than its diameter suggests, so a coverage of 1.1 ± 0.25 x 10^{-10} mol cm^{-2} can be considered densely packed.

The formal potential of the $[Os(bpy)_2PIC]^{2+}$ complex shifts in the negative direction by about 30 mV upon assembly on the surface, indicating that the species is more easily oxidised when immobilised on the surface. The full width at half maximum (FWHM) is expected to be approximately 90 mV for both cathodic and anodic waves of an immobilised species displaying no lateral interactions. In Figure 5.2 the FWHM is approximately 200 mV, suggesting that there are repulsive interactions between adjacent adsorbates on the surface, or perhaps the presence of a distribution of formal potentials on the surface. Upon scanning repetitively over 12 hours the peak height dropped by approximately 50 %, suggesting that the monolayer is only moderately stable over time, so the modified electrodes were not removed from the deposition solution until they were ready to be used.

The complex $[Os(bpy)_2Qbpy]^{2+}$ does not form a stable monolayer on the FDTO surface so for the purposes of these experiments it was immobilised on silver nanoparticle covered FDTO. It was not possible to probe the electrochemistry of $[Os(bpy)_2Qbpy]^{2+}$ immobilised on a silver nanoparticle surface as the available electrochemical potential window on silver electrodes does not cover the formal potential of $[Os(bpy)_2Qbpy]^{2+}$. It has been reported that a similar polypyridyl complex, $[Ru(bpy)_2Qbpy]^{2+}$, forms stable, densely packed monolayers on platinum, with a first-order rate constant for adsorption of 5.1 $\pm$ 0.2 x 10^{-6} s^{-1} [21]. Raman spectroscopy of the silver nanoparticle coated FDTO surface, containing a monolayer of $[Os(bpy)_2Qbpy]^{2+}$ confirmed the presence of $[Os(bpy)_2Qbpy]^{2+}$ on the surface. This is shown in Figure 5.3. As described in Chapter 4, the two-

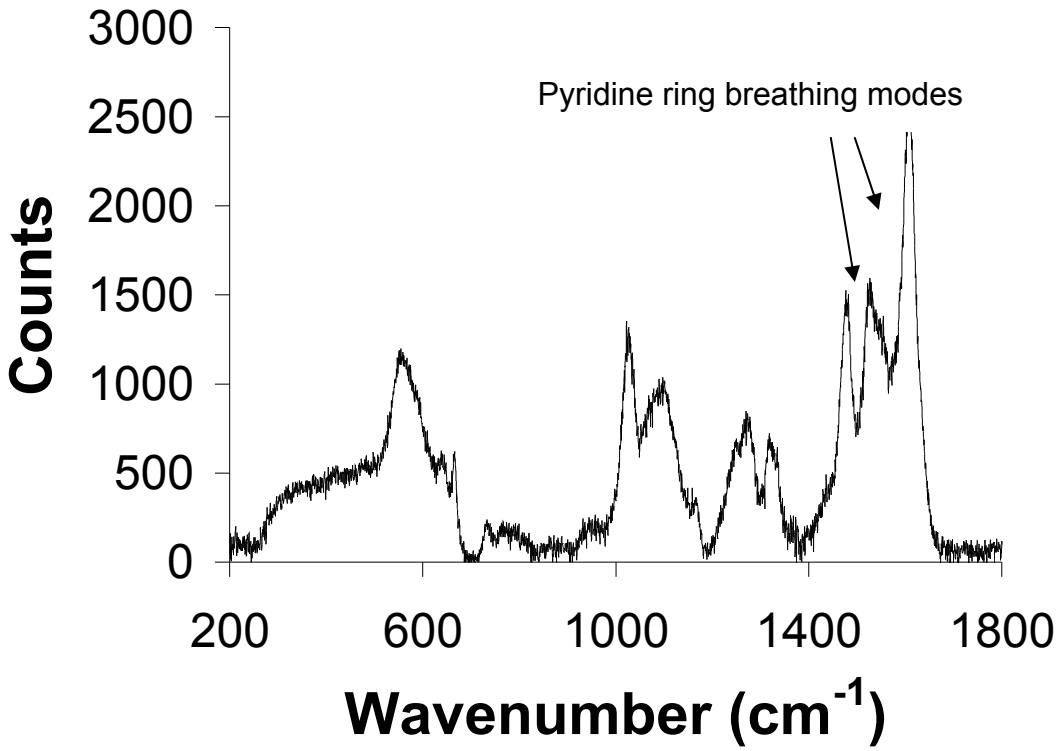

Figure 5.3 Raman spectrum recorded of $[Os(bpy)_2Qbpy]^{2+}$ on FDTO surface electrodeposited with isolated silver nanoparticles of mean diameter 105 nm, mean interparticle separation was 427 nm, excitation wavelength was 514 nm.

peaks centred around 1600 cm^{-1} is indicative of pyridine breathing modes. This spectrum was recorded from the sample surface, in air, having deposited $[Os(bpy)_2Qbpy]^{2+}$ on the surface from a 1 mM methanolic solution. The surface was washed with methanol before the spectrum was acquired, to ensure only strongly adsorbed species were detected. It appears that the spectrum is resonantly enhanced (SERRS), the 514 nm excitation would resonantly enhance the metal to ligand charge transfer (MLCT) of $[Os(bpy)_2Qbpy]^{2+}$. This explains why the two bands at 1600 cm^{-1} are enhanced, while other Raman modes are not. Pyridines are known to adsorb strongly on silver and other metal surfaces, forming closely packed monolayers [22]. This result confirms the presence of $[Os(bpy)_2Qbpy]^{2+}$ adsorbed on the silver nanoparticle modified surface.

5.3 Thermodynamics

The influence of polyoxometalates such as α-$[S_2Mo_{18}O_{62}]^{4-}$ and α-$[S_2W_{18}O_{62}]^{4-}$ on the emission of luminescent transition metal polypyridyl complexes similar to $[Os(bpy)_2Qbpy]^{2+}$ and $[Os(bpy)_2PIC]^{2+}$ has been demonstrated by Keyes et al. [2, 3]. As discussed in the introduction, it was shown that the emission of $[Ru(bpy)_3]^{2+}$ was quenched by α-$[S_2Mo_{18}O_{62}]^{4-}$ through a static quenching mechanism, that involved transfer of an electron from the polypyridyl complex, to the polyoxometalate [3]. To determine if electron transfer is possible in the systems under examination in this study the thermodynamics of the electron transfer were probed.

5.3.1 Low Temperature Emission

In this present work, a photocatalytic reaction is under investigation. A crucial step in the photocatalytic reaction is an electron transfer from excited state $[Os(bpy)_2PIC]^{2+*}$ and $[Os(bpy)_2Qbpy]^{2+*}$ to α-$[S_2W_{18}O_{62}]^{4-}$. A modified form of the Rehm-Weller equation can be used to determine if electron transfer from $[Os(bpy)_2PIC]^{2+}$ and $[Os(bpy)_2Qbpy]^{2+}$ to α-$[S_2W_{18}O_{62}]^{4-}$ (i.e. emission quenching) is energetically favourable [23]:

$$\Delta G = E^0_{D/D^+} - E^0_{A/A^-} - E^*_{00} \qquad (5.1)$$

Where ΔG is the Gibbs free energy, E^0_{D/D^+} is the formal potential of the donor (the osmium complex, determined in section 5.2), E^0_{A/A^-} is the formal potential of the acceptor (α-$[S_2W_{18}O_{62}]^{4-}$, -0.235 V [2]), E^*_{00} is the excited state energy of the osmium complex, which can be determined from the low temperature emission spectrum (Figure 5.4).

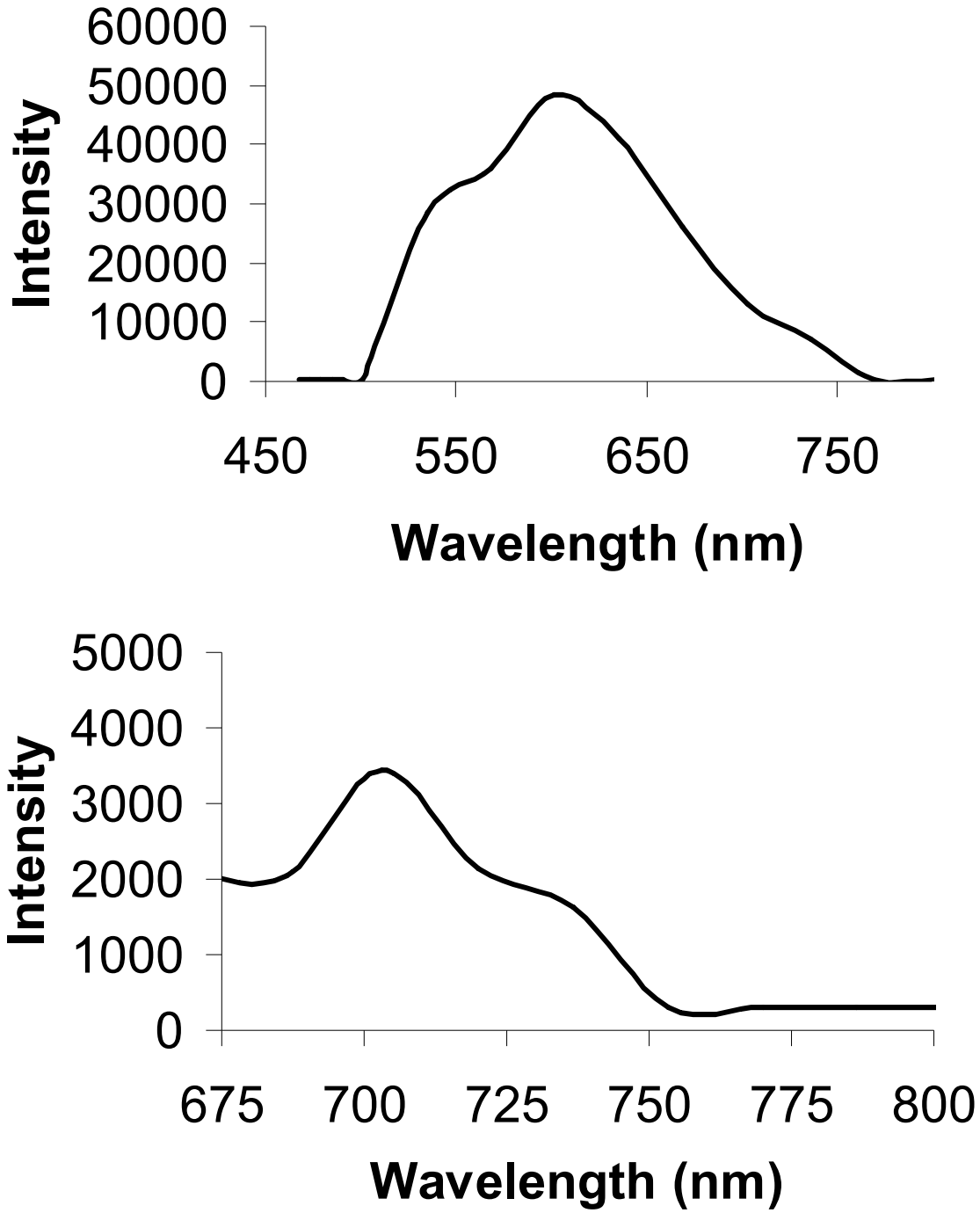

Figure 5.4 Low temperature (77 K) emission spectrum of $[Os(bpy)_2Qbpy]^{2+}$ (top) and $[Os(bpy)_2PIC]^{2+}$ (bottom) at a concentration of 10 μM in butyronitrile: propionitrile (55:45), with 355 nm excitation.

For $[Os(bpy)_2Qbpy]^{2+}$ the low temperature emission maximum was at 602 nm (2.06 eV) (Figure 5.4, Top).

Substituting into eq. 5.1 gives:

$$\Delta G = 0.8\text{ V} - (-0.235\text{ V}) - 2.06\text{ eV}$$
$$\Delta G = -1.025\text{ V}$$

As ΔG is negative the electron transfer reaction from $[Os(bpy)_2Qbpy]^{2+}$ to α-$[S_2W_{18}O_{62}]^{4-}$ is predicted to be exergonic. Similarly $[Os(bpy)_2PIC]^{2+}$ had a maximum emission of 703 nm at 77 K, giving an excited state energy (E^*_{00}) of 1.76 eV, and ΔG = -0.725 eV. Therefore, the electron transfer from both osmium complexes, to α-$[S_2W_{18}O_{62}]^4$ is exergonic, and the driving forces are similar for both electron transfers.

5.4 Quenching Mechanism

The two most commonly encountered mechanisms of emission quenching in solution are static or associative quenching and dynamic or collisional quenching. Dynamic quenching involves diffusive encounters between the emissive species and quencher in solution, during the excited state lifetime of the emitter [24]. During such events, the excited electron on the emissive species either returns to the ground state without emission, by energy transfer, for example, or is transferred to the quencher (without emission). Static quenching is a result of the formation of non-luminescent complex between the luminophore and quencher such that absorption of a photon of light results in a return to the ground state without emission, and may or may not result in a transfer of an electron from the luminophore to the quencher [24]. Understanding the mechanism by which α-$[S_2W_{18}O_{62}]^{4-}$ quenches the emission of the osmium polypyridyl complexes is very important to these studies as it gives important information about the limiting factors in the photocatalytic reaction, and allows the theoretical current from the photo-catalytic experiment to be estimated.

5.4.1 Quenching Studies

Having predicted that electron transfer from the osmium polypyridyl complexes to α-$[S_2W_{18}O_{62}]^{4-}$ is exergonic, the emission properties of both complexes were studied in the presence of α-$[S_2W_{18}O_{62}]^{4-}$ to determine if the osmium emission was quenched. The emission intensities of $[Os(bpy)_2PIC]^{2+}$ and $[Os(bpy)_2Qbpy]^{2+}$ were monitored as the concentration of quencher (α-$[S_2W_{18}O_{62}]^{4-}$) was increased, the results are presented in Figures 5.5 and 5.6. As the concentration of α-$[S_2W_{18}O_{62}]^{4-}$ was increased the emission intensity decreased until the emission was completely quenched when the mole ratio (Os : α-$[S_2W_{18}O_{62}]^{4-}$) was 10:6. This result was similar to the results of Keyes et al. [2, 3], where it was demonstrated that the addition of increasing concentrations of $LiClO_4$ to the quenched $[Ru(bpy)_3]^{2+}$ solution resulted in the emission recovery to the same intensity as the emitter in the absence of quencher [3]. This was attributed to dissociation of the electrostatically bound ion clusters due to competitive interaction of perchlorate with $[Ru(bpy)_3]^{2+}$ and lithium with α-$[S_2W_{18}O_{62}]^{4-}$, forming stronger ion pairs. The same effect was not observed here and the emission of neither complex recovers upon addition of excess $LiClO_4$. This could indicate a stronger electrostatic interaction between the osmium complexes and α-$[S_2W_{18}O_{62}]^{4-}$, or it could indicate that unlike $[Ru(bpy)_3]^{2+}$, which was quenched by a static quenching mechanism by α-$[S_2W_{18}O_{62}]^{4-}$, the osmium complexes could be quenched by a dynamic or mixed static-dynamic quenching mechanism. To probe this issue further, luminescent lifetimes were recorded.

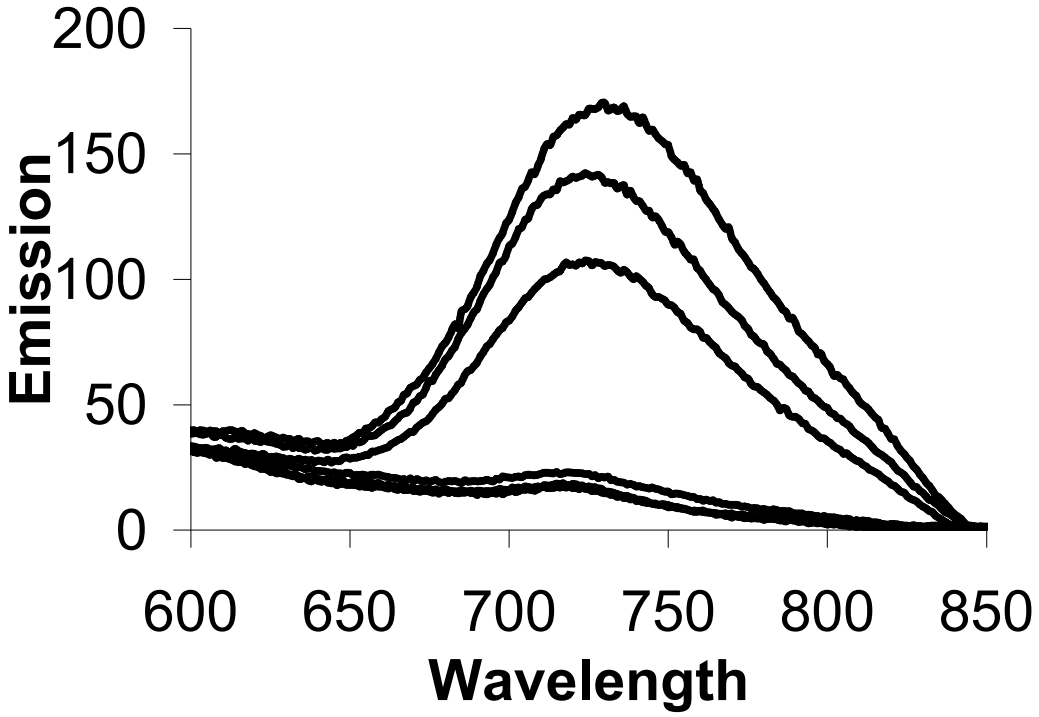

Figure 5.5 Emission Spectra of 10 μM $[Os(bpy)_2PIC]^{2+}$ in acetonitrile with 450nm excitation in the presence of 0 μM, 0.5 μM, 1 μM, 2 μM and 10 μM α-$[S_2W_{18}O_{62}]^{4-}$ (top spectrum to bottom spectrum respectively).

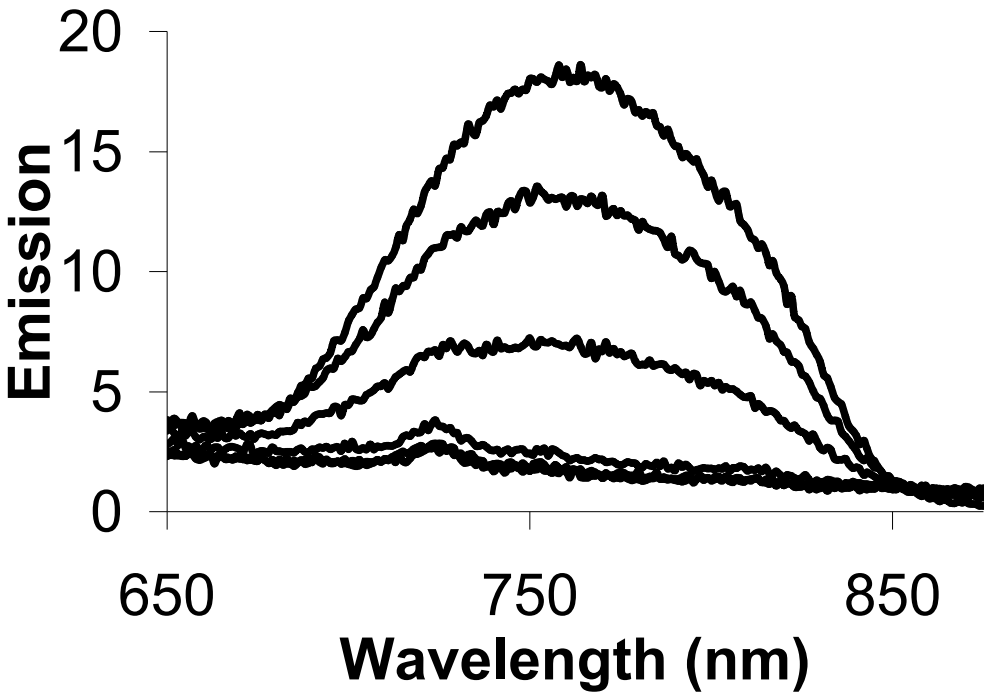

Figure 5.6 Emission Spectra of 10 μM $[Os(bpy)_2Qbpy]^{2+}$ in acetonitrile with 450nm excitation in the presence of 0 μM, 2 μM, 4 μM, 6 μM, 8 μM and 10 μM α-$[S_2W_{18}O_{62}]^{4-}$ (top spectrum to bottom spectrum respectively).

5.4.2 Absorption Spectroscopy

The operation of a static quenching mechanism for $[Os(bpy)_2Qbpy]^{2+}$ quenching by α-$[S_2W_{18}O_{62}]^{4-}$ is evidenced by the presence of a new optical transition in the UV-Vis difference spectrum shown in Figure 5.7. In this Figure, the absorbance spectra of $[Os(bpy)_2Qbpy]^{2+}$ and α-$[S_2W_{18}O_{62}]^{4-}$ recorded separately in solution, were subtracted from the absorbance spectrum of quenched $[Os(bpy)_2Qbpy]^{2+}$ to give a spectrum showing only transitions resulting from an associated complex between $[Os(bpy)_2Qbpy]^{2+}$ and α-$[S_2W_{18}O_{62}]^{4-}$. The new optical transition, seen at 550 nm, is suggestive of the formation of an associated complex between $[Os(bpy)_2Qbpy]^{2+}$ and α-$[S_2W_{18}O_{62}]^{4-}$. The absorption peak present at 550 nm is present only in the spectrum of quenched $[Os(bpy)_2Qbpy]^{2+}$, and not in the absorption spectra of either $[Os(bpy)_2Qbpy]^{2+}$ or α-$[S_2W_{18}O_{62}]^{4-}$ on their own (Figure 5.8). However, the presence of a static quenching mechanism does not rule out the possibility that dynamic quenching is also occurring simultaneously, as mixed quenching is quite common [25]. A similar transition was also evident in the difference spectrum for $[Os(bpy)_2PIC]^{2+}$ quenching by α-$[S_2W_{18}O_{62}]^{4-}$.

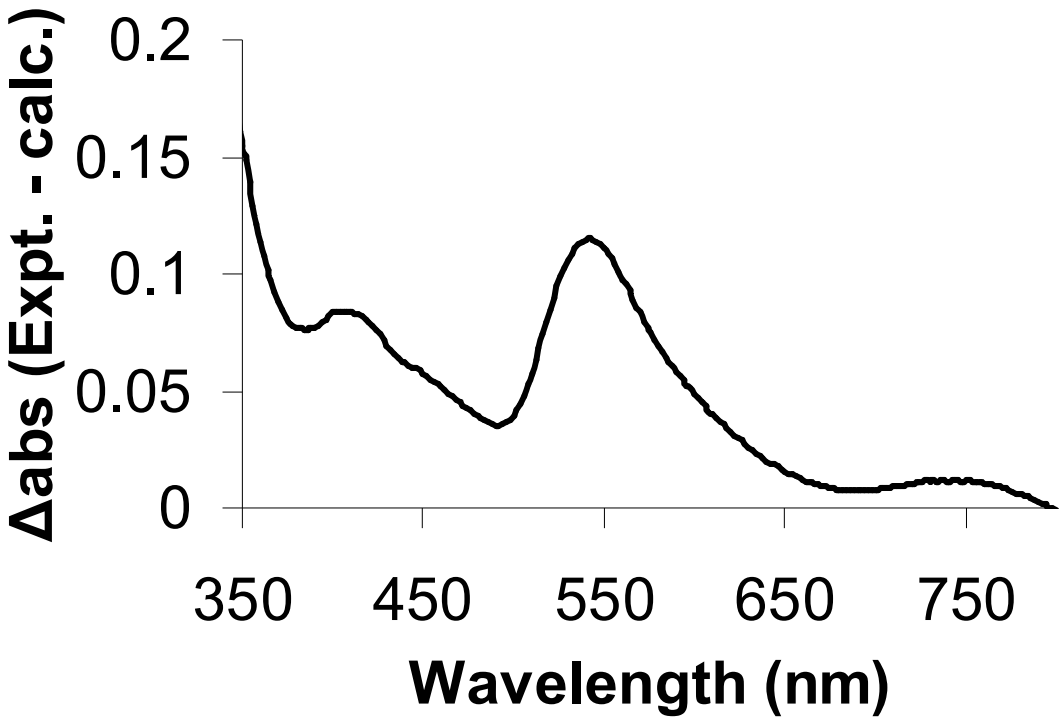

Figure 5.7 Difference UV-Vis spectrum (spectrum of quenched solution – spectra of $[Os(bpy)_2Qbpy]^{2+}$ and α-$[S_2W_{18}O_{62}]^{4-}$ recorded separately) for $[Os(bpy)_2Qbpy]^{2+}$ (10 μM) and α-$[S_2W_{18}O_{62}]^{4-}$ (10 μM) in acetonitrile.

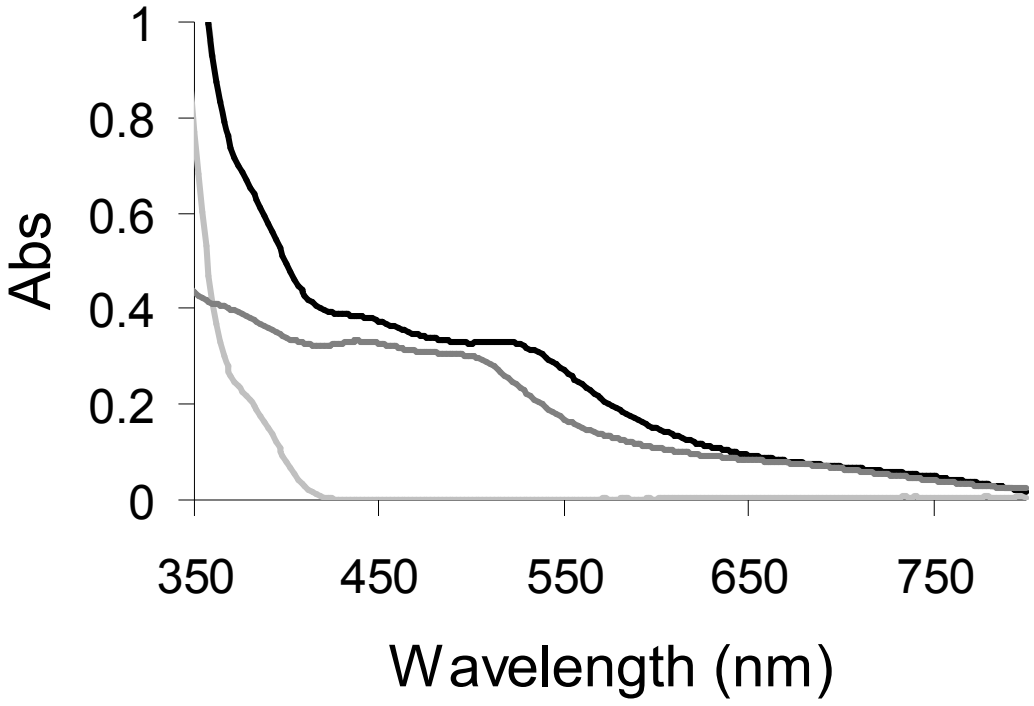

Figure 5.8 UV-Vis spectrum spectra of $[Os(bpy)_2Qbpy]^{2+}$ and α-$[S_2W_{18}O_{62}]^{4-}$ (10 μM) in acetonitrile (black), $[Os(bpy)_2Qbpy]^{2+}$ (10 μM) in acetonitrile (dark grey) and α-$[S_2W_{18}O_{62}]^{4-}$ (10 μM) in acetonitrile (light grey).

5.4.3 Luminescence Lifetimes

Luminescence lifetimes can be used to further probe the quenching mechanism. Static quenching typically results in a decrease in emission intensity, but no change in emission lifetime. Dynamic quenching, on the other hand, results in a decrease in both the emission intensity and the emission lifetime. The luminescence lifetime of both osmium complexes decreased as the concentration of α-$[S_2W_{18}O_{62}]^{4-}$ was increased. This is reflected in the emission decays presented in Figure 5.9 for $[Os(bpy)_2Qbpy]^{2+}$ in acetonitrile. These decays were fitted with sigma-plot software, and all decays were single exponential, indicating that there was only a single emissive species, and that the new transition, evident in the UV-Vis difference spectrum did not result in an emission. In this series of decays the lifetime changes from an initial value of 53 ns in the absence of quencher to a final value of 10 ns.

To understand the nature of the quenching mechanism Stern-Volmer plots were prepared based on the luminescence intensity and lifetimes, see Figure 5.11. The emission intensity plot for $[Os(bpy)_2PIC]^{2+}$ (top) displays an upward curvature characteristic of combined dynamic and static quenching [24]. The lifetime plot displays a straight line with a very small slope. While the decreasing lifetime is indicative of the presence of dynamic quenching, the significantly smaller slope further supports the conclusion that combined static and dynamic quenching is occurring. Similar results were recorded for $[Os(bpy)_2Qbpy]^{2+}$ (Figure 5.11, bottom), the luminescence intensity Stern-Volmer plot curves upwards and the lifetime plot is linear with a small slope again indicating that combined static and dynamic quenching occur for the pairing of $[Os(bpy)_2Qbpy]^{2+}$ with α-$[S_2W_{18}O_{62}]^{4-}$.

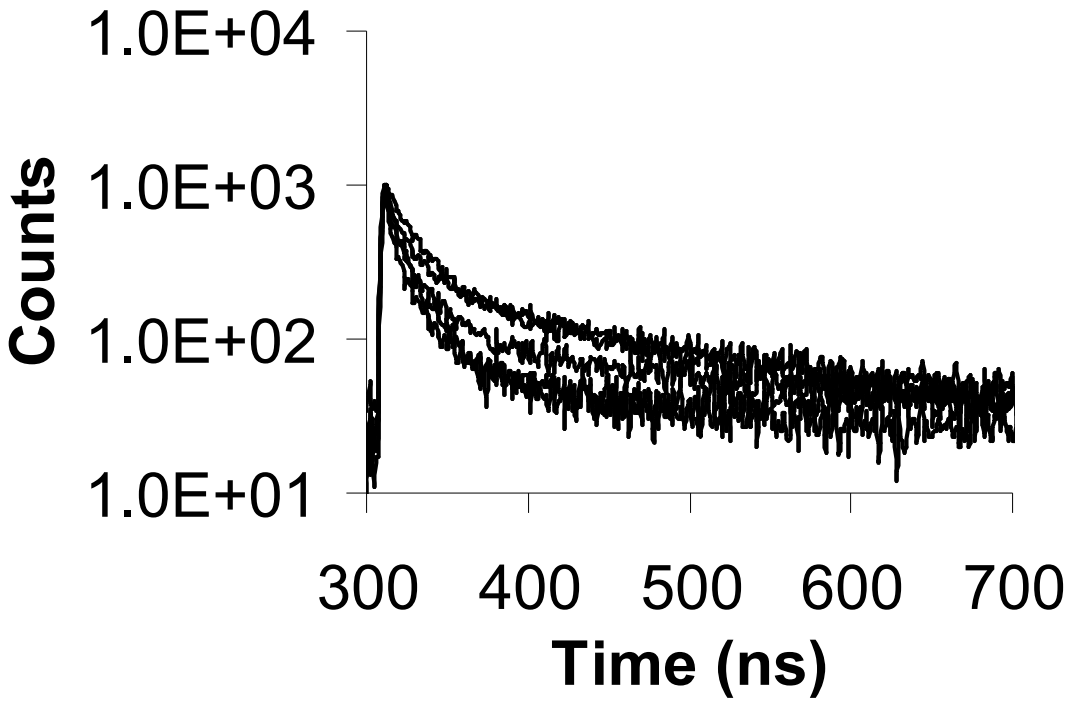

Figure 5.9 Luminescence lifetime decays of 10 μM $[Os(bpy)_2Qbpy]^{2+}$ in acetonitrile with 450nm excitation in the presence of 0 μM, 2 μM, 4 μM, 6 μM, 8 μM and 10 μM α-$[S_2W_{18}O_{62}]^{4-}$.

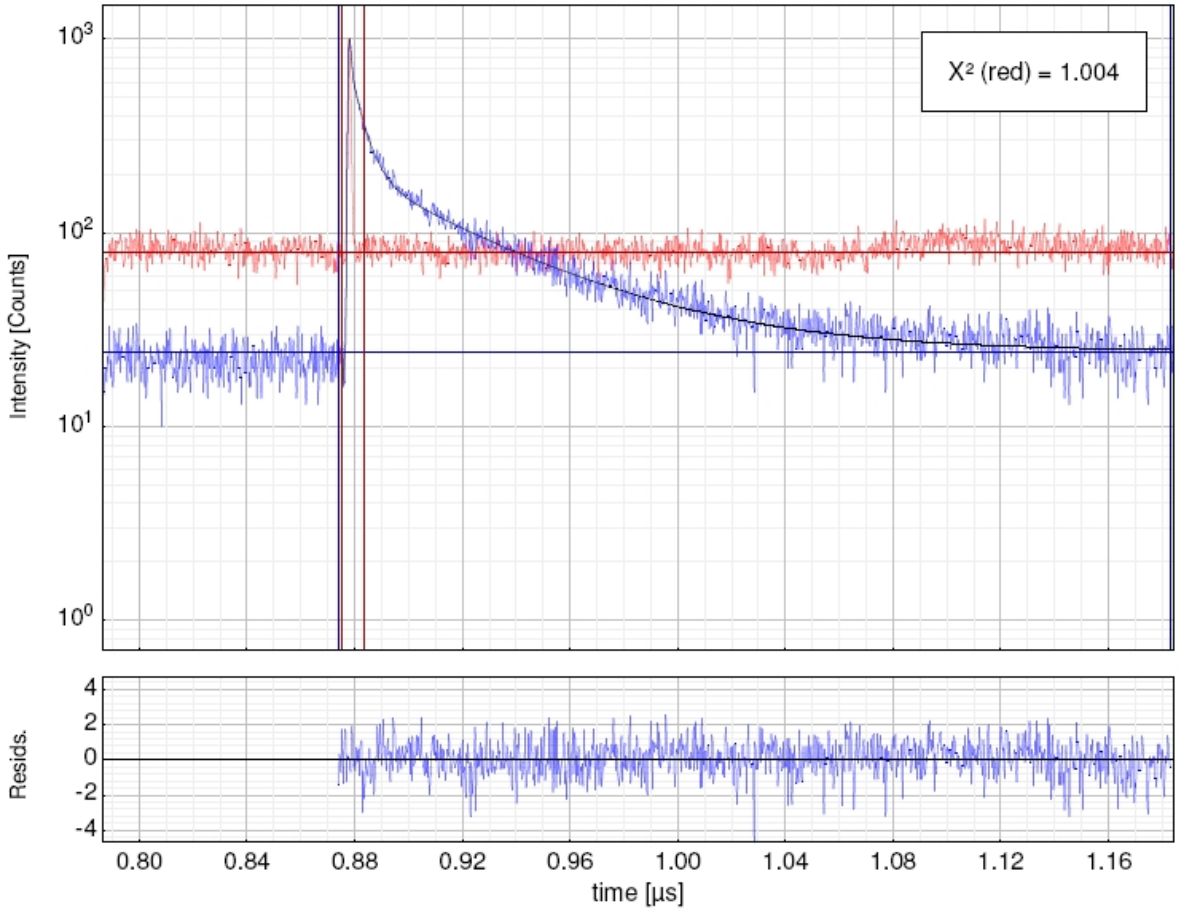

Figure 5.10 Fitting of lifetime decay performed by picoquant software for sample containing 10 µM $[Os(bpy)_2Qbpy]^{2+}$ in acetonitrile with 450nm excitation in the presence 2 µM α-$[S_2W_{18}O_{62}]^{4-}$. Black line is fit to experimental data (blue line). Red line is the instrument response function

If the intensity Stern-Volmer plots are divided into two separate regions, one at low α-$[S_2W_{18}O_{62}]^{4-}$ concentrations, and one at higher α-$[S_2W_{18}O_{62}]^{4-}$ concentrations, greater insight into the nature of the quenching mechanism can be gained. In the case of $[Os(bpy)_2PIC]^{2+}$ quenching, it appears that at concentrations $\leq$ 1 μM α-$[S_2W_{18}O_{62}]^{4-}$ the Stern-Volmer plot of I_0/I and τ_0/τ coincide (See Figure 5.11, top). However, the slopes (0.33 and 0.22 respectively) indicate that these plots do not coincide, so it is likely that static quenching dominates in this concentration range.

At α-$[S_2W_{18}O_{62}]^{4-}$ concentrations greater than 1 μM the I_0/I curve increases rapidly, and the τ_0/τ curve has a significantly smaller slope. The slope of the lifetime plot yields the Stern-Volmer constant (K_{SV}), from which the dynamic quenching rate constant (K_q) can be determined.

$$K_q = \frac{K_{SV}}{\tau_0} \tag{5.2}$$

K_{SV} = 0.2173 μM^{-1}

= 217300 M^{-1}

τ_0 = 65.33 ns

= 6.53 x 10^{-8} s^{-1}

giving

K_q = 3.33 x 10^{12} L mol^{-1} s^{-1}

This value for the dynamic quenching constant is much larger than expected, for purely dynamic processes it is normally approximately 10^{10}, this suggests that the system is more complex than first thought. A possible explanation for the extremely large dynamic quenching constant is that in this higher α-$[S_2W_{18}O_{62}]^{4-}$ concentration range the couple α-$[S_2W_{18}O_{62}]([Os(bpy)_2PIC])_2$ forms, which could be luminescent, and its luminescence is being quenched dynamically by α-$[S_2W_{18}O_{62}]^{4-}$.

The same pattern was observed for the quenching of $[Os(bpy)_2Qbpy]^{2+}$ (Figure 5.11, bottom). The quenching mechanism appears to be dominated by static quenching below the α-$[S_2W_{18}O_{62}]^{4-}$ concentration of 3 μM, and above this concentration the mechanism is complicated, having a dynamic quenching constant (K_q) of 3.57 x 10^{12} L mol^{-1} s^{-1}. This is perhaps due to the formation of α-$[S_2W_{18}O_{62}]([Os(bpy)_2Qbpy])_2$ at higher concentrations, and quenching of its luminescence by α-$[S_2W_{18}O_{62}]^{4-}$.

These results are in agreement with similar studies performed on ruthenium polypyridyl complexes quenched by polyoxometalate anions, where the quenching mechanism was shown to be principally static in nature, but also has a dynamic component [25]. Significantly, the ratio of luminophore to quencher at which nearly all emission was quenched was 10:6 (Os: α-$[S_2W_{18}O_{62}]^{4-}$) for both systems under investigation in this study. This contrasts significantly with the studies of Keyes et al. and Bond et al. where the ratio was typically 1:10 [2-4]. The ratio at which complete quenching occurred could suggest that, in solution, the α-$[S_2W_{18}O_{62}]^{4-}$ molecule associates with two osmium complexes giving a very efficient quenching. The formation of the 2:1 complex in solution has been reported for similar systems [3, 25]. It is likely that upon immobilisation of the osmium complexes on the surface that the 2:1 complex was less likely to form as it would be difficult for a single α-$[S_2W_{18}O_{62}]^{4-}$ complex to interact with two immobilised osmium complexes simultaneously, so a 1:1 complex, which has also been reported, most likely dominates in this configuration [3, 25]. If this is the case then static quenching is expected to dominate when the osmium complexes are immobilised on a surface.

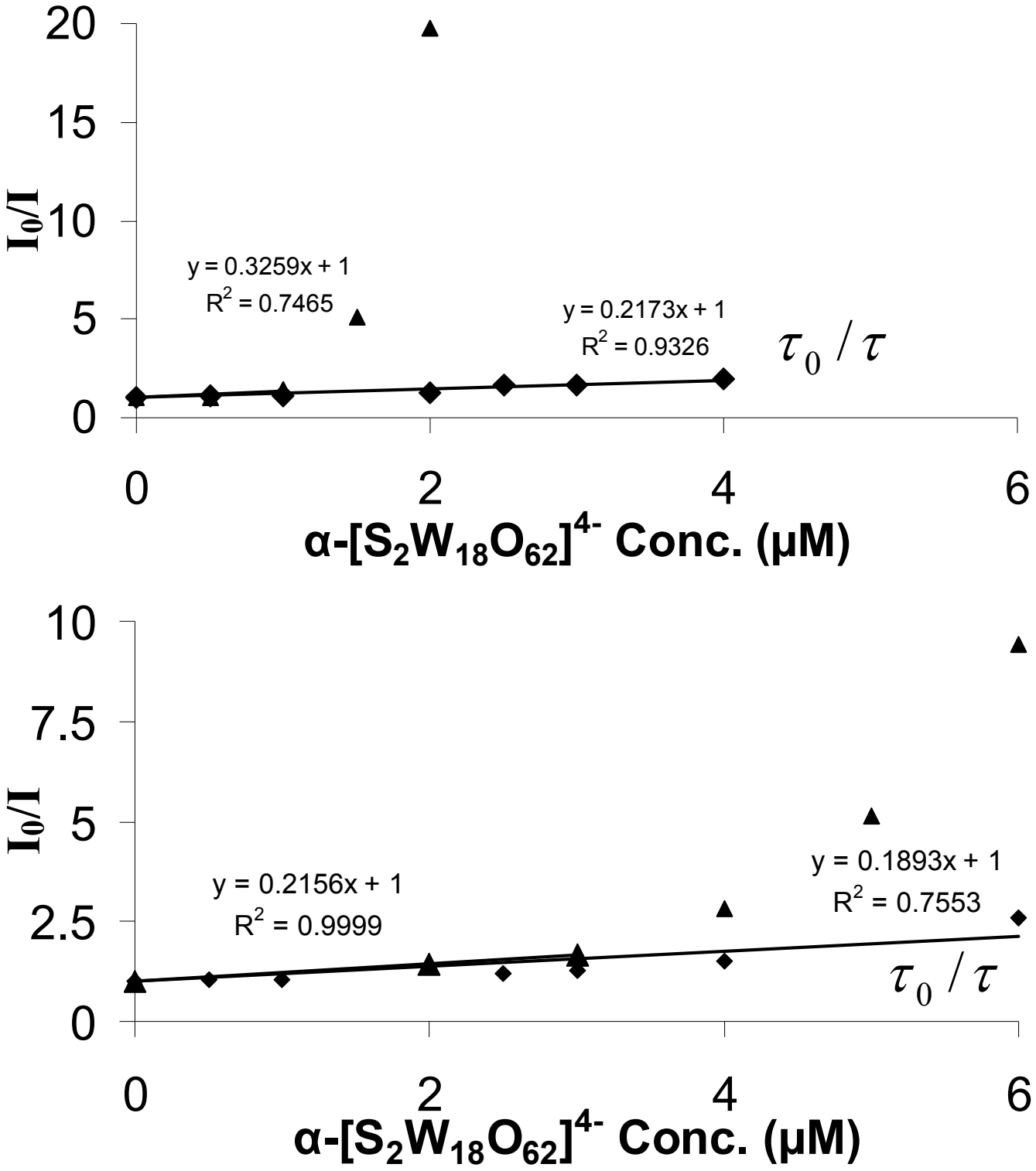

Figure 5.11 Stern-Volmer plot obtained from plotting the luminescence intensity (triangles) and the lifetimes (diamonds) of (top) 10 μM $[Os(bpy)_2PIC]^{2+}$ and (bottom) 10 μM $[Os(bpy)_2Qbpy]^{2+}$ when being quenched by α-$[S_2W_{18}O_{62}]^{4-}$.

5.4.4 Photo-Catalysis

The experiments up to now have demonstrated that $[Os(bpy)_2PIC]^{2+}$ forms a stable, dense monolayer on FDTO, and there is spectroscopic evidence that $[Os(bpy)_2Qbpy]^{2+}$ binds to silver nanoparticles electrodeposited on FDTO. Further, there is evidence that α-$[S_2W_{18}O_{62}]^{4-}$ efficiently quenches the excited state of the two osmium complexes, and when the α-$[S_2W_{18}O_{62}]^{4-}$ concentration is large enough the quenching mechanism is predominantly static. We therefore have the capacity to excite an osmium complex photonically, and transfer the excited electron to an associated α-$[S_2W_{18}O_{62}]^{4-}$ molecule at an electrode surface. The final stage of this series of experiments is to use the reduced α-$[S_2W_{18}O_{62}]^{5-}$ molecule to reduce a methyl viologen molecule in solution, without applying a potential sufficiently negative to reduce methyl viologen directly, and to return the osmium complex and α-$[S_2W_{18}O_{62}]^{4-}$ molecules to their original states so that the methyl viologen reaction proceeds photo-catalytically.

In order to return the osmium complexes to their original Os^{2+} state following their oxidation by α-$[S_2W_{18}O_{62}]^{4-}$ a potential had to be applied to the working electrode that was sufficiently negative to reduce Os^{3+} to Os^{2+} at the electrode surface (which was shown earlier to occur at 0.7 V and 0.8 V respectively) without affecting the redox state of α-$[S_2W_{18}O_{62}]^{4-}$ (E_0 = -0.235 V [2]) or methyl viologen (MV^{2+}, E_0 = -0.44 V). A potential of approximately 0.1 V is sufficiently positive to meet these criteria, and is sufficiently negative of the reduction potential of Os^{3+} to ensure that this reaction proceeds rapidly. The formal potentials of the species involved in the photo-catalytic reaction are detailed in Scheme 6. The potential applied during the reaction is negative of the reduction potential of both of the Os^{3+} species so that this reaction will proceed. The applied potential is positive of the reduction potentials of both MV^{2+} and α-$[S_2W_{18}O_{62}]^{4-}$ so that these reactions should not proceed at the electrode. However, the applied potential is positive of the oxidation potential of the excited state of both of the Os^{2+} species. Therefore, it could be possible for a cycle involving oxidation of Os^{2+*} species followed by reduction of Os^{3+}. However, as discussed in the

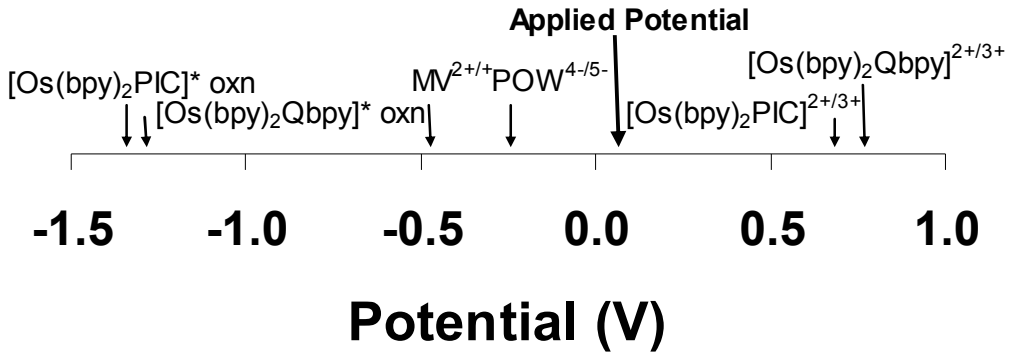

Scheme 6 Formal potentials of the species involved in the photocatalytic reaction

Introduction (Section 5.1), this pathway is slower than other competing pathways, so it is not expected to be significant.

5.4.5 Photo-catalysis based on FDTO/$[Os(bpy)_2PIC]^{2+}$/ α-$[S_2W_{18}O_{62}]^{4-}$ / Methyl Viologen

The proposed catalytic reaction is detailed below:

$$[Os(bpy)_2PIC]^{2+} + \alpha\text{-}[S_2W_{18}O_{62}]^{4-} \xrightarrow{h\nu} [Os(bpy)_2PIC]^{2+*} + \alpha\text{-}[S_2W_{18}O_{62}]^{4-}$$
$$\longrightarrow [Os(bpy)_2PIC]^{3+} + \alpha\text{-}[S_2W_{18}O_{62}]^{5-} + MV^{2+} \longrightarrow [Os(bpy)_2PIC]^{3+} + \alpha\text{-}[S_2W_{18}O_{62}]^{4-} + MV^{+}$$

The reaction at the electrode upon successful completion of the photocatalytic cycle is $[Os(bpy)_2PIC]^{3+}$ reduction, therefore a reductive current is expected. A reductive current was recorded when the $[Os(bpy)_2PIC]^{2+}$ modified FDTO surface was irradiated with the 355 nm laser source in an electrolyte containing 200 μM methyl viologen, 1mM $LiClO_4$ and 100 μM α-$[S_2W_{18}O_{62}]^{4-}$. A typical photocurrent transient from an $[Os(bpy)_2PIC]^{2+}$ surface is presented in Figure 5.12. To eliminate charging current from interfering with the measurement of photo-induced current the potential was applied to the electrode for a sufficient time to allow double-layer charging complete before the laser excitation was applied. This meant that the current transient had a more linear background. After the current caused by non-faradaic processes was allowed to settle, the laser excitation source was switched on and current flowed. Once the laser source had been switched off the current returned to its baseline level. The current recorded was reductive, as expected according to the reaction above. The magnitude of the current was typically 1 x 10^{-7} A. Figure 5.12 also shows one of the control experiments, where the experiment was repeated in the absence of α-$[S_2W_{18}O_{62}]^{4-}$ (Figure 5.12, grey line), this resulted in no current flowing. This transient acts as a baseline so that the photocatalytic current can be quantified.

Based on the results of the Stern-Volmer plot the quenching mechanism of α-$[S_2W_{18}O_{62}]^{4-}$ on $[Os(bpy)_2PIC]^{2+}$ is combined static and dynamic quenching. At higher α-$[S_2W_{18}O_{62}]^{4-}$ concentrations such as this it was concluded that static quenching dominated. It can therefore be assumed that the majority of the $[Os(bpy)_2PIC]^{2+}$ molecules at the surface are complexed with α-$[S_2W_{18}O_{62}]^{4-}$ molecules and the magnitude of the current at the surface might be expected to be determined by diffusion of methyl viologen to the electrode to accept the additional electron from the α-$[S_2W_{18}O_{62}]^{4-}$ at the surface. In this case the expected current can be estimated by:

$$i_{ss} = 4\pi nFDC^{\infty}r_s \qquad (5.3)$$

Where n is the number of electrons transferred
F is Faraday's constant
D is the diffusion coefficient of methyl viologen
C^{∞} is the concentration of methyl viologen in the bulk solution
r_s is the radius of the working electrode

Using this calculation the theoretical current yield from the $[Os(bpy)_2PIC]^{2+}$ photocurrent experiment was estimated as 3.3×10^{-4} A. This is significantly greater than the experimental result of 1×10^{-7} A and suggests a poor current yield from the experiment. The amount of current can be considered proportional to the rate of the photo-catalytic reaction. The fluctuation nature of the photo-current response was not surprising (e.g. in Figure 5.12 the current increased gradually while the laser pulse was incident on the surface) given that the maximum steady state current was not reached. Over repeated exposures within a single run the photo-current remained approximately the same, however the magnitude of the current dropped when the same surface was used for repeated experiments, this was most likely due to photo-bleaching of the osmium luminophore.

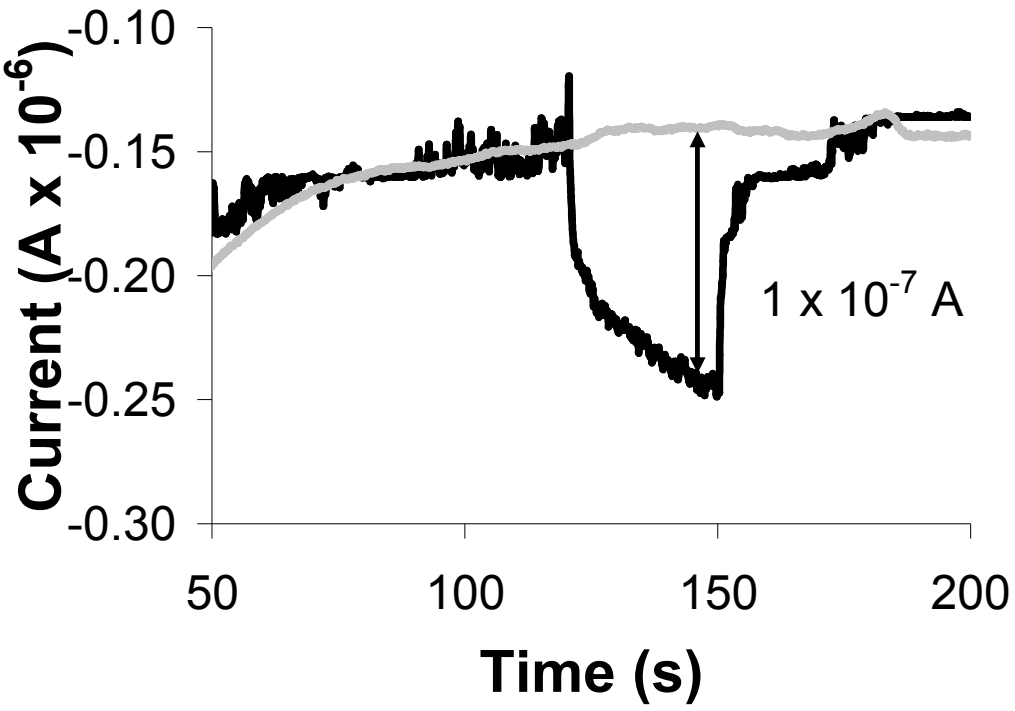

Figure 5.12 Current transient obtained by applying an amperometric potential of 0.1 V for the duration of the experiment and monitoring current through-out. The Photo-excitation (355 nm) was applied at t = 120 s and ceased at t = 150 s. The working electrode was FDTO (geometric surface area = 0.09 cm^2) modified with a monolayer of $[Os(bpy)_2PIC]^{2+}$. The electrolyte was 200 μM methyl viologen, 1mM $LiClO_4$ and 100 μM α-$[S_2W_{18}O_{62}]^{4-}$ (black line), no α-$[S_2W_{18}O_{62}]^{4-}$ (grey line) in acetonitrile, all electrolytes were unstirred.

5.4.6 Control Experiments ($[Os(bpy)_2PIC]^{2+}$)

According to the ideal scheme explained in the introduction, in order for the photo-catalytic reduction of methyl viologen to proceed, all of the steps in the reaction must be present. For example, failure to irradiate the osmium polypyridyl complex, or removal of α-$[S_2W_{18}O_{62}]^{4-}$ or methyl viologen from the electrolyte solution should prevent the reaction from proceeding, and no appreciable current should be recorded. In Figure 5.12 it was noted that in the absence of α-$[S_2W_{18}O_{62}]^{4-}$ no photocurrent flowed, indicating that the photocatalytic reaction did not proceed. This control experiment indicates that two of the parasitic pathways discussed in the introduction did not complete to a significant extent. The absence of current in this control rules out the process of $[Os(bpy)_2PIC]^{2+*}$ oxidation to $[Os(bpy)_2PIC]^{3+}$, followed by reduction at the electrode back to $[Os(bpy)_2PIC]^{2+}$. However, it was stated in the introduction that the excited state of $[Os(bpy)_2PIC]^{2+*}$ did not last for sufficient time to allow electron transfer back to the electrode to complete.

This result confirms that this is the case. Additionally, in the introduction it was considered if electron transfer directly from $[Os(bpy)_2PIC]^{2+*}$ to MV^{2+} might be possible. The absence of current in this control experiment confirms that this was not possible, most likely due to repulsive forces.

Figure 5.13 shows the current transient recorded when a potential of 0.1 V was applied to the $[Os(bpy)_2PIC]^{2+}$ monolayer modified FDTO working electrode in an acetonitrile solution containing only α-$[S_2W_{18}O_{62}]^{4-}$ and supporting electrolyte ($LiClO_4$). When the sample was irradiated there was no appreciable current recorded (Figure 5.13, black line). Any perturbations in the direction of the transient were not large enough to distinguish from electrochemical noise, although there was some drift evident in the transient, this was a result of background processes. This indicates that in the absence of methyl viologen to reductively accept an electron from α-$[S_2W_{18}O_{62}]^{5-}$ current cannot flow. When the experiment was repeated with the control of having no α-$[S_2W_{18}O_{62}]^{4-}$ or MV^{2+} in the electrolyte, the current transient once again did not react to photo-excitation (Figure 5.13 grey line).

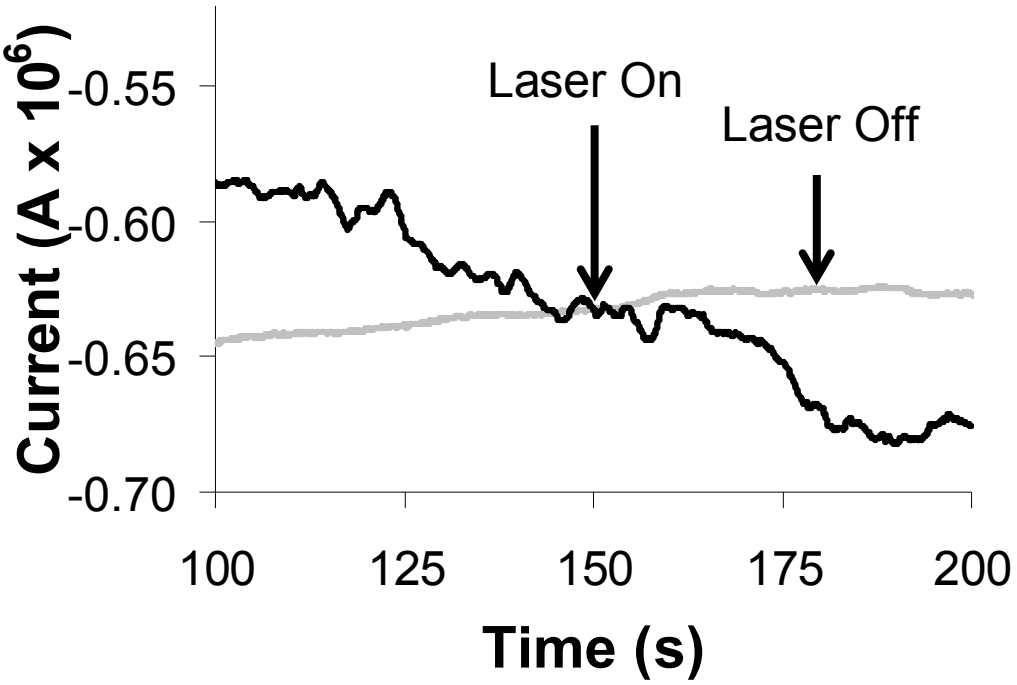

Figure 5.13 Current transient obtained by applying an amperometric potential pulse of 0.1 V for the duration of the experiment and monitoring current through-out. The Photo-excitation (355 nm) was applied at t = 150 s and ceased at t = 180 s. The working electrode was FDTO (geometric surface area = 0.09 cm^2) modified with a monolayer of $[Os(bpy)_2PIC]^{2+}$. The electrolyte was 1mM $LiClO_4$ and 100 μM α-$[S_2W_{18}O_{62}]^{4-}$ (black line), no α-$[S_2W_{18}O_{62}]^{4-}$ (grey line) in acetonitrile, all electrolytes were unstirred.

Finally it was also noted that in the absence of an excitation source there was also no current, this is best seen in Figure 5.12, as there was no current evident before or after the laser pulse.

Figures 5.12 and 5.13 demonstrate that a photocurrent was only recorded when $[Os(bpy)_2PIC]^{2+}$ was excited in the presence of α-$[S_2W_{18}O_{62}]^{4-}$ and methyl viologen. The removal of any one component of the process resulted in no current being recorded. Therefore, it can be concluded that methyl viologen facilitates current flow by accepting an electron from α-$[S_2W_{18}O_{62}]^{5-}$, which allows the α-$[S_2W_{18}O_{62}]^{4-}$ molecule accept further electrons from the $[Os(bpy)_2PIC]^{2+}$ molecule with which it is associated, and this in turn allows the $[Os(bpy)_2PIC]^{2+}$ molecules on the FDTO surface to be continually excited by the laser source and reduced back to its Os^{2+} state by the electrode with the passage of current. Therefore, the passage of current demonstrates that photocatalytic reduction of MV^{2+} to MV^{+} has proceeded successfully.

The reduction of methyl viologen has been achieved photo-catalytically by application of a potential of 0.1 V, significantly positive of the reduction potential of methyl viologen (-0.44 V). The rate of the reaction was significantly lower than that theoretically possible. This could indicate that the rate determining step in the reaction was $[Os(bpy)_2PIC]^{2+}$ regeneration rather than diffusion of methyl viologen.

5.4.7 Photo-catalysis based on FDTO/Ag Nanoparticles/ $[Os(bpy)_2Qbpy]^{2+}$/ α-$[S_2W_{18}O_{62}]^{4-}$/Methyl Viologen

The proposed catalytic reaction of the second system was as follows:

$$[Os(bpy)_2Qbpy]^{2+} + \alpha\text{-}[S_2W_{18}O_{62}]^{4-} \xrightarrow{h\nu} [Os(bpy)_2Qbpy]^{2+*} + \alpha\text{-}[S_2W_{18}O_{62}]^{4-} \longrightarrow [Os(bpy)_2Qbpy]^{3+} + \alpha\text{-}[S_2W_{18}O_{62}]^{5-} + MV^{2+} \longrightarrow [Os(bpy)_2Qbpy]^{3+} + \alpha\text{-}[S_2W_{18}O_{62}]^{4-} + MV^{+}$$

The experimental set-up was the same except in order to attach $[Os(bpy)_2Qbpy]^{2+}$ to the FDTO surface it was first populated with electrodeposited silver nanoparticulate hemispheres. In previous chapters it was described how the real surface area of surfaces such as these can be controlled by altering the density and size of the metal nanoparticles. For these experiments a simple surface was chosen with relatively low density of nanoparticles. This resulted in a decrease in effective surface area for the purpose of this experiment compared to the FDTO surface area available for $[Os(bpy)_2PIC]^{2+}$ adsorption in the previous set of experiments. Figure 5.14 shows the current transient recorded from a typical experiment. The current recorded when the light sensitive species was $[Os(bpy)_2Qbpy]^{2+}$ was over an order of magnitude greater than when $[Os(bpy)_2PIC]^{2+}$ was the light sensitive species. As with the previous example in the absence of α-$[S_2W_{18}O_{62}]^{4-}$ (Figure 5.14 grey line) there was no current recorded when the laser was incident on the sample. Using Equation 5.3, and considering that the surface area of this electrode was significantly smaller than those used for the $[Os(bpy)_2PIC]^{2+}$ photo-catalysis experiments, due to the need to attach $[Os(bpy)_2Qbpy]^{2+}$ to silver nanoparticles, the theoretical current can be estimated as 10.4 μA. A typical result of 1.5 μA is reasonably efficient given the large number of potential parasitic reactions.

It is possible that resonant enhancement of the $[Os(bpy)_2Qbpy]^{2+}$ molecules on the silver surface resulted in a greater degree of excitation, and

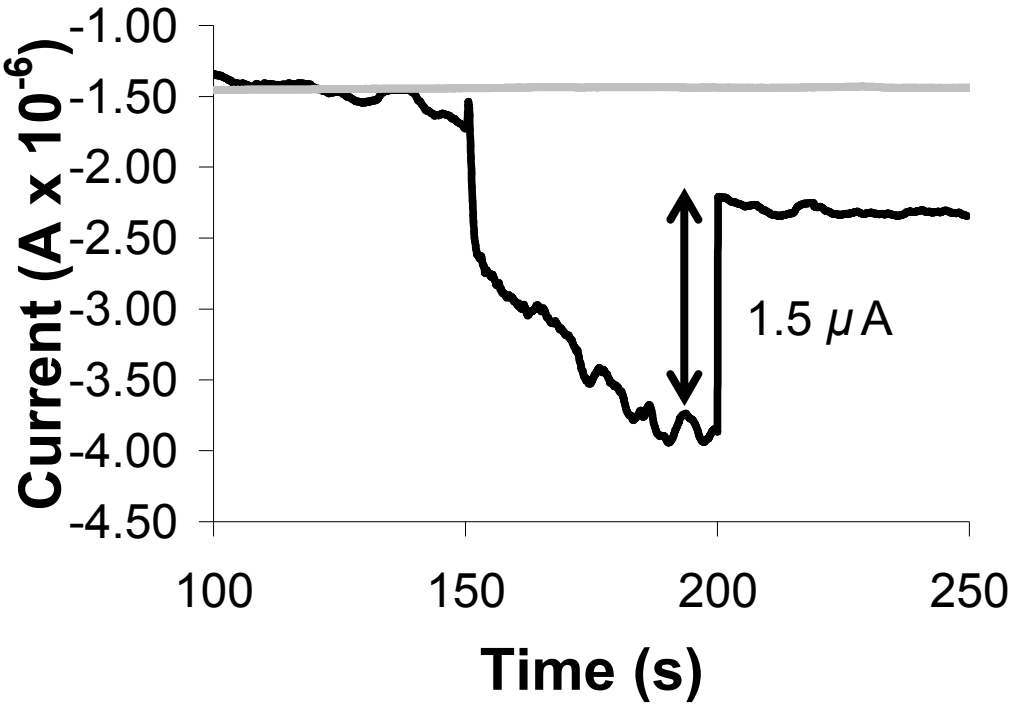

Figure 5.14 Current transient obtained by applying an amperometric potential pulse of 0.1 V for the duration of the experiment and monitoring current through-out. The Photo-excitation (355 nm) was applied at t = 150 s and ceased at t = 200 s. The working electrode was FDTO (geometric surface area = 0.09 cm^2) electrodeposited with 100 nm silver hemispheres (density on surface = 3.5 hemispheres per μm^2) modified with a monolayer of $[Os(bpy)_2Qbpy]^{2+}$. The electrolyte was 200 μM methyl viologen, 1mM $LiClO_4$ and 100 μM α-$[S_2W_{18}O_{62}]^{4-}$ (black line), no α-$[S_2W_{18}O_{62}]^{4-}$ (grey line) in acetonitrile, all electrolytes were unstirred.

subsequently a strong current yield. It was shown in Chapter 4 that the emission intensity of $[Os(bpy)_2Qbpy]^{2+}$ was enhanced up to 100-fold when it was immobilised on a silver nanoparticle surface. It is possible that resonant enhancement of the $[Os(bpy)_2Qbpy]^{2+}$ molecules on the surface resulted in a greater excited state population of the complex, and consequently a greater rate of methyl viologen reduction.

There was also evidence that the photo-catalytic reduction of methyl viologen can be induced at the open circuit potential. When the applied potential at the working electrode was set to 0.38 V, the open circuit potential of the cell, there was still a small current recorded. $[Os(bpy)_2Qbpy]^{2+}$ has the more positive reduction potential of the two osmium complexes investigated in this work (0.8 V), so it is unsurprising that it could be reduced at 0.38 V. Figure 5.15 demonstrates the current recorded from the photo-catalytic reaction under these conditions. The magnitude of the current was unsurprisingly much smaller (approximately 1×10^{-8} A) than that recorded when a more negative potential was applied. At open circuit potential the osmium reduction reaction proceeded at a much slower rate so that the kinetics of the reaction were rate limiting rather than diffusion of methyl viologen to the electrode surface.

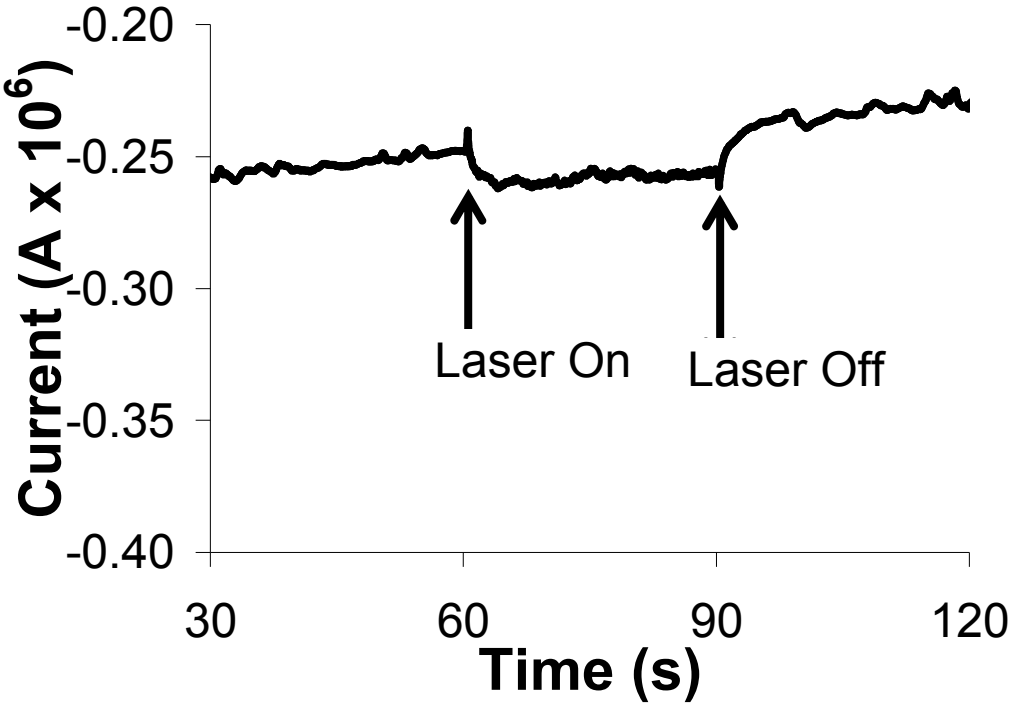

Figure 5.15 Current transient obtained by applying an amperometric potential pulse of 0.38 V for the duration of the experiment and monitoring current through-out. The Photo-excitation (355 nm) was applied at t = 60 s and ceased at t = 90 s. The working electrode was FDTO (geometric surface area = 0.09 cm^2) electrodeposited with 100 nm silver hemispheres (density on surface = 3.5 hemispheres per μm^2) modified with a monolayer of $[Os(bpy)_2Qbpy]^{2+}$. The electrolyte was 200 μM methyl viologen, 1mM $LiClO_4$ and 100 μM α-$[S_2W_{18}O_{62}]^{4-}$, all electrolytes were unstirred.

5.4.8 Control Experiments ($[Os(bpy)_2Qbpy]^{2+}$)

As mentioned above when the successful photocatalytic experiment was repeated in the absence of α-$[S_2W_{18}O_{62}]^{4-}$ (Figure 5.14, grey line) no photocurrent was recorded. As with the previous system this confirms that the parasitic reactions involving $[Os(bpy)_2Qbpy]^{2+*}$ oxidation to $[Os(bpy)_2Qbpy]^{3+}$, followed by reduction at the electrode back to $[Os(bpy)_2Qbpy]^{2+}$ and electron transfer directly from $[Os(bpy)_2Qbpy]^{2+*}$ to MV^{2+} did not proceed to a significant extent.

The current recorded when the silver nanoparticle surface, modified with $[Os(bpy)_2Qbpy]^{2+}$ was irradiated and held at a potential of 0.1 V in a solution containing α-$[S_2W_{18}O_{62}]^{4-}$, but no methyl viologen, is presented in Figure 5.16. Unlike the equivalent experiment with $[Os(bpy)_2PIC]^{2+}$, there was a current recorded in this experiment. The magnitude of the current was very small, approximately 2 x 10^{-8} A. The nature of the current was fleeting; it began to decay after only a few seconds, and had returned to baseline within 20 seconds (i.e. before the excitation source was switched off). A possible explanation for this current could be that $[Os(bpy)_2Qbpy]^{2+}$ reduction occurred following quenching by α-$[S_2W_{18}O_{62}]^{4-}$. The absence of methyl viologen meant that the α-$[S_2W_{18}O_{62}]^{5-}$ molecules associated with the $[Os(bpy)_2Qbpy]^{2+}$ on the surface could not be returned to their original α-$[S_2W_{18}O_{62}]^{4-}$ state, so further excitation, quenching and reduction cycles were not possible. This is the reason why the current was a small in magnitude, and did not continue to flow through-out the duration of the laser pulse. When the experiment was repeated without α-$[S_2W_{18}O_{62}]^{4-}$ or MV^{2+} in solution there was once again no current recorded (Figure 5.16, grey line). This indicates that α-$[S_2W_{18}O_{62}]^{4-}$ played a crucial role in the passage of current in Figure 5.16 (black line).

Similarly to the first system, the control experiments demonstrated that removing a single component from the photocatalytic reaction resulted in the passage of almost no current. When all of the components were present a

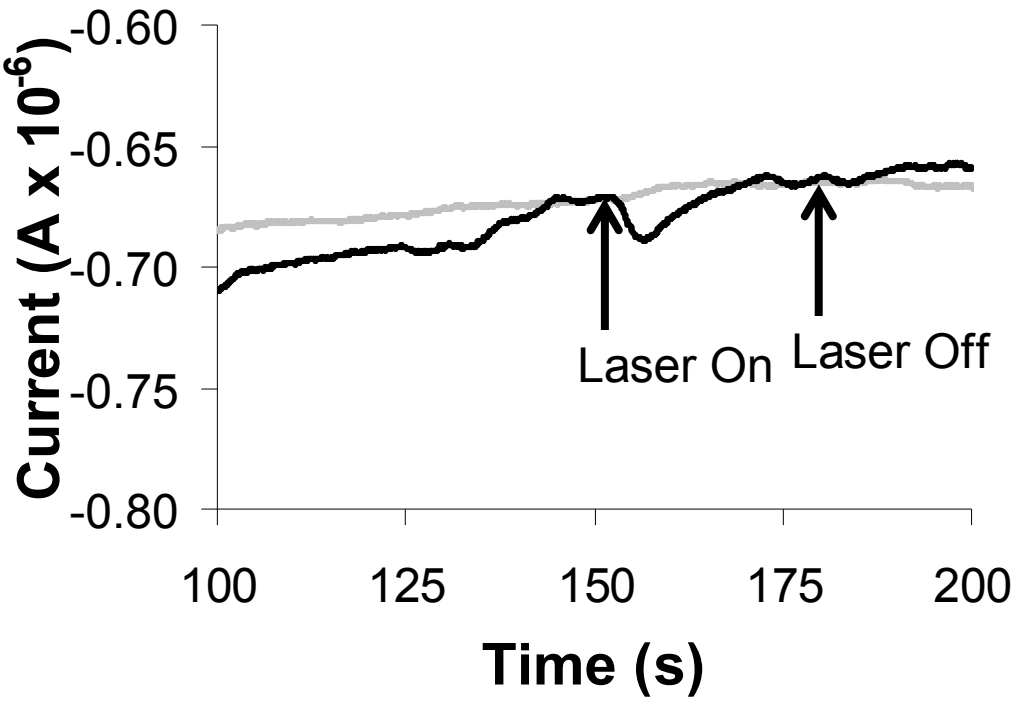

Figure 5.16 Current transient obtained by applying an amperometric potential of 0.1 V for the duration of the experiment and monitoring current through-out. The Photo-excitation (355 nm) was applied at t = 150 s and ceased at t = 180 s. The working electrode was FDTO (geometric surface area = 0.09 cm^2) electrodeposited with 100 nm silver hemispheres (density on surface = 3.5 hemispheres per μm^2) modified with $[Os(bpy)_2Qbpy]^{2+}$. The electrolyte was 1mM $LiClO_4$ and 100 μM α-$[S_2W_{18}O_{62}]^{4-}$ (black line), no α-$[S_2W_{18}O_{62}]^{4-}$ (grey line) in acetonitrile, all electrolytes were unstirred.

significant current was passed. Therefore, this experiment was also successful at photo-catalytically reducing methyl viologen at a potential at which the reduction would normally not be possible. The rate of this photocatalytic experiment was reasonably efficient, and significantly more efficient than the $[Os(bpy)_2PIC]^{2+}$ based system. It is likely that increasing the surface area of the electrode, by increasing the diameter and density of silver nanoparticles, would result in more $[Os(bpy)_2Qbpy]^{2+}$ molecules adsorbing on the surface and consequently a larger current being recorded.

5.5 Conclusions

Osmium polypyridyl complexes have been spontaneously assembled onto a conducting substrate. The electrochemical properties of the films were probed and confirmed the presence of a monolayer on the surface and indicated that the monolayer was densely packed. In solution Stern-Volmer plots indicated that the quenching action of α-$[S_2W_{18}O_{62}]^{4-}$ on the osmium polypyridyl complexes was via a combined collisional and associative mechanism, but that at higher α-$[S_2W_{18}O_{62}]^{4-}$ concentrations the quenching was predominantly associative in nature.

When the osmium polypyridyl complexes were assembled on an electrode surface, irradiated with a 355 nm laser source, and held at a potential of 0.1 V a significant current was recorded if the electrode was immersed in a solution containing α-$[S_2W_{18}O_{62}]^{4-}$ and methyl viologen. There was no current in the absence of α-$[S_2W_{18}O_{62}]^{4-}$, and very little current in the absence of methyl viologen. The conclusion that can be drawn is that the excited osmium complex was quenched by an associated α-$[S_2W_{18}O_{62}]^{4-}$, and the excited electron was accepted from the α-$[S_2W_{18}O_{62}]^{4-}$ molecule by a solution phase methyl viologen molecule, reducing it in the process. The osmium complex was reduced to its native state at the electrode. In order for continued reduction of osmium to occur methyl viologen molecules had to be continually reduced, so the current recorded was proof that methyl viologen reduction was occurring. In the absence of irradiation, excitation and quenching did not occur and consequently there was no methyl viologen reduction. The photo-catalytic reaction could be initiated and discontinued by switching the irradiation source on and off.

The potential applied to the electrode was over 500 mV positive of the reduction potential of methyl viologen yet the reaction proceeded, and the beginning and final states of the osmium complex and the α-$[S_2W_{18}O_{62}]^{4-}$ molecule were the same making it a photo-catalytic reaction. A possible reason for the impressive current yield from the $[Os(bpy)_2Qbpy]^{2+}$ immobilised on silver nanoparticles system is that on the nanoparticle

surface the emission of osmium may be plasmonically enhanced, perhaps increasing the number of excited $[Os(bpy)_2Qbpy]^{2+}$ molecules on the surface. Ultimately this work has demonstrated the harnessing of photonic energy and conversion into chemical energy.

References

[1] Usubharatana, P., McMartin, D., Veawab, A., and Tontiwachwuthikul, P., *Industrial & Engineering Chemistry Research*, 2006. **45**(8): 2558-2568.

[2] Fay, N., Hultgren, V. M., Wedd, A. G., Keyes, T. E., Forster, R. J., Leane, D., and Bond, A. M., *Dalton Transactions*, 2006(35): 4218-4227.

[3] Keyes, T. E., Gicquel, E., Guerin, L., Forster, R. J., Hultgren, V., Bond, A. M., and Wedd, A. G., *Inorganic Chemistry*, 2003. **42**(24): 7897-7905.

[4] Fay, N., Bond, A. M., Baffert, C., Boas, J. F., Pilbrow, J. R., Long, D. L., and Cronin, L., *Inorganic Chemistry*, 2007. **46**(9): 3502-3510.

[5] Seery, M. K., Guerin, L., Forster, R. J., Gicquel, E., Hultgren, V., Bond, A. M., Wedd, A. G., and Keyes, T. E., *Journal of Physical Chemistry A*, 2004. **108**(36): 7399-7405.

[6] Neier, R., Trojanowski, C., and Mattes, R., *Journal of the Chemical Society-Dalton Transactions*, 1995(15): 2521-2528.

[7] Mansuy, D., Bartoli, J. F., Battioni, P., Lyon, D. K., and Finke, R. G., *Journal of the American Chemical Society*, 1991. **113**(19): 7222-7226.

[8] Nomiya, K., Torii, H., Nomura, K., and Sato, Y., *Journal of the Chemical Society-Dalton Transactions*, 2001(9): 1506-1512.

[9] Chen, C. C., Lei, P. X., Ji, H. W., Ma, W. H., Zhao, J. C., Hidaka, H., and Serpone, N., *Environ. Sci. Technol.*, 2004. **38**(1): 329-337.

[10] Maldotti, A., Molinari, A., Varani, G., Lenarda, M., Storaro, L., Bigi, F., Maggi, R., Mazzacani, A., and Sartori, G., *J. Catal.*, 2002. **209**(1): 210-216.

[11] Friesen, D. A., Headley, J. V., and Langford, C. H., *Environ. Sci. Technol.*, 1999. **33**(18): 3193-3198.

[12] Ruther, T., Hultgren, V. M., Timko, B. P., Bond, A. M., Jackson, W. R., and Wedd, A. G., *Journal of the American Chemical Society*, 2003. **125**(33): 10133-10143.

[13] Forster, R. J. and Keyes, T. E., *Journal of Physical Chemistry B*, 1998. **102**(49): 10004-10012.

[14] Walsh, J., *Correspondance*. 2008.

[15] Kalyanasundaram, K., *Coord. Chem. Rev.*, 1982. **46**(OCT): 159-244.

[16] Maruszewski, K., Jasiorski, M., Hreniak, D., and Strek, W., *J. Mol. Struct.*, 2001. **597**(1-3): 273-277.

[17] Kameyama, A., Nambu, Y., and Endo, T., *J. Polym. Sci. Pol. Chem.*, 1992. **30**(6): 1199-1202.

[18] de la Rosa, F. F., Montes, O., and Galvan, F., *Biotechnol. Bioeng.*, 2001. **74**(6): 539-543.

[19] Brennan, J. L., Howlett, M., and Forster, R. J., *Faraday Discuss.*, 2002. **121**: 391-403.

[20] Bard, A. and Faulkner, L., *Electrochemical Methods: Fundamentals and Applications*. 2 ed. 2001, USA: Wiley.

[21] Forster, R. J., Pellegrin, Y., Leane, D., Brennan, J. L., and Keyes, T. E., *J. Phys. Chem. C*, 2007. **111**(5): 2063-2068.

[22] Suzuki, T., Hirooka, T., Kondow, T., and Kuchitsu, K., *Surf. Sci.*, 1985. **158**(1-3): 515-524.

[23] Rehm, D. and Weller, A., *Israel Journal of Chemistry*, 1970. **8**(2): 259-&.
[24] Lakowicz, J. R., *Principles of Fluorescence Spectroscopy*. 2 ed. 1999, New York: Plumen Publishers.
[25] Ballardini, R., Gandolfi, M. T., and Balzani, V., *Inorganic Chemistry*, 1987. **26**(6): 862-867.

6 Wireless Electrogenerated Chemiluminescence Microsensor for DNA Detection

6.1 Introduction

Electrochemiluminescence has become an analytical technique of considerable interest in recent years owing to its sensitivity, selectivity and large linear range, in particular for the detection of scientifically important molecules such as amino acids, biomolecules and pharmaceutical compounds [1-4]. One of the draw-backs of using electrochemical and electrochemiluminescence (ECL) based detection is the requirement for the analyte to participate in the sensing event. This is either in the reduction or oxidation event at the electrode in an electrochemical cell, or as part of the ECL reaction. This limitation severely restricts the scope of a sensor device based on one of these detection methods as typically only a single analyte can be identified in a single measurement. However, Crooks et al. have shown that the detection event for an electrochemical reaction can be decoupled from the reaction event through the use of a wireless bipolar electrode within a channel [5, 6].

In these devices, one or more bipolar electrodes of either gold or indium-tin oxide (ITO) were deposited on a glass support, which was surrounded by a poly(dimethylsiloxane) (PDMS) microchannel as shown in Scheme 1. The electrode was not connected electrically to any source, and its potential was controlled by controlling the potential of the solution in which it was immersed. The solution potential was controlled by applying a potential difference between the ends of the microchannel. Resistance within the channel results in a potential gradient along the channel. The potential drop of the solution across the electrode surface (E_{elec}) can be considered to be equal to the potential drop across the channel (E_{tot}) multiplied by the fraction of the channel occupied by the electrode (L_{elec}/L_{tot}), this is illustrated in Scheme 2. In a standard device with channel length 12 mm, and electrode

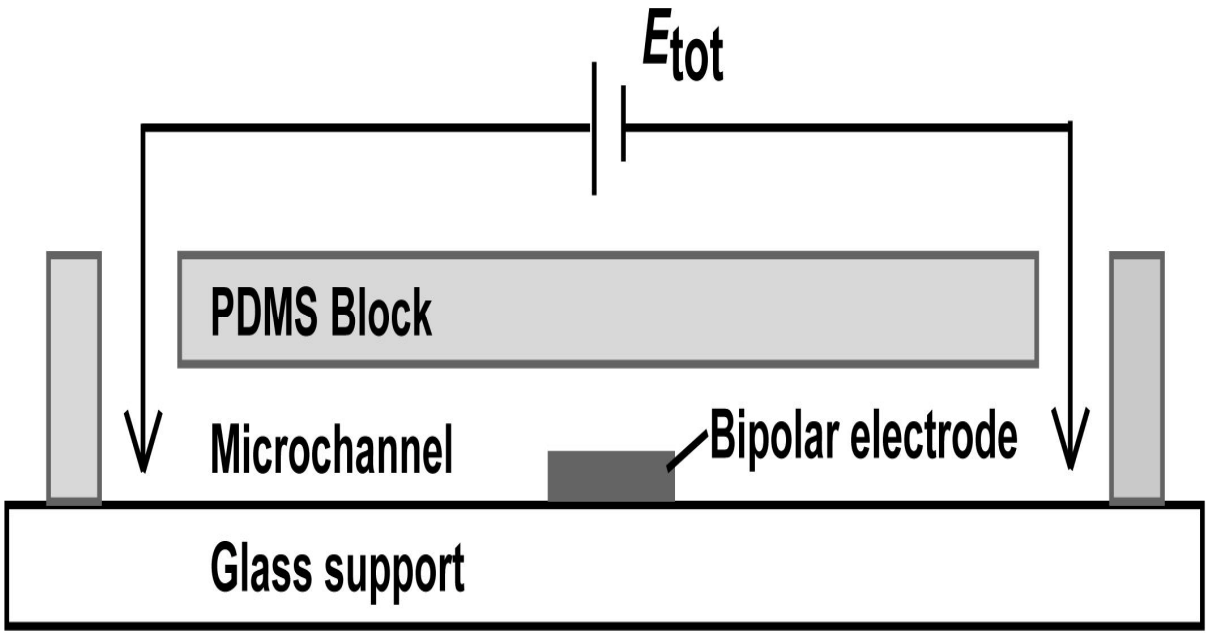

Scheme 1: Set-up of device used by Crooks et al. [6].

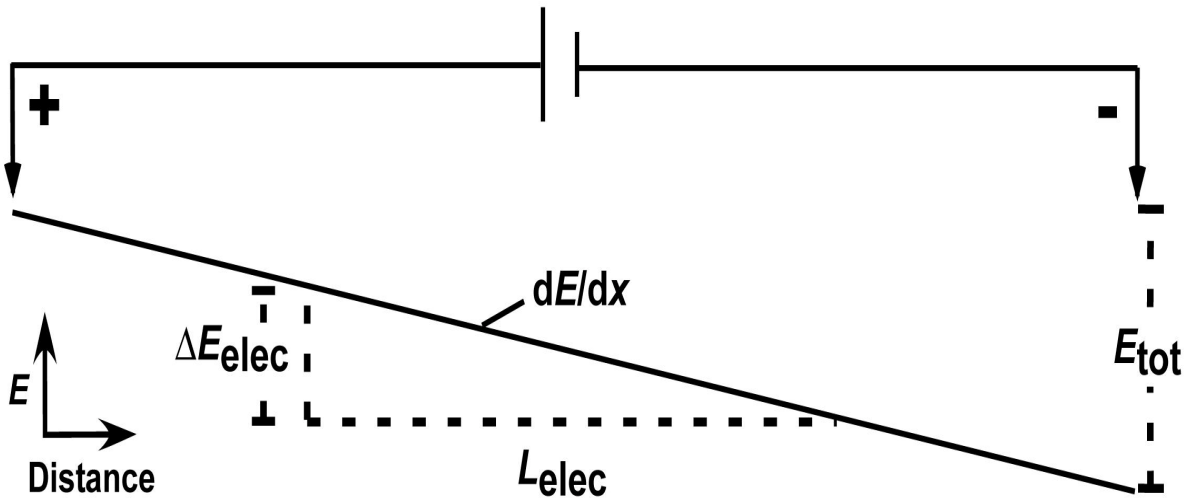

Scheme 2: Potential drop across the microchannel length, taken from Crooks et al. [6].

length 1 mm, a potential difference of 12 V across the channel would result in a potential difference in the solution across the electrode surface of 1 V. The current passing at the bipolar electrode was not measured directly, but instead indirectly by measuring the ECL signal.

As the electrode is not grounded to any electron source, its potential can float, and can sit at an energy level intermediate of the potentials of species in solutions to facilitate electron transfers between them. Scheme 3 illustrates how the electrochemical reaction can proceed without applying potential directly to the electrode. In a standard electrochemical experiment the energy of the electronic levels in the metal electrode are shifted by changing the electrode potential. When the energy levels of the electrode are sufficiently high or low that an electron can be transferred to or from the solution the electrochemical reaction can proceed. When an electrochemical reaction proceeds at a bipolar electrode the solution potential changes along the length of the microchannel such that the potential of the solution is different at each pole of the electrode. The electrode potential is floating and thus can take up a potential intermediate of the reduction and oxidation potentials of two of the solution phase species. If the potential drop across the length of the electrode is sufficiently large, the electrode can facilitate the reduction and oxidation processes simultaneously as shown in Scheme 3. Significantly, neither redox process can occur without the other occurring. Also the requirement for charge balance at the electrochemical cell means that the rate of oxidation and reduction are equal. In order for the reactions to occur at the bipolar electrode the potential drop in solution across the bipolar electrode must equal the difference between the oxidation and reduction potentials of the two electrochemically active species.

In the work of Crooks et al. [5, 6] the electrochemical reactions being driven at the cathode and anode of the bipolar electrode were oxygen reduction and $[Ru(bpy)_3]^{2+}$ and tripropylamine (TPrA) oxidation (resulting in ECL emission). Therefore, the reporting event for a positive assay result for the electrochemical reaction was ECL emission at the anode. In their later article, Crooks et al. demonstrated that such a device could be used for DNA

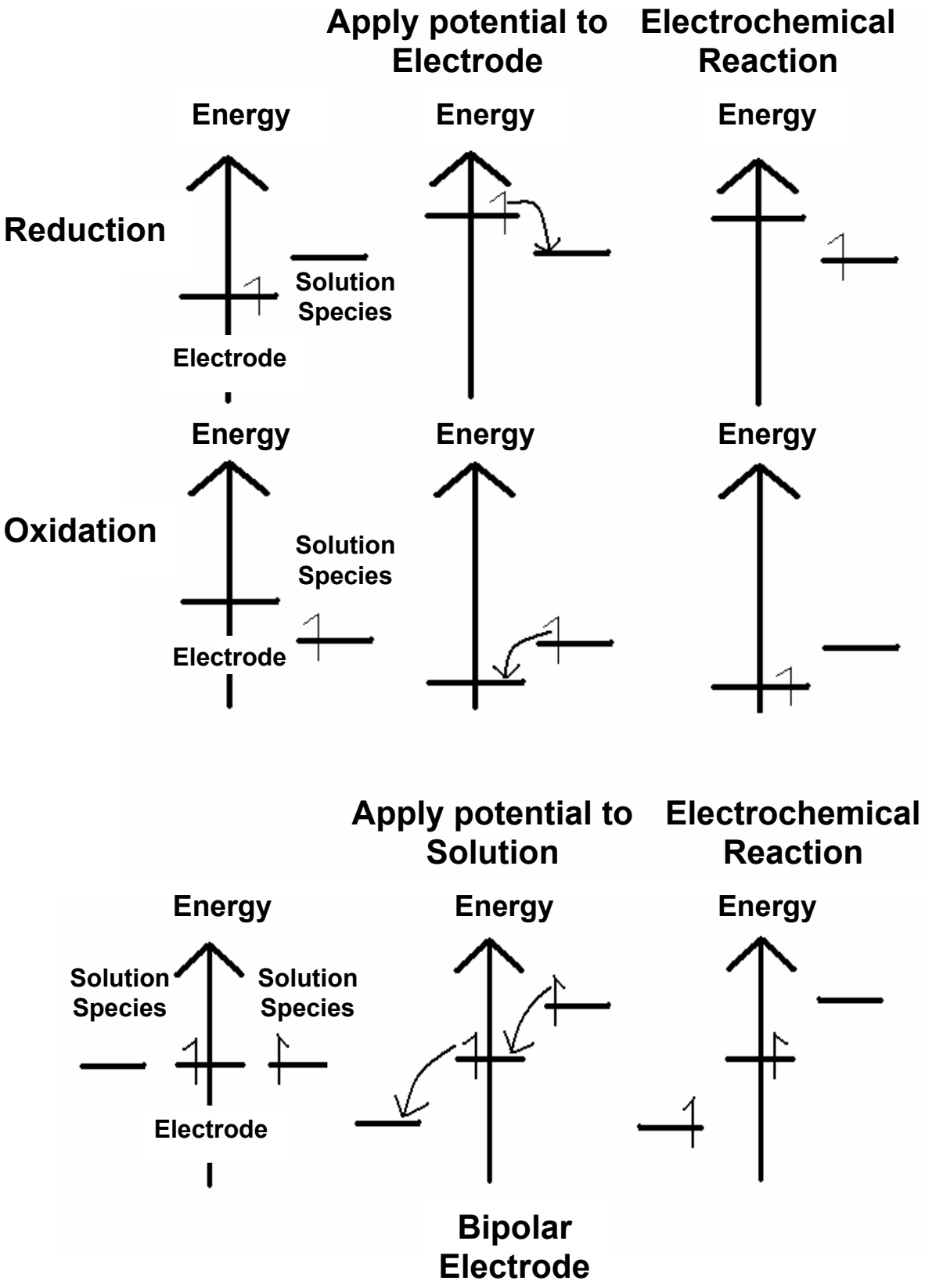

Scheme 3: Energy level diagrams showing energy levels of electrode and solution species for an oxidation and reduction reaction in a standard electrochemical experiment (top), and at a bipolar electrode when a potential gradient is applied to the solution instead of the electrode

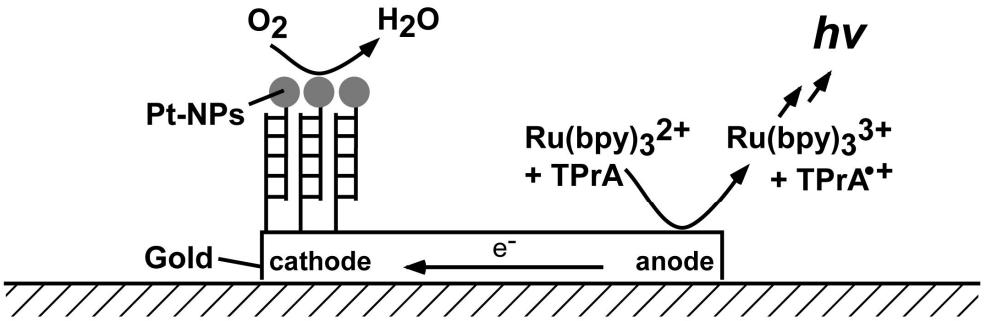

Scheme 4: Oxygen reduction and $[Ru(bpy)_3]^{2+}$/TPrA oxidation at the bipolar electrode surface. The oxygen reduction reaction occurs at the surface of platinum nanoparticles yielding a positive assay result.

sensing by linking platinum nanoparticles to a DNA sequence. When platinum nanoparticles are immobilised on the electrode surface (as in Scheme 4) the reduction of oxygen is electrocatalysed so it proceeds at a less negative potential. Therefore, a smaller potential difference across the microchannel is required to allow the ECL reaction to proceed in the case of a positive assay result. Therefore, the result of the assay is determined by the onset potential of ECL.

A significant advantage of decoupling the electrochemical and ECL reactions is that many bipolar electrodes can be placed within the microchannel. Each could be decorated with different probe DNA sequences, and therefore it would be possible to analyse for many different sequences in a single assay. The limit to the number of different sequences that could be assayed simultaneously is only restricted by the size of the microchannel and the size of the electrodes. In theory, a single sample could be injected into the device and the presence of hundreds of analytes could be assayed for in a single measurement by controlling the potential of the solution with just two wires.

Further details of the device of Crooks et al, and of other similar devices, and comparison with the work contained within this chapter can be found in the literature review.

The work in this chapter was performed in collaboration with the research group of Prof. Crooks. All ECL measurements in this chapter were performed on devices similar to those described above, a number of 1 mm long gold bipolar electrodes on a glass support, within a PDMS microchannel of length 12 mm. A potential difference was applied to either end of the microchannel, which was filled with ECL solutions as detailed in the chapter.

6.2 Optimisation of ECL solution for use in Microsensor

The wireless DNA microsensor of the Crook's group works on the principle of a detection electrochemical reaction occurring at the cathode of a bipolar electrode in an electric field, triggering an ECL reaction at the anode of the same electrode. The intensity of the ECL reaction is proportional to the detection reaction occurring at the cathode, and thus the sensing event (e.g. a DNA binding event) can be identified qualitatively and quantitatively by measuring the ECL intensity. In order for such a device to be useful as an actual sensing device one of the characteristics it must have is high sensitivity. In order to achieve this it is essential that the emission intensity from the ECL reaction is maximised such that each sensing event at the cathode results in the optimum signal.

There have been several studies into the optimum conditions for ECL reactions, particularly by Bard and co-workers [7-9]. The $[Ru(bpy)_3]^{2+}$, tripropyl-amine (TPrA) couple is the most widely used ECL reaction in solution in the literature [1, 10-13]. It also has a very efficient quantum yield of 0.125 [14] which makes it ideal for this sensing device. Efficient ECL relies on having the appropriate ratio of $[Ru(bpy)_3]^{2+}$ to TPrA in the ECL solution. The ratio that will give the strongest ECL signal depends on the electrode material and the potential applied [8]. Additionally previous studies have involved ECL at a standard electrode, such as a gold disk electrode, rather than at a wireless bipolar electrode such as this, where the potential is floating, consequently the optimal ECL solution concentrations are likely to be different.

To optimise the ECL signal for this device a series of solutions containing different ratios of $[Ru(bpy)_3]^{2+}$ and TPrA were prepared and their ECL intensity measured by exposing them to sufficient potential difference at an otherwise bare gold bipolar electrode. Figure 6.1 shows the CCD camera image of the three gold bipolar electrodes in the solution filled microchannel prior to the experiment. Figure 6.2 displays CCD images of some of the results obtained upon application of a potential of 21V between the

Figure 6.1: CCD microscope image of bipolar electrodes in the sample solution filled channel. Each bipolarr electrode (white) is 1 mm long.

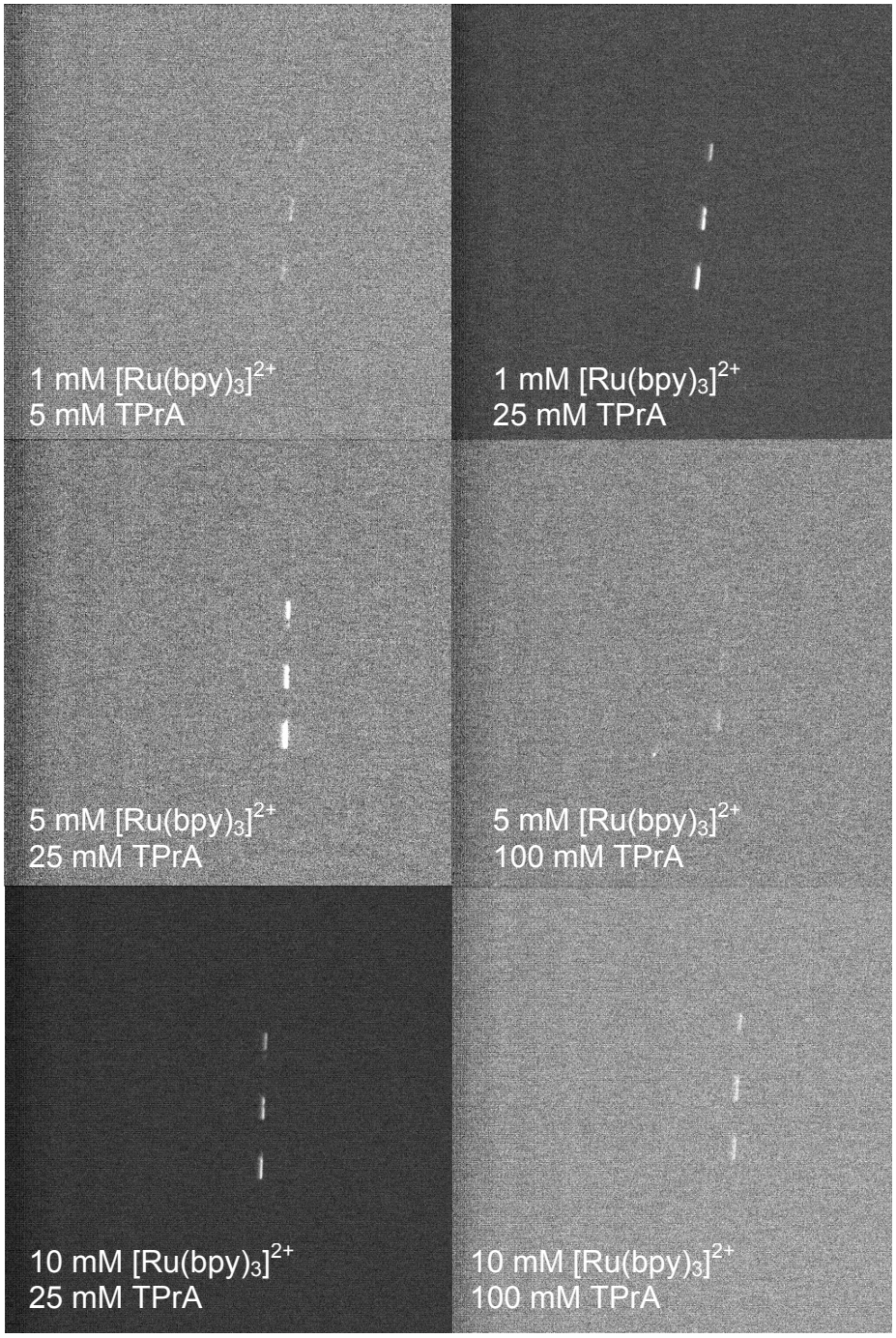

Figure 6.2: CCD camera image of ECL emission from the three bipolar electrodes upon application of a potential of 21 V to the device. ECL solution 0.1 M phosphate buffer (pH 6.9) and the indicated concentrations of $[Ru(bpy)_3]^{2+}$ and TPrA. ECL emission occurs only at the far right edge of the bipolar electrodes.

microchannel reservoirs. Due to the digital range of the CCD detector, the background intensity appears darker in CCD images where the ECL intensity is stronger. Due of this effect it was sometimes difficult to judge which images had greater ECL intensity, so it was better to quantify the intensity with computer software. The complete set of results is shown in Table 6.1, where the intensity of ECL emission in the CCD image has been quantified using the V++ software package image analysis tool. The effect of changing the $[Ru(bpy)_3]^{2+}$ and TPrA concentrations is summarized graphically in Figures 6.3 and 6.4.

The optimum ECL signal was recorded from a solution of 5mM $[Ru(bpy)_3]^{2+}$ and 25 mM TPrA. A high ratio of TPrA to $[Ru(bpy)_3]^{2+}$ is unsurprising given the mechanism of the ECL reaction at a gold surface under these conditions (see eqn's 6.1-6.5) as the $[Ru(bpy)_3]^{3+}$ molecule must interact with a significantly smaller TPrA molecule in order for ECL to proceed. The odds of this happening are significantly enhanced by an excess of TPrA molecules. The $[Ru(bpy)_3]^{2+}$ concentration must be high enough such that the TPrA radical has a chance to interact with a $[Ru(bpy)_3]^{3+}$ molecule during its short lived excited state lifetime (half-life ~0.2 ms), but should not be so high that self quenching of the excited state $[Ru(bpy)_3]^{2+*}$ molecules is caused by $[Ru(bpy)_3]^{2+}$ in solution, to a significant extent, in favour of ECL emission. When the TPrA concentration was increased from 25 mM to 100 mM the decrease in ECL intensity probably resulted from an increase in the rate of TPrA oxidation by $[Ru(bpy)_3]^{3+}$ (eqn 6.2) and a decrease in the rate of $TPrA^{\cdot}$ oxidation by $[Ru(bpy)_3]^{3+}$ to produce $[Ru(bpy)_3]^{2+*}$ (eqn 6.4). This shift results from an excess of TPrA molecules making the likelihood of an interaction between $TPrA^{\cdot}$ and $[Ru(bpy)_3]^{3+}$ lower. Bard has reported an optimum ECL solution make-up of 1 mM $[Ru(bpy)_3]^{2+}$ with 100 mM TPrA [7, 8]. However, this result was reported in the presence of additives such as bromide or Triton-X, which results in a different mechanism for the ECL reaction. This issue will be discussed next.

Table 6.1: ECL intensities measured from solutions containing different ratios of $[Ru(bpy)_3]^{2+}$: TPrA in the presence of 0.1 M phosphate buffer (pH 6.9) by applying a potential of 21 V between the reservoirs on the device.

Solution	I_1	I_2	I_3	I_{mean}	St. Dev	RSD (%)
0.5 mM $[Ru(bpy)_3]^{2+}$, 2.5 mM TPrA	0.00	0.00	0.00	0.00	0.00	0.00
0.5 mM $[Ru(bpy)_3]^{2+}$, 5 mM TPrA	0.00	0.00	0.00	0.00	0.00	0.00
0.5 mM $[Ru(bpy)_3]^{2+}$, 25 mM TPrA	0.00	0.00	0.00	0.00	0.00	0.00
1 mM $[Ru(bpy)_3]^{2+}$, 5 mM TPrA	6.00	8.00	7.00	7.00	1.00	14.29
1 mM $[Ru(bpy)_3]^{2+}$, 25 mM TPrA	43.00	51.00	60.00	51.33	8.50	16.57
1 mM $[Ru(bpy)_3]^{2+}$, 100 mM TPrA	0.00	0.00	0.00	0.00	0.00	0.00
5 mM $[Ru(bpy)_3]^{2+}$, 25 mM TPrA	61.00	71.00	80.00	70.67	9.50	13.45
5 mM $[Ru(bpy)_3]^{2+}$, 100 mM TPrA	5.00	5.00	6.00	5.33	0.58	10.83
10 mM $[Ru(bpy)_3]^{2+}$, 25 mM TPrA	44.00	52.00	63.00	53.00	9.54	18.00
10 mM $[Ru(bpy)_3]^{2+}$, 100 mM TPrA	6.00	6.00	5.00	5.67	0.58	10.19

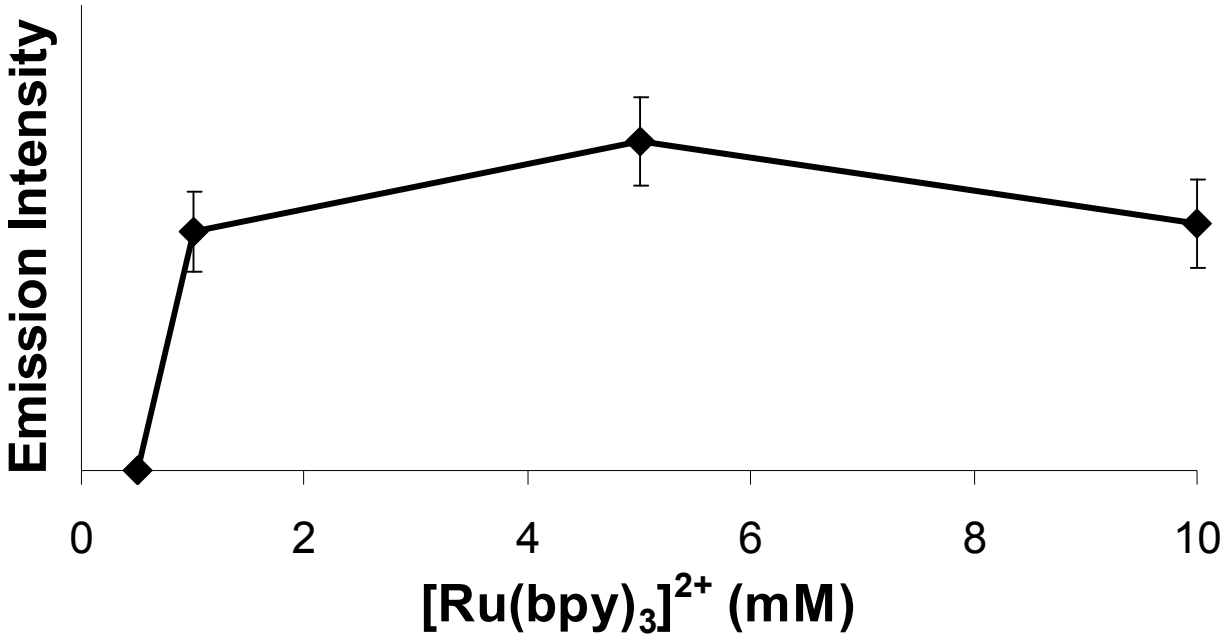

Figure 6.3: Effect of Changing $[Ru(bpy)_3]^{2+}$ Concentration on ECL intensity, whilst maintaining TPrA concentration at 25 mM, in the presence of 0.1 M phosphate buffer (pH 6.9) by applying a potential of 21 V between the reservoirs on the device.

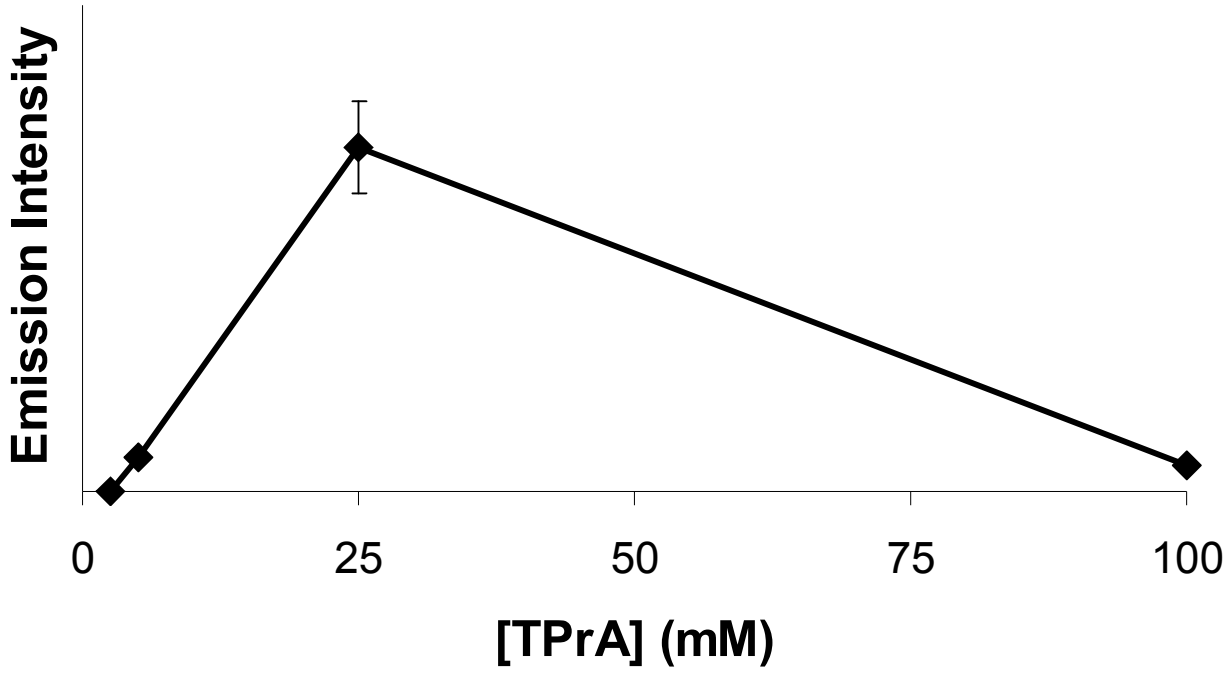

Figure 6.4: Effect of Changing TrPA Concentration whilst maintaining $[Ru(bpy)_3]^{2+}$ concentration at 5 mM, in the presence of 0.1 M phosphate buffer (pH 6.9) by applying a potential of 21 V between the reservoirs on the device.

6.3 Detection of DNA binding event using Wireless DNA Microsensor

In the introduction it was explained that, due to the difference in reduction potential of oxygen at gold (-0.45 V) and platinum (-0.2 V), the ECL reaction proceeds in the presence of platinum nanoparticles at a significantly lower potential. Therefore, a qualitative diagnostic for a DNA binding event can be performed by linking platinum nanoparticles either to the target DNA, or more easily by linking platinum nanoparticles to a second probe DNA sequence in a "sandwich" assay. The optimised ECL solution was used to examine two devices, one unmodified as in the previous section, and one modified with the probe DNA sequence, and the target DNA sequence, linked to platinum nanoparticles. This modified set-up is the equivalent of a positive assay for the target DNA sequence. Successively increasing potentials were applied to the two devices until the onset of the ECL reaction. The results are presented in Figure 6.5. In the absence of DNA and platinum nanoparticles the turn-on potential for ECL was 20 V, as already reported. In the presence of DNA and platinum nanoparticles on the surface the turn on potential for ECL was 16 V. Therefore in a real assay, if a potential of 16 V – 19 V is applied to the device, ECL will only proceed if the target DNA sequence is present so that platinum nanoparticles can catalyse the ECL reaction.

By immobilising different probe DNA sequences on different electrodes within the microchannel it would be possible to test for a number of different sequences in a single assay. In such a scenario, the positive assay results would yield ECL and the negative results would not, so the positive results could easily be read from the CCD image. The number of electrodes, and therefore potential simultaneous assays is only limited by the dimensions of the electrodes, and the dimensions of the channel, so it could be possible to assay for hundreds of targets in a single assay.

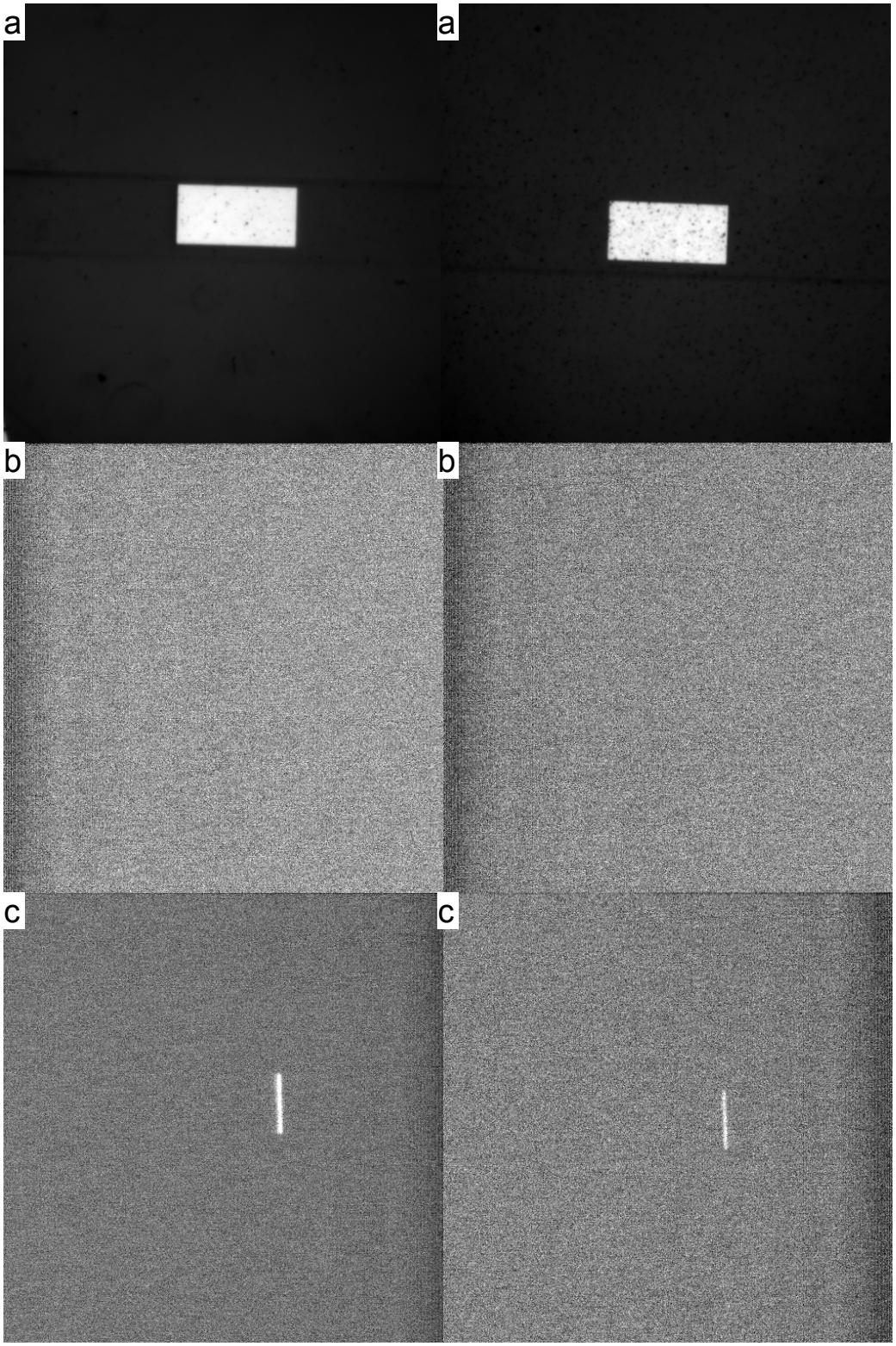

Figure 6.5: LHS; CCD images of gold bipolar electrode modified with probe DNA and Pt nanoparticle linked target DNA, (a) before ECL experiment, (b) upon application of 15 V potential difference across device, (c) upon application of 16 V potential difference across device. RHS; CCD images of unmodified gold bipolar electrode, (a) before ECL experiment, (b) upon application of 19 V potential difference across device, (c) upon application of 20 V potential difference across device. ECL solution in all images was 5 mM $[Ru(bpy)_3]^{2+}$, 25 mM TPrA, 0.1 M phosphate buffer.

6.4 Enhancement of ECL intensity through use of additives

The ECL reaction involving $[Ru(bpy)_3]^{2+}$ and TPrA can proceed via two possible pathways. These are summarised in equations 6.1-6.9:

(6.1) $[Ru(bpy)_3]^{2+} - e^- \rightarrow [Ru(bpy)_3]^{3+}$

(6.2) $[Ru(bpy)_3]^{3+} + TPrA \rightarrow [Ru(bpy)_3]^{2+} + TPrA^{\cdot+}$

(6.3) $TPrA^{\cdot+} \rightarrow TPrA^{\cdot} + H^+$

(6.4) $TPrA^{\cdot} + [Ru(bpy)_3]^{3+} \rightarrow [Ru(bpy)_3]^{2+*} + TPrA$

(6.5) $[Ru(bpy)_3]^{2+*} \rightarrow [Ru(bpy)_3]^{2+} + h\nu$

(6.6) $TPrA - e^- \rightarrow TPrA^{\cdot+}$

(6.7) $TPrA^{\cdot+} \rightarrow TPrA^{\cdot} + H^+$

(6.8) $TPrA^{\cdot} + [Ru(bpy)_3]^{3+} \rightarrow [Ru(bpy)_3]^{2+*} + TPrA$

(6.9) $[Ru(bpy)_3]^{2+*} \rightarrow [Ru(bpy)_3]^{2+} + h\nu$

Studies by Bard et al. [7, 8] have found that the second mechanism above (Eqns 6.1-6.9) is a significantly more efficient ECL process than the first mechanism and results in up to 100 times greater ECL signal intensity. The reason for the far greater efficiency of the latter mechanism can be explained by the extremely short excited state lifetime of TPrA [15]. The first mechanism involves a TPrA molecule being oxidised by an oxidised $[Ru(bpy)_3]^{3+}$ molecule, then the radicalised $TPrA^{\cdot}$ molecule must interact with a different $[Ru(bpy)_3]^{3+}$ molecule before it loses its excited state through non-radiative processes. The second mechanism involves direct oxidation of the TPrA molecule so that it does not have to diffuse to two different $[Ru(bpy)_3]^{3+}$ molecules making it a much more efficient process.

It is therefore desirable to select the second TPrA oxidation mechanism over the first, less efficient, mechanism beginning with $[Ru(bpy)_3]^{2+}$ oxidation in order to maximise the ECL intensity and therefore device sensitivity. TPrA

(E_0 = 0.8 V [8]) is oxidised at a less positive potential than $[Ru(bpy)_3]^{2+}$ (E_0 = 1.1 V) so the second pathway can be encouraged by controlling the potential applied to the device. However, TPrA oxidation is hindered at a gold surface due to the formation of gold oxide (occurring particularly in conditions such as this where positive potentials are applied), and the hydrophilic nature of the gold surface. The presence of bromide ions at low concentrations has been reported to inhibit gold oxide formation at the gold electrode and therefore encourage the second ECL pathway, resulting in up to a 100 fold increase in the ECL signal [8]. Similarly, the additive triton-X, a surfactant, alters the hydrophobicity of the gold surface allowing TPrA to adsorb at the surface, and encouraging the TPrA oxidation pathway. This has been reported to yield up to 10 times enhancement of the ECL intensity [7].

The current ECL based sensor differs from the studies mentioned in that the ECL takes place at a wireless bipolar gold electrode whose potential is floating. To investigate the effectiveness of these additives they were added to the regular ECL solution so that the ECL intensity could be compared. The concentrations of additive added to the solutions were 0.1 mM KBr and 0.1 wt % triton-X. As the two additives influence the TPrA oxidation process via different mechanisms a solution containing both additives was also prepared to investigate if the positive effects of the additives could act simultaneously. To determine the relative enhancement of the ECL signal the ECL intensity in the presence of additives was quoted relative to the ECL intensity of the same ECL solution, lacking the additive(s), under identical conditions. The results are presented in Table 6.2, and are summarised graphically in Figures 6.6 and 6.7 and 6.8.

The largest ECL signals were recorded when the greatest potential differences were applied across the ECL microchannel regardless of the additives present in the ECL solution. This is in agreement with the results presented in Table 6.1. The greatest ECL signal enhancements were recorded at lower potential differences (20-22 V). It was expected that ECL signal enhancement would be greatest when the second mechanism (TPrA

Table 6.2: Comparison of ECL intensity enhancement of bromide and triton-x additives at different potentials

Solution	I_{mean} 20 V	En 20 V	I_{mean} 21 V	En 21 V	I_{mean} 22 V	En 22 V	I_{mean} 23 V	En 23 V	I_{mean} 25 V	En 25 V
ECL soln*	2.0 ± 1	N/A	5.0 ± 3	N/A	6.3 ± 2	N/A	27.7 ± 6	N/A	43.5 ± 9	N/A
ECL soln. + 0.1 mM KBr	69.0 ± 10	34.5 ± 5	96.7 ± 15	19.3 ± 3	225.3 ± 11	35.6 ± 2	199.3 ± 21	7.2 ± 0.8	204.5 ± 4	4.7 ± 0.1
ECL soln. + 0.1 wt % triton-x	60.3 ± 5	30.2 ±2	61.0 ± 4	12.2 ± 1	85.7 ± 7	13.5 ± 1	110.3 ± 5	4.0 ± 0.2	117.0 ± 6	2.7 ± 0.1
ECL soln. + 0.1 mM KBr + 0.1 wt % triton-x	10.7 ± 3	5.3 ± 2	46.7 ± 6	9.3 ± 1	107.7 ± 5	17.0 ± 0.8	143.0 ± 5	5.2 ± 0.2	86.5 ±1	2.0 ± 0.0

*Where ECL soln is 5mM $[Ru(bpy)_3]^{2+}$, 25 mM TPrA, 0.1 M phosphate buffer

I_{mean} is the mean signal intensity taken from 3 replicate measurements

En is the enhancement compared to I_{mean} of the ECL solution with no additive

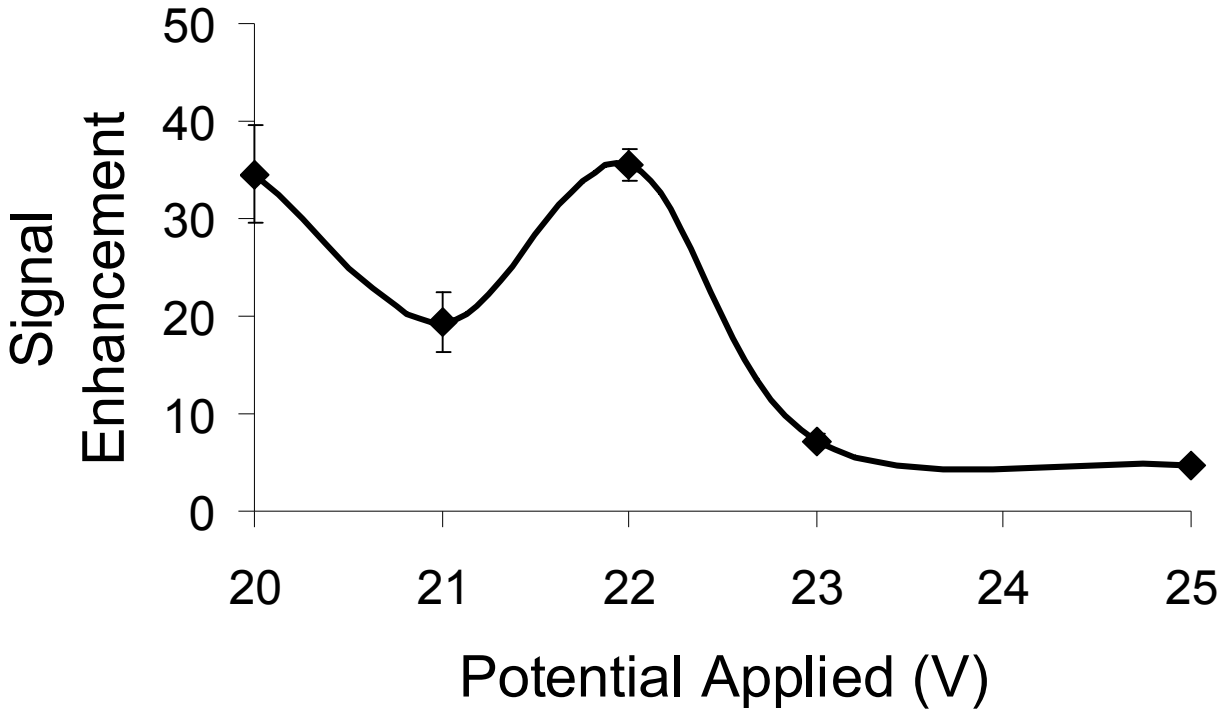

Figure 6.6: ECL signal enhancement at various potential differences resulting from adding 0.1 mM KBr to the regular ECL solution (5 mM $[Ru(bpy)_3]^{2+}$, 25 mM TPrA and 0.1 M phosphate buffer).

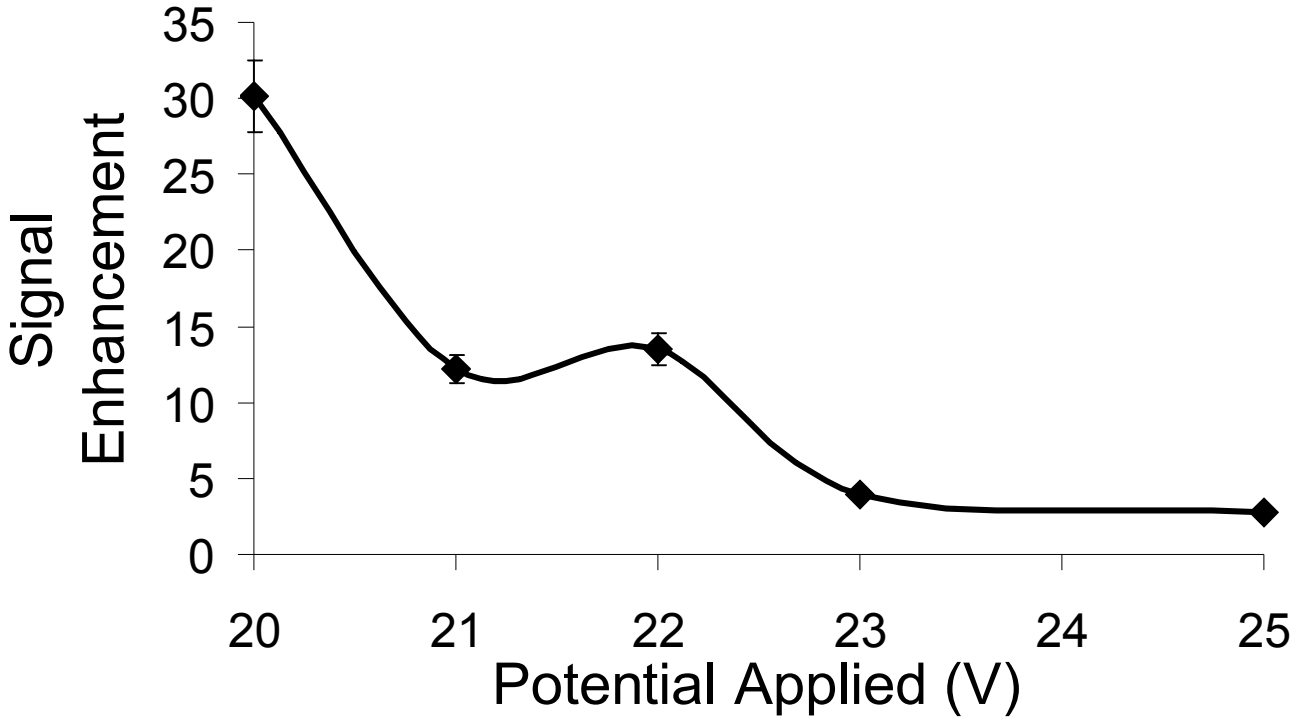

Figure 6.7: ECL signal enhancement at various potential differences resulting from adding 0.1 wt % triton-X to the regular ECL solution (5 mM $[Ru(bpy)_3]^{2+}$, 25 mM TPrA and 0.1 M phosphate buffer).

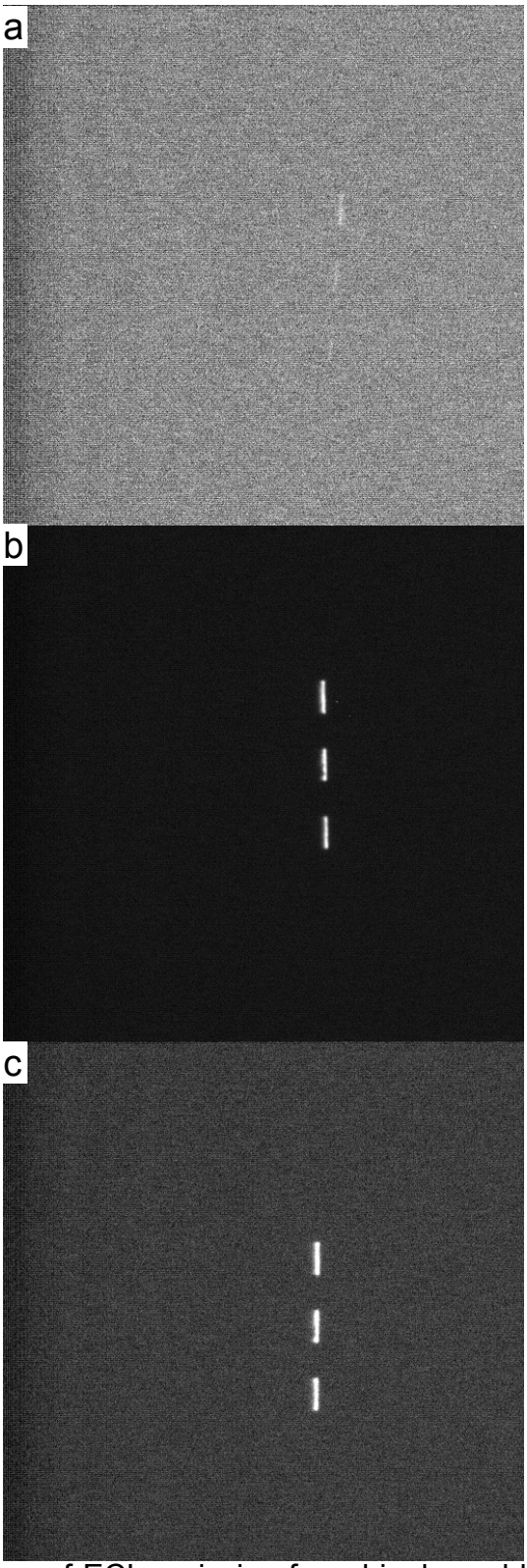

Figure 6.8: CCD images of ECL emission from bipolar gold electrodes at a applied potential of 22 V in a microchannel containing 5 mM $[Ru(bpy)_3]^{2+}$, 25 mM TPrA, 0.1 M phosphate buffer and (a) no additive, (b) 0.1 mM KBr, (c) 0.1 wt % triton-X.

oxidation, Eqns 6.6-6.9) was promoted ahead of the first mechanism ($[Ru(bpy)_3]^{2+}$ oxidation, Eqns 6.1-6.5). In the presence of these additives both TPrA oxidation and $[Ru(bpy)_3]^{2+}$ oxidation can readily occur. Due to their similar oxidation potentials both species are likely to undergo oxidation simultaneously when a sufficiently large potential difference is applied. However, as TPrA has the less positive oxidation potential of the two species at lower potentials the ratio of TPrA oxidation is expected to be greatest relative to $[Ru(bpy)_3]^{2+}$ oxidation. There is evidence that this is what occurred as the greatest ECL enhancements occurred at lower potential differences. Furthermore, in the presence of both additives the onset potential of ECL was 19 V, while in the absence of additives the onset potential was 20 V. In this case at 19 V in the presence of additives TPrA oxidation is possible resulting in ECL emission, but without additives TPrA oxidation is not possible, and the potential is not positive enough to oxidise $[Ru(bpy)_3]^{2+}$ so no emission occurs. It was not possible to calculate the ECL enhancement at 19 V as there was no emission intensity from the solution containing no additives for comparison at this potential.

Despite the ECL signal being greater when larger potential differences were applied (23-25 V) the enhancement was lower. This indicates that at greater potentials a greater amount of TPrA and $[Ru(bpy)_3]^{2+}$ oxidation occurs, however of the additional oxidation processes occurring due to the increased potential, a greater ratio of $[Ru(bpy)_3]^{2+}$ oxidation is occurring resulting in a lower enhancement compared to the ECL signal from an additive free ECL solution. It is undesirable to apply such large potentials as it can result in other oxidation/reduction reactions occurring simultaneously, and can also cause damage to the bipolar electrode in the device. Therefore the desired situation is to apply a relatively small potential difference to the channel so that control over the reactions occurring is maintained, and at the same time the signal is enhanced as much as possible so that sensitivity is high.

The enhancement to the ECL signal of 35 in the presence of bromide and 30 in the presence of triton-X is an important improvement in the ECL intensity, and such improvements are necessary if such a device is to be used as a

sensor for sub-micromolar quantities of analytes. The signal enhancement is similar to that reported by Bard et al. of almost 100 in the presence of bromide ions, which was at a conventional gold disk electrode, which was easy to clean and at which potential control was more simple compared to the bipolar electrode device employed herein [8]. In the presence of triton-X the signal enhancement of 30 was greater than that reported by bard et al, of approximately 10, at a conventional electrode surface [7]. Importantly, as both additives act differently to affect the ECL mechanism it is less likely that complications, such as the additive interfering with or binding to a proposed analyte of the sensor, will affect both additives. Therefore, despite triton-X providing a lower enhancement than bromide, both results are noteworthy. In the presence of both additives the ECL enhancement was not as high. The reduced efficiency of the enhancement in the presence of both additives was most likely due to the fact that both additives must adsorb on the surface of the gold electrode in order to act on the surface. Bromide adsorbs at the surface and prevents formation of gold oxide, and triton-X adsorbs on the surface and changes the hydrophobicity. When both additives were present, and adsorbed at the surface it is likely that steric hindrance resulted in neither additive acting completely so that the surface was partially oxidised and partially hydrophilic, resulting in a decreased enhancement of the ECL signal.

6.5 Re-optimisation of ECL solution in the presence of enhancing additives

As the additives discussed alter the mechanism of the $[Ru(bpy)_3]^{2+}$ and TPrA oxidation it is possible that the optimal ratio of $[Ru(bpy)_3]^{2+}$ to TPrA could be different than the ratio of 5 mM: 25 mM found in the absence of additives. Bard et al. has reported optimum ECL ratio of 1 mM: 100 mM for the same ECL solution in the presence of bromide ions [8], however this was for a different system. Therefore, the experiment to optimise the ratio of the ECL components was repeated. A series of solutions were prepared in which the ratio of $[Ru(bpy)_3]^{2+}$ and TPrA was varied, and all solutions were analysed on the same device under identical conditions to determine the ratio which gave the greatest ECL signal. The results are summarised in Table 6.3, and Figures 6.9 and 6.10.

6.5.1 Bromide additive

In the presence of Bromide (Figure 6.9) the optimum ratio of $[Ru(bpy)_3]^{2+}$ to TPrA was found to be 5 mM to 25 mM or 5 mM to 5 mM, depending on the potential applied across the microchannel. In the absence of additives the optimum ratio of $[Ru(bpy)_3]^{2+}$ to TPrA was found to be 5 mM to 25 mM. The presence of bromide in the solution is believed to remove gold oxide from the surface, and prevent further gold oxide formation. The mechanism of gold removal from the electrode surface by bromide is reported to follow the following mechanism [8];

(6.10) $\quad Au + 4Br^- \quad \rightarrow \quad AuBr_4^- + 3e^-$

This reaction is reported to occur at potentials positive of 0.8 V, this is also the potential region in which gold oxide formation occurs [8]. As already shown this results in a shift towards the second ECL pathway (Eqns 6.6-6.9) which initiates with TPrA oxidation, and a subsequent inclease in ECL signal. It was therefore expected that in the presence of bromide ions the optimum ratio of $[Ru(bpy)_3]^{2+}$ to TPrA would shift towards a higher TPrA concentration. On the contrary, the overall trend was for the ratio to either remain the same

Table 6.3: Comparison of ECL intensity of different ratios of $[Ru(bpy)_3]^{2+}$ and TPrA in the presence of ECL enhancing additives at various potentials

Solution	I_{mean} 19 V	I_{mean} 20 V	I_{mean} 21 V	I_{mean} 22 V	I_{mean} 23 V	I_{mean} 24 V	I_{mean} 25 V
0.1 mM KBr + 5 mM $[Ru(bpy)_3]^{2+}$ + 5 mM TPrA	19 ± 1	33 ± 3	145 ± 14	134 ± 24	334 ± 23	334 ± 23	468 ± 34
0.1 mM KBr + 5 mM $[Ru(bpy)_3]^{2+}$ + 25 mM TPrA	20 ± 1	34 ± 1	10 ± 2	29 ± 4	155 ± 21	454 ± 40	702 ± 31
0.1 mM KBr + 1 mM $[Ru(bpy)_3]^{2+}$ + 50 mM TPrA	0	0	0	25 ± 6	17 ± 4	59 ± 4	64 ± 12
0.1 mM KBr + 1 mM $[Ru(bpy)_3]^{2+}$ + 100 mM TPrA	0	0	0	0	0	0	0
0.1 wt % Triton-x + 5 mM $[Ru(bpy)_3]^{2+}$ + 5 mM TPrA	0	33 ± 5	105 ± 10	49 ± 24	30 ± 10	75 ± 37	190 ± 74
0.1 wt % Triton-x + 5 mM $[Ru(bpy)_3]^{2+}$ + 25 mM TPrA	0	8 ± 4	7 ± 3	65 ± 5	122 ± 18	50 ± 26	52 ± 23
0.1 wt % Triton-x + 1 mM $[Ru(bpy)_3]^{2+}$ + 50 mM TPrA	22 ± 8	27 ± 8	25 ± 5	18 ± 6	14 ± 6	22 ± 7	33 ± 18
0.1 wt % Triton-x + 1 mM $[Ru(bpy)_3]^{2+}$ + 100 mM TPrA	0	0	0	0	0	0	0

I_{mean} is the mean signal intensity taken from 3 replicate measurements

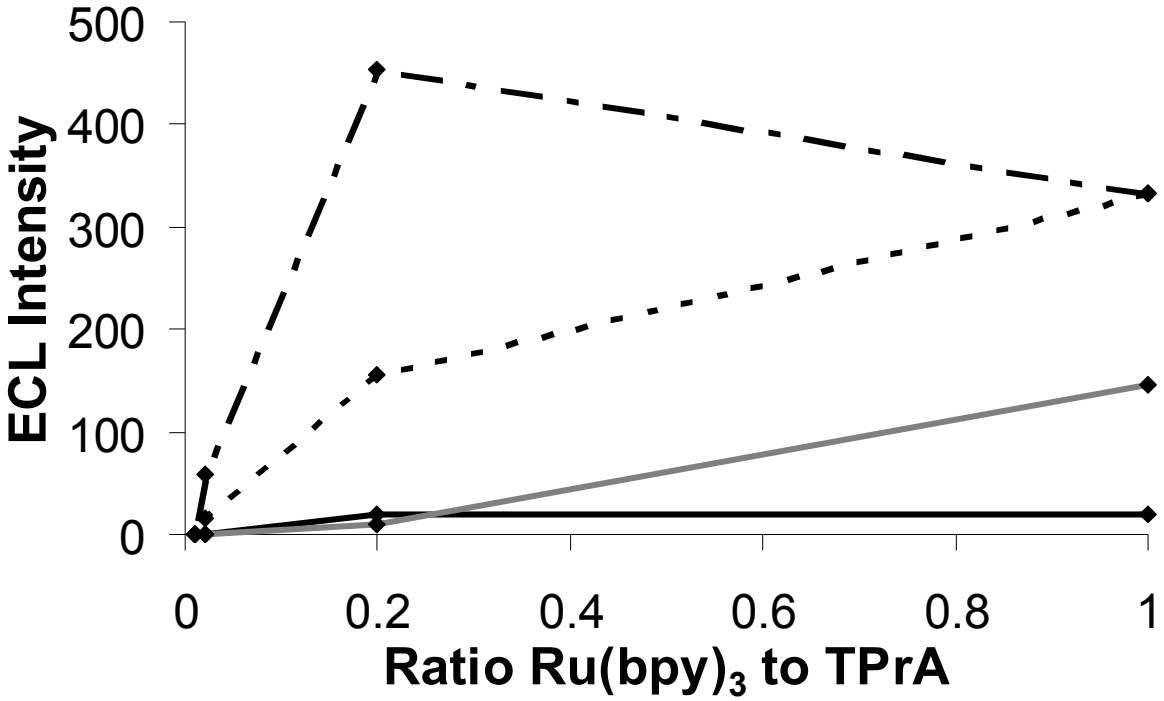

Figure 6.9: ECL signal from ECL solutions containing 0.1 mM KBr and the indicated ratio of $[Ru(bpy)_3]^{2+}$ to TPrA (as per Table 6.3) in 0.1 M phosphate buffer). The potential applied across the microchannel was (**–**) 19 V, (–) 21 V, (---) 23 V, (**– - –**) 25 V.

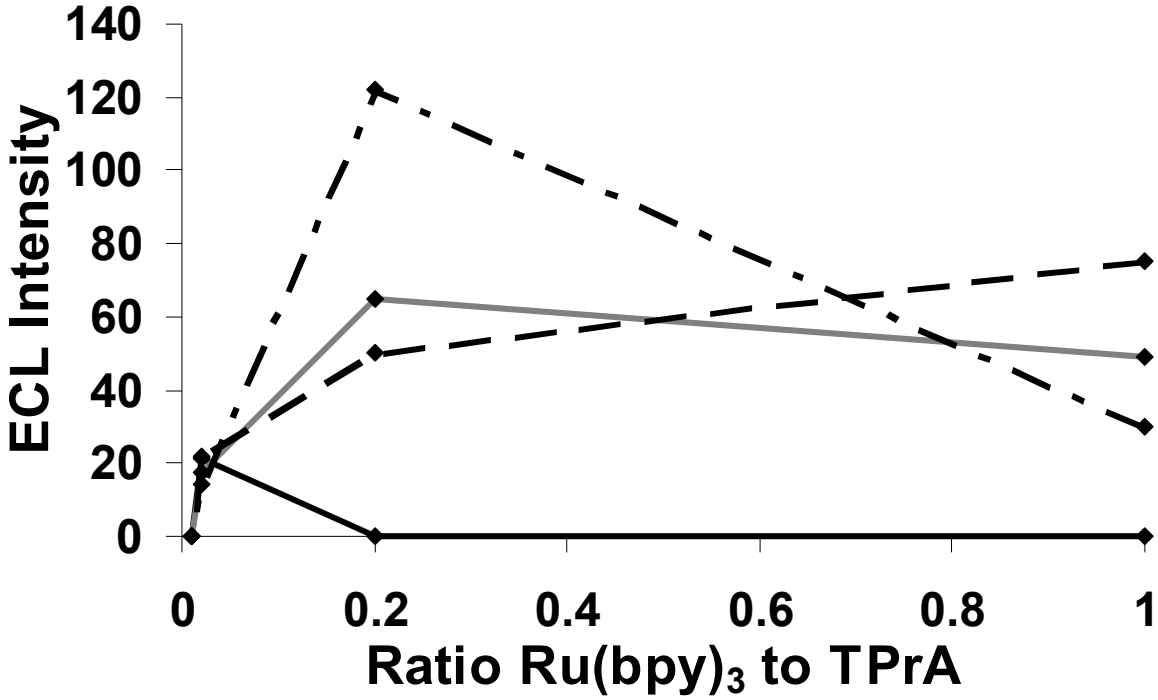

Fgure 6.10: ECL signal from ECL solutions containing 0.1 wt. % triton-X and the indicated ratio of $[Ru(bpy)_3]^{2+}$ to TPrA (as per Table 6.3) in 0.1 M phosphate buffer). The potential applied across the microchannel was (**–**) 19 V, (–) 22 V, (---) 23 V, (**– - –**) 24 V.

(5:25), or decrease (5:5). The explanation for this result is most likely that the relative ease at which TPrA oxidation occurs in the presence of bromide ions means that a greater proportion of the available TPrA molecules at the surface are becoming oxidised, so that all of the available $[Ru(bpy)_3]^{2+}$ molecules are being reacted with without needing to further increase the TPrA concentration. The optimum ratio of $[Ru(bpy)_3]^{2+}$ to TPrA is therefore 5 mM to 25 mM or 5 mM to 5 mM. In order to simplify the experiment, and to make comparison of results more facile, the ratio of 5 mM to 25 mM was chosen as the optimum ratio for further experiments, when bromide is present as the additive, as this happens to be the optimum ratio in the absence of additives also.

6.5.2 Triton-X additive

When the additive in the ECL solution was triton-X the results were similar to those found in the presence of bromide ions. The effect of the ratio of $[Ru(bpy)_3]^{2+}$ to TPrA is presented graphically in Figure 6.10. Like bromide, triton-X encourages the second ECL pathway (Eqns 6.6-6.9), in this case by changing the hydrophobicity of the gold surface and encouraging TPrA adsorption. As with bromide as the additive, this resulted in an optimum ratio of 5 mM to 25 mM and 5 mM to 5 mM. One difference noted between Figures 6.9 and 6.10 is that in the presence of triton-X at 19 V the optimum ratio of $[Ru(bpy)_3]^{2+}$ to TPrA was 1:50. This was the only potential at which this occurred. Triton-X was less efficient than bromide at facilitating TPrA oxidation at the gold electrode (as evidenced by the lower enhancement of the ECL signal already demonstrated). Therefore, at 19 V, the onset potential for the ECL reaction in the presence of additives, it is likely that only a very small amount of TPrA molecules were oxidised, particularly when the less efficient triton-X additive was used. It is therefore understandable that a greater concentration of triton-X would be optimal under conditions where the potential applied to the microchannel imparts only the minimum amount of energy required for oxidation of the TPrA molecule to proceed. As with bromide, the optimal ECL solution composition in the presence of triton-X was found to be 5 mM to 25 mM or 5 mM to 5 mM $[Ru(bpy)_3]^{2+}$ to TPrA, and

for the same reasons given above for bromide, the ratio used for further experiments was 5 mM : 25 mM.

6.6 Selective adsorption of DNA to one end of bipolar electrode

In order to ascertain if the effects demonstrated in the previous section of bromide ions and triton-X on the ECL signal will increase the signal intensity in a DNA detector based on this technology it must be possible to limit the adsorption of DNA to a single end of the electrode. This is because when DNA is adsorbed on the entire surface, it assembles on the anode end of the electrode, where it is not required, potentially blocking it. DNA is only required at the cathode where the ORR occurs. Furthermore, by allowing DNA to cover the entire surface there is an increased likelihood of DNA interfering with and reacting with the additives KBr and triton-X. Finally one of the principle advantages of this device over other electrochemistry and ECL sensors is that it provides the opportunity to test for many different DNA sequences in a single measurement. In order to achieve this goal, it must be possible to selectively adsorb DNA on different electrodes and on different parts of the electrode. The methods considered to limit the adsorption of DNA are discussed below.

6.6.1 Reductive desorption of DNA from Anode of bipolar electrode

Reductive desorption of DNA from an electrode surface is common practice in the literature [16-18]. However in the instances where it has been achieved in the literature it has been performed at a standard disk electrode (or similar), and desorption was from the entire surface. The aim of this experiment was to reductively desorb DNA from a wireless gold bipolar electrode, at the anode end only. The difficulty with achieving this is that every reduction at the anode end of the electrode in this device must be matched by an oxidation at the cathode, so avoiding simultaneous oxidation and reduction of DNA, which would remove the DNA from both ends of the electrode, is an important challenge.

Thiol-bound DNA reductively desorbs at approx. -1.0 V according to literature reports [16-18]. $[Ru(bpy)_3]^{2+}$ oxidation occurs at approx. +1.1 V, so a potential difference of 2.0 V – 2.2 V should be applied across bipolar electrode to induce $[Ru(bpy)_3]^{2+}$ oxidation and thiol reduction. This corresponds to potential difference of 24.0 – 26.4 V between wells in the device. This potential is sufficiently large to induce oxygen reduction (reduction potential -0.45 V) and thiol reduction simultaneously. The potential difference was applied for 30 s to 10 min in 5 mM $[Ru(bpy)_3]^{2+}$ in KOH at a DNA/Pt NP modified surface. This was performed, however when standard ECL solution (5 mM $[Ru(bpy)_3]^{2+}$, 25 mM TPrA, 0.1 M phosphate buffer) was subsequently added it was not possible to record ECL from the surface at a potential difference of less than 20 V across the channel. This indicated that there was no DNA at either end of the gold bipolar electrode. It is likely that the reductive desorption of DNA was successful, however oxidative desorption seems to have occurred concurrently, this is not surprising given the oxidation potential of the thiol bond is approximately 0.7-0.8 V [19]; i.e. less positive than that of $[Ru(bpy)_3]^{2+}$. It might be possible to add a sacrificial oxidant with an oxidation potential negative of the oxidation potential of thiol bound DNA. However, adding such a species would likely induce further complications to the eventual ECL-DNA detection mechanism so it was decided to pursue a physical barrier to prevent DNA adsorption instead.

6.6.2 Physical barrier for the prevention of DNA adsorption at anode

A more efficient method of limiting the placement of DNA molecules to one end of the gold bipolar electrode is to only expose one half of the electrode to the DNA solutions. In order to achieve this, the microchannel had to be initially placed perpendicularly across the electrodes such that half of each electrode is within the channel and half of each electrode is outside the channel as shown in Scheme 5. Then once the probe DNA and target (Pt nanoparticle linked) DNA has been deposited in the usual manner the channel can be lifted up, placed down on the surface again, this time parallel

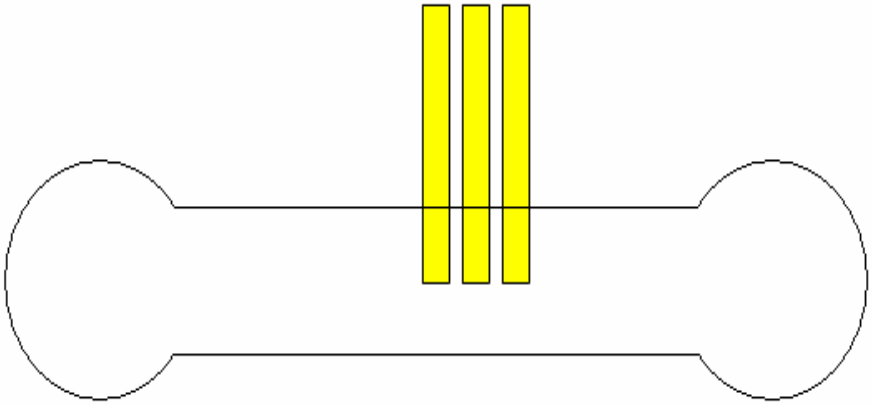

Scheme 5: Alignment of microchannel to limit DNA adsorption to one half of the electrode.

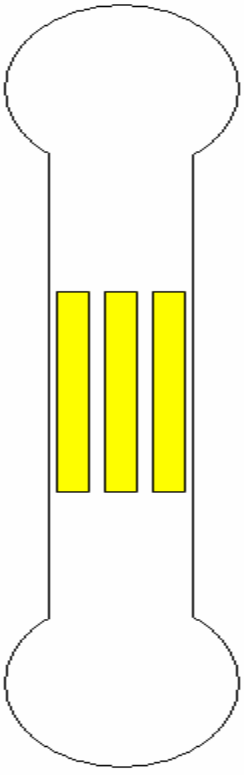

Scheme 6: Alignment of microchannel to limit expose whole electrode to solution.

to the electrodes such that the entire electrode surface is within the channel. This allowed the ECL experiment to proceed as normal, with ECL solution exposed to the entire electrode surface (scheme 6). For this adaptation to the method it was not possible to plasma fuse the glass slide and microchannel together as normal as this would make it impossible to move the channel after DNA deposition. Therefore, the microchannel was held in position over the electrodes using clamps. This resulted in an imperfect seal so the device was more prone to leaking; nevertheless with proper care during solution injection it was possible to perform the experiment without any leakage.

If the method was successful then when a potential of 16 V is applied across the microchannel it should only be possible to produce ECL from one end of the gold bipolar electrode (the end with no DNA on it). This is because ECL at 16 V is only possible when there are immobilised Pt nanoparticles at the opposite end of the electrode to catalyse the ORR at the cathode. When a potential of 20 V is applied it should be possible to produce ECL from both ends of the electrode as at this potential Pt nanoparticles are not required to catalyse the ORR. Figure 6.11 demonstrates that this was in fact the case, when a standard ECL solution was injected into the microchannel, ECL is limited to the end of the electrode without DNA at 16 V, and is seen at both ends of the electrodes (upon reversing the potential bias) when 20 V is applied across the device. This experiment demonstrates that the method was successful in limiting the adsorption of DNA to one half of the electrode, and that this does not adversely influence the ECL experiment. This result is important within the context of this work, as it facilitated examination of the ECL signal in the presence of additives without DNA adsorbed at the anode, which could possibly have been interfering in the action of the additives in enhancing the ECL signal. In addition, it is also important for future applications of the device to be able to selectively adsorb species to different parts of the bipolar electrode. For instance, using this method it could be possible to selectively adsorb different probe DNA sequences onto many bipolar electrodes in the same microchannel. It would then be possible to assay for many different DNA sequences in one sample simultaneously.

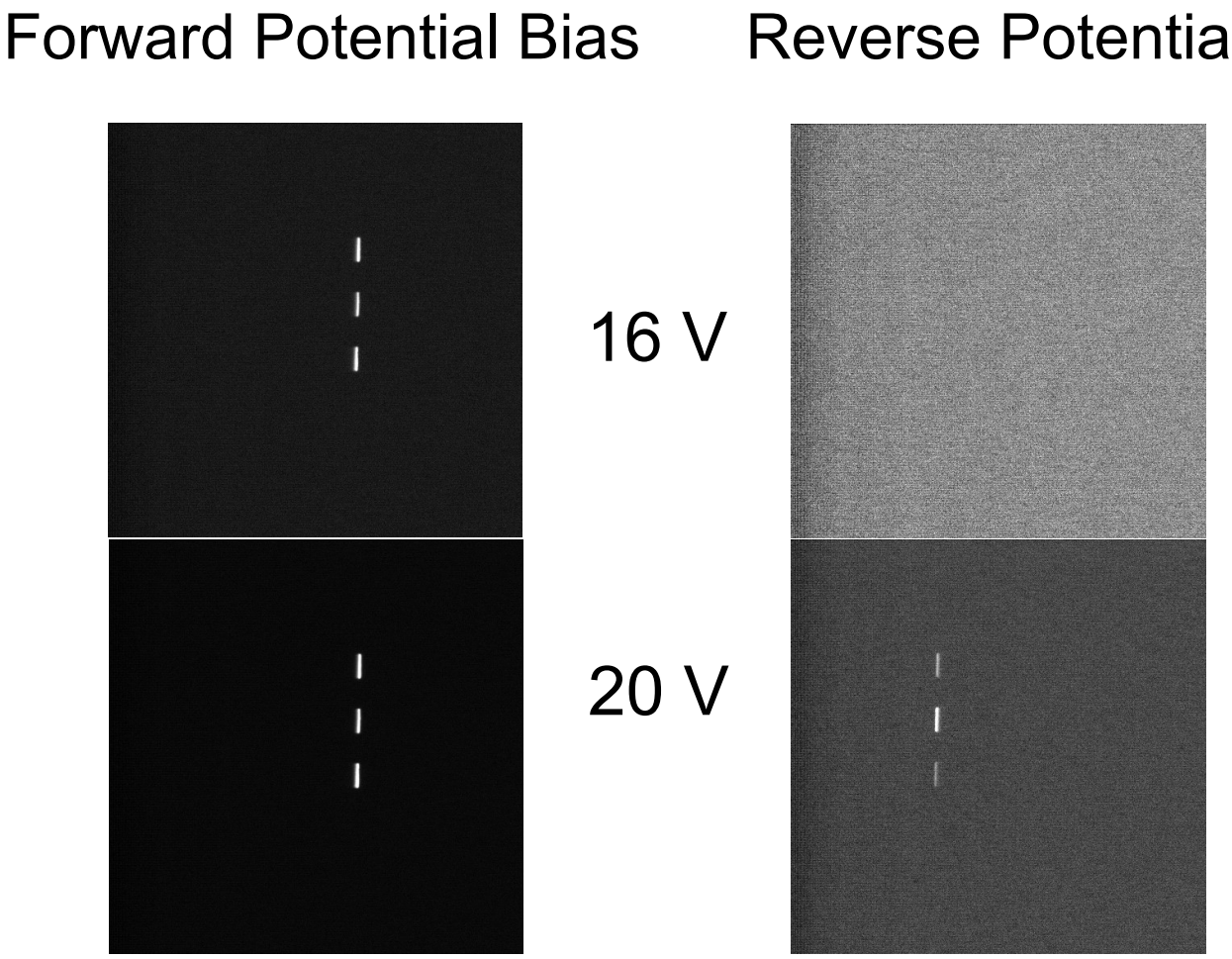

Figure 6.11: CCD images of ECL from application of 16 V and 20 V potential difference to a single device which had DNA adsorbed on the left hand (cathode) end only. The solution in the microchannel was 5 mM $[Ru(bpy)_3]^{2+}$, 25 mM TPrA and 0.1 M phosphate buffer.

6.7 Detection of DNA binding event using Wireless DNA Microsensor and optimised ECL solution

Having demonstrated the use of this device to detect a DNA binding event already (Section 6.3), it must be shown that the impressive improvements to sensitivity reported in Section 6.4 are applicable to the DNA sensing application. It is possible that DNA bound to the bipolar electrode surface could interfere with the ECL signal enhancement by the two additives, KBr and triton-X. This possibility is particularly significant as both additives act on the gold surface upon which the DNA binds, so blocking and other interactions are a distinct possibility.

6.7.1 Bromide additive

In the absence of an additive in the microchannel it was possible to detect the binding of DNA at the gold bipolar electrode surface. This was demonstrated in Section 6.3, where a DNA binding event was detected by the decrease in potential required for the onset of ECL, caused by the catalysis of the oxygen reduction reaction by DNA bound platinum nanoparticles. This experiment was repeated, under identical conditions, with 0.1 mM KBr added to the ECL solution. It was hoped that the ECL signal would increase by a factor of 30 or more, in accordance with the results in Section 6.4. However, the result was that, not only did the ECL signal not increase in the presence of KBr, surprisingly there was no ECL signal at all in the presence of KBr. Possible reasons for the failure of the device when KBr and DNA linked platinum nanoparticles are both present are;

- Surface bound DNA blocking access to surface for KBr, preventing it from acting on the surface
- KBr adsorbing on platinum surface, preventing ORR
- KBr causing dissociation of surface bound DNA

In an attempt to discover which of the above scenarios was causing the device failure it was decided to limit the placement of DNA to the cathode end of the bipolar electrode, as this would prevent surface bound DNA

blocking KBr from accessing the surface at the anode, where it must act in order to influence the ECL reaction. The original method for device preparation and DNA immobilisation results in DNA adsorbing on the entire gold bipolar electrode surface, although the DNA is only active (i.e. the DNA bound Pt nanoparticles only catalyse the ORR) at the cathode. It is unclear if the presence of DNA on the entire electrode surface has any disadvantages. However, the ability to limit the placement of DNA, or any other adsorbate, to one end of the electrode is desirable as it is likely that future applications of this device may include the necessity to use analytes and probes that cannot come into direct contact. In the previous section, it was shown how DNA was successfully limited to one end of the bipolar electrode by use of a physical barrier.

Having limited the adsorption of DNA to one end of the bipolar electrode it was possible to determine if the presence of DNA at the anode was responsible for the failure of the previous experiment, where the there was no ECL signal from a DNA modified electrode in the presence of bromide ions. Therefore, the ECL experiment was repeated with DNA adsorbed at one end of the electrode, and this time the ECL solution was 5 mM $[Ru(bpy)_3]^{2+}$, 25 mM TPrA, 0.1 M phosphate buffer and 0.1 mM KBr. The effect of bromide ions in the solution shown in Figure 6.12 shows a stark contrast to the situation where there are no bromide ions in solution, and the set-up is otherwise identical (Figure 6.11). In the presence of bromide ions there is no ECL reaction at either end of the electrode. As the ECL reaction is prevented at both ends of the electrode it is unlikely that the reason for the failure of the ECL reaction in the presence of bromide and DNA is because the DNA layer is blocking access to the gold surface for the bromide ions, as one end of the electrode is clear of DNA in this case. This leaves the possibility that in the presence of bromide and DNA the ECL reaction is being retarded either by an interaction between bromide and DNA or bromide and the platinum nanoparticles tethered to the DNA, that catalyse the ORR.

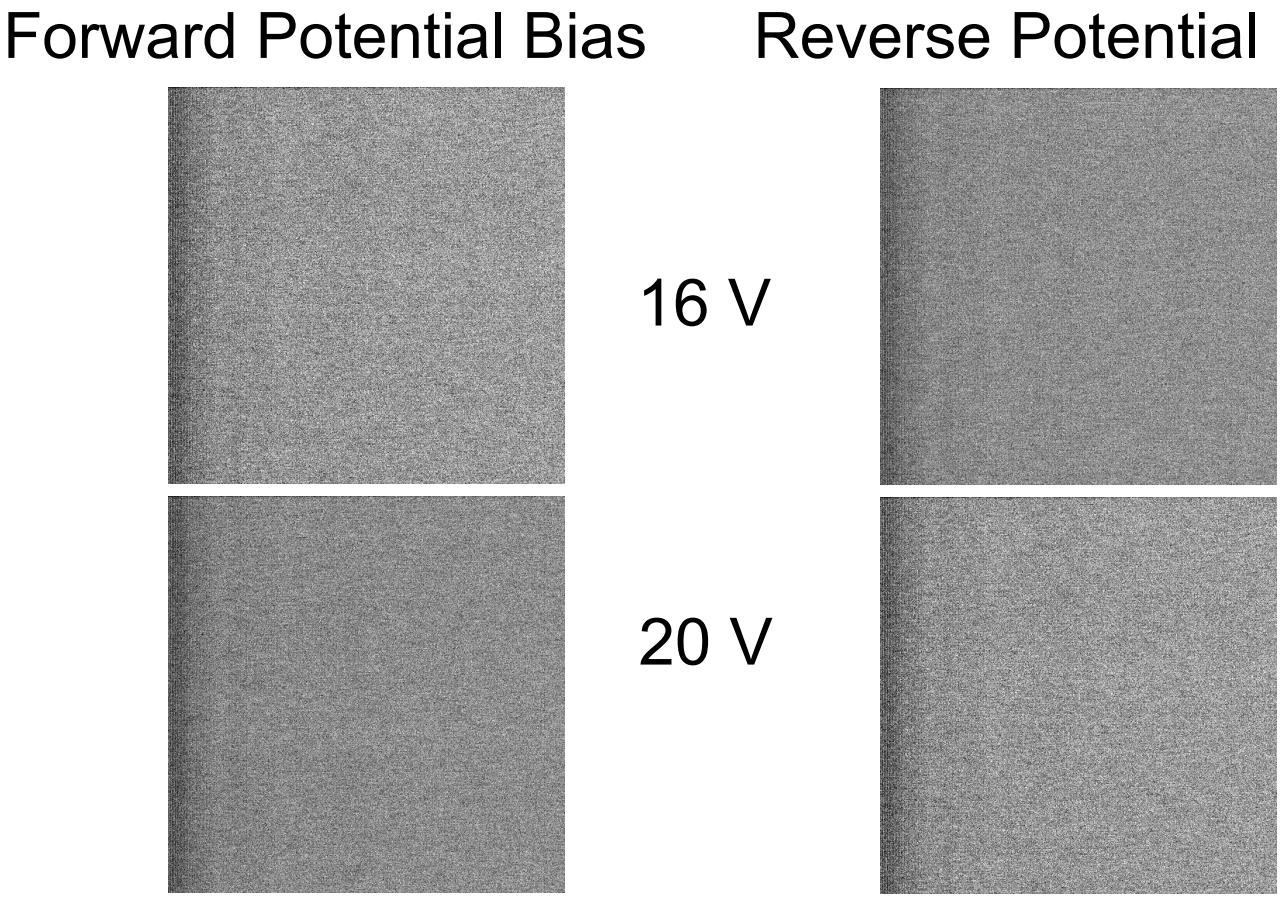

Figure 6.12: CCD images of ECL from application of 16 V and 20 V potential difference to a single device which had DNA adsorbed on the left hand (cathode) end only. The solution in the microchannel was 5 mM $[Ru(bpy)_3]^{2+}$, 25 mM TPrA, 0.1 M phosphate buffer and 0.1 mM KBr.

Cyclic voltammetry at a DNA modified gold disk electrode (modified with probe DNA and target DNA linked to Pt nanoparticles) showed that in the absence of bromide ions (in phosphate buffer alone) the ORR occurs at about -0.1 V (Figure 6.13). This is typical of the ORR occurring at a platinum surface [20]. When bromide ions are added to the solution (Figure 6.14), the potential of the reaction shifts to approximately -0.4 V, typical of the ORR occurring at a gold surface. This suggests that in the presence of bromide ions the ORR cannot occur at the platinum surface. This is most likely due to adsorption of bromide ions on the platinum surface. Furthermore, the adsorption of DNA and platinum nanoparticles at the gold surface is likely to hinder the ORR by covering large portions of the gold surface. Figure 6.15 shows the ORR occurring at a bare gold disk electrode in the absence of bromide ions or DNA, but under otherwise identical conditions to Figure 6.13. The charge passed is significantly greater at the bare gold surface (1.06 μC, Figure 6.15) compared to the DNA/Pt nanoparticle modified surface where the catalysis of the ORR by the Pt nanoparticles has been poisoned by the presence of bromide ions (0.08 μC Figure 6.14). This gives a plausible explanation for the failure of the ECL experiment in the presence of bromide ions. There is strong evidence that bromide adsorbs on the platinum surface and poisons the ORR catalysis thereby preventing ECL at 16 V (at both ends of the bipolar electrode). Additionally at 20 V, a potential at which the ECL reaction can proceed at the gold surface, the ORR is significantly hindered by the surface of the gold bipolar electrode being blocked by adsorbed DNA and poisoned Pt nanoparticles.

These experiments show that the enhancements achieved by adding bromide to the ECL solution in Section 6.4 cannot be transferred to a DNA sensor of this kind based on the ORR. However, the possibility remains to use the device for the detection of other species directly instead of the ORR, and the use of other reductants instead of oxygen, and for these applications the enhancements achieved in the presence of bromide ions will be important.

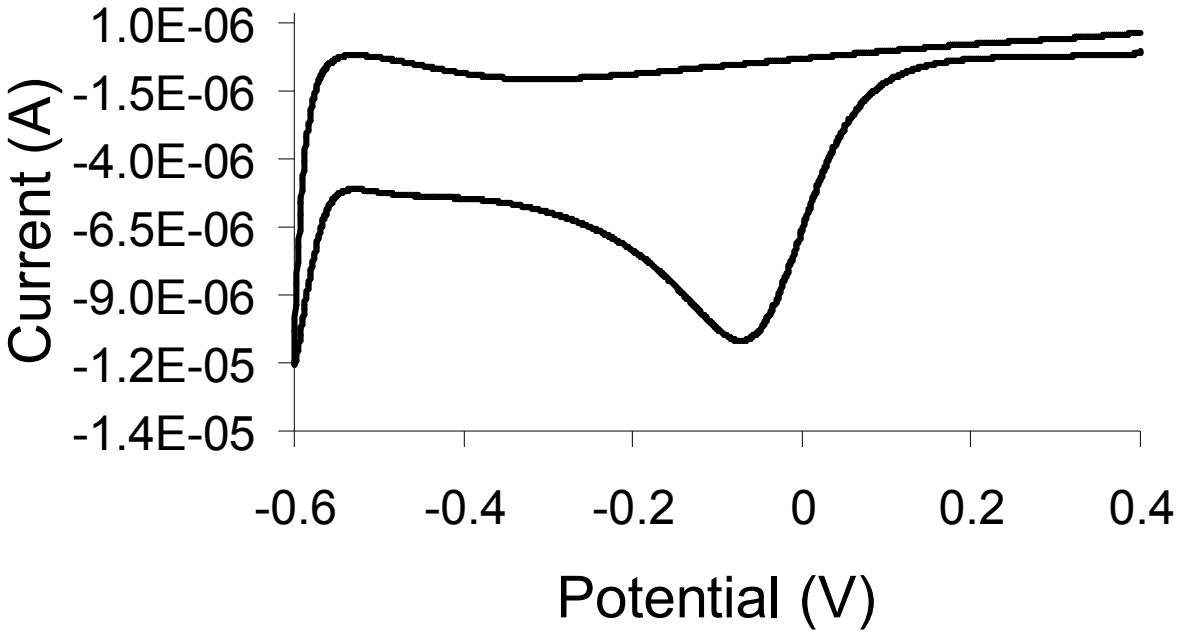

Figure 6.13: CV of 0.1 M phosphate buffer at a gold disk electrode (d = 2 mm) modified with capture DNA, target DNA and platinum nanoparticles, scan rate = 0.1 V s^{-1}.

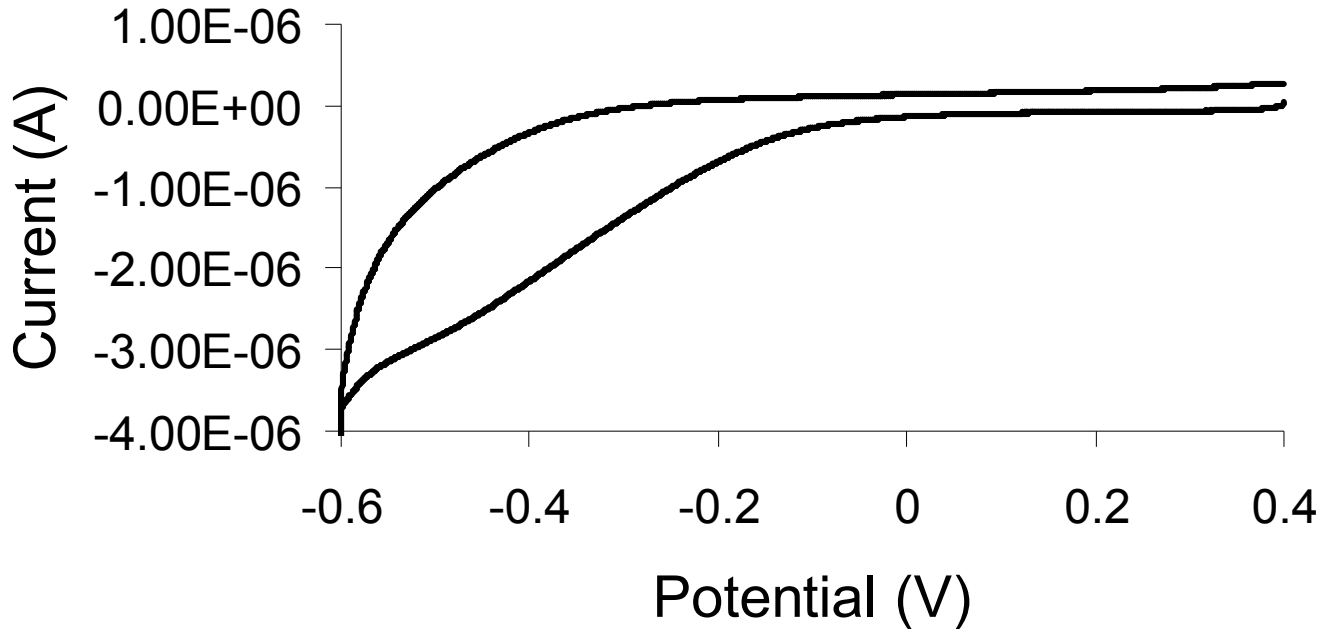

Figure 6.14: CV of 0.1 M phosphate buffer and 0.1 mM KBr at a gold disk electrode (d = 2 mm) modified with capture DNA, target DNA and platinum nanoparticles, scan rate = 0.1 V s^{-1}.

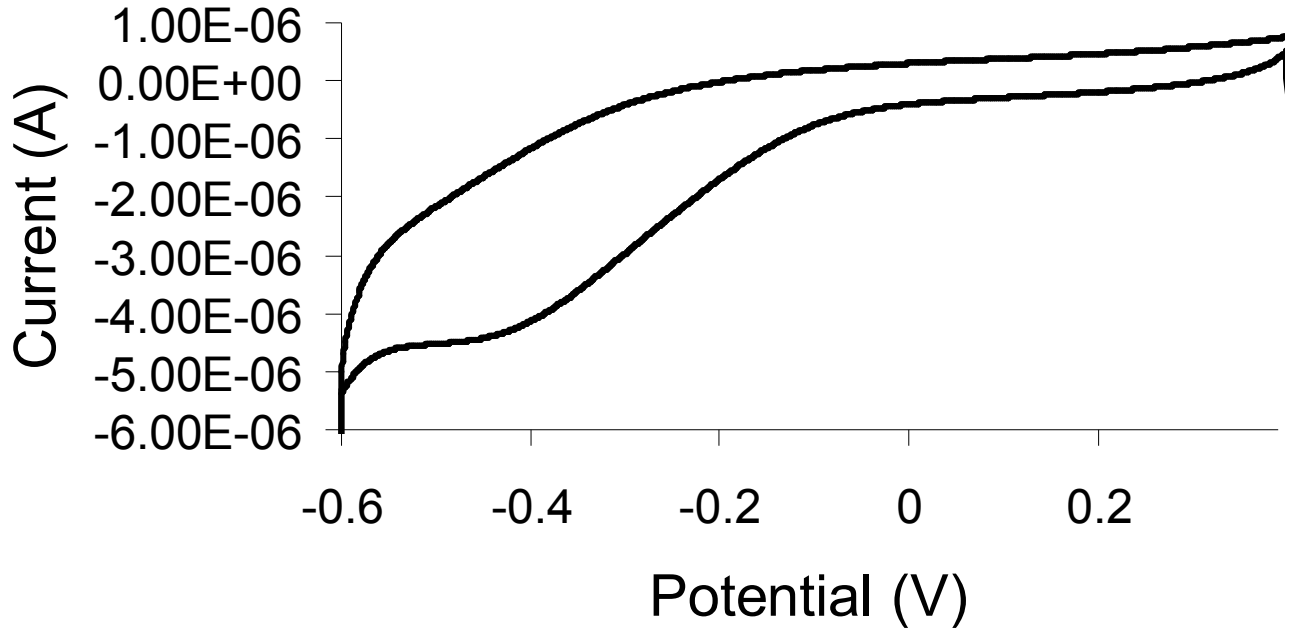

Figure 6.15: CV of 0.1 M phosphate buffer at a gold disk electrode (d = 2 mm), scan rate = 0.1 V s^{-1}.

6.7.2 Triton-X additive

In Section 6.4 it was pointed out that triton-X produced a smaller enhancement of the ECL signal compared to bromide ions in these devices. However, the mechanism of enhancement by triton-X is different. In the previous section it was demonstrated that bromide is an ineffective additive for these devices when platinum nanoparticle linked to DNA was the analyte. The increase in signal by a factor of 30 achieved with triton-X is impressive if it can be transferred from the basic unmodified device to the DNA/Pt modified device.

Initially, the experiment from Section 6.4, where triton-X was added to the basic ECL experiment, was repeated with capture DNA and platinum nanoparticle linked target DNA adsorbed on the surface of the gold bipolar electrode. The result of this experiment is presented in Figure 6.16. In the presence of triton-X, the ECL signal was quite strong when a potential of 16 V was applied across the device (Figure 6.16, LHS). In the control experiment, in the absence of triton-X the signal was significantly lower (Figure 6.16, RHS). This indicates that triton-X does not interfere with the ECL process in the presence of DNA/Pt as bromide does, and the signal is still enhanced. When the ECL intensity of Figure 6.16 was quantified by the CCD camera computer software, V++, it was found that the signal increased from 2.7 ($\pm$ 0.6) to 60 ($\pm$ 11), an enhancement of a factor of 22. This falls somewhat short of the enhancement factor of 30 obtained in the absence of DNA and platinum nanoparticles, however, it is nonetheless a significant increase in the signal. The presence of DNA at the anode end of the gold bipolar electrode, where ECL occurs, probably reduced the efficiency of the device by blocking parts of the electrode. Nevertheless, there is no evidence of interactions between DNA or platinum and triton-X, and the signal enhancement was demonstrated to translate from the basic device to the DNA modified device.

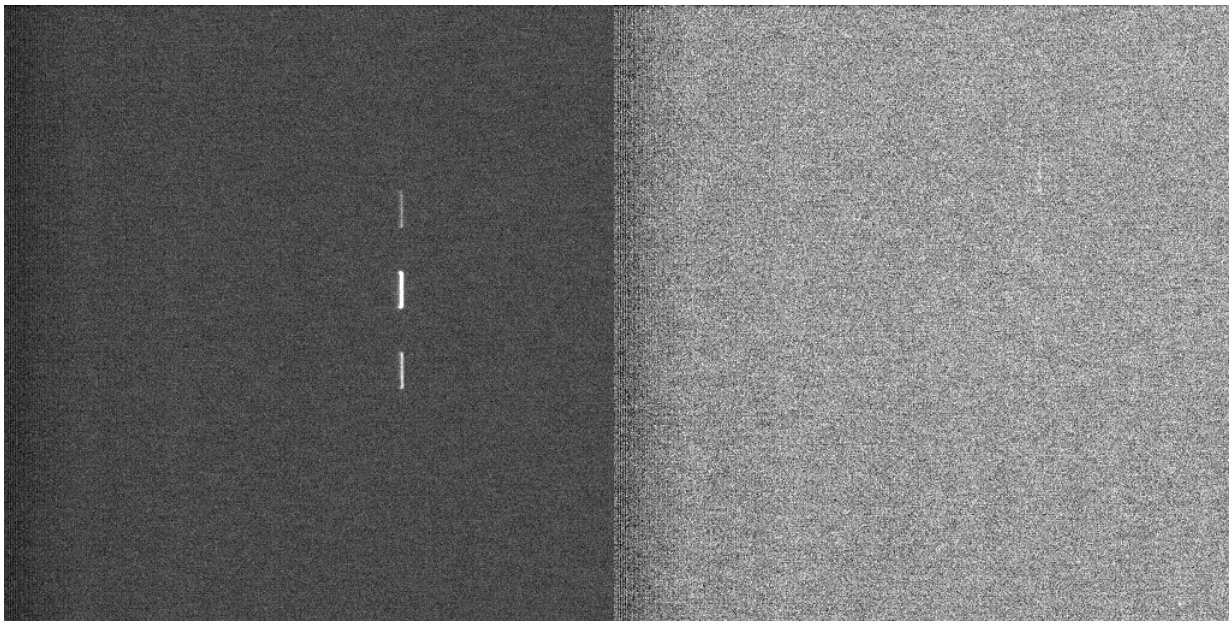

Figure 6.16: CCD images of ECL signal obtained by imposing a potential of 16 V across a microchannel device which had capture DNA and platinum nanoparticle linked target DNA immobilised on the gold bipolar electrode surface. The ECL solution was 5 mM $[Ru(bpy)_3]^{2+}$, 25 mM TPrA, 0.1 M phosphate buffer and 0.1 wt % triton-X (left image), no additive (right image).

Cyclic voltammetry was performed at a DNA/Pt nanoparticle modified gold disk electrode to confirm the absence of interactions influencing the oxygen reduction reaction. The electrolyte was 0.1 M phosphate buffer and 0.1 wt % triton-X. The result in Figure 6.17 demonstrates that the ORR occurs at approximately -0.1 V, which indicates that the ORR has occurred at a platinum surface. The shape and magnitude of the CV is similar to Figure 6.13 which contains no additive. Therefore, it can be concluded that triton-X does not influence the ORR, as bromide does, in the presence of DNA/Pt. However triton-X still enhanced the ECL signal.

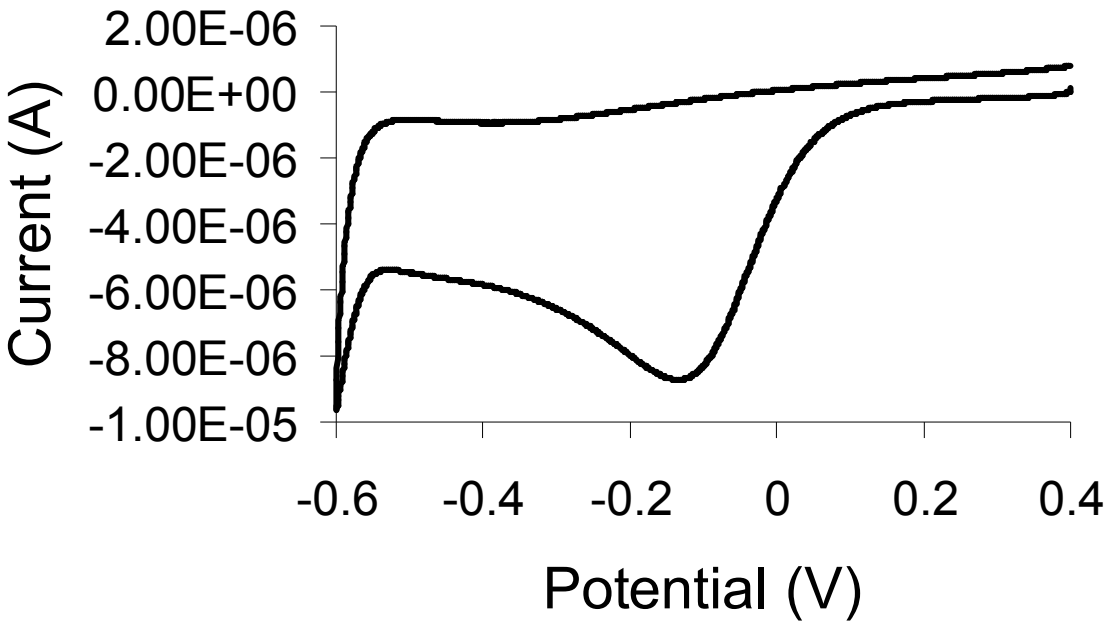

Figure 6.17: CV of 0.1 M phosphate buffer and 0.1 wt % triton-X, at a gold disk electrode (d = 2 mm) modified with capture DNA, target DNA and platinum nanoparticles, scan rate = 0.1 V s^{-1}.

6.8 Replacement of the oxygen reduction reaction and preparation of a calibration plot

The oxygen reduction reaction utilised in this device is necessary in order for the ECL reaction to proceed. In the last section, it was demonstrated that blocking the ORR at the cathode is sufficient to prevent the ECL from occurring at the anode. However, it is possible to replace the ORR with the reduction of another species, and this would allow the ECL reaction to proceed in the same manner. There are several advantages to using the ORR in this ECL device; namely oxygen is present in all aqueous ECL solutions, and although it is possible to de-gas these solutions, keeping the solutions oxygen free would be very difficult given the permeability of oxygen through PDMS. Moreover, oxygen is very well suited to use in this type of device as its electro-reduction is catalysed by platinum, meaning the potential at which the ORR and therefore the ECL occurs can be shifted by the presence or absence of platinum nanoparticles. However, oxygen is far from ideal at the task of sacrificial reductant. Because oxygen is not highly soluble in water it isn't possible to increase its concentration above approximately 500 μM (without changing its temperature or salinity), so it is possible that the resulting slow rate of the ORR limits the ECL reaction occurring at the anode. Also, unlike solution phase species, it is very difficult to control the concentration of oxygen in the ECL solution so it is impossible to prepare a calibration curve by varying oxygen concentration. Therefore, to overcome some of the above mentioned problems, and to demonstrate the diversity of the device, alternative reductants were sought.

6.8.1 Selection of alternate species

The new reduced species needed to be water soluble (so the $[Ru(bpy)_3]^{2+}$, TPrA ECL couple could be utilised) and as it would be extremely difficult to de-oxygenate the solution, the reduction potential of the new species needed to be more positive than oxygen so that it could be reduced without reducing oxygen simultaneously. A list of some of the species that meet these criteria is given in Table 6.4. Cyclic voltammograms demonstrating the reduction

Table 6.4: Reduction potential of species considered as replacement for oxygen as reduced species in microchannel sensing device.

Species	Reduction Potential
Oxygen	-0.45 V
Benzyl Viologen	-0.53 V
Copper Sulphate	-0.18 V
Ruthenium Hexamine (Ru Hex)	-0.21 V
Anthraquinone	0.17 V

Reduction potentials taken from Figure 6.15 and Figure 6.18.

peak of each of these species at a gold disk electrode are presented in Figure 6.18. Each of these CVs also contains a $[Ru(bpy)_3]^{2+}$ oxidation peak at approximately 1.2 V. When the reactions are performed within the microchannel, at an electrode of floating potential, the oxidation and reduction reactions that occur at the anode and cathode respectively are the $[Ru(bpy)_3]^{2+}$ oxidation, and reduction of the appropriate reducible species present, provided sufficient potential difference is applied across the microchannel.

In order to achieve the goal of reducing one of the listed species without reducing oxygen a potential must be chosen at which the alternate species is reduced, and oxygen is not reduced. Clearly given the data in Table 6.4 benzyl viologen is not a candidate given its more positive reduction potential compared to oxygen. Copper sulphate and Ru Hex have reduction potentials positive of oxygen's, however given that the difference between reduction potentials is so slight (0.07 V and 0.04 V respectively) it would be very difficult to achieve reduction of these alternate species without simultaneously reducing oxygen. Finally, anthraquinone is a promising alternative. Its reduction potential is 0.42 V more positive than oxygen so it should be easy to select a potential at which only anthraquinone is reduced in the device, without having to remove oxygen from the ECL solution. Furthermore, anthraquinone is more soluble in water than oxygen (2.5 mM vrs 0.5 mM) so it is an ideal candidate to replace oxygen as the reduced species in the ECL reaction.

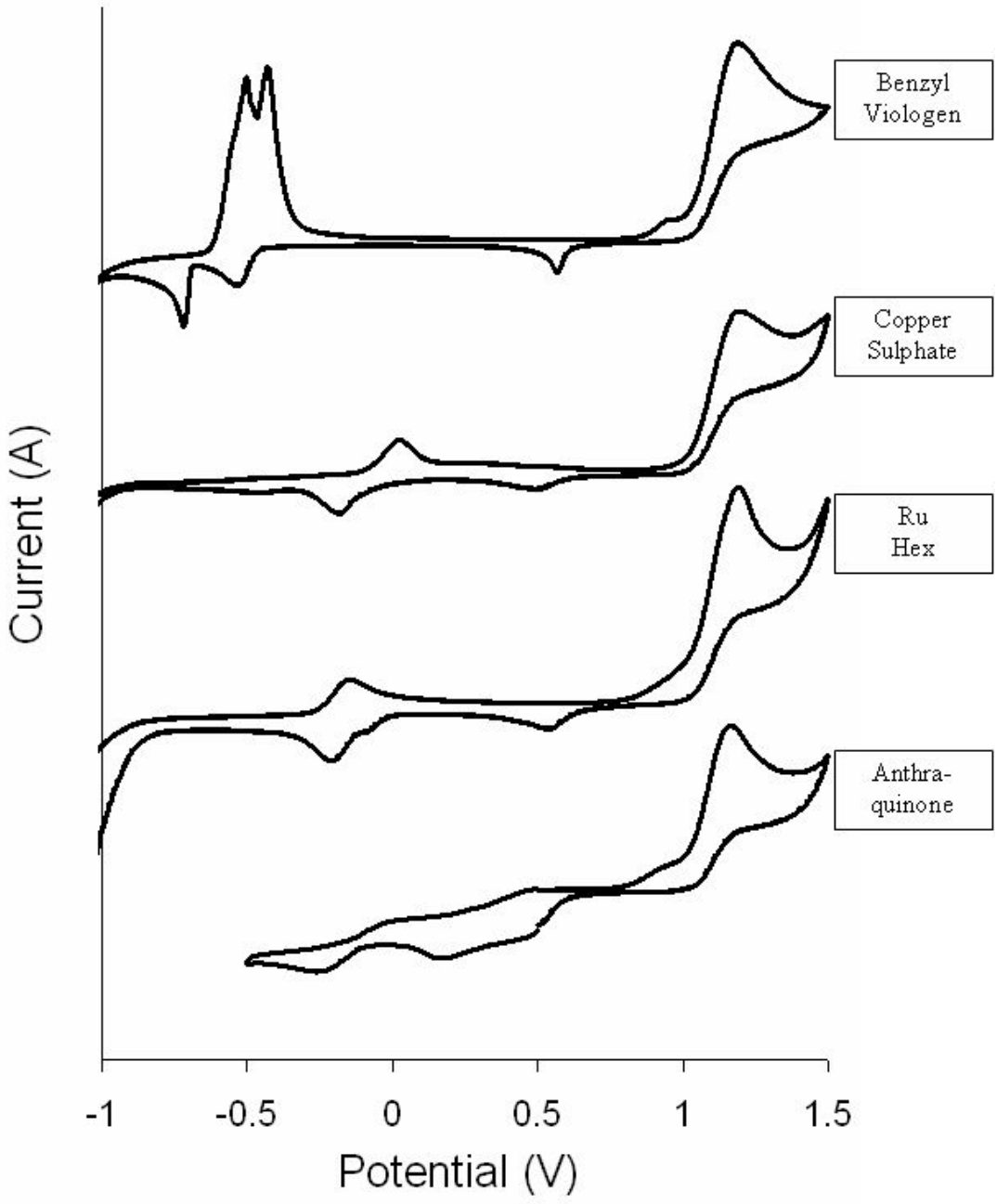

Figure 6.18: CV at bare gold disk electrode (d = 2 mM) of solutions containing 0.1 M phosphate buffer, 5mM $[Ru(bpy)_3]^{2+}$ and 25 mM TPrA with the indicated species added at a concentration of 5 mM, scan rate = 0.1 V s^{-1}.

6.8.2 Proof of concept: Copper reduction and simultaneous electrodeposition

In order to prove that the oxygen reduction reaction can be replaced within the devices sensing mechanism an experiment was performed in which the ECL reaction was induced as normal at an unmodified (no DNA/Pt) gold bipolar electrode. The ECL solution injected into the device was the usual ECL solution (5 mM $[Ru(bpy)_3]^{2+}$, 25 mM TPrA and 0.1 M phosphate buffer) with 5 mM copper sulphate added. According to Table 6.4 oxygen and copper sulphate have approximately the same reduction potential so it is likely that they would co-reduce when a sufficiently large potential is applied to the device. Figure 6.19 shows a CCD image of the ECL emission from the device upon application of a potential of 21 V across the device, and more significantly it shows an image of the device before and after the potential has been applied. The images show that a deposit has formed on the cathode of the device (left hand edge), where the reduction reaction has occurred. In the absence of copper sulphate in the ECL solution this deposit does not form (Figure 6.20) therefore it can be assumed that the deposit formed is copper metal, and therefore it has been shown that the ECL reaction has proceeded as normal when copper sulphate was reduced at the cathode. Note that a deposit also forms on the anode end of the device; this is believed to be reduced $[Ru(bpy)_3]^{2+}$, which rinses off upon flushing with buffer solution. It was pointed out in the previous section that copper sulphate is a poor candidate for the replacement of the ORR, this experiment demonstrates that the ORR can be replaced without preventing the device from functioning.

6.8.3 Anthraquinone reduction

Of the species considered in Table 6.4 anthraquinone is the one with the most positive reduction potential. Therefore, it should be possible to apply a potential across the microchannel device, such that anthraquinone is reduced and oxygen is not reduced. This potential corresponds to a potential negative of 0.17 V and positive of -0.45 V, at these potentials anthraquinone is reduced and oxygen is not reduced. In order to achieve

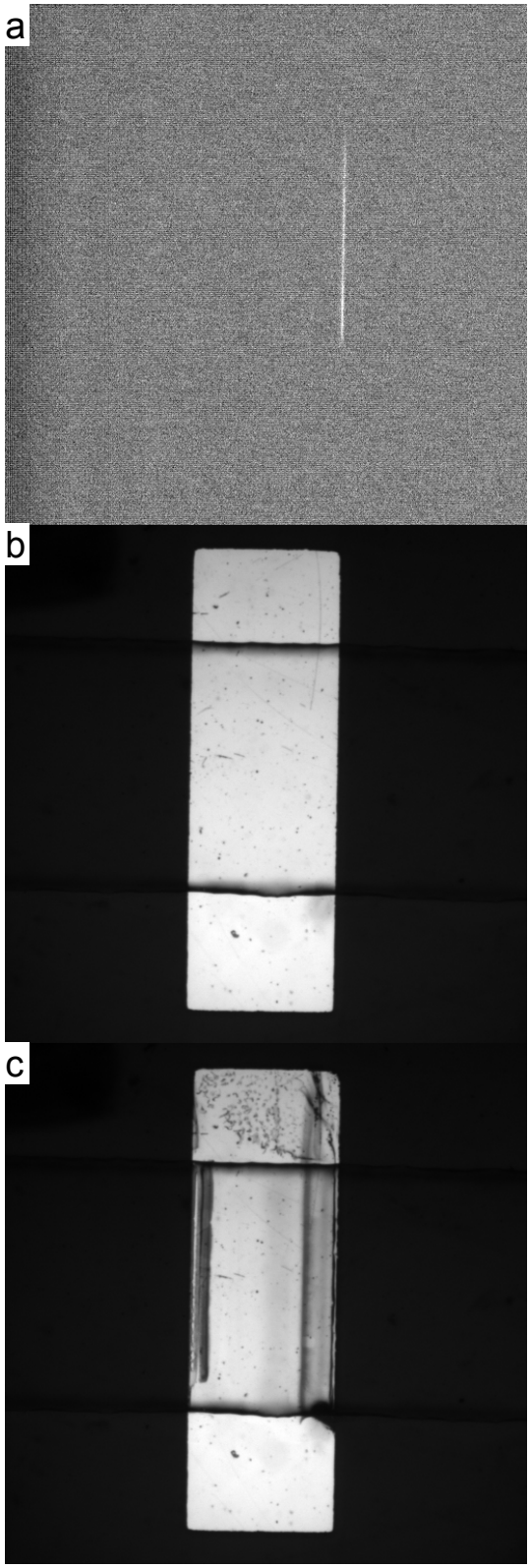

Figure **6.19**: (a) CCD image of the ECL emission from a single gold bipolar electrode upon application of a potential of 21 V across the device. The ECL solution was 5 mM $[Ru(bpy)_3]^{2+}$, 25 mM TPrA, 0.1 M phosphate buffer and 5 mM $CuSO_4$. (b) CCD image of gold bipolar electrode before ECL experiment. (c) CCD image of gold bipolar electrode after ECL experiment.

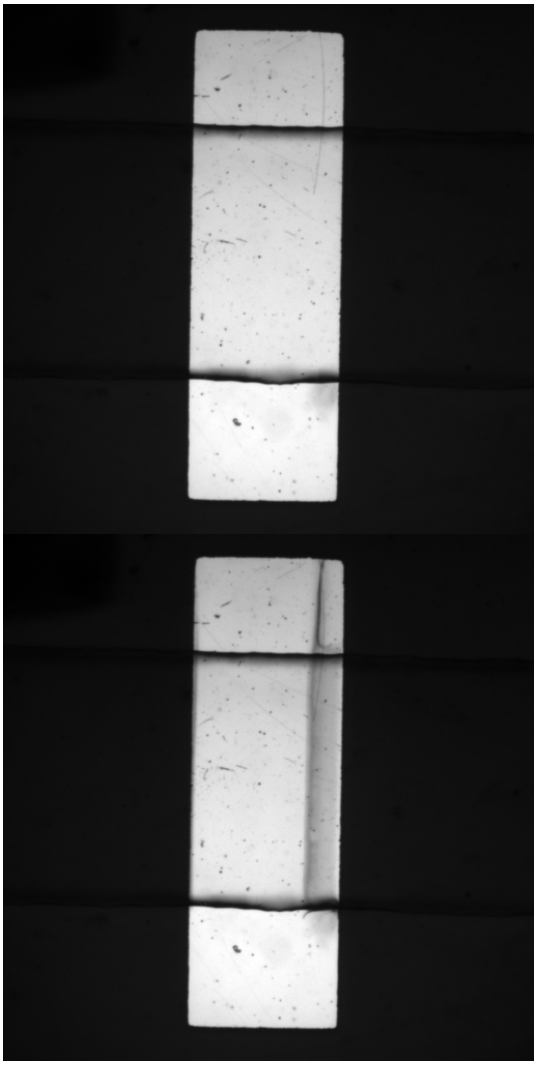

Figure **6.20**: CCD image of gold bipolar electrode before (top) and after (bottom) ECL experiment. A potential of 21 V was applied across the device. The ECL solution was 5 mM $[Ru(bpy)_3]^{2+}$, 25 mM TPrA, and 0.1 M phosphate buffer.

this potential difference across the length of the gold bipolar electrode a potential of less than 19.5 V must be applied between the wells of the microchannel device (see calculation below). In the absence of platinum nanoparticles ECL did not occur when the ECL solution contained 5 mM $[Ru(bpy)_3]^{2+}$, 25 mM TPrA and 0.1M phosphate buffer when a potential of less than 20 V was applied across the microchannel. This is demonstrated in Figure 6.21. However, when 5 mM anthraquinone was added to the same solution, ECL occurred at potentials as low as 18 V, as shown in Figure 6.22. There is no ECL signal in the absence of anthraquinone at 18 V and 19 V, and in the presence of anthraquinone the ECL reaction occurs so it can be concluded that adding anthraquinone to the ECL solution results in ECL at these potentials, and the reasonable explanation for this result is that anthraquinone reduction is occurring, thus facilitating the ECL reaction at the anode. Oxygen reduction is not occurring at these potentials, evidenced by no ECL at 18 V and 19 V in the absence of anthraquinone.

Calculation of potential required for ORR to occur

Reduction potential of oxygen at gold electrode: -0.45 V

Oxidation potential of $[Ru(bpy)_3]^{2+}$ at gold electrode: 1.2 V

Potential difference required across electrode for ORR:

1.2 V – (-0.45 V) = 1.65 V

Length of microchannel = 12 mm

Length of bipolar electrode = 1 mm

Potential applied between wells to induce 1.65 V potential difference across length of bipolar electrode = (12/1) x 1.65 V

= **19.8 V**

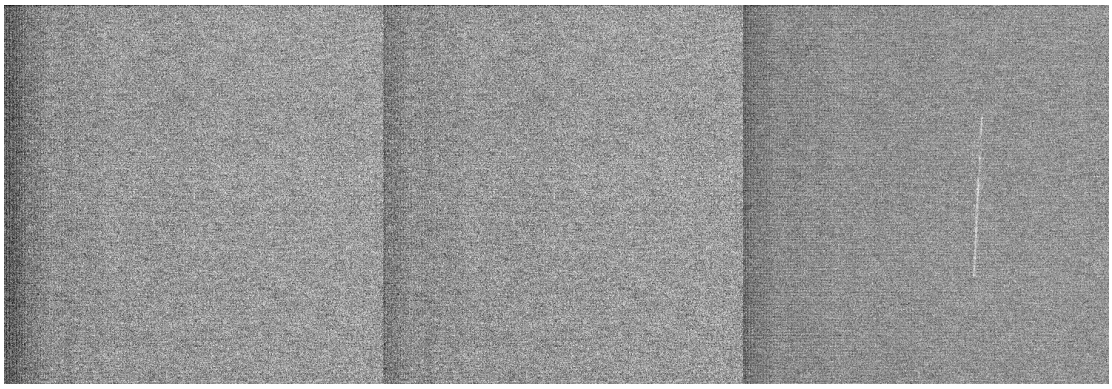

Figure 6.21: CCD images of ECL signal obtained by imposing a potential of 18 V (left), 19 V (centre) and 20 V (right) across a microchannel device containing a single unmodified gold bipolar electrode. The ECL solution was 5 mM $[Ru(bpy)_3]^{2+}$, 25 mM TPrA and 0.1 M phosphate buffer.

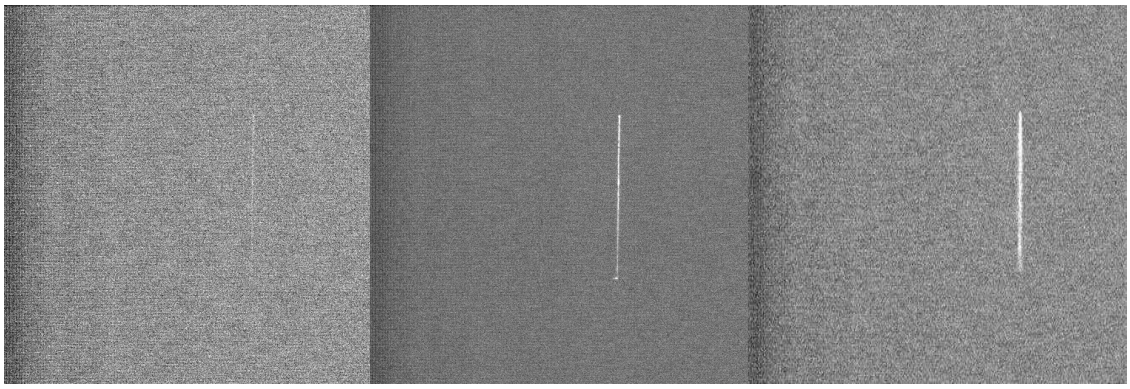

Figure 6.22: CCD images of ECL signal obtained by imposing a potential of 18 V (left), 19 V (centre) and 20 V (right) across a microchannel device containing a single unmodified gold bipolar electrode. The ECL solution was 5 mM $[Ru(bpy)_3]^{2+}$, 25 mM TPrA, 0.1 M phosphate buffer and 5 mM anthraquinone.

6.8.4 Linearity of ECL response

Having demonstrated that it was possible to facilitate the ECL reaction with anthraquinone reduction instead of oxygen reduction it was possible to construct a calibration curve by varying the anthraquinone concentration in the ECL solutions. The linear range considered was 1 μM to 10 mM anthraquinone, however the lowest concentration at which ECL could be recorded was 50 μM anthraquinone. And it was not possible to dissolve anthraquinone completely above 5 mM. The solutions consisted of the standard ECL solution (5 mM $[Ru(bpy)_3]^{2+}$, 25 mM TPrA, 0.1 M phosphate buffer), with KBr (0.1 mM) added to enhance the ECL signal and anthraquinone added at varying concentrations. The measurements were recorded from devices containing a single gold bipolar electrode, unmodified by DNA or platinum. The calibration curve obtained is presented in Figure 6.23. The linearity of the curve was questionable, as indicated by the r^2 value of 0.9443. This departure from linearity was likely a result of problems dissolving anthraquinone at concentrations above 1 mM, as these are the points that deviate most from the trend line. The error bars in Figure 6.23 also highlight the difficulty in reproducing results with the same solution, which doubtless also affected the linearity of the calibration curve.

The results indicate that the device can be used to qualitatively detect a species in the μM range. Quantitative determination is also possible; however such measurements would not be as precise as more established methods of analyte determination such as HPLC and GC-MS. It should be possible to extend the linear range of the device further when the analyte is more water soluble. It is not envisaged that this device will be used for the detection of anthraquinones, or other suitable species, because the choice of species would be severely limited by the reduction potential of the species, and its solubility in water. However, this experiment demonstrates that the ECL response of the device is linear with the concentration of reducing species in the solution.

Instead this device is more suited to the detection of DNA and other biological molecules based on platinum nanoparticle electrocatalysis as already described. In this area the device's greatest advance comes as a qualitative assay for the presence of many analytes simultaneously, with the option to quantify the amount of analyte if required.

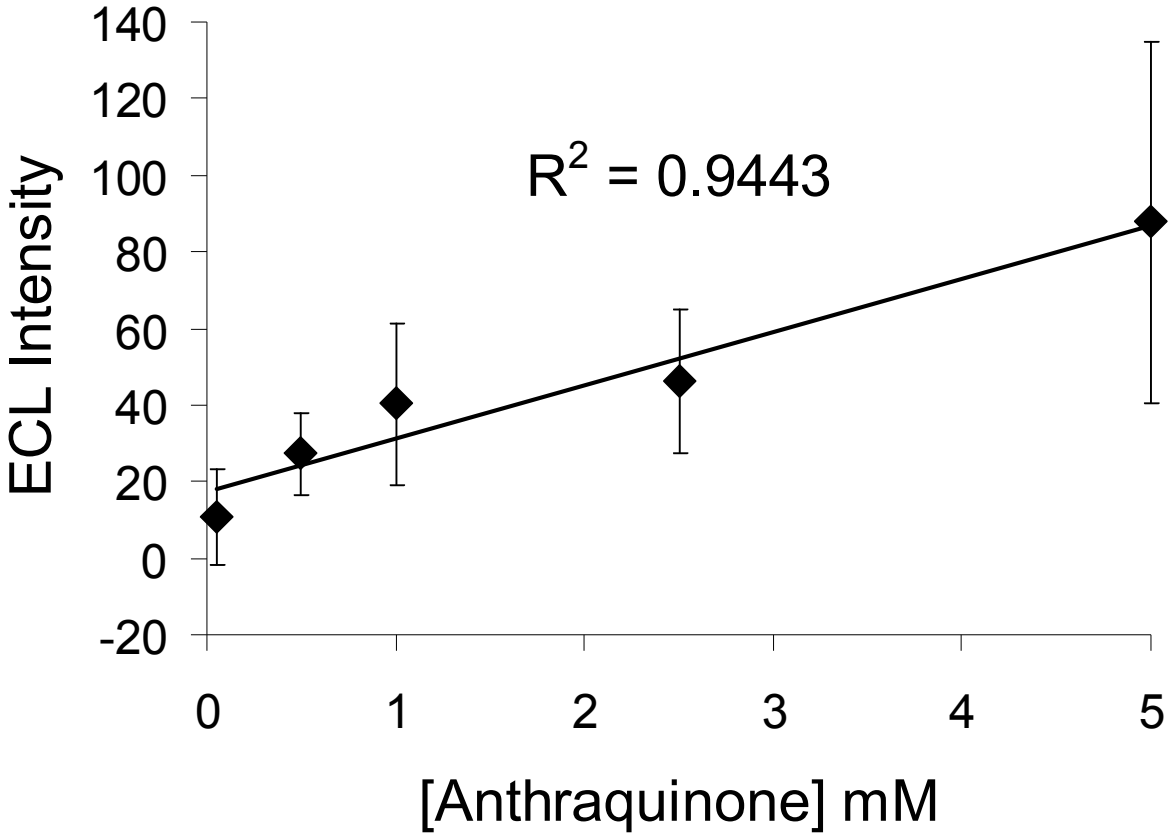

Figure 6.23: Calibration curve for ECL intensity yields from different anthraquinone concentrations. Intensity was mean intensity recorded from a single device containing a single gold bipolar electrode over three measurements. The ECL solution was 5 mM $[Ru(bpy)_3]^{2+}$, 25 mM TPrA, 0.1 M phosphate buffer, 0.1 mM KBr and the indicated concentration of anthraquinone, the potential applied across the device was 20V.

6.9 Conclusions

A wireless electrochemical sensor has been produced, in which the electrochemiluminescent sensing event was decoupled from the electrochemical reaction under investigation. The device worked by applying a potential gradient across a microchannel so that a potential difference existed between two ends of a bipolar electrode within the channel, whose potential was floating. The potential difference across the length of the electrode was sufficient to induce oxidation and simultaneous reduction at each end of the electrode if a sufficiently large potential difference was applied across the length of the channel, and if the appropriate species were in solution such that the electrode could facilitate the redox reactions. When a sufficiently large potential difference was applied reduction of oxygen at one end of the bipolar electrode could be coupled to $[Ru(bpy)_3]^{2+}$ and TPrA oxidation so that ECL emission could be recorded to detect the oxygen reduction reaction (ORR). As the ORR is catalysed at the surface of platinum nanoparticles, this device could be used to detect the presence of biomolecules, such as DNA, using platinum nanoparticles as tags. The presence of the nanoparticles reduced the potential difference required to induce ECL emission in the device.

The ECL solution was optimised in order to maximise device efficiency and sensitivity. The most efficient ECL mechanism was selected by the use of additives such as bromide and triton-X, resulting in up to a 35 fold increase in the ECL signal. Additionally, the optimum ratio of $[Ru(bpy)_3]^{2+}$ and TPrA in the ECL solution was determined. Detection of selective DNA binding was demonstrated, and the potential to selectively decorate different electrodes within the channel with different DNA sequences was explored. This could eventually lead to a DNA sensor capable of detecting many different DNA sequences simultaneously in a single measurement. It was shown that the ORR could be replaced, so that the device could be used to detect other reduction reactions, such as anthraquinone reduction. The ECL response was seen to be linear with anthraquinone concentration. This suggested that it might be possible to use the device for quantitative as well as qualitative

determination of analytes, such as DNA sequences, or other relevant species for which anti-bodies can be prepared for specific interactions.

References

[1] Lee, W. Y., *Mikrochim. Acta*, 1997. **127**(1-2): 19-39.

[2] Gerardi, R. D., Barnett, N. W., and Lewis, S. W., *Analytica Chimica Acta*, 1999. **378**(1-3): 1-41.

[3] Brune, S. N. and Bobbitt, D. R., *Analytical Chemistry*, 1992. **64**(2): 166-170.

[4] Bard, A. J., *Electrogenerated Chemiluminescence*. 2004, New York: Marcel Dekker.

[5] Zhan, W., Alvarez, J., and Crooks, R. M., *Journal of the American Chemical Society*, 2002. **124**(44): 13265-13270.

[6] Chow, K. F., Mavre, F., and Crooks, R. M., *Journal of the American Chemical Society*, 2008. **130**(24): 7544-+.

[7] Zu, Y. B. and Bard, A. J., *Analytical Chemistry*, 2001. **73**(16): 3960-3964.

[8] Zu, Y. B. and Bard, A. J., *Analytical Chemistry*, 2000. **72**(14): 3223-3232.

[9] Blum, W., *Journal of the Electrochemical Society*, 1952. **99**(2): C31-C33.

[10] Choi, H. N., Cho, S. H., and Lee, W. Y., *Analytical Chemistry*, 2003. **75**(16): 4250-4256.

[11] Guo, Z. H. and Dong, S. J., *Analytical Chemistry*, 2004. **76**(10): 2683-2688.

[12] Zhang, L. H. and Dong, S. J., *Analytical Chemistry*, 2006. **78**(14): 5119-5123.

[13] Wang, H. Y., Zhang, X. L., Tan, Z., Yao, W., and Wang, L., *Electrochem. Commun.*, 2008. **10**(1): 170-174.

[14] Zhou, M., Robertson, G. P., and Roovers, J., *Inorganic Chemistry*, 2005. **44**(23): 8317-8325.

[15] Kanoufi, F., Zu, Y. B., and Bard, A. J., *Journal of Physical Chemistry B*, 2001. **105**(1): 210-216.

[16] Sanchez-Pomales, G., Santiago-Rodriguez, L., Rivera-Velez, N. E., and Cabrera, C. R., *J. Electroanal. Chem.*, 2007. **611**(1-2): 80-86.

[17] Mali, P., Bhattacharjee, N., and Searson, P. C., *Nano Letters*, 2006. **6**(6): 1250-1253.

[18] Wackerbarth, H., Grubb, M., Zhang, J. D., Hansen, A. G., and Ulstrup, J., *Langmuir*, 2004. **20**(5): 1647-1655.

[19] Musgrove, A., Kell, A., and Bizzotto, D., *Langmuir*, 2008. **24**(15): 7881-7888.

[20] Takasu, Y., Ohashi, N., Zhang, X. G., Murakami, Y., Minagawa, H., Sato, S., and Yahikozawa, K., *Electrochim. Acta*, 1996. **41**(16): 2595-2600.

7 Conclusions

The electrodeposition of precious metal nanoparticles, of gold, onto an electrically conducting, optically transparent fluorine-doped tin-oxide coated glass was investigated. The influence of changing experimental conditions such as electrolyte composition and applied potential were examined to determine the influence of these parameters on electrodeposition kinetics, and the properties of the resulting nanoparticles. It was found that by increasing the gold salt concentration, and by applying a more negative potential to the working electrode, the kinetics of electrodeposition could be influenced. Analysis of the kinetics of the deposition by use of dimensionless plots indicated that instantaneous nucleation could be achieved by controlling these parameters. However, SEM image analysis indicated that when the dimensionless plots indicated that instantaneous nucleation had occurred the maximum density of nanoparticles on the surface had not in fact been achieved, and the density of nanoparticles could be further increased at even more negative potentials.

Two methods to control the nucleation and growth modes of electrodeposition of gold nanoparticles on FDTO were investigated. Chemically modifying the FDTO electrode with a silane terminated alkane-thiol (ADMMS) influenced the current transient of the electrodepositions such that analysis of the kinetics of the deposition by use of dimensionless plots indicated that instantaneous nucleation could be achieved with application of a less negative potential, compared to electrodeposition onto unmodified FDTO. Achieving instantaneous nucleation without applying such a large overpotential would be advantageous as it would facilitate growth of nanoparticles at a slower rate, resulting in a reduction in diffusion zone coupling and therefore increasing particle size monodispersity. However, SEM image analysis indicated that even though the dimensionless plots indicated that instantaneous nucleation had occurred, the density of gold nanoparticles on the chemically modified surface was significantly less than

the densities seen when a larger overpotential was applied to the unmodified FDTO surface.

Use of a double-pulse electrodeposition scheme, such that nucleation of nanoparticles on unmodified FDTO was achieved at a very high density, by a very short time-scale potential pulse of high overpotential, and growth then proceeded by a much longer duration, lower overpotential pulse was also investigated. Using this method it was possible to significantly increase the density of nanoparticles on the surface, compared to the other investigated methods. In addition, despite the increase in nanoparticle density on the surface, the particle size polydispersity did not change to a significant extent. This indicates that the double-pulse technique was successful in limiting the affects of diffusion zone coupling. The size and interparticle spacing of the nanoparticles could be controlled within certain limits by controlling the potential and duration of the nucleation and/or growth pulse. This technique was successfully used to electrodeposit silver nanoparticles on FDTO in the same way. Electromagnetically interacting gold nanoparticles of controlled size, as well as electromagnetically isolated gold and silver nanoparticles of controlled size could be produced using this method.

The above method for controlled electrodeposition of gold and silver nanoparticles was utilised to produce surfaces optimised for spectroscopic sensing applications. The application of these surfaces to SERS has been demonstrated, producing up to a 3 orders of magnitude enhancement factor with silver nanoparticles under optimal conditions, and 2 orders of magnitude with gold nanoparticles. A potential problem with this approach is the large relative standard deviation of the enhancement factor at different locations on the surface, typically 20-30%. Much of the imprecision could be due to the size distribution of nanoparticles which was typically around 40% for the isolated silver nanoparticles. Future work may concentrate on performing these experiments on a smoother surface than FDTO that may enable the narrowing of this size distribution. Nonetheless the standard deviation of the enhancement factor is comparable to similar results in the literature. These

surfaces therefore provide a relatively reproducible, strong enhancement of the SERS signal and could be used as part of a diagnostic device.

The fluorescence signal was also significantly enhanced on the silver nanoparticle surfaces, by a factor of greater than 100. Although direct comparison to similar systems was not possible, as fluorescence enhancement factor is dependent on the fluorophore used, this result is impressive compared to similar literature studies, and the fluorescence signal was much more reproducible than the SERS signal. A strong, reproducible fluorescence signal is yielded from these surfaces, making them an ideal platform for fluorescence based diagnostics.

Osmium polypyridyl complexes have been spontaneously assembled onto the conducting substrate, FDTO. The electrochemical properties of the films were probed and confirmed the presence of a monolayer on the surface and indicated that the monolayer was densely packed. In solution Stern-Volmer plots indicated that the quenching action of POW on the osmium polypyridyl complexes was via a combined collisional and associative mechanism, but that at higher POW concentrations the quenching was predominantly associative in nature.

When the osmium polypyridyl complexes were assembled on an electrode surface, irradiated with a 355 nm laser source, and held at a potential of 0.1 V a significant current was recorded if the electrode was immersed in a solution containing POW and methyl viologen. There was no current in the absence of POW, and very little current in the absence of methyl viologen. The conclusion that can be drawn is that the excited osmium complex was quenched by an associated POW, and the excited electron was accepted from the POW molecule by a solution phase methyl viologen molecule, reducing it in the process. The osmium complex was returned to its original charge by reduction at the electrode. In order for continued reduction of osmium to occur methyl viologen molecules had to be continually reduced, so the current recorded was proof that methyl viologen reduction was occurring. In the absence of irradiation, excitation and quenching did not

occur and consequently there was no methyl viologen reduction. The photo-catalytic reaction could be initiated and discontinued by switching the irradiation source on and off.

The potential applied to the electrode was over 500 mV positive of the reduction potential of methyl viologen yet the reaction proceeded, and the beginning and final states of the osmium complex and the POW molecule were the same making it a photo-catalytic reaction. A possible reason for the impressive current yield from the $[Os(bpy)_2Qbpy]^{2+}$ immobilised on silver nanoparticles system is that on the nanoparticle surface the emission of osmium may be plasmonically enhanced, perhaps increasing the number of excited $[Os(bpy)_2Qbpy]^{2+}$ molecules on the surface. Ultimately this work has demonstrated the harnessing of photonic energy and conversion into chemical energy.

A wireless electrochemical sensor has been produced, in which the electrochemiluminescent sensing event was decoupled from the electrochemical reaction under investigation. The device worked by applying a potential gradient across a microchannel so that a potential difference existed between two ends of a bipolar electrode within the channel, whose potential was floating. The potential difference across the length of the electrode was sufficient to induce oxidation and simultaneous reduction at each end of the electrode if a sufficiently large potential difference was applied across the length of the channel, and if the appropriate species were in solution such that the electrode could facilitate the redox reactions. When a sufficiently large potential difference was applied reduction of oxygen at one end of the bipolar electrode could be coupled to $[Ru(bpy)_3]^{2+}$ and TPrA oxidation so that ECL emission could be recorded to detect the oxygen reduction reaction (ORR). As the ORR is catalysed at the surface of platinum nanoparticles, this device could be used to detect the presence of biomolecules, such as DNA, using platinum nanoparticles as tags. The presence of the nanoparticles reduced the potential difference required to induce ECL emission in the device.

The ECL solution was optimised in order to maximise device efficiency and sensitivity. The most efficient ECL mechanism was selected by the use of additives such as bromide and triton-X, resulting in up to a 35 fold increase in the ECL signal. Additionally, the optimum ratio of $[Ru(bpy)_3]^{2+}$ and TPrA in the ECL solution was determined. Detection of selective DNA binding was demonstrated, and the potential to selectively decorate different electrodes within the channel with different DNA sequences was explored. This could eventually lead to a DNA sensor capable of detecting many different DNA sequences simultaneously in a single measurement. It was shown that the ORR could be replaced, so that the device could be used to detect other reduction reactions, such as anthraquinone reduction. The ECL response was seen to be linear with anthraquinone concentration. This suggested that it might be possible to use the device for quantitative as well as qualitative determination of analytes, such as DNA sequences, or other relevant species for which anti-bodies can be prepared for specific interactions.

Overall this work has presented some novel and interesting advances in the fields of nanoparticle science, diagnostics, sensing and photo-catalysis.

8 Appendix: Publications

Available online at www.sciencedirect.com
ScienceDirect
Journal of Electroanalytical Chemistry 608 (2007) 1–7
Journal of Electroanalytical Chemistry
www.elsevier.com/locate/jelechem

Electrodeposition of gold nanoparticles on fluorine-doped tin oxide: Control of particle density and size distribution

Eoin Sheridan, Johan Hjelm [1], Robert J. Forster *

National Centre for Sensor Research, School of Chemical Sciences, Dublin City University, Dublin 9, Ireland

Received 2 August 2006; accepted 16 November 2006
Available online 10 July 2007

Abstract

Electrodeposition of gold island films of nanometre dimensions (<100 nm) on fluorine-doped tin oxide (FDTO) coated glass is reported. The effect of altering the overpotential of the potentiostatic transient, the use of both nucleation and growth pulses as well as the immobilisation of a spontaneously adsorbed monolayer of, 3-aminopropyldimethylmethoxysilane, is reported. Deposits ranging from isolated particles to dense arrays of nanometre dimension particles have been formed. For example, by using a 10 ms nucleation pulse at −1200 mV followed by growth at 600 mV, a high particle density (46 particles/μm^2) and a mean particle size of 36 nm with an RSD of 29% were obtained. Double potential step approaches coupled with interfacial engineering via monolayer formation allows gold nanoparticles to be created on optically transparent FDTO with controlled particle size, density and particle size distribution in a facile, inexpensive, reproducible manner.

Keywords: Nanoparticles; Electrodeposition; Chronoamperometry; Modified electrodes

1. Introduction

The production of nanometre sized gold deposits at interfaces with high particle density and small particle size distribution is an area of intense research [1–5]. This interest is driven in part by the production of nanostructured electrode surfaces with the aim of creating high sensitivity amperometric sensors, as well as surface enhanced Raman scattering (SERS) and plasmonic surfaces for luminescence enhancement [6–9].

For many of these applications, the desired properties of the gold deposits include a small particle size, a narrow size distribution and a high particle density. Control over particle size is vital since it allows tuning of the surface plasmon frequency [10,11] and the production of smaller particles consumes less gold to achieve a large surface area. Particle density is important also for tuning and maximising the surface plasmon band [10]. However, controlling the uniformity of electrodeposited nanoparticles can be problematic due to diffusion zone coupling and progressive nucleation [12,13]. These effects lead to a distribution of lifetimes and growth rates both of which cause deleterious broadening of the particle size distribution.

Previously, various approaches have been investigated to produce metal nanoparticles of controlled size and separation on electrodes using electrodeposition [2,12,14]. Penner's group has had particular success with a slow growth technique involving the application of a large overpotential nucleation pulse for a very short time (5–10 ms) followed by a longer lasting low overpotential growth pulse [12]. A slower rate of growth served to reduce the thickness of the depletion layer around each growing nanoparticle thereby reducing or eliminating diffusion zone coupling

* Corresponding author. Tel.: +353 1 700 5943; fax: +353 1 700 5503.
E-mail address: Robert.Forster@dcu.ie (R.J. Forster).
[1] Present address: Fuel Cells and Solid State Chemistry Department, Risoe National Laboratory, Frederiksborgvej 399, DK-4000 Roskilde, Denmark.

0022-0728/$ - see front matter © 2006 Elsevier B.V. All rights reserved.
doi:10.1016/j.jelechem.2006.11.015

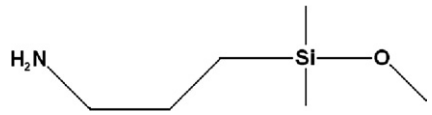

Scheme 1.

giving greater particle size uniformity. The high overpotential nucleation pulse encourages instantaneous nucleation giving high particle density and also increasing particle size monodispersity.

In this contribution, we report on the production of immobilised gold nanoparticles by applying a potentiostatic transient to an optically transparent fluorine-doped tin oxide (FDTO) coated glass slide electrode. Fluorine-doped tin oxide has been chosen as the substrate because its optical transparency facilitates spectroscopic characterisation of the metal deposits as well as opening up novel applications in SERS and electrochemiluminesce based sensing. However, FDTO is a challenging surface to seek to achieve narrow particle size distributions because of the rough nature of the substrate on the nanometre scale [15]. This significant surface roughness is likely to result in less uniform nucleation and growth.

Here, we report on the formation of gold nanodeposits using Penner's slow growth technique [12]. The ability to control the nucleation mode, particle density, particle size and particle size distribution by controlling the potentiostatic deposition conditions is described. Also, the effect of modifying the FDTO surface with a self-assembled monolayer (SAM) on the nucleation and growth kinetics is considered. A monolayer of a simple amine terminated group, 3-aminopropyldimethylmethoxysilane (ADMMS, Scheme 1), may provide a more uniform surface on which electrodeposition can occur. Moreover, it alters the surface energy and kinetics of deposition at the surface making instantaneous nucleation possible at lower overpotentials thereby reducing diffusion zone coupling.

2. Experimental

2.1. Electrochemistry

All electrochemical experiments were carried out in a three-electrode cell at room temperature using a CH instruments model 660 electrochemical workstation. The cell consisted of a working electrode, a platinum mesh counter electrode and a Ag/AgCl (sat. KCl) reference electrode. All potentials are quoted vs. Ag/AgCl (sat. KCl). Fluorine doped tin oxide (FDTO) coated glass (Hartford Glass Inc.) was used as the working electrode (resistance 8 Ω/cm^2, geometric surface area 0.25 cm^2). Experiments were carried out with potassium chloride (Aldrich) as the supporting electrolyte. Hydrogen tetrachloroaurate(III) trihydrate (Aldrich) was the gold salt used. All solutions were made up using Milli-Q water and were purged with argon gas prior to use and were made fresh each day.

2.2. FDTO electrodes

FDTO electrodes were prepared by rinsing in water, then in acetone prior to heating at 400 °C for 10 min to remove any adsorbed species. Teflon insulating tape was wrapped around the slide leaving a surface area of 0.25 cm^2 of the FDTO surface. Slides were stored FDTO side up in petri dishes to minimise their exposure to the environment. When they were ready to be used as working electrodes the uncovered FDTO surface was immersed in the electrolyte.

2.3. Monolayer formation

FDTO electrodes were modified with a 3-aminopropyldimethylmethoxysilane (ADMMS) (Fluorochem) monolayer by immersing the FDTO slides in a 0.001 M ADMMS solution in toluene (Aldrich) for 48 h. When removed from the solution, the FDTO was rinsed with pure toluene to remove any physically adsorbed material and then dried in a stream of high purity argon.

2.4. Characterisation of metal deposits

Scanning electron microscopy was carried out using the Hitachi S-3000N scanning electron microscope. Image analysis was carried out using Image J version 1.37d image analysis software.

2.5. Single pulse deposition

A single potential pulse was applied to the FDTO working electrode. The potentials applied ranged from 600 to 200 mV until a set charge had been passed. Following deposition the FDTO electrode was removed from the electrolyte, rinsed with Milli-Q water and dried under a stream of high purity argon.

2.6. Double pulse deposition

A 10–250 ms nucleation pulse was applied to the FDTO working electrode at a potential ranging from −400 to −2000 mV followed by a growth pulse at 300–700 mV until a set charge had been passed. Following deposition the FDTO electrode was removed from the electrolyte, rinsed with Milli-Q water and dried under a stream of high purity argon.

2.7. Gold nanoparticles on ADMMS modified FDTO

A single potential pulse was applied to the ADMMS modified FDTO samples. The potential applied ranged from 420 to 200 mV until a set charge had been passed. Following deposition the FDTO electrode was removed from the electrolyte, rinsed with Milli-Q water and dried under a stream of high purity argon.

3. Results and discussion

3.1. Cyclic voltammetry

Fig. 1A illustrates cyclic voltammograms for a 1 mM tetrachloroaurate plating solution at an FDTO electrode. The first scan contains a characteristic "nucleation loop" which arises from the greater overpotential required for nucleation onto FDTO compared to deposition of gold onto gold [16]. In the first negative going scan the peak potential is approximately −200 mV while in subsequent scans the peak potential is approximately 350 mV. The significant reduction in the overpotential for deposition following the first scan indicates that the stripping process is incomplete, that gold nuclei remain on the FDTO surface and that subsequent growth occurs predominantly at the remaining gold sites rather than onto the bare FDTO surface.

Depositing a spontaneously adsorbed monolayer will affect the rate of heterogeneous electron transfer to the $AuCl_4^-$ ion in solution and may alter its interfacial concentration. Fig. 1B illustrates the effect of modifying the FDTO electrode with an ADMMS monolayer on the electrodeposition process. The cyclic voltammograms exhibit a similar overall response to that seen at the bare electrode and the characteristic nucleation loop is again present. Significantly, the peak potential for the first scan shifts in a positive potential direction by approximately 380 mV at the modified electrode. This shift indicates that nucleation on the ADMMS surface is thermodynamically more facile than on the bare FDTO surface. This behaviour most likely reflects a reduction in the activation energy of surface diffusion of adions (E_{adi}) at the modified surface [17]. As expected, for subsequent scans, gold on gold deposition proceeds and the presence of the ADMMS monolayer has relatively little effect on the energetics of deposition.

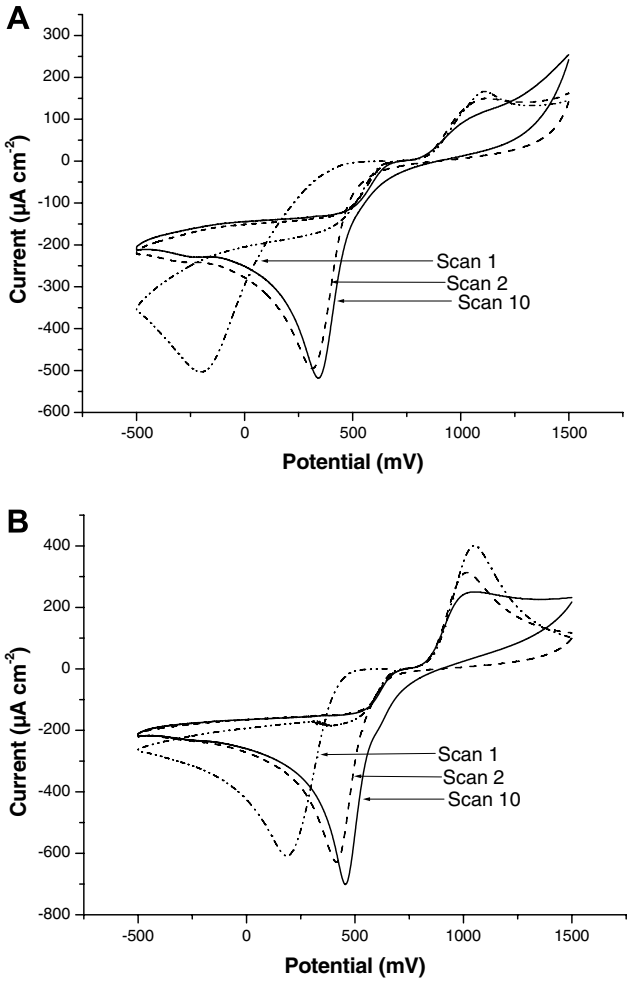

Fig. 1. Cyclic voltammograms at 100 mV s^{-1} for the deposition of gold from 0.001 M $HAuCl_4$ in 0.1 M KCl on (A) FDTO and (B) FDTO modified with ADMMS.

3.2. Gold nanoparticles on bare FDTO by single pulse deposition

Various studies of electrodeposition of metals have shown that increasing the overpotential, e.g., in chronoamperometry, results in a shift from progressive 3D diffusion limited nucleation and growth to instantaneous 3D diffusion limited nucleation and growth [18–20]. This ability to control the nucleation and growth dynamics through the applied potential has been investigated for this system by comparing the dimensionless $[(I/I_{max})^2$ vs. $t/t_{max}]$ form of the current transients with the theoretical curves for 3D progressive and instantaneous nucleation with diffusion controlled growth of Scharifker and Hills [21].

Fig. 2 illustrates dimensionless I–t plots for electrodeposition from a 0.001 M $HAuCl_4$ solution onto clean FDTO as well as the theoretical curves for instantaneous and progressive nucleation. This figure shows that the nucleation mode shifts from progressive nucleation for relatively more positive applied potentials, 400 and 340 mV, to instantaneous nucleation at approximately 280 mV. This

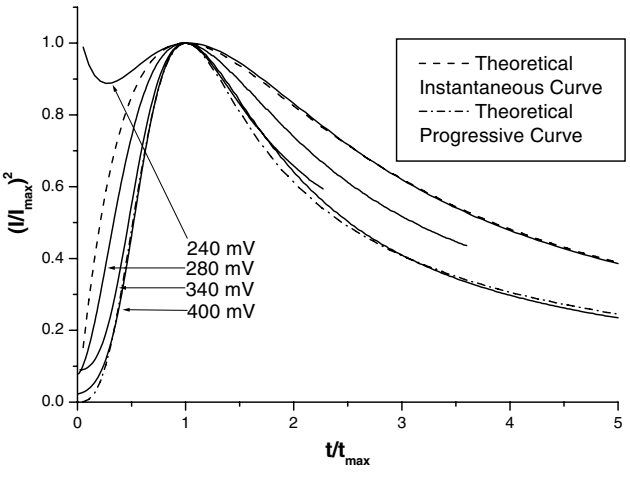

Fig. 2. Dimensionless current transients for the chronoamperometric deposition of gold nanoparticles from 0.001 M $HAuCl_4$ in 0.1 M KCl at different potentials.

observation is significant because instantaneous nucleation is important in order to maximise particle size monodispersity. However it is also desirable to grow the particles at a small overpotential in order to control diffusion zone coupling. Therefore finding a balance between a large nucleation overpotential and a small overpotential for particle growth is a key objective.

3.3. Control of nucleation and growth mode by modifying the electrode surface

In order to achieve instantaneous nucleation without having a large driving force for growth, it is necessary to separate the nucleation and growth steps. For example, a nucleation pulse with a sufficiently large overpotential to achieve instantaneous nucleation is first applied to effectively seed the surface with nuclei. Then, the potential can be changed so that growth proceeds at the desired rate.

Fig. 3 illustrates the effect of the use of a nucleation pulse on the nucleation mode. When a potential of 400 mV is applied to a bare FDTO electrode, the transient for the electrodeposition of gold nanoparticles from $HAuCl_4$ solution agrees quite closely with the theoretical dimensionless curve for progressive nucleation with 3D growth. However, when a nucleation pre-pulse of −400 mV is applied for 100 ms the transient changes and becomes significantly more similar to the theoretical curve for instantaneous nucleation with 3D growth.

Fig. 3 also shows the effect of modifying the FDTO surface with an ADMMS monolayer. In the presence of this monolayer, the nucleation and growth mode shifts from progressive nucleation to instantaneous nucleation as an applied potential of 400 mV is employed. The ADMMS molecule used for modification of the FDTO surface is bound to the surface via the methoxy-silane end, forming a Si–O–Sn bond, leaving the amine head-group exposed. As the gold salt used is an acid the electrolyte has a low pH (∼pH 3). This low pH causes the amine group to become protonated and electrostatic association of the negatively charged $AuCl_4^-$ ions at the electrode surface may occur resulting in the interfacial gold concentration being higher than that found in the bulk solution. If this is the case the increased concentration of $AuCl_4^-$ ions at the surface could be responsible for the shift from progressive towards instantaneous nucleation at a single potential as seen in Fig. 3. To investigate this possibility, a single pulse experiment on bare FDTO was performed with different gold salt concentrations. The concentration range from 0.001 to 0.02 M $HAuCl_4$ was investigated (concentrations greater than 0.02 M did not result in diffusion controlled growth and could not therefore be analysed by dimensionless transients). Fig. 4 shows the dimensionless form of the deposition transients. These transients indicate that at higher bulk salt concentrations the response shifts from progressive to instantaneous nucleation thereby confirming the possibility that preconcentration of $AuCl_4^-$ ions at the monolayer modified electrode could switch the nucleation mode. We have estimated the density of ADMMS molecules on the FDTO surface at approximately 3.4×10^{14} molecules per cm^2 based on the geometric cross sectional area of the ADMMS molecule calculated using the simulation software Gaussian. This figure is similar to the values estimated for similar molecules on various surfaces [22,23]. If a significant fraction of these sites were associated with an $AuCl_4^-$ ion it would result in up to a 20-fold increase in the concentration of $AuCl_4^-$ ions at the FDTO surface which the results of Fig. 4 confirm is sufficient to induce instantaneous nucleation.

When a nucleation pre-pulse is applied, the transient response is very insensitive to the presence of the ADMMS monolayer especially at longer times. This behaviour arises because the ADMMS monolayer affects only the nucleation and not the subsequent growth process.

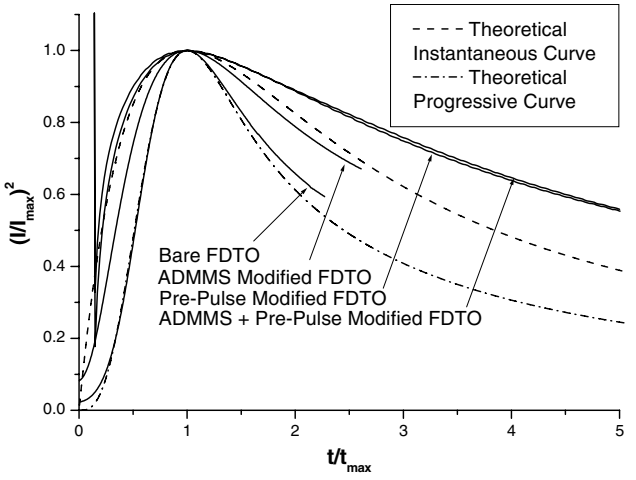

Fig. 3. Dimensionless current transients for different FDTO treatments prior to chronoamperometric deposition of gold nanoparticles from 0.001 M $HAuCl_4$ in 0.1 M KCl at a potential of 400 mV.

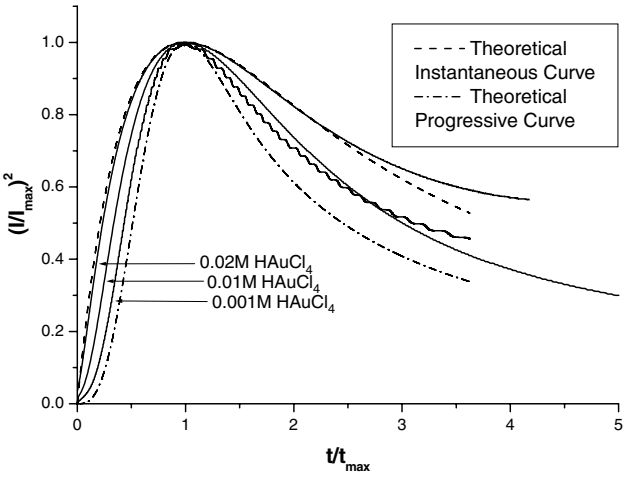

Fig. 4. Dimensionless current transients of varying bulk gold salt concentrations in the electrolyte for the deposition of gold onto FDTO by chronoamperometry at a potential of 400 mV.

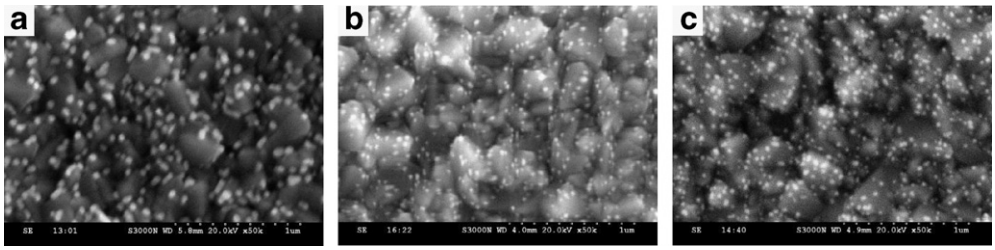

Fig. 5. SEM images of nanoparticles electrodeposited from 0.001 M $HAuCl_4$ in 0.1 M KCl (a) −700 mV for 100 ms then 400 mV, charge passed 8.6 mC cm^{-2}. (b) −1200 mV for 10 ms then 600 mV, charge passed 2.2 mC cm^{-2}. (c) −1200 mV for 10 ms then 400 mV, charge passed 4.3 mC cm^{-2}.

Table 1
Effect of nucleation and growth potentials and times on the mean diameter and density of gold nanoparticles electrodeposited on fluorine-doped tin oxide

E_{nu} (mV)	t_{nu} (ms)	E_{gr} (mV)	Q_{gr} (10^{-3} C cm^{-2})	Mean diameter (nm)[a]	Density (particles μm^{-2})[a]	RSD (%)[a]
–	–	400	4.3	985	0.01	27
−700	100	400	8.6	66	42.7	40
−1200	10	600	4.3	36	46.1	29
−1400	10	600	4.3	43	41.8	32
−1600	10	600	4.3	36	45.8	30
−1800	10	600	4.3	43	35.1	34
−2000	10	600	4.3	45	25.7	33
−1200	100	600	4.3	39	50.9	33
−1200	5	600	4.3	39	30.7	34
−1200	10	600	2.2	32	35.5	25
−1200	10	400	4.3	39	62.5	32

[a] Calculated by analysis of six SEM images captured at random locations on the FDTO surface.

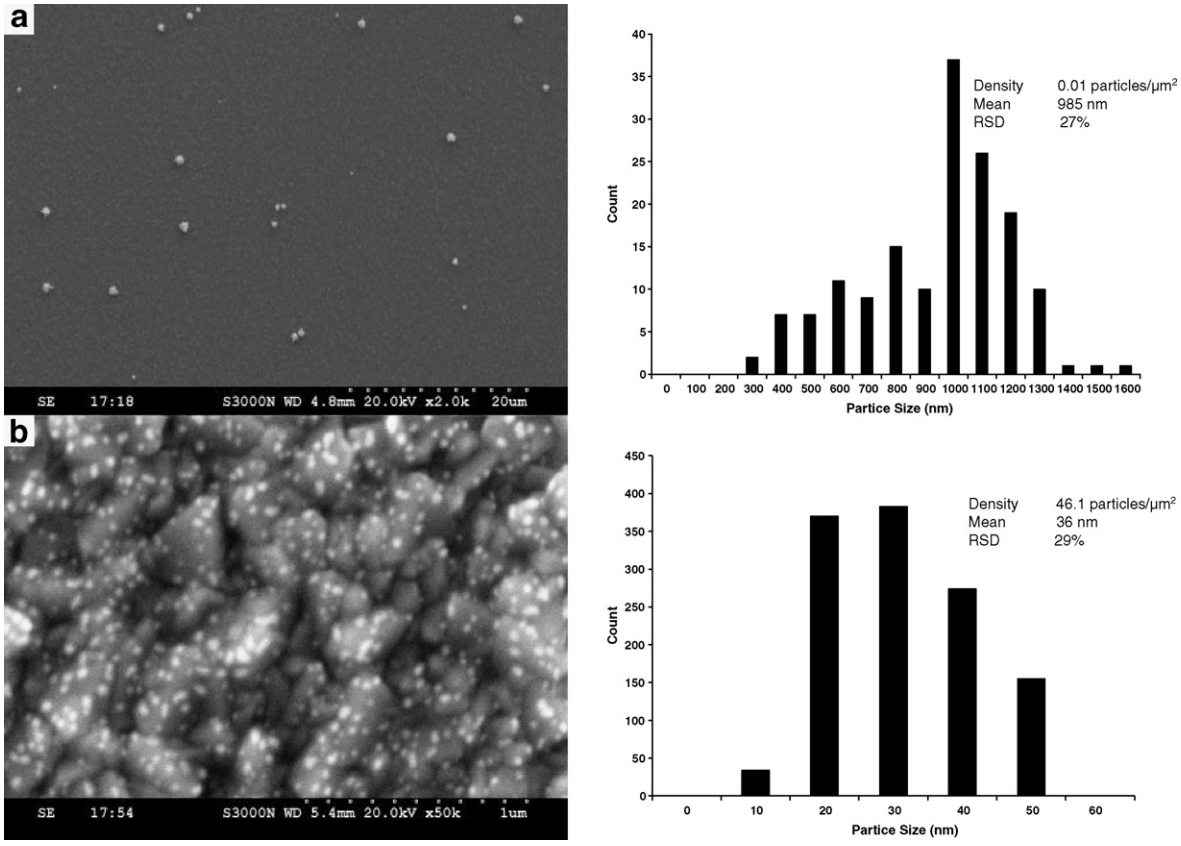

Fig. 6. SEM images and particle diameter distribution histograms for gold nanoparticles electrodeposited from 0.001 M $HAuCl_4$ in 0.1 M KCl until a charge of 4.3 mC cm^{-2} had been passed at (a) 400 mV (×2 k) and (b) −1200 mV for 10 ms then 600 mV (×50 k).

3.4. Optimisation of nanoparticle size and distribution

To optimise the two-pulse method for production of high density, low size, monodisperse nanoparticles conditions such as the length and potential of the nucleation pulse and the potential and charge passed of the growth pulse were varied. Fig. 5 illustrates typical SEM images of the nanoparticle arrays produced. These SEM images show the relatively rough underlying FDTO surface with the metallic nanoparticles appearing as small bright spots. The most significant results of these experiments are presented in Table 1. It was found that the greatest nucleation densities were achieved at nucleation potentials (E_{nu}) negative of −1000 mV with the nucleation density dropping off at potentials negative of −1600 mV presumably due to gas evolution. The length of the nucleation pulse (t_{nu}) also affected the nucleation density with greater densities at longer nucleation times up to 100 ms. The growth potential (E_{gr}) affected the size and monodispersity of the resultant particles with best results being obtained at 600 mV. Unsurprisingly, the greater the charge passed (Q_{gr}) the greater the resultant mean particle diameter.

As discussed in the Introduction, a significant objective is to create high density nanoparticles with low particle size distribution. Fig. 6a illustrates SEM images obtained following electrodeposition of gold particles on unmodified FDTO at 400 mV. The result is large particles on the FDTO surface (mean diameter 985 nm) that are randomly spaced at an extremely low density (0.01 particles/μm^2). The particle size distribution is not especially large (RSD 27%) which probably arises from the low density of particles resulting in reduced coupling of diffusion zones of adjacent particles. When the FDTO electrode was modified with a −1200 mV nucleation pulse of 10 ms duration and then particle growth was allowed to occur at a more positive potential (600 mV), the resulting SEM images (Fig. 6b) showed a greater than three orders of magnitude increase in the particle density (46 particles/μm^2) and the mean particle size is reduced by more than an order of magnitude (36 nm). The particle size distribution did not change significantly (29%) despite the increase in particle density. This result is significant since one would expect that a decrease in inter-particle separation would promote diffusion zone coupling leading to a greater range of particle sizes. The observation that the particle size distribution remains acceptably narrow, indicates that the slow growth approach is relatively successful in minimising diffusion zone coupling.

The presence of the ADMMS monolayer did not significantly affect the size, density and size distribution of nanoparticles on the surface (results not shown). This was somewhat unexpected as there was clear evidence that the presence of the monolayer influenced the nucleation mode

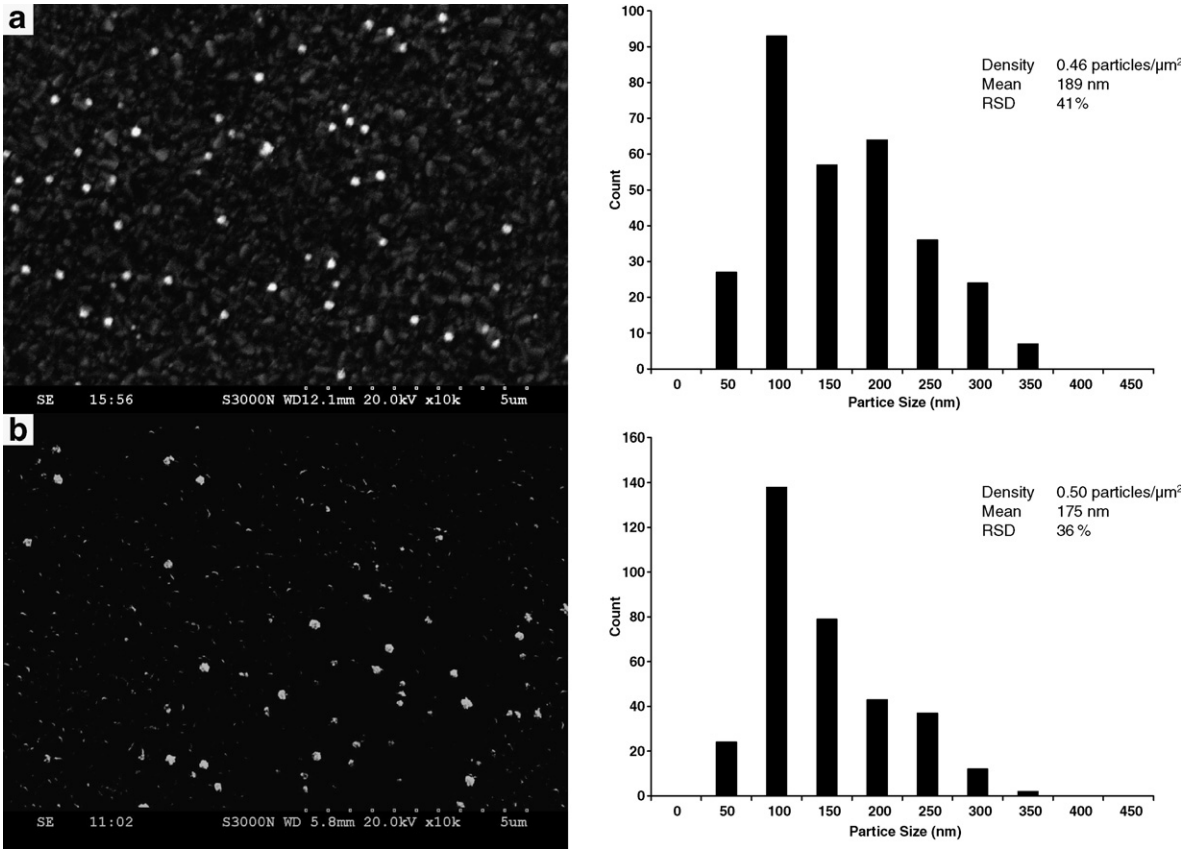

Fig. 7. SEM images and particle diameter distribution histograms for gold nanoparticles electrodeposited from 0.001 M $HAuCl_4$ in 0.1 M KCl onto FDTO (a) imaged the same day and (b) imaged three months after preparation.

facilitating growth by a single pulse method at lower overpotentials.

3.5. Stability of surfaces

By imaging samples a second time a number of weeks after preparation it was possible to determine if the samples remained unchanged during the elapsed time. Samples consisting of gold nanoparticles of the type described in this paper were unchanged in particle number, size and density after two months. Samples of this type have only been prepared in the last two months, however samples consisting of larger, less dense gold nanoparticles prepared using the same set-up have proved to be stable over six months after preparation. Fig. 7 shows SEM images and particle diameter distribution histograms prepared by imaging the same sample three months after preparation. There is no significant change in the density, mean diameter or size distribution over the elapsed time. Similar results were obtained for samples greater than six months old.

4. Conclusion

Two methods to control the nucleation and growth modes of electrodeposition of gold on FDTO were investigated. It was found that instantaneous nucleation followed by 3D diffusion controlled growth could be achieved at lower potentials in the presence of these modifications than possible without modification. The two pulse slow growth method could be applied to achieve high density, low particle size nanoparticles with RSD $< 30\%$ that remain stable for at least two months after preparation. Future work will investigate the possible use of these low cost substrates for SERS, SPR and amperometric based sensing devices.

Acknowledgements

We thank the Irish Research Council for Science, Engineering and Technology for support under the Embark initiative as well as Science Foundation Ireland under the Frontiers Research Programme (Award No. No.05/RFP/CHE0085).

References

[1] M.C. Daniel, D. Astruc, Chem. Rev. 104 (2004) 293–346.
[2] M.S. El-Deab, T. Sotomura, T. Ohsaka, J. Electrochem. Soc. 152 (2005) C1–C6.
[3] M.S. El-Deab, T. Sotomura, T. Ohsaka, J. Electrochem. Soc. 152 (2005) C730–C737.
[4] P. Zhang, P.S. Kim, T.K. Sham, Appl. Phys. Lett. 82 (2003) 1470–1472.
[5] W. Barnes, A. Dereux, T.W. Ebbesen, Nature 424 (2003) 824–830.
[6] X. Dai, R.G. Compton, Anal. Sci. 22 (2006) 567–570.
[7] L. Wang, J. Bai, P. Huang, H. Wang, L. Zhang, Y. Zhao, Electrochem. Commun. 8 (2006) 1035–1040.
[8] N. Felidj, J. Aubard, G. Levi, J.R. Krenn, A. Hohenau, G. Schider, A. Leitner, F.R. Aussenegg, Appl. Phys. Lett. 82 (2003) 3095–3097.
[9] J. Zhang, J. Lakowicz, J. Phys. Chem. B 110 (2006) 2387–2392.
[10] A. Campion, P. Kambhampati, Chem. Soc. Rev. 27 (1998) 241–250.
[11] K.C. Grabar, R.G. Freeman, M.B. Hommer, M.J. Natan, Anal. Chem. 67 (1995) 735–743.
[12] R.M. Penner, J. Phys. Chem. B 106 (2002) 3339–3353.
[13] H. Liu, R.M. Penner, J. Phys. Chem. B 104 (2000) 9131–9139.
[14] B. Ilic, D. Czaplewski, P. Neuzil, T. Stanczyk, J. Blough, G. Maclay, J. Mater. Sci. 35 (2000) 3447–3457.
[15] T. Fang, W. Chang, Appl. Surf. Sci. 252 (2005) 1863–1869.
[16] M. Palomar-Pardavéa, B.R. Scharifker, E.M. Arce, M. Romero-Romo, Electrochim. Acta 50 (2005) 4736–4745.
[17] M. Paunovic, M. Schlesinger, Fundamentals of Electrochemical Deposition, Wiley, USA, 1998.
[18] S. Sadale, P. Patil, Solid State Ion. 167 (2004) 273–283.
[19] L.M. Depestel, K. Strubbe, J. Electroanal. Chem. 572 (2004) 195–201.
[20] O. Brylev, L. Roue, D. Be langer, J. Electroanal. Chem. 581 (2005) 22–30.
[21] B. Scharifker, G. Hills, Electrochim. Acta 28 (1983) 879–889.
[22] S.R. Wasserman, Y. Tao, G.M. Whitesides, Langmuir 5 (1989) 1075–1087.
[23] J.C. Love, L.A. Estroff, J.K. Kriebel, R.G. Nuzzo, G.M. Whitesides, Chem. Rev. 105 (2005) 1103–1169.

Electrodeposited noble metal SERS: Control of single nanoparticle size and control of array interparticle spacing

Eoin Sheridan, Obianuju Inya-Agha, Tia Keyes and Robert Forster
National Centre for Sensor Research, School of Chemical Sciences,
Dublin City University, Dublin 9, Ireland
*Corresponding author: Robert.Forster@dcu.ie

ABSTRACT

Gold and silver nanoparticles have been electrodeposited onto fluorine-doped tin oxide by a two pulse method. The statistical distribution of the size and interparticle spacing of nanoparticles can be controlled by altering the overpotential and duration of the nucleation and growth pulses. Isolated gold and silver nanoparticle covered surfaces prepared in this way display a localized surface plasmon absorption. Raman spectra for immobilized trans-1,2-bis(4-pyridyl) ethylene have been recorded from isolated gold and silver nanoparticle surfaces with different mean particle size, and at different excitation wavelengths. The optimal SERS conditions determined for isolated gold and for silver nanoparticles produce enhancement factors of 5.6×10^2 and 4.0×10^3 , respectively. Reproducibility is typically 20-30% RSD due to variations in the SERS active area exposed in different measurements and perhaps variations in the enhancement factor at different sites on a single electrodeposited surface.

Keywords: Electrodeposition, nanoparticles, SERS, chronoamperometry, controlled nucleation

1. INTRODUCTION

Raman spectroscopy, though a powerful method for structural interrogation, is hampered by the inherent weakness of the Raman scattering process. Only approximately one in every million photons incident on a substrate is Raman scattered. An important means of improving signal is to exploit metal surface plasmons in surface enhanced Raman spectroscopy (SERS). The production of SERS active substrates has been studied intensely over the last decade[1-5]. The potential to incorporate such surfaces into sensor devices has frequently been discussed[6-9], the sensitivity of Raman spectroscopy under such surface enhanced conditions rivals that of fluorescence with the added advantage of selectivity due to the quality of structural information available from Raman spectroscopy. Electrodeposition of gold and silver nanoparticles onto conducting interfaces is one method of producing Raman enhancing substrates which has received attention in recent years[10-14]. The potential advantage to using electrodeposition is the ability to control the driving force behind the electrochemical growth of nanostructures, and accordingly control the physical properties of the resulting deposits such as particle size and interparticle spacing. In addition, electrodeposited nanoparticles are more strongly bound to the underlying surface compared to physically or chemically linked nanoparticles; making the nanoparticle arrays more stable when immersed in sample solutions. Finally, an essential element of a SERS based sensor is that it should be inexpensive and quick to prepare in a reproducible manner. Fluorine-doped tin oxide coated glass slides are conducting slides that can be prepared for use as a surface for electrodeposition (working electrode) in a short time as they do not require mechanical polishing and they are appreciably less expensive than most commonly used working electrodes for electrodeposition.

1.1. Electromagnetic theory of SERS enhancement

At the metal/dielectric interface of nanoparticulate metallic materials localized surface plasmon fields are supported. Localized surface plasmons occur only at nanoparticulate interfaces and result primarily due to the quantum size effect, which is that the de Broglie wavelength of the valence electrons is of the same order of the size of the particle itself. This means that from a quantum mechanical point of view the nanoparticles act as quantum dots of zero dimensions[15]

Plasmonics in Biology and Medicine IV, edited by Tuan Vo-Dinh, Joseph R. Lakowicz,
Proc. of SPIE Vol. 6450, 64500U, (2007) · 1605-7422/07/$18 · doi: 10.1117/12.725069

and the valence electrons of the atoms within the nanoparticle oscillate collectively, in a much stronger fashion than the oscillation observed at smooth metal/dielectric interfaces. The collective oscillation of electrons is at a frequency characteristic of the metal itself and the nanoparticle size. When electromagnetic radiation at the appropriate wavelength is incident on such metal nanoparticles, the electromagnetic field of the incoming light increases the amplitude of the plasmon field oscillations.

There are two very important results of this effect. Firstly, noble metal nanoparticles in solution or immobilized on a suitable substrate display an absorption maximum corresponding to the frequency of light resonant with the frequency of oscillation of the surface plasmon electrons of the nanoparticles. This is called the localized surface plasmon absorption. For metals like silver, gold and copper it is found in the UV-Vis region of the spectrum, and is not detected in the absorption spectrum of the corresponding bulk metal. Secondly, molecules adsorbed on the surface of nanoparticles under resonant excitation are subjected to electromagnetic fields of much greater intensity than the intensity of the incident light alone (intensity is proportional to square of electric field amplitude). This results in a substantial increase in the intensity of Raman scatter. This effect is considered the major contributor towards the enhancement of signal in surface enhanced Raman scattering[16-18]. The physical properties of metal nanoparticles that affect the SERS signal intensity are the size of nanoparticles, the interparticle spacing and the particle size distribution. These are the attributes that must be controlled when forming nanoparticles by electrodeposition.

1.2. Control of nanoparticle size

Control of nanoparticle size on SERS substrates is highly desirable due to the relationship between nanoparticle size and SERS response. It has long been established that the wavelength of the surface plasmon band depends on the size of the nanoparticles from which the surface plasmon originates[19]. The link between a strong surface plasmon band and strong SERS enhancements has also been detailed extensively by other researchers[16,20]. Consequently, the ability to control the size of nanoparticles on SERS substrates is of paramount importance in order to maximize the SERS enhancement factor. Studies by Nie and Emory[22-23] have demonstrated that for isolated silver nanoparticles the strongest SERS is recorded with particles in the 80-120nm range. They also reported strongest SERS for isolated gold nanoparticles in the 60-70 nm size range[23]. Producing nanoparticles in these size ranges can be achieved without great difficulty as nanoparticle size is a function of deposition time and potential in electrodeposition.

1.3. Control of interparticle spacing

According to electrostatic theory, the degree of electronic interaction between neighboring nanoparticles is a function of interparticle spacing. Generally, in order to ensure efficient electronic coupling of two nanoparticles the interparticle spacing should be less than their diameters. A nanoparticle can be considered isolated from nearby nanoparticles if the interparticle spacing is greater than 1.33 times their diameters. Control of nanoparticle density (and therefore interparticle spacing) in electrodeposition has been described previously in the literature[24-26]. The most important variable which can be changed to control density is the nucleation overpotential. The greater the overpotential applied the greater the density of nucleation sites on the electrode surface due to a simultaneous reduction of a greater number of metal ions at the surface when the potential is first applied. For any particular experimental set-up there are limits of minimum and maximum nanoparticle densities achievable through variations in the nucleation overpotential. These limits can in some cases be further extended by the use of various additives in the electrolyte solution such as citric acid[27], iodide ions[24] and lead acetate[28].

1.4. Control of particle size distribution

In order to produce surfaces of high particle density a large nucleation overpotential is applied to the working electrode. This results in a high nucleation density and also a fast rate of growth. This is problematic as a fast growth rate results in a rapid expansion of the diffusion zone around the growing nucleus. The diffusion zone is the volume of electrolyte around the nucleus that has a lower concentration of metal ions present compared to the bulk electrolyte as a result of the ions being reduced and incorporated into the growing nuclei. As these diffusion zones expand, adjacent zones eventually couple. When this occurs the nuclei whose diffusion zones have coupled experience retarded growth compared to nuclei with isolated diffusion zones. Therefore, diffusion zone coupling results in different growth rates at different nuclei and this increases the range of particle sizes created. A large particle size distribution can result in

considerable problems with the reproducibility of SERS enhancement factors at different sites on a single SERS substrate. Penner et al have reported a method to significantly reduce particle size distribution in electrodeposited nanoparticles[25,29]. Their technique involves separating the nucleation and growth stages of electrodeposition into two separate pulses. The nucleation pulse consists of a large overpotential applied for a very short time (<100ms). This results in instantaneous nucleation at a very high density, but does not permit enough time for diffusion zone coupling to occur. The second pulse is at a low overpotential and lasts for a much longer timescale until the desired particle diameter is reached. The low overpotential results in a much slower growth rate thereby keeping diffusion zone coupling to a minimum and resulting in size monodisperse nanoparticles.

In this contribution we report a simple two pulse method for the electrodeposition of noble metal nanoparticles of controlled size, interparticle spacing and size distribution on an inexpensive conducting substrate that is easy to prepare (FDTO). We demonstrate the use of these surfaces as SERS substrates and estimate enhancement factors for some of the surfaces.

2. EXPERIMENTAL

2.1. Electrochemistry

All electrochemical experiments were carried out in a three-electrode cell at room temperature using a CH instruments model 660 electrochemical workstation. The cell consisted of a working electrode, a platinum mesh counter electrode and a Ag/AgCl (sat KCl) reference electrode. Silver electrodeposition was carried out using a 0.1M nitric acid salt bridge connecting the reference electrode to the cell. All potentials are quoted Vs. Ag/AgCl (sat KCl). Fluorine doped tin oxide (FDTO) coated glass (Hartford Glass Inc.) was used as the working electrode (resistance 8Ω /cm^2, geometric surface area 0.25cm^2). All electrolyte solutions were made up using Milli-Q water and were purged with argon gas prior to use and were made fresh each day.

2.2. Gold nanoparticle electrodeposition

Gold electrodeposition experiments were carried out with potassium chloride (Aldrich) (0.1M) as the supporting electrolyte. Hydrogen tetrachloroaurate(III) trihydrate (Aldrich) (0.001M) was the gold salt used. The deposition was carried out in two stages; a short nucleation pulse lasting up to 100 ms was followed by a longer growth pulse, lasting up to 100s.

2.3. Silver nanoparticle electrodeposition

Silver electrodeposition experiments were carried out with nitric acid (Riedel de Haen) (0.1M) as the supporting electrolyte. Citric acid (Sigma Aldrich) (0.015M) was added to the silver electrolyte to improve nanoparticle uniformity. Silver nitrate (Sigma Aldrich) (0.001M) was the silver salt used. The deposition was carried out in two stages; a short nucleation pulse lasting up to 100 ms was followed by a longer growth pulse, lasting up to 100s.

2.4. FDTO electrodes

FDTO electrodes were prepared by rinsing in water, then in acetone prior to heating at 400^o C for 10 minutes to remove any adsorbed species. Teflon insulating tape was wrapped around the slide leaving a surface area of 0.25cm^2 of the FDTO surface uncovered. Slides were stored FDTO side up in petri dishes to minimize their exposure to the environment. When they were ready to be used the uncovered FDTO surface was immersed in the electrolyte.

2.5. Characterisation of metal nanoparticle surfaces

Scanning electron microscopy (SEM) was carried out using the Hitachi S-3000N scanning electron microscope. Image analysis was carried out using Image J version 1.37d image analysis software. UV-Vis spectrophotometry was carried out with the Perkin Elmer Lambda 900 UV-Vis Spectrophotometer. Samples were immersed in acetonitrile (Sigma Aldrich) for UV-Vis analysis. Raman spectroscopy was carried out on the HORIBA Jobin-Yvon Labram HR 2000

confocal Raman microscope using 632 nm and 785 nm excitation from a solid-state laser. An argon ion tuneable laser (Coherent) was used to excite at 458 nm, 488 nm and 514 nm. The lasers were focused with a 10x objective in each case; the laser spot diameter was calculated as the laser diameter (λ) x 3.874 x 10^{-3}. The probe molecule selected for Raman spectrometry was Trans-1,2-bis(4-pyridyl)ethylene (BPE) (Aldrich). A monolayer of BPE was formed on the nanoparticle surfaces by immersing the surface in a 5mM methanolic solution of BPE for 48 hours prior to Raman analysis. When the sample was removed from the methanolic solution it was rinsed with pure methanol to remove any unbound or physisorbed BPE to ensure only a chemisorbed monolayer of BPE was present.

3. RESULTS & DISCUSSION

3.1. Production of electrodeposited gold nanoparticulate surfaces

The effect of manipulating the electrodeposition potential on the nucleation and growth dynamics was investigated. Application of a single electrodeposition pulse resulted in growth of very large nanoparticles at an extremely low density. This was because the potentials applied (from -500 to -200mV) were sufficiently negative of the reduction potential of tetrachloroaurate (+1.0V) to result in a fast growth rate, but not negative enough to instantaneously nucleate the surface at all possible nucleation sites. The resultant nanoparticles were typically in the size range 300-1500 nm and were therefore too large to result in useful SERS enhancements. Furthermore, the density of particles (typically <1 particle per μm^2) was not sufficiently high to ensure that at least one nanoparticle would be within the diameter of the exciting laser when irradiated at a random location on the surface.

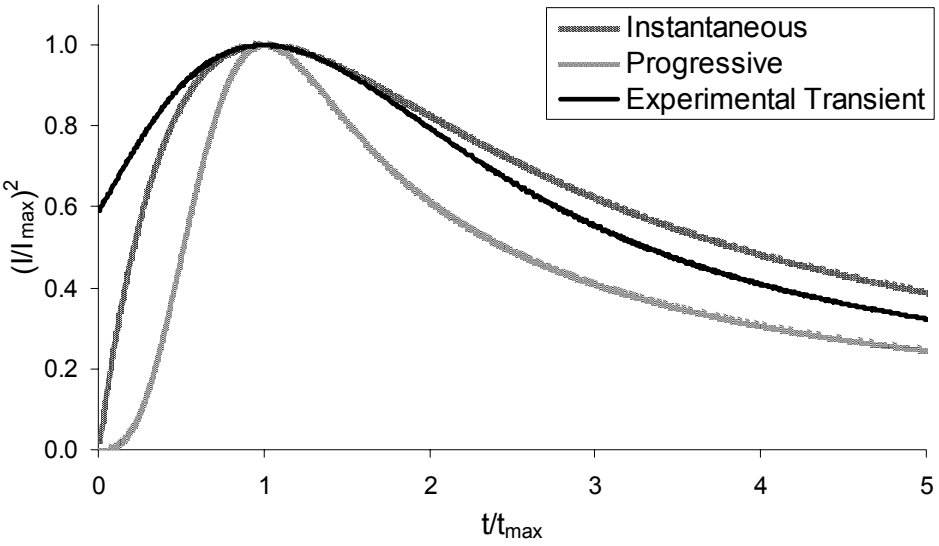

Fig. 1. Dimensionless current transients for electrodeposition of gold nanoparticles on FDTO using a two pulse method. Deposition was carried out in 0.001M $HAuCl_4$ + 0.1M KCl at -1.200 V for 100 ms followed by 0.725 V until a charge of 4.3 mC cm^{-2} had been passed.

In order to increase the nanoparticle density and lower nanoparticle size it was decided to separate the stages of nanoparticle formation into two individual pulses, a nucleation and a growth pulse as described by Penner et al[25]. For example, a nucleation pulse with a sufficiently large overpotential to achieve instantaneous nucleation is first applied to seed the surface with nuclei. The potential can then be changed so that growth proceeds at the desired rate. The potential and duration of each pulse was varied in order to determine the effect of these variables on the final nucleation density and size. The dimensionless plot of Scharifker and Hills[30] [$(I/I_{max})^2$ vs. t/t_{max}, where I is current (A) and t is time (s)] was used to determine whether nucleation was proceeding progressively or instantaneously. An example is demonstrated in Figure 1, in this case the nucleation pulse was -1.200 V for 100 ms and the growth pulse was 725mV until a charge of 4.3 mC cm^{-2} had been passed. The dimensionless form of the curve is seen to follow more closely the

form of the theoretical transient for 3D instantaneous nucleation and growth, indicating that the nucleation pulse was sufficiently negative to achieve instantaneous nucleation.

By using dimensionless plots to characterize the nucleation mode and analysing the SEM images as shown in Figure 2 it was possible to determine the optimum conditions for production of nanoparticles at maximum density with controlled size using this approach. It was found that the greatest nucleation densities were achieved at nucleation pulse potentials (E_{nu}) negative of -1000 mV with the nucleation density dropping off at potentials negative of -1600 mV presumably due to gas evolution. Alternatively it was possible to achieve lower particle densities by applying a potential positive of -1000 mV, in this manner it was possible to control the density of nanoparticles within the limits of maximum and minimum nanoparticle densities (approximately 0.5 and 80 particles per μm^2 respectively). This is demonstrated in the SEM images shown in Figure 2, where the white spots are electrodeposited gold. The rough nature of the FDTO surface is evident beneath the gold nanoparticles. It is clear from the SEM images that at more negative

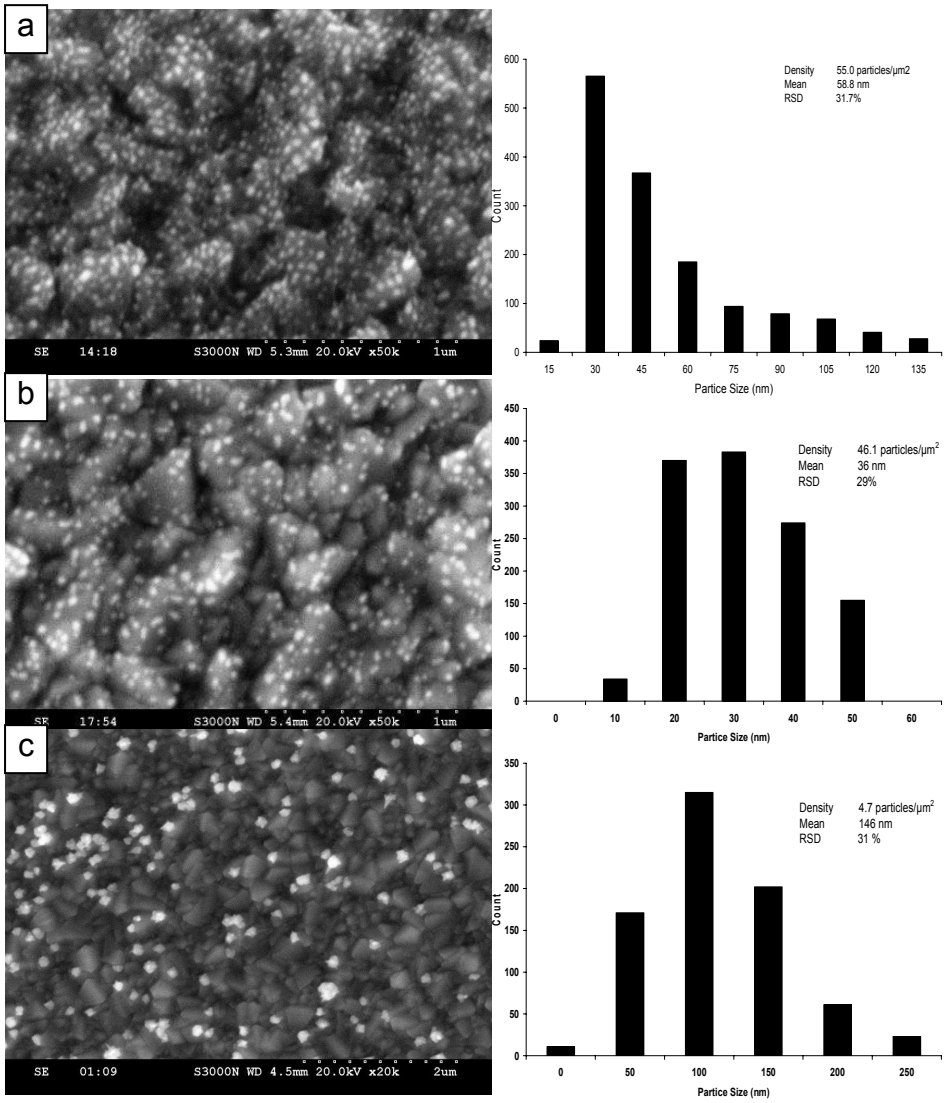

Fig. 2. SEM images and particle size distribution histograms for gold nanoparticles electrodeposited onto FDTO from 0.001M $HAuCl_4$ and 0.1M KCl using a two pulse method. Nucleation pulse was for a duration of 100ms at a potential of (a) -2.000V (b) -1.200 V (c) -0.450 V. The growth pulse was 0.400 V until a charge of (a) 8.0 mC cm^{-2} (b) 6.0 mC cm^{-2} (c) 10.0 mC cm^{-2} had been passed.

potentials the nucleation density was greatest (2a). At less negative potentials (2b and 2c) the nucleation density decreased. Computer software analysis of the SEM images confirms these findings (see particle size histograms). Note that the mean particle size increases as particle density increases, this is a result of the same amount of gold being deposited over a smaller number of nucleation sites. The length of the nucleation pulse (t_{nu}) also affected the nucleation density with greater densities at longer nucleation times up to 100 ms. The growth pulse potential (E_{gr}) affected the size and monodispersity of the resultant particles with more monodisperse particles of controlled size obtained between 400 and 600mV (RSD = ~30%). Unsurprisingly, the greater the charge passed (Q_{gr}) the greater the resultant mean particle diameter. The details of this experiment have been discussed in more detail elsewhere[31].

3.2. Production of electrodeposited silver nanoparticulate surfaces

Silver nanoparticles have been reported to yield stronger SERS enhancements than gold nanoparticles[32] therefore the method for electrodeposition of gold nanoparticles on FDTO was applied to silver nanoparticles to investigate the

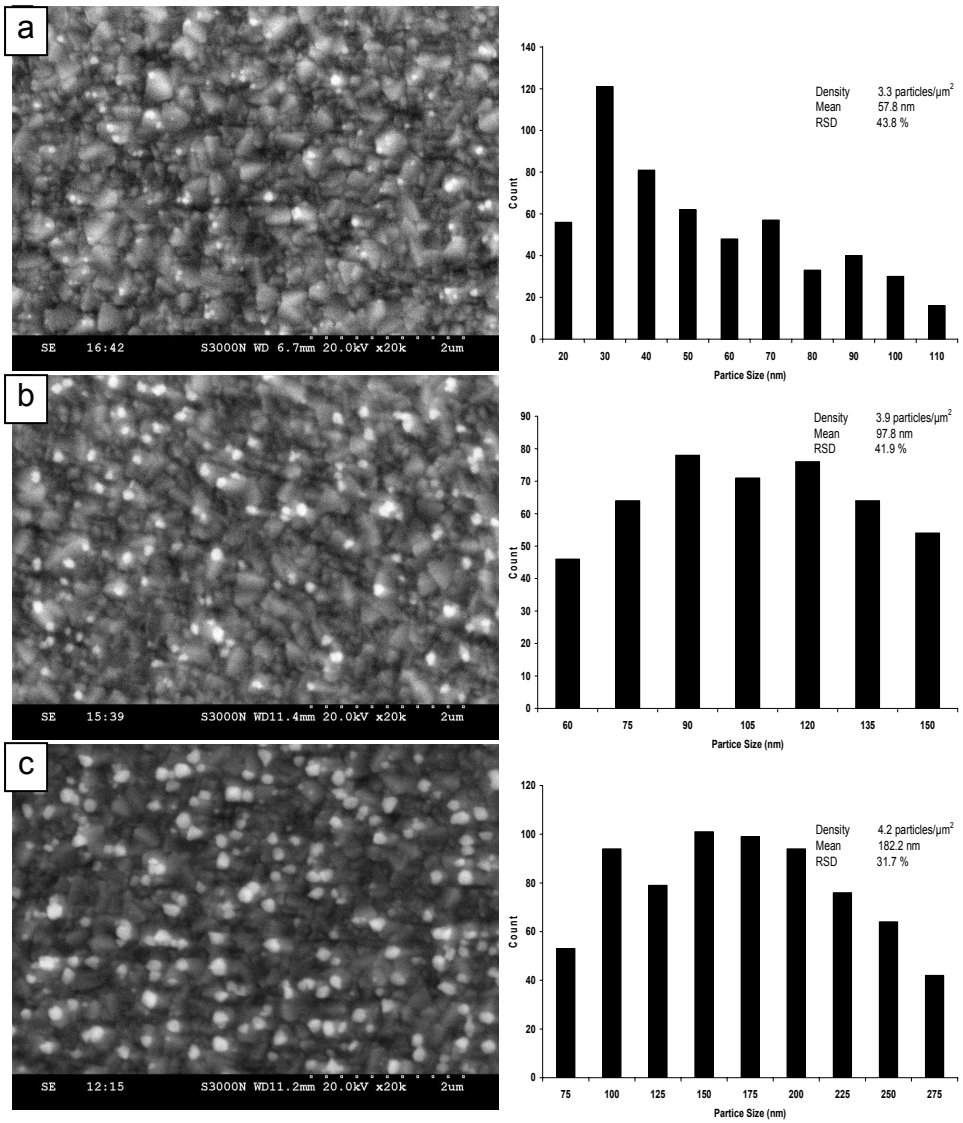

Fig. 3. SEM images and particle size distribution histograms for silver nanoparticles electrodeposited onto FDTO from 0.001M $AgNO_3$, 0.015M citric acid and 0.1M HNO_3 using two pulse method. The nucleation pulse potential was -1.600 V for 20 ms, the growth pulse was 0.300 V until the charge passed was (a) 2 mC cm^{-2}, (b) 5 mC cm^{-2}, (c) 15 mC cm^{-2}.

degree of control that could be achieved over the size, density and size monodispersity of the nanoparticles. The same two pulse method was applied to the electrodeposition of silver nanoparticles and the experimental variables were optimized in the same way. The greatest nucleation density was achieved with a nucleation pulse of -1.600 V for a duration of 20 ms. For greater control over particle size and minimization of particle size distribution a growth pulse of 300mV was applied. As described for the gold nanoparticles, the mean diameter depends on the amount of charge passed during the growth pulse. This is reflected in Figure 3, when a small charge is passed (3a) the mean nanoparticle size was small (58 nm), and as greater charge is passed (3b & 3c) the mean particle size becomes greater (98 nm & 183 nm). Despite optimizing these conditions it was not possible to produce silver nanoparticle surfaces of the same density and monodispersity as achieved for gold. The maximum density of silver nanoparticles on FDTO obtained was 6 particles per μm^2 (minimum density = 0.5 particles per μm^2). The distribution of nanoparticle size was RSD = ~40%. From electrostatic theory the SERS enhancement factor is estimated to vary with interparticle spacing as $(1+D/d)^4$, where d is the interparticle space and D is the mean particle diameter. Therefore, for a system like this with such low particle densities, the nanoparticles cannot be considered to be electrostatically interacting and any SERS enhancements observed can be considered to be coming from electrostatically isolated nanoparticles. It was decided to investigate the maximum SERS enhancement observable from isolated silver nanoparticles of this type, and to compare the result with the maximum enhancement factor from isolated gold nanoparticles on the same substrate.

3.3. UV-Vis characterization of nanoparticles

The gold and silver nanoparticulate surfaces produced were characterized by UV-Vis spectrophotometry. A broad surface plasmon absorption band is expected at 520-550 nm for gold nanoparticles in the size range 80-160 nm according to Mie theory[33]. This broad band is present (Figure 4) confirming the presence of a localized surface plasmon absorption. For silver nanoparticles the surface plasmon absorption is usually expected at around 400 nm for electrostatically interacting nanoparticles. In cases where the silver nanoparticles are essentially electrostatically isolated, the surface plasmon absorption band is reported to occur as a broad peak somewhere between 400 nm and 700 nm[19] depending on the nanoparticle size. The silver nanoparticles presented in Figure 4 have a mean diameter of 95 nm and, consistent with Figure 4, exhibit an absorption maximum between 500 and 600 nm,

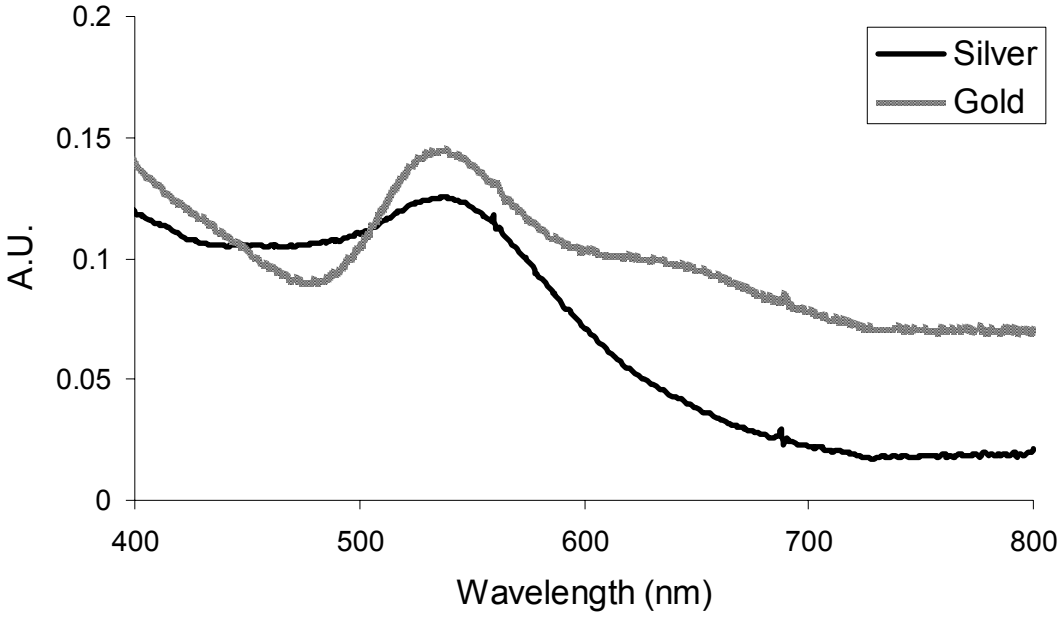

Fig. 4. UV-Vis spectra demonstrating the surface plasmon band of isolated gold and silver nanoparticle surfaces with mean particle size of 150 nm and 95 nm respectively.

3.4. Raman spectroscopy

Using a monolayer of the probe molecule BPE, Raman spectra of the gold and silver nanoparticles were recorded at five different excitation wavelengths; 458 nm, 488 nm, 514 nm, 632 nm and 785 nm. A typical spectrum is presented in Figure 5, the main bands at 1600 cm^{-1} and 1650 cm^{-1} are ring breathing modes typical of the pyridine ring. Figure 5 was recorded from a silver nanoparticle sample (on FDTO). To confirm that the Raman signal could be attributed only to BPE molecules adsorbed on silver the experiment was repeated with bare FDTO which had been immersed in BPE solution, this resulted in a blank spectrum containing no bands characteristic of BPE.

Raman spectra were recorded from 6 randomly spaced positions on each surface so that an average enhancement factor (EF) could be determined for the surface. To estimate the SERS enhancement factor the integrated intensity of the doublet at 1600-1650 cm^{-1} was determined for each sample and compared to the integrated intensity of the same peaks from a spectrum recorded of BPE in 5mM solution. The integrated intensities of these peaks were normalized to the number of BPE molecules excited to produce the signal in order to more accurately determine the enhancement factor.

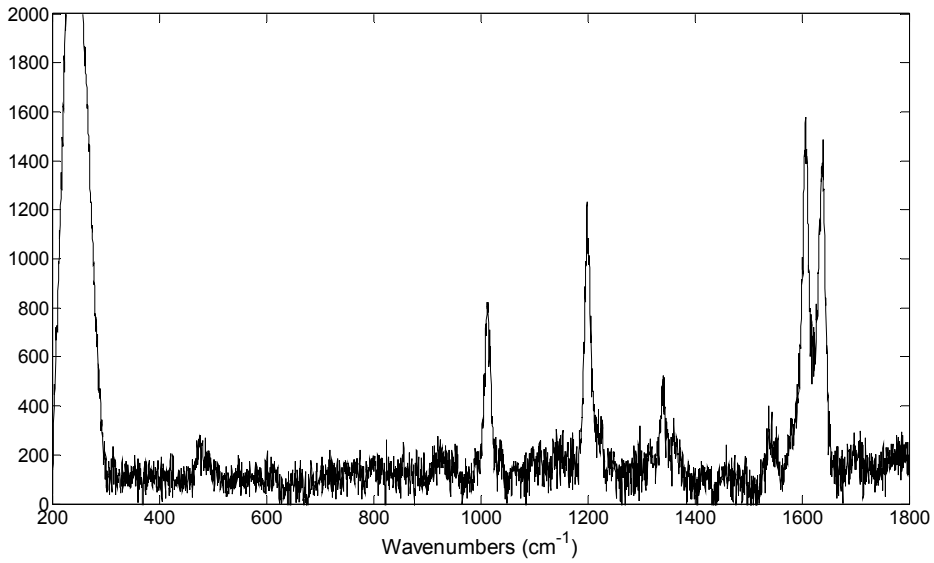

Fig. 5. Raman spectrum recorded of BPE on FDTO surface electrodeposited with isolated silver nanoparticles of mean diameter 95 nm, excitation wavelength was 632 nm. Enhancement factor = 3575.

For BPE immobilized on silver or gold nanoparticles the number of molecules excited (N_{Im}) is given by:

$$N_{Im} = \rho_{np} \times 2\pi r^2 \times S \times \rho_{bpe} \qquad \text{(eq. 1)}$$

Where ρ_{np} is the density of nanoparticles on the surface, r is the mean nanoparticle radius on the surface, ρ_{bpe} is the density of BPE molecules in a monolayer (estimated at 2×10^{14} cm^{-2})[34] and S is the exciting laser spot size = $\pi(f\# \times \lambda)^2$. f# = focal length/aperture, λ is the excitation wavelength.

For BPE in solution the number of BPE molecules excited (N_{Sol}) is given by:

$$N_{Sol} = [BPE] \times V_{ex} \times N_A \qquad \text{(eq.2)}$$

Where V_{ex} is the volume of excitation of the exciting laser which is equivalent to 2 x the volume of a truncated cone with a base of diameter 1.41 x (2f# x λ), a top of diameter (2f# x λ) and a height of (*DoF*/2), *DoF* is the depth of field. N_A is Avogadro's number.

The most significant enhancement factors are summarized in Table 1.

Table 1: Summary of enhancement factors estimated from silver and gold nanoparticulate surfaces.

Nanoparticle Metal	Mean Diameter(nm)	λ_{ex}(nm)	EF_{mean}	St. Dev.	RSD (%)	EF_{best}
Silver	94.8	458	66	13	20	105
		488	196	37	19	214
		514	411	47	11	581
		632	2519	317	13	3575
Silver	97.8	488	671	49	7	844
		514	2935	144	5	4022
Silver	110.7	458	34	18	53	66
		488	152	43	28	214
		514	118	44	37	192
		632	1071	280	26	1673
Silver	119.4	632	873	89	10	936
Gold	130.3	632	427	98	23	556

Of the five excitation wavelengths investigated the greatest enhancement factor was recorded at 632 nm. It is perhaps significant that this excitation wavelength is not coincident with $\lambda_{max, abs}$. The enhancement factor at 632 nm was as large as 3 orders of magnitude for silver nanoparticles (best EF = 3575). There was a general trend towards greater enhancement factors at longer excitation wavelengths up to 632 nm. It was not possible to obtain enhancement factors at 785 nm as a broad peak was present in the spectrum from 1200 cm^{-1} to 1800cm^{-1} which masked the doublet at 1600 cm^{-1} and 1650 cm^{-1} at this wavelength. This broad peak was also observed on a bare (undeposited) FDTO slide therefore the band was believed to result from background processes associated with either the glass or the FDTO. The enhancement factors at 488 nm and 514 nm were smaller (2 orders of magnitude for silver) in most cases; however one sample had a maximum enhancement factor of 4022 at 514 nm excitation.

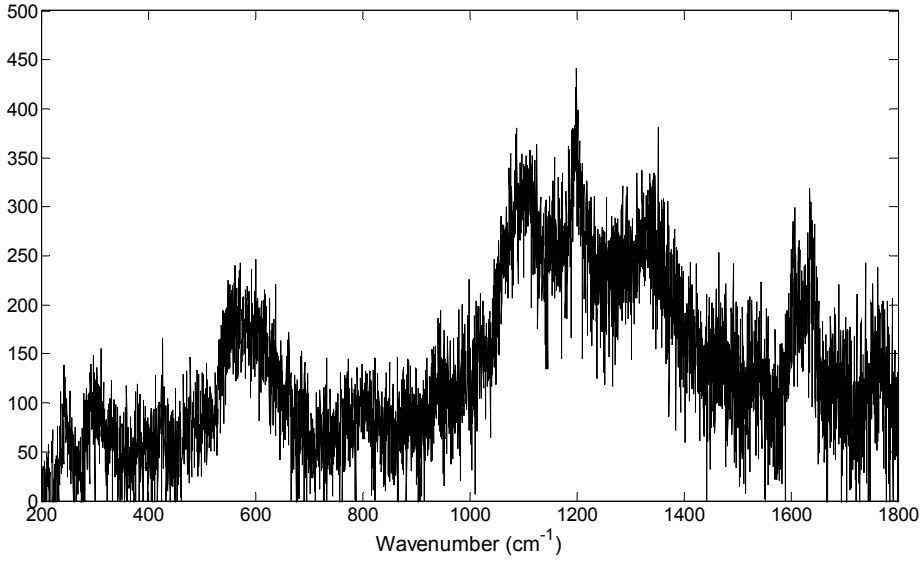

Fig. 6. Raman spectrum recorded of BPE on FDTO surface electrodeposited with isolated gold nanoparticles of mean diameter 130 nm, excitation wavelength was 632 nm. Enhancement factor = 556.

60 days later its enhancement factor had decreased by over 75% at all wavelengths. Of the silver samples analysed the best enhancement factors were recorded from samples with mean particle sizes in the range 90-100 nm, this is in agreement with the literature data available for isolated silver nanoparticles[21-22]. Silver nanoparticle samples of mean sizes between 50 nm and 200 nm were analysed and those not presented in Table 1 either did not yield a defined spectrum, or had a very low estimated enhancement factor.

Of the gold samples analysed with mean nanoparticle diameters in the range 50 nm to 250 nm only one sample produced a sufficiently strong Raman response to calculate the SERS enhancement factor. This sample, with mean diameter 130 nm had a 2 orders of magnitude enhancement at 632 nm excitation and did not have a defined spectrum at the other wavelengths. A Raman spectrum recorded from this sample is presented in Figure 6, the signal to noise ratio of this sample was significantly poorer than the spectra recorded from isolated silver nanoparticle samples (for example the spectrum in figure 5). It has been reported that isolated colloidal gold nanoparticles of mean diameter 60-70 nm yield the best SERS enhancements[23], this does not agree with the results reported here, however this could be due to differences in shape between colloidal spheres and electrodeposited hemispheres, or it could result from interactions between the FDTO surface and the electrodeposited gold nanoparticles.

The relative standard deviation of enhancement factor for both silver and gold nanoparticles samples is quite large, typically 20-30%, up to 53%. This represents a significant obstacle to incorporation of such a surface into a SERS based sensing device. The largest source of this imprecision is likely to be the size distribution of the nanoparticles, which for silver nanoparticles was approximately 40% for most samples. The rough nature of the chosen substrate, FDTO, encouraged diffusion zone coupling and afforded an imperfect surface for electrodeposition, making it difficult to narrow the size distribution below 40%.

4. CONCLUSION AND OUTLOOK

Silver and gold nanoparticles have been electrodeposited on fluorine-doped tin oxide in a controlled manner. The size and interparticle spacing of the nanoparticles could be controlled within certain limits by controlling the kinetics of nucleation and growth through a two pulse deposition scheme. Using this method it was possible to produce surfaces covered with isolated gold or silver nanoparticles of controlled size. The application of these surfaces to SERS has been demonstrated, producing up to a 3 orders of magnitude enhancement factor with silver nanoparticles under optimal conditions, and 2 orders of magnitude with gold nanoparticles. A potential problem with this approach is the large relative standard deviation of the enhancement factor at different locations on the surface, typically 20-30%. Much of the imprecision could be due to the size distribution of nanoparticles which is typically around 40% for the isolated silver nanoparticles. Future work may concentrate on performing these experiments on a smoother surface than FDTO that may enable the narrowing of this size distribution.

5. ACKNOWLEDGEMENTS

The financial support of the Irish Research Council for Science, Engineering and Technology under the Embark initiative and the Postdoctoral Fellowship Scheme is gratefully acknowledged. We also appreciate the on-going financial support from Science Foundation Ireland under the Research Frontiers Programme (Award No. 05/RFP/CHE0085), the Biomedical Diagnostics Institute (Award No. 05/CE3/B754) and the Investigator Programme (05/IN1/B30).

References

1. Dieringer, J. McFarland, A. Shah, N. Stuart, D. Whitney, A. Yonzon, C. Young, M. Zhang, X. Van Duyne, R. "Surface enhanced Raman spectroscopy: new materials, concepts, characterization tools, and applications". Faraday Discuss. **132**, 9-26, 2006.
2. Cintra, S. Abdelsalam, M. Bartlett, P. Baumberg, J. Kelf, T. Sugawara, Y. Russell, A. "Sculpted substrates for SERS". Faraday Discuss. **132**, 191-199, 2006.
3. Tian, Z. Ren, B. Wu, D. "Surface-enhanced Raman scattering: From noble to transition metals and from rough surfaces to ordered nanostructures". J. Phys. Chem. B. **106,** 9463-9483, 2002.
4. Zhang, X. Zhao, J. Whitney, A. Elam, J. Van Duyne, R. "Ultrastable substrates for surface-enhanced Raman spectroscopy: Al_2O_3 overlayers fabricated by atomic layer deposition yield improved anthrax biomarker detection". J. Am. Chem. Soc. **128**, 10304-10309, 2006.
5. Kahl, M. Voges, E. Kostrewa, S. Viets, C. Hill, W. "Periodically structured metallic substrates for SERS". Sens. Actuators, B. **51**, 285-291, 1998.
6. Zhang, X. Shah, N. Van Duyne, R. "Sensitive and selective chem/biosensing based on surface-enhanced Raman spectroscopy (SERS)". Vib. Spectrosc. **42**, 2-8, 2006.
7. Yonzon, C. Haynes, C. Zhang, X. Walsh, J. Van Duyne, R. "A glucose biosensor based on surface-enhanced Raman scattering: Improved partition layer, temporal stability, reversibility, and resistance to serum protein interference". Anal. Chem. **76**, 78-85, 2004.
8. Zhang, Y. Gu, C. Schwartzberg, A. Zhang, J. "Surface-enhanced Raman scattering sensor based on D-shaped fiber". Appl. Phys. Lett. **87**, 1-3, 2005.
9. Schmidt, H. Ha, N. Pfannkuche, J. Amann, H. Kronfeldt, H. Kowalewska, G. "Detection of PAHs in seawater using surface-enhanced Raman scattering (SERS)". Mar. Pollut. Bull. **49**, 229-234, 2004.
10. Sauer, G. Brehm, G. Schneider, S. "Preparation of SERS-active gold film electrodes via electrocrystallization: their characterization and application with NIR excitation". J. Raman Spectrosc. **35**, 568-576, 2004.
11. Tourwe, E. Hubin, A. "Preparation of SERS-active electrodes via ex situ electrocrystallization of silver in a halide free electrolyte". Vib. Spectrosc. **41**, 59-67, 2006.
12. Sandmann, G. Dietz, H. Plieth, W. "Preparation of silver nanoparticles on ITO surfaces by a double-pulse method". J. Electroanal. Chem. **491**, 78-86, 2000.
13. Sun, F. Cai, W. Li, Y. Cao, B. Lu, F. Duan, G. Zhang, L. "Morphology control and transferability of ordered through-pore arrays based on electrodeposition and colloidal monolayers". Adv. Mater. **16**, 1116-1121, 2004.
14. He, P. Liu, H. Li, Z. Liu, Y. Xu, X. Li, J. "Electrochemical deposition of silver in room-temperature ionic liquids and its surface-enhanced Raman scattering effect". Langmuir, **20,** 10260-10267, 2004.
15. Daniel, M. Astruc, D. "Gold nanoparticles: Assembly, supramolecular chemistry, quantum-size-related properties, and applications toward biology, catalysis, and nanotechnology". Chem. Rev. **104**, 293-346, 2004.
16. Campion, A. Kambhampati, P. "Surface-enhanced Raman scattering". Chem. Soc. Revs. **27**, 241-250, 1998.
17. Moskovits, M. "Surface-enhanced spectroscopy". Rev. Mod. Phys. **57**, 783-826, 1985.
18. Otto, A. "Surface-enhanced Raman-scattering of adsorbates". J. Raman Spec. **22**, 743-752, 1991.
19. Jensen, T. Kelly, L. Lazarides, A. Schatz, G. "Electrodynamics of Noble Metal Nanoparticles and Nanoparticle Clusters". **10**, 295-317, 1999.
20. Zeman, E. Schatz, G. "An accurate electromagnetic theory study of surface enhancement factors for Ag, Au, Cu, Li, Na, Al, Ga, In, Zn, and Cd". J. Phys. Chem. **91**, 634-643, 1987.
21. Emory, S. Haskins, W. Nie, S. "Direct observation of size-dependent optical enhancement in single metal nanoparticles". J. Am. Chem. Soc. **120**, 8009-8010, (1998).
22. Nie, S. Emory, S. "Probing single molecules and single nanoparticles by surface-enhanced Raman scattering". Science, **275**, 1102-1106, 1997.
23. Krug, J. Wang, G. Emory, S. Nie, S. "Efficient Raman enhancement and intermittent light emission observed in single gold nanocrystals. J. Am. Chem. Soc. **121**, 9208-9214, (1999).
24. El-Deab, M. Ohsaka, T. "Size and crystallographic orientation controls of gold nanoparticles electrodeposited on GC electrodes". Electrochem. Comm. **4**, 288-292, 2002.
25. Liu, H. Favier, F. Ng, K. Zach, M. Penner, R. "Size-selective electrodeposition of meso-scale metal particles: a general method". Electrochim. Acta. **47**, 671-677, 2001.

26. Davila-Martinez, R. Cueto, L. Sanchez, E. “Electrochemical deposition of silver nanoparticles on TiO2/FTO thin films”. Surf. Sci. **600**, 3427-3435, 2006.
27. Zarkadas, G. Stergiou, A. Papanastasiou, G. “Influence of citric acid on the silver electrodeposition from aqueous AgNO3 solutions”. Electrochim. Acta. **50**, 5022-5031, 2005.
28. Bonroy, K. Friedt, J. Frederix, F. Laureyn, W. Langerock, S. Campitelli, A. Sára, M. Borghs, G. Goddeeris, B. Declerck, P. “Realization and characterization of porous gold for increased protein coverage on acoustic sensors”. Anal. Chem., **76**, 4299-4306, 2004.
29. Penner, R. “Mesoscopic metal particles and wires by electrodeposition”, J. Phys. Chem. B. **106**, 3339-3353, 2002.
30. Scharifker, B. Hills, G. “Theoretical and experimental studies of multiple nucleation”. Electrochim. Acta. **28,** 879-889, 1983.
31. Sheridan, E. Hjelm, J. Forster, R. “Electrodeposition of gold nanoparticles on fluorine-doped tin oxide: control of particle density and size distribution”. J. Electroanal. Chem. doi: 10.1016/jjelechem.2006.11.015, 2006.
32. Baker, G. Moore, D. “Progress in plasmonic engineering of surface-enhanced Raman-scattering substrates toward ultra-trace analysis”. Anal. Bioanal. Chem. **382**, 1751-1770, 2005.
33. Mie, G. “Contributions to the optics of turbid media, especially colloidal metal solutions”. Annalen der Physik, **25**, 377-445, 1908.
34. Felidj, N. Truong, S. Aubard, J. Levi, G. Krenn, J. Hohenau, A. Leitner, A. Aussenegg, F. “Gold particle interaction in regular arrays probed by surface enhanced Raman scattering”. J. Chem. Phys. **120**, 7141-7146, 2004.